University of Sussex

Strongly-correlated phases in trapped-ion quantum simulators

Pedro Nevado Serrano

Submitted for the degree of Doctor of Philosophy

University of Sussex

March 2017

Esta tesis está dedicada a mi hermano, Gustavo Nevado Celdrán,
que me dijo que sería una locura no hacer este doctorado.
Si algún éxito tengo en esta vida,
que sea tan tuyo como mío.

Declaration

I hereby declare that this thesis has not been and will not be submitted in whole or in part to another University for the award of any other degree.

The original concepts for the projects in this thesis were proposed by Diego Porras, and have been carried out by myself in collaboration with him. Chapters 3 and 4 of this thesis are, respectively, based on the following publications:

- P. Nevado and D. Porras, "Hidden frustrated interactions and quantum annealing in trapped-ion spin-phonon chains", Phys. Rev. A 93, 013625 (2016).

  This paper was written jointly between Diego Porras and myself. The DMRG calculations were performed by Diego Porras, whereas I did the mean-field calculations for the quantum annealing, and the derivation of the effective spin couplings.

- P. Nevado and D. Porras, "Rabi lattice models with discrete gauge symmetry: Phase diagram and implementation in trapped-ion quantum simulators", Phys. Rev. A 92, 013624 (2015).

  This paper was written mainly by myself, with minor adjustments and additions by Diego Porras. I performed the DMRG calculations, as well as the perturbative and variational studies.

Signature:

Pedro Nevado Serrano

UNIVERSITY OF SUSSEX

Pedro Nevado Serrano, Doctor of Philosophy

Strongly-correlated phases in trapped-ion quantum simulators

Summary

We study quantum ($T = 0$) phases of strongly-correlated matter, and their possible implementation in a quantum simulator. We focus on the non-perturbative regimes of 1D spin-boson models. As a reference physical system we consider trapped-ion chains.

We realize complex many-body states, such as a ground state exhibiting magnetic frustration, a lattice gauge theory, and a topological insulator. The exquisite control over these phases offered by a quantum simulator opens up exciting possibilities for exploring the exotic phenomena emerging in these systems, such as enhanced fluctuations and correlations.

We address the non-perturbative regimes of the phase diagrams by means of mean-field theories and the numerical algorithm DMRG. We have established the universality class of the continuous transition in the spin-boson chain, the existence of a first order phase transition when the system is endowed with a gauge symmetry, and the possibility of probing topological states of matter in these systems.

Our results show that some of the most exotic phases of quantum matter can be readily realized in trapped-ion quantum simulators. This offers the possibility of exploring these physical models beyond their original realm of applicability, which may provide us with new insights on both theoretical and applied fields of physics, ranging from high-energy processes to low-energy cooperative phenomena.

Acknowledgements

First and foremost, I would like to thank my supervisor Diego Porras. Four years ago, he gave me the opportunity to embark on the adventure of a PhD, whose fruits are gathered in this thesis. This experience has been enormously rewarding, and I could not be any more grateful.

It has been a privilege to work with Diego. His physical insight and scientific qualities are impressive. He always managed to give me a useful answer to every question I asked him. He has also cared about my career, by helping me to publish my research from the early stages of the PhD, and by offering me advice on the options that lied ahead. Finally, he has taken the trouble to read this thesis, and his suggestions have helped to thoroughly improve this work.

I am greatly indebted to the University of Sussex as well, for providing me with the means, financial and logistic, to make the most of my PhD. The diversity of its students has broadened my horizons, and made me more aware of the issues that different cultures face in their daily life.

On a more personal note, I want to thank the people who have supported me during these four years, or with whom I have shared this journey.

To begin with, I want to acknowledge my family, because of the encouragement they have given to me in the hardest moments. Without them, I would have not had the strength to reach the end.

Tom and Justyna gave me the warmth and love that I needed, whenever I needed it. Their friendship all these years has been very important to me, and I will always remember them with much affection. I hope that our friendship lasts for many years to come. I must thank Irene too, because she accompanied me in the tough beginnings, and Lucía, whose smile lit up many of my Brighton days.

Hiroki and Ezra, with whom I have shared many laughs, deserve my gratitude as well. They have taught me a lot about many things, not only physics. I am

especially honoured of having worked with Hiroki in his idea of a MS gate in a cavity QED architecture. I hope we can keep in touch, to see you thrive.

Graeme, who started the PhD at the same time, has been an invaluable friend all this time. He has tried his best to explain to me some of this country's unfathomable mysteries, and he has all my gratitude.

I want also to remember Tania and Magok, who told me about the gifts of love and the misfortunes of war.

My desk has been a nicer place to work because of Sahar and her many presents, for which I am thankful. I wish you the best of lucks in life.

I am grateful to Claire as well, for lodging me these years, and making my life easy.

Finally, this thesis has benefited from the wise advice of Kathryn, whose guidance on writing this document has made it possible.

Post-viva acknowledgements

I would also like to thank my examiners, Jacob Dunningham and Igor Lesanovsky, for useful discussions and suggestions during the viva voce examination which have helped to greatly improve the published version of this work.

Contents

List of Figures

Chapter 1

Introduction

In our daily life we are surrounded by ordinary, classical matter. Beyond our everyday experience, though, it turns out that quantum matter is as prevalent in nature as its classical counterpart. It is present at the core of neutron stars, which are prevented from collapsing because of the degeneracy pressure, or in the nuclear matter comprising every atomic species. Interactions among the particles that made up both classical and quantum matter render the description of these systems very challenging. In the latter case, though, matters are even more complicated, since quantum particles are indistinguishable, and their behaviour can only be described collectively. This has not prevented us from explaining many interesting instances of quantum matter, as long as they can be described in terms of weakly-interacting collective excitations, or *quasi-particles*. In these cases, we can deal with the interactions by performing a weak coupling expansion about the free quasi-particles. Nevertheless, when interactions are exceedingly large, the weak coupling point of view has to be abandoned. Strong interactions lead to the appearance of strong correlations between the particles, and to the emergence of qualitatively new behaviour compared to weakly interacting systems [1–3].

Phases where strong interactions play a major role often occur in the context of condensed-matter physics. Examples include quantum spin liquids (QSLs) in frustrated magnets[1] [4–7], or topologically ordered phases, such as the fractional quantum Hall states [8], to name a few. Some of these phases are very appealing

[1] Conclusive experimental evidence for these states is still missing, and it heavily depends on the theoretical interpretation.

from the theoretical point of view, since they may exhibit exotic properties such as emergent gauge fields [9] or fractional particle excitations [10]. They are also interesting from a practical point of view, because they could find application in areas such as quantum information processing [11, 12]. Nevertheless, strong correlations are not limited to the realm of low-energy physics. Gauge theories, the conceptual building blocks of the standard model of particle physics [13, 14], may feature strongly-correlated phases as well, such as the quark-gluon plasma of quantum chromodynamics (QCD) [15–17].

The description of strongly-correlated phases from first principles is a highly non-trivial task. One may develop microscopic many-body models that capture the physics of the strongly-correlated phase, but usually they cannot be exactly solved. Furthermore, the computational simulation of these models requires resources that scale up exponentially with the size of the problem, a difficulty that cannot be circumvented with any classical computer [18]. This state of affairs seems to render many-body models intractable, but fortunately quantum technologies have matured up to the point where they can provide us with a novel route to deal with these problems. We can build a device that follows the laws of quantum mechanics, and engineer the interactions in such a system to mimic those of a given model. Then, we can obtain the quantities of physical interest by performing a measurement upon the system. This idea lies at the core of the field of quantum simulation [19, 20], and constitutes the major theme of this thesis.

Our motivation in the present work is to show that the aforementioned phases can be naturally realized in quantum simulators. We study a system hosting enhanced quantum fluctuations and correlations, which are phenomena associated with spin-liquid phases. We also show how to implement a simple instance of a gauge theory, that is a model endowed with a local invariance. Finally, we explain how one can engineer a topological insulator [21–23] that, in spite of being a non-interacting system, is associated with the existence of a bulk invariant, which is one of the defining features of topological order. These models are strung together by the feasibility of implementing them in a particular experimental platform, that will be our reference system along the thesis, and that has emerged as one of the most promising quantum technologies: trapped-ion quantum simulators [24–29].

1.1 Overview of the thesis

This thesis is structured as follows:

- In chapter 2 we summarize the background theory and the methods that we use along the thesis for the study of the different quantum simulations. We begin by introducing the concept of a quantum phase transition, which is closely linked to the occurrence of strongly-correlated phases. We also present the concept of quantum simulation, and describe the specifics of trapped-ion quantum simulators. Finally, we briefly review the numerical algorithm that we have utilized in the thesis to establish the properties of the different strongly-correlated phases, known as the Density Matrix Renormalization Group (DMRG).

- In chapter 3 we introduce the cooperative Jahn-Teller (cJT) model. We begin by illustrating the concept of magnetic frustration, which naturally arises in the ground state of the cJT model. Then, we present the implementation of the model with trapped ions. We discuss the phase diagram of the model, firstly without frustration, and afterwards with frustrated interactions. We study as well an algorithm to prepare the ground state in the presence of frustration, known as quantum annealing. Finally, we present some experimental parameters for the implementation with trapped ions, and the conclusions of the chapter.

- In chapter 4 we introduce the concept of local invariance, and illustrate it in a generalization of the cJT model, known as Ising-Rabi lattice (IR) model. Then we show how to implement the model with trapped ions, and discuss its phase diagram by means of perturbation theory, two variational wave functions, and the DMRG. Finally, we present the experimental parameters for an eventual implementation, and comment on the conclusions of the chapter.

- In chapter 5 we briefly explain what is a topological insulator, and illustrate its properties for the Su-Schrieffer-Heeger (SSH) model. We show how to implement the model with trapped ions. We discuss the effect of the effective interactions on the edge states associated with the topological phase, and present

a protocol to probe them. We also study the many-body ground state, to seek for any trace of the localized components occurring in the one-body spectrum. We present the experimental parameters for an eventual implementation, and the conclusions of the chapter.

- Finally, in chapter 6 we present the main conclusions and the outlooks for further work on these strongly-correlated systems.

1.2 Summary of results

The central theme of this thesis is the simulation of strongly-correlated phases in trapped-ion quantum simulators. Our motivation for studying the particular models covered is the feasibility of their implementation in these systems. We will establish that:

- **The simulation of frustrated interactions is scalable**

  We show that the dressing of the spin interactions associated with trapped-ion quantum matter suffices to induce frustration. This is advantageous with respect to other proposals, since our method does not rely on addressing a specific motional mode, and it is therefore scalable to many ions.

- **The cooperative Jahn-Teller model belongs to the universality class of the quantum Ising chain**

  We study the phase diagram of this model in the regime of strong spin-phonon coupling, departing from the usual simulations of quantum magnetism with trapped ions. By means of numerical calculations with the DMRG we establish the universality class of the spin-phonon chain, a result that had not been properly demonstrated so far, to the best of our knowledge.

- **Features of a quantum spin-liquid phase can occur in trapped-ion quantum matter**

  We show that in the frustrated regime of the cJT model, defined on a finite chain, there is a stable phase exhibiting enhanced quantum fluctuations and correlations, as expected of a QSL.

- **Quantum annealing performs poorly in presence of frustration in the cJT model**

  We carry out a mean-field study of the quantum dynamics in the cJT model under quantum annealing. We show that the algorithm significantly fails to find the ground state whenever this is not uniquely defined. Nevertheless, this study is not completely conclusive about the performance of quantum annealing, since it neglects the quantum correlations.

- **Minimal extensions of the cooperative Jahn-Teller model can realize a gauge theory**

  We show that the phononic degrees of freedom of a trapped-ion quantum simulator can give rise to a local symmetry so that the resulting cJT model no longer belongs to the Ising universality class. We refer to these new class of models as Ising-Rabi lattices, and show that the global symmetry analogous to the parity invariance of the Ising chain is broken all over the phase diagram of the IR lattice.

- **The Ising-Rabi lattice model undergoes a quantum first-order phase transition**

  We establish that the IR lattice presents a level crossing for finite system size, a signature of a first-order phase transition. The absence of a diverging correlation length prevents the classification of the critical behaviour in terms of the paradigm of universality classes. Nevertheless, there are examples of systems undergoing an analogous transition, such as the liquid-gas transition of magnetic monopoles in spin ice [30], or the sudden magnetization jump in metamagnetic samples [31].

- **The engineering of interactions by periodic drivings allows the implementation of a 1D topological insulator**

  We show that dressing the effective spin interactions of the cJT model allows the simulation of a simple instance of a topological insulator, the SSH model. In the long range regime of the spin interactions there is an enhancement of the localization length associated with the topological edge states.

- **The edge states of the Su-Schrieffer-Heeger model survive to the interactions between ions**

  We show that the coupling between ions in the simulation of the SSH model gives rise to a strongly-interacting fermionic model. We study the ground state of the resulting problem, and show that it retains some localization at the edges, at least in the event of short range interactions.

Chapter 2

Theoretical framework and methods

The aim of this chapter is to present the main theoretical concept underlying this thesis: quantum phase transitions. All the strongly-correlated phases that we shall study arise as a result of quantum phase transitions, and therefore we need to introduce the tools to establish their emergence, and to tell the different phases apart. We also motivate the necessity for quantum simulation, that arises not only in the context of strongly-correlated models, but in quantum statistical mechanics or quantum chemistry as well. We later describe the degrees of freedom and the interactions that can be engineered in the experimental systems of reference used in the thesis, trapped-ion quantum simulators. Finally, we summarize the numerical method that we have utilized to gain insight into the physical properties of the 1D systems that we shall study, known as the Density Matrix Renormalization Group [32–35].

2.1 Quantum phase transitions

Our understanding of a strongly-correlated phase begins with the construction of its corresponding many-body model, which is defined by a Hamiltonian. The Hamiltonian depends on the parameters of the model, and changes on these can lead to dramatic qualitative differences in the ground state. The strongly-correlated phase, in particular, may occur in the ground state for specific values of the parameters.

The description of the phases of a model in terms of its parameters is summarized in the phase diagram. Different phases are separated by boundary lines, which signal the appearance of a phase transition [36–40].

Quantum phase transitions happen at zero temperature. They are associated with points in the phase diagram where the energy of the ground state is no longer an analytic function of the parameters. The non-analyticity stems from a level crossing, either appearing at finite system size or in the thermodynamic limit [40].

We will encounter two types of quantum phase transitions in this thesis, which are referred to as *first-* and *second-order* [41]. This nomenclature originates from the order of the first derivative of the energy which is discontinuous at the transition.

First-order phase transitions are characterized by a discontinuity in some observable at the transition. The nature of correlations at phase boundaries does not exhibit a qualitative change, and they decay exponentially with the distance all over the phase diagram. We will encounter an example in chapter 4.

On the other hand, second-order phase transitions are accompanied by a qualitative change in the correlations. Away from the transition, two-point correlators of any observables decay exponentially with the distance, as happens in first-order transitions. However, exactly at the transition, known in this context as the *critical point*, correlations follow a power law [40]. This is associated the divergence of the typical length of the fluctuations or, equivalently, with the vanishing of their typical energy (cf. the relationship between the energy (mass) of a scalar field and the range of the Yukawa potential discussed in appendix A). We will find this type of phase transition in chapter 3.

The power-law behaviour of the correlations is a feature shared with other quantities at criticality, such as the susceptibility to an external field. It turns out that the exponents of these power laws are independent of the microscopic details of the model, and solely depend on its generic symmetries and dimensionality. This phenomenon is characteristic of second-order phase transitions, and is known as *universality* [40]. Two microscopic models sharing the same critical exponents are said to belong to the same *universality class*. We will establish the universality class of the cJT model in chapter 3.

Let us illustrate now a phase transition in a simple example.

2.1.1 Case study: the quantum Ising chain

The quantum Ising chain in a transverse field is one of the simplest examples of a model undergoing a (second-order) phase transition [42]. It can be exactly diagonalized, and it is possible to obtain formulas for the energy of the ground state and the correlations in the thermodynamic limit. Therefore, it will serve us to illustrate the vanishing of the energy of the fluctuations and the non-analyticity of the observables at the transition, and the qualitative change of correlations at criticality.

We can visualize this model as describing a set of interacting spin-1/2 particles, each of them located at one of the N sites of a one-dimensional (1D) chain (cf. Fig. 2.1). The Hamiltonian of the Ising chain is given as

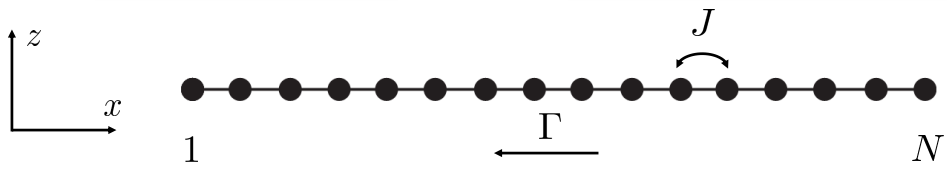

Figure 2.1: Spin chain on which the Ising model is defined. Neighbouring sites are coupled with magnitude J, and an external field is applied in the $-x$ direction.

$$H_{\mathrm{I}} = -J\sum_{j=1}^{N-1}\sigma_j^z\sigma_{j+1}^z - \Gamma\sum_{j=1}^{N}\sigma_j^x, \quad J,\Gamma>0. \tag{2.1}$$

The spin operators correspond to the Pauli matrices

$$\sigma^z = \begin{pmatrix} 1 & 0 \\ 0 & -1 \end{pmatrix}, \quad \sigma^x = \sigma^+ + \sigma^- = \begin{pmatrix} 0 & 1 \\ 0 & 0 \end{pmatrix} + \begin{pmatrix} 0 & 0 \\ 1 & 0 \end{pmatrix}. \tag{2.2}$$

The interaction couples spins in neighbouring sites, and favours their alignment in the z direction, since $-J\sigma_j^z\sigma_{j+1}^z$ assigns a lower energy to states in which spins point parallel to each other. A spin state at site j pointing upwards (downwards) is written as $|\uparrow\rangle_j$ ($|\downarrow\rangle_j$), and fulfils $\langle\sigma_j^z\rangle = +1(-1)$. On the other hand, the former interaction competes against the effect of a transverse field in the $-x$ direction. This field induces the mixing (tunnelling) of states $|\uparrow\rangle_j$ and $|\downarrow\rangle_j$, since $\sigma_j^x = \sigma_j^+ + \sigma_j^-$ flips their orientation.

We can diagonalize the Hamiltonian of the Ising model by mapping the spin operators to fermions, and then applying a canonical transformation to render a

representation which is diagonal in the fermionic operators. The necessity of this mapping stems from the fact that there is no canonical transformation respecting the mixed commutation relations associated with σ_j^+ and σ_j^-; they behave as fermions, since

$$\left\{\sigma_j^-, \sigma_j^+\right\} = 1, \quad \left(\sigma_j^+\right)^2 = \left(\sigma_j^-\right)^2 = 0, \tag{2.3}$$

and, simultaneously, as bosons, since

$$\left[\sigma_j^+, \sigma_k^-\right] = \left[\sigma_j^+, \sigma_k^+\right] = \left[\sigma_j^-, \sigma_k^-\right] = 0, \quad j \neq k. \tag{2.4}$$

Fortunately, it is possible to express the raising and lowering spin operators in terms of solely fermionic creation and annihilation operators $c_j^\dagger$ and c_j. The fermionic vacuum is then identified with the spin state $|\downarrow\rangle_j$. This is known as the Jordan-Wigner transformation [43], and allows the exact solution of many spin problems, such as the XY model [44], or the Kitaev honeycomb model [45]. It is usually stated as

$$\begin{aligned} \sigma_1^- &= c_1, \quad \sigma_i^- = \prod_{j=1}^{i-1}(1-2c_j^\dagger c_j)c_i \quad (i=2,\ldots,N), \\ \sigma_1^+ &= c_1^\dagger, \quad \sigma_i^+ = c_i^\dagger \prod_{j=1}^{i-1}(1-2c_j^\dagger c_j) \quad (i=2,\ldots,N). \end{aligned} \tag{2.5}$$

The string of operators $\prod_{j=1}^{i-1}(1-2c_j^\dagger c_j)$ compensates for the anticommutation of fermions under exchange. Before applying this mapping to H_{I}, it is customary to rotate the system, so that $\sigma_j^x \to \sigma_j^z$, $\sigma_j^z \to \sigma_j^x$. Also, the Hamiltonian is scaled with Γ, and we define the parameter $\lambda = J/\Gamma$. Assuming Periodic Boundary Conditions (PBC) for our spin chain,

$$H_{\mathrm{I}} = -\lambda \sum_{j=1}^{N} \sigma_j^x \sigma_{j+1}^x - \sum_{j=1}^{N} \sigma_j^z, \quad \sigma_{N+1}^\alpha = \sigma_1^\alpha. \tag{2.6}$$

We perform now the Jordan-Wigner transformation, and thus

$$H_{\mathrm{I}} = N - 2\sum_{j=1}^{N} c_j^\dagger c_j - \lambda \sum_{j=1}^{N} (c_j^\dagger - c_j)(c_{j+1}^\dagger + c_{j+1}) - \lambda (c_N^\dagger - c_N)(c_1^\dagger + c_1)(e^{i\pi L}+1), \tag{2.7}$$

where $L = \sum_{j=1}^{N} c_j^\dagger c_j$. For simplicity, we will ignore the last term on the grounds that its contribution is negligible in the thermodynamic limit. Now we consider

fermions in momentum space

$$c_q = \frac{1}{\sqrt{N}} \sum_{j=1}^{N} c_j e^{iqj}, \qquad c_q^\dagger = \frac{1}{\sqrt{N}} \sum_{j=1}^{N} c_j^\dagger e^{-iqj}, \tag{2.8}$$

where $q = 2\pi m/N$, and $m = -N/2, \ldots, N/2$. The Hamiltonian becomes

$$H_{\rm I} = N - 2\sum_q (1 + \lambda \cos q) c_q^\dagger c_q - \lambda \sum_q (e^{-iq} c_q^\dagger c_{-q}^\dagger - e^{iq} c_q c_{-q}). \tag{2.9}$$

In terms of $q > 0$ modes only, the Hamiltonian can be recast as

$$H_{\rm I} = -2\sum_{q>0} \left(c_q^\dagger, c_{-q}\right) \begin{pmatrix} 1 + \lambda \cos q & -i\lambda \sin q \\ i\lambda \sin q & -(1 + \lambda \cos q) \end{pmatrix} \begin{pmatrix} c_q \\ c_{-q}^\dagger \end{pmatrix}, \tag{2.10}$$

where the constant N has been exactly cancelled by using that $c_{-q}^\dagger c_{-q} = 1 - c_{-q} c_{-q}^\dagger$. The former manipulations have allowed us to write $H_{\rm I}$ as a sum of $N/2$ decoupled problems, labelled by the wave vector q. Each of these problems can be diagonalized by a Bogoliubov transformation [43], which is a canonical transformation of the operators $c_q^\dagger$ and c_q into a linear combination of new operators $\eta_q^\dagger$ and η_q. We skip the details of this last step, that can be found in [42], and present the final form of the Hamiltonian,

$$H_{\rm I} = 2\sum_q \omega_q \eta_q^\dagger \eta_q + E_0, \quad E_0 = -\sum_q \omega_q. \tag{2.11}$$

where $\omega_q = \sqrt{1 + 2\lambda \cos q + \lambda^2}$.

The diagonalized form of the Hamiltonian in (2.11) allows us to compute all the observables of the model. To begin with, we see that the energy of any single excitation about the ground state is dictated by its dispersion relation ω_q. There is always a finite energy gap in the excitation spectrum, with the only exception of $\lambda \equiv \lambda_{\rm c} = 1$ for wave vector $q = \pi$, since in this case

$$\omega_{q \to \pi} = |1 - \lambda|. \tag{2.12}$$

The vanishing of the energy of the fluctuations at $\lambda = \lambda_{\rm c}$ indicates the emergence of the quantum phase transition. On the other hand, to characterize the phases at both sides, it is customary to attend at the presence or absence of long-range order,

that is, if distant points in the system fluctuate in a correlated manner [40]. The measure of the degree of order in a system is associated with an *order parameter*, which is defined so that it only takes non-zero values in the ordered phase. The form of the order parameter depends on the specificities of every particular system. In the case of the Ising chain, it is given by the magnetization perpendicular to the external field, that can be computed from the exact solution as [42]

$$\langle \sigma_j^x \rangle = \pm(1-\lambda^{-2})^{1/8}, \lambda > 1; \quad \langle \sigma_j^x \rangle = 0, \lambda < 1, \tag{2.13}$$

where the sign freedom stems from the parity symmetry of the interaction term. As can be seen from Fig. 2.2, the order parameter takes a non-zero value only for

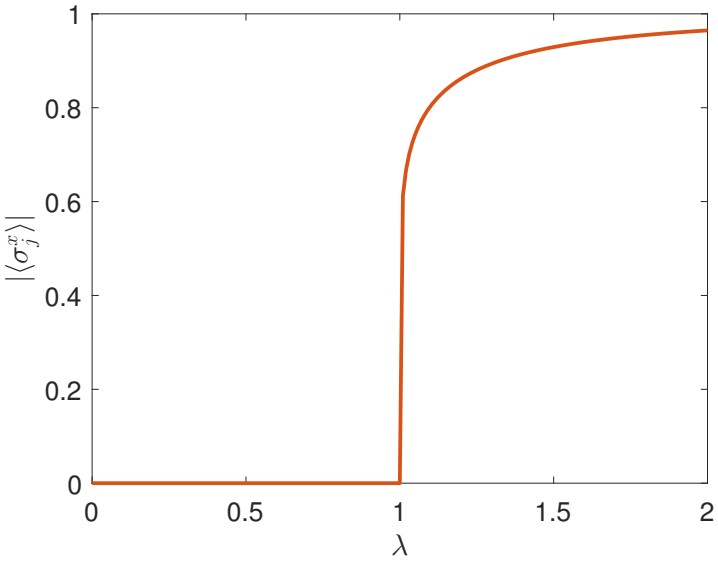

Figure 2.2: Expectation value of the operator σ_j^x upon the ground state of the quantum Ising chain.

$\lambda > 1$. We note that close to the transition the magnetization follows a power-law, whose exponent is $\beta = 1/8$. This is one of the critical exponents of the Ising model.

We see that the order parameter is a continuous function at the transition, although its first derivative is discontinuous. This is shared by other quantities at criticality and is a consequence of the thermodynamic limit. Let us illustrate this for the energy of the ground state, that is given by E_0. We note that this energy is a sum of continuous functions, and therefore analytic in the parameter λ. Nevertheless, this situation may change when $N \to \infty$. In that case, the energy can be expressed

in terms of the elliptic integral of the second kind [46, 47]

$$\mathcal{E}(\phi,\theta) \equiv \int_0^{\phi} \sqrt{1-\theta^2\sin^2 k}\,dk, \tag{2.14}$$

so that

$$-\frac{E_0}{N} = \frac{2}{\pi}(1+\lambda)\mathcal{E}\left(\frac{\pi}{2},\theta\right); \quad \theta^2 = \frac{4\lambda}{(1+\lambda)^2}. \tag{2.15}$$

We have plotted this expression in Fig. 2.3, along with its derivatives. We note that

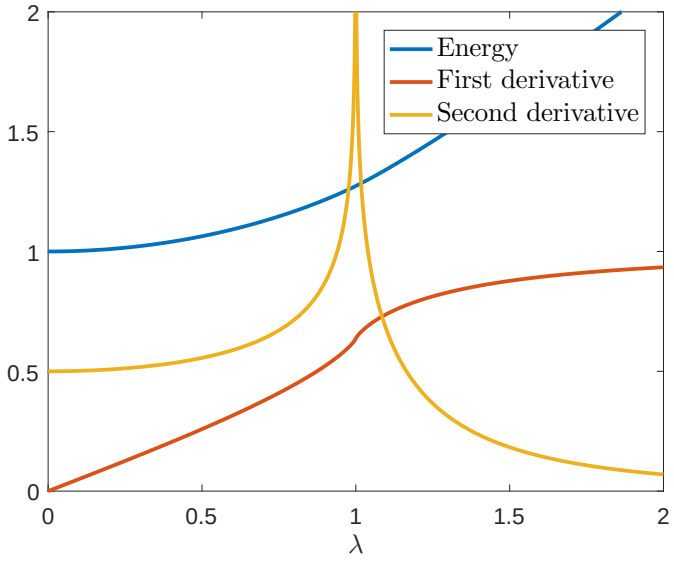

Figure 2.3: Energy (2.15) as a function of the parameter λ, along with its first and second derivatives. We note the discontinuity at the transition $\lambda = \lambda_c$.

E_0 is no longer an analytic function of λ for $\lambda_c = 1$, since the *second derivative* is discontinuous at that point. This illustrates the fact that phase transitions strictly appear in the thermodynamic limit.

The range of fluctuations upon the ground state is given by the correlations [40]. In the transverse direction, for instance, fluctuations are measured by the connected correlator

$$C^{zz}_{j,l} = \langle\sigma^z_j\sigma^z_l\rangle - \langle\sigma^z_j\rangle\langle\sigma^z_l\rangle. \tag{2.16}$$

This quantity can be computed from the exact solution in terms of the Jordan-Wigner fermions. One must make use of Wick's theorem [48] to express four-fermion expectation values as products of two-fermions; details can be found in [42]. Finally, one obtains $C^{zz}_{j,l} = G^2_{j,l}$, where

$$G_{j-l} = \int_{-\pi}^{\pi} \frac{dq}{2\pi} e^{iq(j-l)} \left(\frac{1+\lambda e^{iq}}{1+\lambda e^{-iq}}\right)^{1/2}. \tag{2.17}$$

We plot this expression in Fig. 2.4. It admits a closed form at the critical value $\lambda_c = 1$, where it decays with the distance as a power law

$$C^{zz}_{j,l} = \frac{4}{\pi^2}\frac{1}{4|j-l|^2-1}. \tag{2.18}$$

This result has the important consequence that fluctuations are scale free, since there is no typical length appearing in $C^{zz}_{j,l}$. Also, this provides us with another critical exponent[1], as $C^{zz}_{j,l} \sim |j-l|^{-\nu}$, and $\nu = 2$ (cf. Fig. 2.4). We will use this result in chapter 3 to establish that the cJT model belongs to the same universality class of the Ising chain. Outside criticality there is no closed form of $C^{zz}_{j,l}$, but we see from Fig. 2.4 that $C^{zz}_{j,l} \sim Ae^{-|j-l|/\xi}$, with finite correlation length ξ. In this case, fluctuations in the system have a typical length associated with them, and they are restricted to a particular scale.

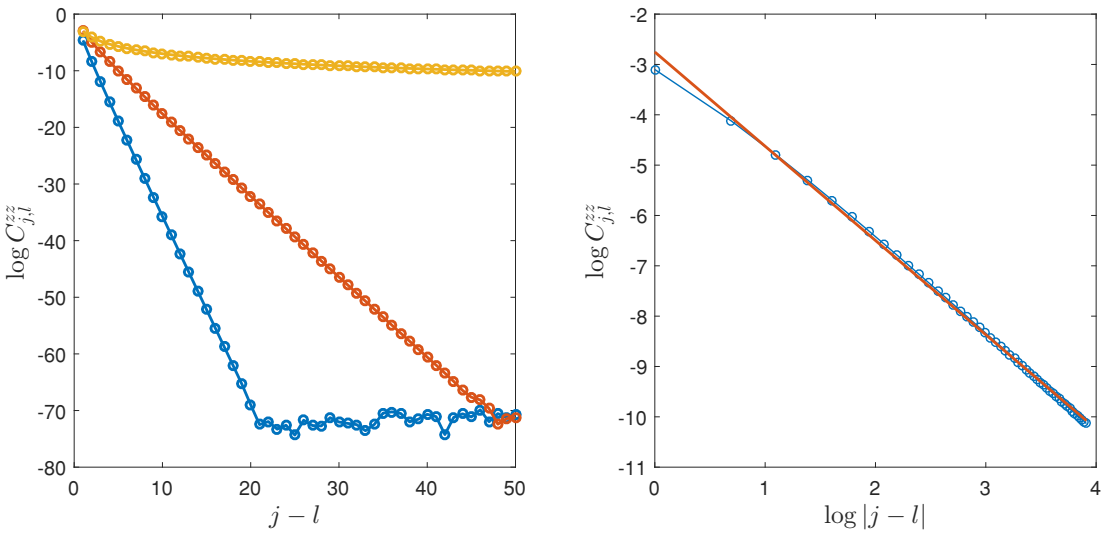

Figure 2.4: (Left panel) Semi-log plot of the correlations $C^{zz}_{j,l}$ on the ground state, for $\lambda = 0.2$ (blue line), 0.5 (red line) and 1 (yellow line). Outside the critical value the correlations follow an exponential decay. (Right panel) Log-log plot of the correlations for $\lambda = \lambda_c = 1$. We fit the result to a line, whose slope is $-2 \implies \nu = 2$.

The availability of the exact solution for the Ising model has provided us with exact values for the observables. Typically, however, many-body models cannot be exactly diagonalized, and one must rely on approximations to describe qualitatively

[1]Although we do not follow this convention, it is customary to use the greek letter ν for the exponent of the correlation length.

their phase diagrams. The standard procedure in the context of quantum phase transitions is known as mean-field theory, which involves replacing all the interactions by an average, or *mean-field* [40]. Equivalently, the mean-field approximation neglects any quantum correlations, meaning that $C^{zz}_{j,l} \equiv 0$ in this approximation.

2.1.2 Mean-field theory

We will use a mean-field theory in conjunction with the variational method [49–51] to investigate the phases of the Ising-Rabi lattice model in chapter 4. It is known that mean-field theory is a poor approximation for systems below four dimensions, or may even lead to wrong results [52, 53]. Therefore, we will have to support any mean-field prediction with numerical and/or perturbative arguments. In particular, the Density Matrix Renormalization Group will be our method of choice to establish solid evidences about the phases being investigated.

The variational method is a technique to approximate the wave function of the ground state. It begins by assuming a particular form for the wave function, an *ansatz*, which is defined in terms of some parameters. One computes the energy upon this ansatz, which in the mean-field approximation contains no correlations. The energy is minimized with respect to the parameters of the ansatz. The wave function, for the values that optimally minimize the energy, is the closest approximation to the actual ground state that can be attained with that ansatz.

We can illustrate the former ideas in the particular case of the quantum Ising chain. To investigate the existence of a phase transition in H_{I}, as given in (2.1), we use a trial wave function to approximate the actual ground state. Let us assume the ansatz

$$|\Psi_{\mathrm{MF}}\rangle = \bigotimes_{j=1}^{N} \left(\cos\frac{\theta_j}{2} |\uparrow\rangle_j + \sin\frac{\theta_j}{2} |\downarrow\rangle_j \right), \tag{2.19}$$

which it is a separable wave function of spin states at every site of the chain. This structure neglects correlations between different sites, and therefore $|\Psi_{\mathrm{MF}}\rangle$ is a mean-field ansatz. Assuming Periodic Boundary Conditions (PBC), and that the ground state is homogeneous, the mean-field energy per spin is given as

$$E_{\mathrm{MF}}(\theta) = -J\cos^2\theta - \Gamma\sin\theta. \tag{2.20}$$

This expression attains a minimum whenever $\cos\theta = 0$, unless

$$\sin\theta = \frac{\Gamma}{2J} \leq 1. \tag{2.21}$$

The former result shows that the Ising model undergoes a quantum phase transition at a critical field $\Gamma_c = 2J$. This prediction is qualitatively correct, as we know from the exact solution, but the position of the critical point within mean-field theory is *twice* the actual value. The variational wave function for the values of θ that minimize $E_{\rm MF}$ provides the mean-field ground state, in terms of which we can define

- **The ferromagnetic phase,** $\Gamma \leq \Gamma_c$

$$|\Psi_{\rm MF}\rangle = \bigotimes_{j=1}^{N} \left(\frac{\Gamma}{2J} |\uparrow\rangle_j + \sqrt{1 - \frac{\Gamma^2}{4J^2}} |\downarrow\rangle_j \right), \tag{2.22}$$

- **The paramagnetic phase,** $\Gamma \geq \Gamma_c$

$$|\Psi_{\rm MF}\rangle = \bigotimes_{j=1}^{N} \frac{1}{\sqrt{2}} \left(|\uparrow\rangle_j + |\downarrow\rangle_j \right). \tag{2.23}$$

If we evaluate the magnetization upon the ansatz (2.19), and take into account Eq. (2.21), we have that

$$\langle \Psi_{\rm MF} | \sigma_j^z | \Psi_{\rm MF} \rangle = \cos\theta = \sqrt{1 - \frac{\Gamma^2}{4J^2}}, \quad \Gamma \leq 2J. \tag{2.24}$$

This must be compared with the exact magnetization (2.13), which is given in the rotated basis $\sigma_j^x \to \sigma_j^z$, $\sigma_j^z \to \sigma_j^x$. We see that the exponent of the magnetization in mean-field, $\beta_{\rm MF} = 1/2$, differs from the exact value of $\beta = 1/8$. Again, we find a numerical mismatch between an exact value and the mean-field prediction. This issue is even worse in the case of the exponent of the correlator $C_{j,l}^{zz}$, since the current mean-field treatment does not predict any dependence on j, l for this quantity.

In spite of these shortcomings, the qualitative insight gained from mean-field theory, supplemented with a numerical calculation of the critical exponents, is a standard procedure to establish the physical properties of many models [40]. For completeness we will mention that there is a technique beyond mean-field theory that would allow us to get the correct value of β, or to compute the exponent of $C_{j,l}^{zz}$. In Landau theory of phase transitions [54, 55], we promote the order parameter to a field $\phi(x)$ which, most importantly, can depend on the position. This field can be

understood as a coarse-grained average of the order parameter. The description of the phase transition in terms of $\phi(x)$ is motivated by the divergence of the length scale of fluctuations. Its value upon the ground state is obtained by minimizing a certain energy functional $\mathcal{F}[\phi(x)]$ [40]. Landau theory below four dimensions requires the use of the renormalization group to render physical results [56]. Although these considerations lie beyond the scope of this thesis, there is one aspect of Landau theory that we need to introduce. Phases that exhibit long-range order can sometimes be associated with the concept of a broken symmetry. Considerations based on the symmetries of the ground state and the Hamiltonian are very general, and prove very useful to tell different phases apart. Thus, we finish this introduction to phase transitions with an illustration of these aspects.

2.1.3 Spontaneous symmetry breaking

If the Hamiltonian H of a many-body model is invariant under a transformation P, such that $[H, P] = 0$, the ground state is simultaneously an eigenstate of H and P [49–51]. This is strictly true only for finite systems, though. Conversely, in the thermodynamic limit there may be states which are no longer invariant under P, but still minimize the energy [54, 55]. We say that in this case the symmetry is *spontaneously broken*. Very often spontaneous symmetry breaking occurs only at one side of the phase transition, and therefore it becomes a powerful tool to distinguish different phases.

Let us use the Ising model again to illustrate these ideas. We note that H_{I} is invariant under the transformation $\sigma_j^z \to -\sigma_j^z$. This parity symmetry is generated by the operator $P = \otimes_{j=1}^{N} \sigma_j^x$, and since $[H_{\mathrm{I}}, P] = 0$, the ground state $|\Psi\rangle$ must fulfil $P|\Psi\rangle \propto |\Psi\rangle$. Actually, since $P^2 = \mathbb{I}$ and $P^\dagger = P$, we have that $P|\Psi\rangle = \pm|\Psi\rangle$. One consequence of this is that the magnetization in the z direction is zero all over the phase diagram

$$\langle\Psi|\sigma_j^z|\Psi\rangle = \langle\Psi|P^2\sigma_j^z P^2|\Psi\rangle = -\langle\Psi|\sigma_j^z|\Psi\rangle \implies \langle\Psi|\sigma_j^z|\Psi\rangle = 0. \tag{2.25}$$

Nevertheless, we have claimed that this argument may break down in the thermodynamic limit. To see if this is the case, we are going to carry out a perturbation

theory in Γ upon the exact ferromagnetic eigenstates at zero field, that are given as

$$|\uparrow\rangle \equiv \bigotimes_{j=1}^{N} |\uparrow\rangle_j \,, \quad |\downarrow\rangle \equiv \bigotimes_{j=1}^{N} |\downarrow\rangle_j \,. \tag{2.26}$$

We note that these states break the parity, so our aim is to show that the symmetry breaking remains for finite Γ.

States (2.26) are degenerate, with energy $E_0 = -NJ$ (we assume PBC). The effect of a small transverse field Γ must be dealt within the framework of degenerate perturbation theory [49–51], which shows that degeneracy is lifted at order N, and that $|\uparrow\rangle$ and $|\downarrow\rangle$ get mixed with an amplitude

$$\Delta = \Gamma^N \sum_{\substack{n_1,n_2,\ldots,n_{N-1} \\ j_1,j_2,\ldots,j_{N-1}}} \frac{\langle\uparrow| \sigma^x_{j_1} |n_1\rangle \langle n_1| \sigma^x_{j_2} |n_2\rangle \langle n_2| \cdots |n_{N-1}\rangle \langle n_{N-1}| \sigma^x_{j_{N-1}} |\downarrow\rangle}{(E_{n_1} - E_0)(E_{n_2} - E_0) \cdots (E_{n_{N-1}} - E_0)}. \tag{2.27}$$

The n_i label all the eigenstates of H_{I} for zero transverse field apart from $|\uparrow\rangle$ and $|\downarrow\rangle$. Because of the action of σ^x_j, (2.27) is non-zero if and only if $|n_i\rangle$ are comprised of all the spins to the left of site j pointing upwards, and all the spins to the right pointing downwards. It is straightforward to see that $E_{n_i} - E_0 = 2J \,\forall i$ and, thus,

$$\Delta = \left(\frac{\Gamma}{2J}\right)^N . \tag{2.28}$$

This prediction holds only deep in the ferromagnetic phase, where we can assume that $\Gamma \ll 2J$. In this case, the limit $N \to \infty$ has a very important consequence: the tunnelling amplitude between states $|\uparrow\rangle$ and $|\downarrow\rangle$ becomes zero, and they are degenerate for finite values of the transverse field. This degeneracy makes these states infinitesimally susceptible to fluctuations, and the system chooses as minimum energy configuration only one of the two. This illustrates the spontaneous breaking of the parity symmetry.

2.2 Quantum simulation

The exact solution of the quantum Ising chain has provided us with all the information about the model. In particular, we have been able to extract the value of the exponent in the power-law decay of the correlations at the transition. Other quantities, such as the magnetization or the susceptibility, also follow power laws at criticality [42], whose exponents can be equally read from the exact solution.

The importance of knowing all the critical exponents can hardly be overemphasized, since they determine the physical properties of the systems described by the quantum Ising model. Real examples include ferroelectrics[2] such as KH_2PO_4 [57], or ferromagnets[3] such as $CoNb_2O_6$ [58].

The availability of an exact solution is the exception and not the rule for many-body models. Without a solution, there are still analytical techniques, such as the renormalization group [56], that may offer some insight into the nature of the phase transition. Ultimately, though, one must rely on numerical simulations to get an accurate value for the critical exponents. Unfortunately, the complexity of simulating quantum systems with classical computers is in many cases insurmountable, as already noted by Feynman at the dawn of the computer simulations of physical problems [18]. The underlying reason for this complexity is actually easy to illustrate.

Let us imagine that we have a Hamiltonian H of a many-body model. We want to calculate the values of some observables upon its ground state $|\Psi\rangle$. In the absence of an analytical solution, we can try to find $|\Psi\rangle$ by diagonalizing the matrix representation of H in a computer. Assuming that the model is defined on a chain with L sites, and that the dimension of the Hilbert space at every site is N_{site}, the size of the total state space is given as N_{site}^L. This means that we need N_{site}^L numbers to describe $|\Psi\rangle$. Because this quantity increases exponentially with the system size, the dimension of the state space becomes unmanageable already for modest numbers of particles. Some methods have managed to cleverly bypass this issue, such as Monte Carlo simulations [59], but it is known that they cannot deal with fermionic or frustrated problems for dimensions 2 or more, because of the so-called sign problem [60].

Therefore, in general we are faced with the necessity of an exponentially large amount of resources for the classical simulation of many-body problems. This prevents us from gaining any insight into many interesting phase transitions and universality classes. Fortunately, though, Feynman also pointed a possible solution to

[2] A ferroelectric material is defined by having a spontaneous electric polarization in absence of an external electric field.

[3] A ferromagnet presents spontaneous magnetic polarization in absence of external magnetic fields.

this problem [18]. He suggested to use 'quantum simulators', devices which function following the laws of quantum mechanics. Such a device, composed of the same degrees of freedom as the model we want to simulate, must allow us to engineer the interaction between them, so that to mimic the model Hamiltonian. In this way, the value of any physical observable is read at the end of the process by performing suitable measurements [61–64].

The potential applications of quantum simulators are not limited to the study of phase transitions, and encompass many problems in condensed-matter physics, quantum statistical mechanics, high-energy physics or quantum chemistry [63]. For instance, being able to perform exact calculations of the molecular electronic Hamiltonian of a generic stable molecule would revolutionize quantum chemistry, and could have a deep industrial impact. These kind of computations are seemingly intractable for classical algorithms, but quantum simulators have been shown to provide us with the possibility of tackling these problems [65, 66]. Furthermore, chemical reactions are dynamical processes, and there is evidence that simulation of generic quantum long-time dynamics cannot be performed efficiently by classical means either [67]. Quantum simulation would consequently emerge as the only practical tool to answer these questions.

Nevertheless, a quantum simulator is not only interesting because it may outperform the computational capabilities of classical machines. A very promising avenue is the realization of many-body models which may not correspond with any real physical system, but can be used as test-beds of numerical methods or approximations. Furthermore, this opens up the possibility of exploring completely new physical models, or parameter regimes that are unattainable in real systems.

Any quantum simulation of a many-body model requires, primarily, of suitable quantum degrees of freedom. These can correspond with many different physical systems. In addition, the simulation of any model hosting a strongly-correlated phase must consist of the following three steps:

Initialization: The simulator is prepared in a state that is easy to realize experimentally. Usually, this is the ground state of a trivial limit of the many-body model.

Implementation of the interactions: The Hamiltonian is physically realized by

engineering the interactions between the particles, or between these and external fields. Usually its role is to drive the system from the initial state into a target state of the many-body model.

Detection: The strongly-correlated phase is probed by performing suitable measurements upon the final state.

Quantum simulators benefit from the possibility of representing and manipulating large amounts of information in a relatively small number of degrees of freedom. For instance, the exponentially large amount of numbers (2^N) required to specify the state of a system of N spin-1/2 particles can be encoded in an amount of qubits which are a polynomial function of N. The key for the success of quantum simulation is, thus, being able to realize the initial-state preparation, the implementation of the evolution, and the measurement with polynomial resources. Depending on how this is done we distinguish two classes of quantum simulations, that we introduce now.

2.2.1 Analogue and digital quantum simulation

Feynman originally devised using quantum computers to simulate quantum systems [18]. A quantum computer is any generic device comprised of quantum degrees of freedom, that exploits quantum features such as the superposition principle and entanglement to carry out computational tasks more efficiently than any classical machine [68]. A quantum computer can act as an universal quantum simulator, meaning that it can be programmed to simulate any quantum system. This intuition was put on solid ground by Seth Lloyd [61], making use of the result that any local Hamiltonian can be realized as a finite sequence of quantum gates. A local Hamiltonian is of the form

$$H = \sum_{i=1}^{\ell} h_i \tag{2.29}$$

where each h_i acts on a Hilbert space of dimension m_i, comprised of at most k operators. He showed that the number of gates necessary to implement the dynamics generated by H scales polynomially with the number of particles. Therefore, the evolution of any quantum system can be efficiently simulated.

The idea behind Lloyd's argument is the following. Let us imagine that we are given a many-body model whose Hamiltonian is of the form (2.29), and an initial

state $|\Psi(0)\rangle$. We want to determine the physical properties of the state at some later time t, and therefore we need to compute $|\Psi(t)\rangle = e^{itH}|\Psi(0)\rangle$. To avoid storing the exponentially large amount of numbers associated with $|\Psi(0)\rangle$, we encode it in the computational basis in terms of qubits [69]. Then we apply the Trotter formula to approximate e^{itH} by [69]

$$e^{itH} \approx \left(e^{ith_1/n} \cdots e^{ith_\ell/n}\right)^n . \tag{2.30}$$

This formula shows that the dynamics under H is equivalent to the repeated application of the terms $e^{ith_i/n}$, in n time slices of duration t/n. The insight of Lloyd was to note that the simulation of h_i only requires $O(m_i^2)$ operations, and therefore the total computational overhead is $O(n\ell m^2)$, where $m \equiv \max_i m_i$. For typical local interactions, $\ell \propto N$, the number of degrees of freedom [61]. Thus, simulating e^{itH} only needs an amount of resources scaling polynomially in the system size. Of course, the time-slicing of the evolution introduces an error, but it can be made as small as desired by making n sufficiently large[4] [61]. The final state is then appropriately measured to extract the desired physical properties. However, there is a caveat to be made with regards to this process. If we were to recover all the parameters comprising the state, this would require again the storage of an exponentially large set of numbers. Therefore, we need quantum algorithms for the direct estimation of quantities of physical interest, such as energies or correlation functions [70, 71].

The process of sequentially applying logic operations to the state in the computational basis is analogous to the functioning of any digital device, and has been consequently named as digital quantum simulation [72–80]. In principle, a digital quantum simulator would be able to simulate any Hamiltonian, by reducing it to a combination of simple quantum gates. We can illustrate this fact for the simulation of e^{itH}, where H is a three-body Hamiltonian such as $H = \otimes_{j=1}^{3}\sigma_j^z$, and whose corresponding quantum circuit is shown in Fig. 2.5. We note that although H involves a term with three operators, it can be reduced to a sequence of two- and one-qubit gates. It is clear, however, that a digital quantum simulator would be as difficult to build as a quantum computer. In particular, it would require the full control of the quantum many-body system, and the implementation of error-correction protocols to achieve fault tolerance [63]. These are still long-term goals, although some digital

[4] So long as it does not get exponentially large.

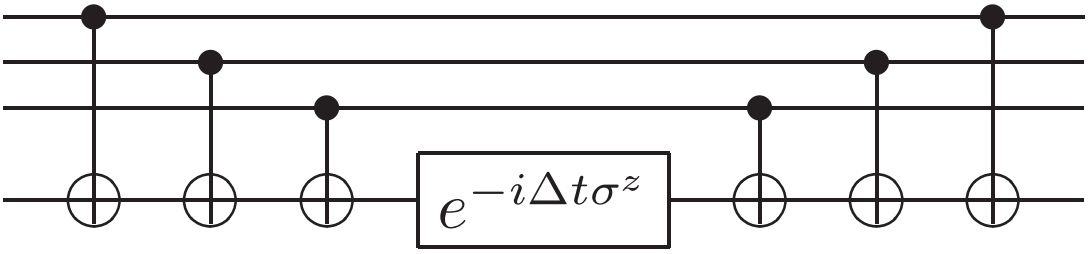

Figure 2.5: Quantum circuit for the simulation of the Hamiltonian $H = \sigma_1^z \otimes \sigma_2^z \otimes \sigma_3^z$. The circles represent CNOT gates, whose action is given as $|c\rangle|t\rangle \rightarrow |c\rangle|t \oplus c\rangle$. The circuit works by computing the parity of the state of the three upper qubits, storing it in the fourth (ancilla) qubit, applying the phase shift to the ancilla, and then undoing the parity operations to revert the ancilla to its initial state. (Image reproduced from ref. [64]).

quantum simulations have been performed for modest ($\sim$ 10 qubits) system sizes [81, 82].

If we leave momentarily aside the idea of building a full quantum computer, and focus on simulating certain physical systems that cannot be classically simulated, we may still obtain a device able to provide answers to interesting questions. In opposition to digital simulation, the approach of implementing specific models with synthetic degrees of freedom is known as analogue quantum simulation [83–87]. Analogue quantum simulators are based on the physical identification of the Hamiltonian of the model to be simulated and the Hamiltonian describing the quantum simulator. This mapping may be straightforward, as for the Hamiltonian describing the atoms trapped in an optical lattice, which is already a Bose-Hubbard model [88]. On the other hand, one can also identify different degrees of freedom, and engineer interactions in the quantum simulator that account for those in the target model. A nice illustration of this case is the simulation of the Dirac equation with a single trapped ion [89, 90]. One identifies the dynamics of the electron with that of the effective spin located in the ion. In this way, the physics associated with the relativistic particle can be studied in a non-relativistic quantum system [91].

Errors and decoherence may hinder the reliability of a quantum simulation [92]. Analogue simulators, however, can operate in the presence of errors up to a certain

tolerance level, and still offer meaningful information. A phase transition, for instance, can be at least qualitatively established even if the control over the tuning parameters is not completely accurate [64]. Regarding decoherence, it places an upper bound for the time scales of the simulation. For many analogue quantum simulators this bound is not critical: trapped-ion experiments, for instance, have durations of μs [93], whereas qubit coherence times are of the order of ms [94].

The main element required to realize a quantum simulator is the availability of quantum degrees of freedom. These can correspond with many different physical systems. This thesis is concerned with trapped-ion analogue quantum simulators, whose physics we describe in detail in section 2.3. Nevertheless, many different systems can be used for this purpose. We refrain from giving a thorough account of all of them, and refer the interested reader to the review article [64]. For illustration purposes, we will mention the effective degrees of freedom and typical models arising in trapped ultracold atoms [95–99] and superconducting circuits [100–103], since the effective physics that can be realized in these systems is similar to the one encountered in trapped-ion simulators.

2.2.2 Experimental platforms

Ultracold atoms trapped in optical lattices [95–99] are well-suited for the simulation of strongly-correlated phases, since they allow the manipulation of large numbers of particles. For instance, the superfluid-Mott insulator transition in the Bose-Hubbard model (cf. Fig. 2.6) has been realized in a 3D optical lattice with ~ 65 lattice sites

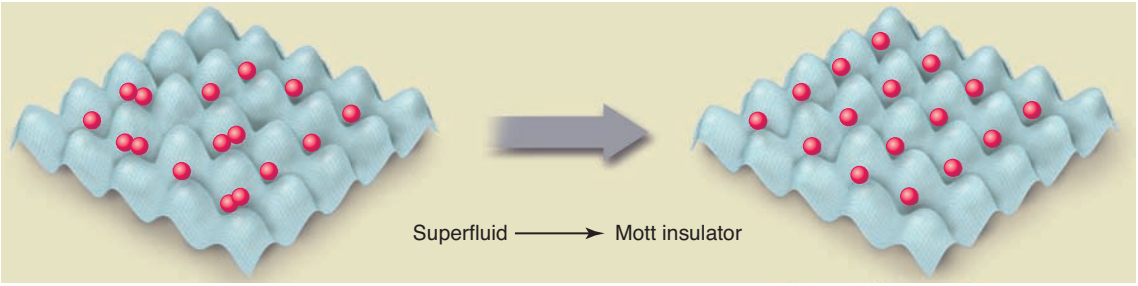

Figure 2.6: Ground-state phase transition of the Bose-Hubbard Hamiltonian (2.31) of cold atoms in an optical lattice. In the superfluid phase the atoms are delocalized all over the lattice, whereas in the Mott-insulating regime they are pinned to the sites of the lattice. (Image reproduced from ref. [62]).

in every direction [104]. Flexibility in the geometry of the trapping potentials makes possible to create intricate arrangements, such as triangular or kagome lattices [105]. The typical degrees of freedom available in these systems are fermions and bosons, which are directly realized by loading fermionic or bosonic species into the lattice. For example, the dynamics of an interacting boson gas in a lattice potential is given by the Bose-Hubbard Hamiltonian

$$H_{\mathrm{BH}} = -J \sum_{\langle j,l \rangle} a_j^\dagger a_l + \sum_j \epsilon_j n_j + \frac{1}{2} U \sum_j n_j (n_j - 1). \tag{2.31}$$

Operators $a_j^\dagger$ and a_j correspond to bosonic creation and annihilation operators of atoms at site j, $n_j = a_j^\dagger a_j$, ϵ_j denotes the local energy offset stemming from the harmonic trapping potential, U is the magnitude of the on-site repulsion, and J gives the strength of the tunnelling between neighbouring sites. For $U/J \ll 1$ (superfluid phase), the atoms delocalize all over the lattice, and they can be described by a macroscopic wave function with long-range phase coherence. For $U/J \gg 1$ (Mott-insulating phase), a fixed number of atoms pin to every site of the lattice. This state has no phase coherence, but there is a correlation between the number of atoms between lattice sites. One can study as well the effect of artificial gauge fields (e.g., a magnetic field), which are incorporated by site-dependent phases into the operators, so that $a_j \to a_j e^{i\Delta_j}$. They are implemented by rotation of the trapping potentials [98], or by periodic driving of the confining forces [106]. These systems suffer from the difficulty of individual particle addressing with laser fields, since typical lattice constants are of hundreds of nm [104]. This hinders the measurement of interesting observables like correlators, or the preparation of localized excitations for the study of their dynamics. Nevertheless, current efforts are devoted to overcome this issue [107]. Finally, cold gases in optical lattices can realize spin systems as well [96]. For instance, it should be possible to simulate the Kitaev model [45],

$$H_{\mathrm{Kitaev}} = \sum_{j+l:\mathrm{even}} \left(J_\perp \sigma_{j,l}^x \sigma_{j+1,l}^x + J_\perp \sigma_{j-1,l}^y \sigma_{j,l}^y + J_z \sigma_{j,l}^z \sigma_{j,l+1}^z \right), \tag{2.32}$$

by trapping polar molecules [108], and using an electric-field to induce the interaction between their dipole moments, which realizes the spin couplings. Another possibility is given by exploiting the large dipole moments of Rydberg atoms [109], that could be used to realize exotic forms of magnetism, such as emergent gauge theories or compass models [110].

Superconducting circuits [100–103] involve lithographically printed waveguide structures on the surface of a chip, which is then operated at low temperatures and currents. Qubits are made up of linear elements, such as inductors and capacitors, along with Josephson junctions to give rise to an anharmonic spectrum of the resulting Hamiltonian. This anharmonicity allows us to encode the qubit in the two lowest energy levels, since they lie far from excited states. Physically, the qubit can correspond to, e.g., the presence or absence of superconducting electrons on a small 'island', or to the direction of a current around a loop. These two examples are known as charge and flux qubits, respectively. Typical time scales in these systems are in the MHz-GHz regime, and therefore they seem very promising candidates for the realization of digital quantum simulation, which requires many operations. Nevertheless, the macroscopicity of these systems makes them very sensitive to noise, and coherence times do not exceed 100 μs [64]. This constitutes the current bottleneck for the eventual application of error-correction protocols that would render digital simulation reliable. Furthermore, the parameters in these circuits, that determine qubit frequencies etc., are subjected to fluctuations from one fabrication batch to another. Also, time-dependent fluctuations due to mobile material defects can spoil the quality of the qubits. Leaving these issues aside, the qubits can be coupled to form arrays (cf. Fig. 2.7), which are then described by the Hamiltonian

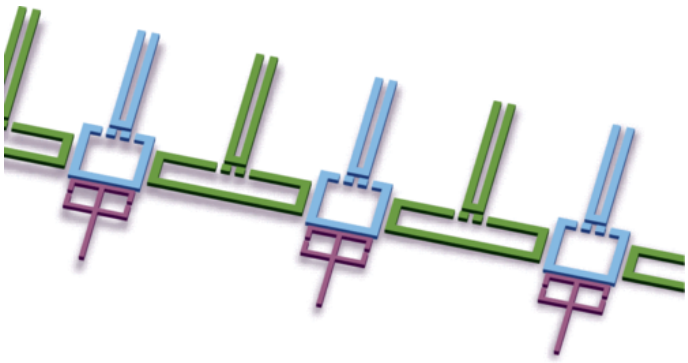

Figure 2.7: Array of superconducting flux qubits. The green circuit elements couple the flux qubits, shown in blue. The smaller circuits perform the readout of the qubit state. The gaps represent Josephson junctions. (Image reproduced from ref. [64]).

$$H_{\text{spin}} = -\sum_j \frac{\Delta_j}{2}\sigma_j^z - \sum_{\langle j,l\rangle} J_{j,l}\sigma_j^x\sigma_l^x. \tag{2.33}$$

In this expression, Δ_j denotes the qubit level splitting, and $J_{j,l}$ is their effective coupling. There has been a proposal to simulate this Hamiltonian in a superconducting circuit, but embedding multiple qubits on one chip spoils dramatically their overall coherence times, and makes an eventual implementation difficult [111]. On the other hand, the qubits can be coupled to photons in resonators, which allows the implementation of Jaynes-Cummings models [112]

$$H_{JC} = \omega_r a^\dagger a + \epsilon \sigma^+ \sigma^- + g(a\sigma^+ + a^\dagger \sigma^-). \tag{2.34}$$

Here, ω_r and ϵ are the photon and qubit excitation frequencies, and $a^\dagger, a, \sigma^+$ and σ^- denote the corresponding raising and lowering operators. If several resonators are coupled together, one could realize lattices that allow for analogue quantum simulation of spin-boson systems [113].

2.3 Trapped-ion quantum simulators

The phases that we explore in this thesis are not specific to any experimental platform. However, our reference system will be trapped-ion chains. One of the main motivations for the study of the specific models covered in this thesis is the feasibility of realizing them with trapped-ion quantum matter.

Trapped-ion quantum simulators benefit from some comparative advantages with respect to other platforms [28]. Typical distances between ions in traps are of the order of microns, which grants the possibility of addressing individually every ion. This allows experimentalists to prepare localized excitations, or to directly measure local observables. Also, trapped ions feature short- and long-range interactions, the latter stemming from their Coulomb repulsion. Since interactions are controlled by external parameters, such as the trap potential, their range can be another parameter of the phase diagram, making it possible to explore the interplay between the short- and long-range interactions regimes [114]. The exquisite degree of control in these platforms has allowed the realization of one of the most complex quantum simulations so far (as of 2016), the first digital simulation of a lattice gauge theory [81]. Other recent achievements include establishing the violation of the Lieb-Robinson bound for the propagation of correlations [115, 116], or studying the emergence of thermalization in quantum systems [117].

The idea of using trapped atomic ions as a platform for quantum simulation emerged with the seminal contributions by Porras and Cirac [118, 119]. In these works, the authors suggested that the internal levels could play the role of spins, and interactions between them could be induced by employing laser fields to engineer conditional forces upon the ions. Since the original proposals, many works have aimed at realizing phases of strongly-correlated quantum matter [119–122]. The simulation of quantum magnetism in particular has been carried out by many groups, that have realized the symmetry-breaking transition of the Ising model [93, 123], or instances of frustrated interactions [124, 125].

The three different models studied in this thesis can be understood as generalizations of these latter works. We do not limit ourselves to spin models alone, since the vibrational degrees of freedom may be an asset for the realization of new strongly-correlated quantum phases. In particular, we shall see in chapter 3 that magnetic frustration can be simulated considering the whole spin-phonon Hamiltonian describing the trapped-ion chain. Also, the phonons allow for the implementation of the lattice gauge theory of chapter 4. Finally, in chapter 5 we focus on a spin system that goes beyond the simulation of quantum magnetism for the realization of a topological insulator.

We begin this chapter explaining the physics associated with the vibrations of the ions in the trap. Then we proceed to present the different interactions between the internal and motional degrees of freedom of the ions. We conclude with some comments on the initialization and readout of a trapped-ion quantum simulator.

2.3.1 Coulomb crystals in ion traps

In this section we are going to derive the phonon Hamiltonian associated with the oscillations of the ions around their equilibrium positions.

A set of atomic ions confined in a potential can undergo a phase transition from a plasma state into a crystalline arrangement, known as Coulomb crystal [126, 127]. This occurs whenever the kinetic energy of the ions is made fairly smaller than their Coulomb repulsion, which is accomplished by means of Doppler cooling [128, 129]. The resulting form of the crystal depends on the trap geometry and the trapping frequencies along different spatial directions (cf. Fig. 2.8).

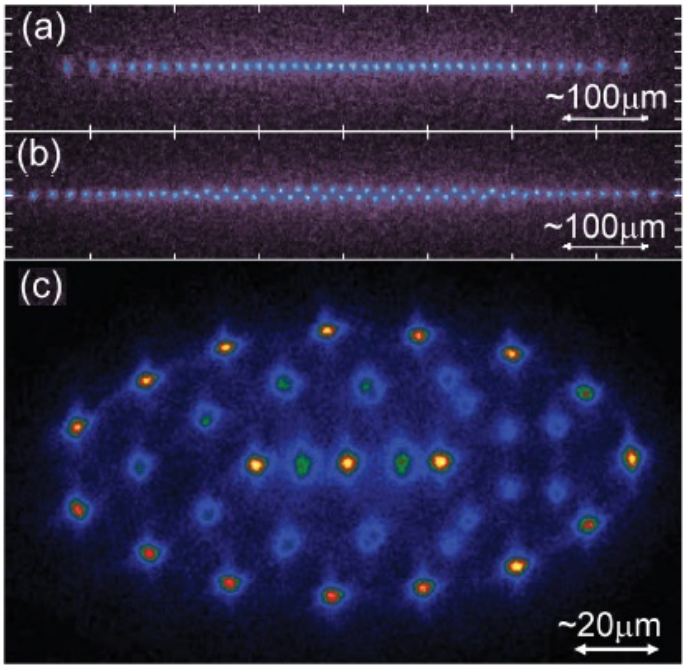

Figure 2.8: Fluorescence images of a Coulomb crystal of trapped ions undergoing a structural phase transition, which can be induced by reducing the ratio of radial to axial trapping frequencies. (a) A linear chain of ions along the z axis, with trapping frequencies $\omega_{x,y} \gg \omega_z$. (b) Zigzag structure for $\omega_{x,y} > \omega_z$. (c) Three-dimensional structure for $\omega_{x,y} \gtrsim \omega_z$. (Image reproduced from ref. [28]).

We will consider linear Paul/RF traps [130], or linear arrays of microtraps [131–133]. These latter systems, although originally proposed for quantum information processing, have proved successful for quantum simulation as well [134–139]. Other trapping schemes for trapped ions are possible, such as Penning [140] and optical traps [141–143]. Structural phase transitions and effective Ising models can be readily realized in 2D Penning crystals [144–148], opening up an avenue for the exploration of physics beyond one-dimensional systems.

The confining potentials are effectively harmonic in every direction, with magnitude $\omega_\beta^2, \beta = x, y, z$ [149]. Along with the Coulomb repulsion of the ions, the potential energy of the crystal can be written as

$$V = \frac{m}{2} \sum_{j=1}^{N} \sum_{\beta} \omega_\beta^2 r_{\beta,j}^2 + \sum_{j>l=1}^{N} \frac{e^2}{|\mathbf{r}_j - \mathbf{r}_l|}, \tag{2.35}$$

for N ions of charge e and mass m. Throughout the thesis we will assume units of $\hbar = 1$ and the Gaussian (CGS) system of units. For strong radial confinement

$\omega_x = \omega_y \gg \omega_z$, the ions arrange along the trap axis z, and occupy equilibrium positions $r_j^{(0)}$. These are determined by the equation $(\partial V/\partial \mathbf{r}_j)_{\mathbf{r}_j=\mathbf{r}_j^{(0)}} = 0$. The position of the ion j is given as

$$\mathbf{r}_j = \delta r_{x,j}\hat{\mathbf{x}}_j + \delta r_{y,j}\hat{\mathbf{y}}_j + (r_j^{(0)} + \delta r_{z,j})\hat{\mathbf{z}}_j, \tag{2.36}$$

where $\delta r_{x,j}, \delta r_{y,j}$ and $\delta r_{z,j}$ are the displacements from the potential minima. We perform a Taylor expansion of V around the equilibrium positions up to second order in the displacements. This is justified as long as the displacements are small compared to the separation between ions. Since terms of the form $\delta r_{x,j}\delta r_{y,j}, \delta r_{x,j}\delta r_{z,j}$ or $\delta r_{y,j}\delta r_{z,j}$ do not occur in this approximation, and higher order terms are neglected, vibrations in different directions decouple. The Hamiltonian describing the motional degrees of freedom reads [118]

$$H_{\text{motion}} = \frac{1}{2m}\sum_{j=1}^{N}\sum_{\beta} p_{\beta,j}^2 + \frac{m}{2}\sum_{j=1}^{N}\sum_{\beta}\omega_\beta^2 \delta r_{\beta,j}^2 - \frac{1}{2}\sum_{j>l=1}^{N}\sum_{\beta}\frac{c_\beta e^2}{|r_j^{(0)} - r_l^{(0)}|^3}(\delta r_{\beta,j} - \delta r_{\beta,l})^2, \tag{2.37}$$

where $c_x = c_y = 1$ and $c_z = -2$.

Now we second quantize H_{motion} by promoting the momenta $p_{\beta,j}$ and displacements $\delta r_{\beta,j}$ to operators, that admit a representation in terms of local phonons, namely

$$p_{\beta,j} = i\sqrt{\frac{m\omega_\beta}{2}}(a_{\beta,j}^\dagger - a_{\beta,j}), \quad \delta r_{\beta,j} = \frac{1}{\sqrt{2m\omega_\beta}}(a_{\beta,j} + a_{\beta,j}^\dagger). \tag{2.38}$$

In terms of these local phonon operators, the motional Hamiltonian of the chain is given as

$$H_{\text{phonon}} = \sum_{j=1}^{N}\sum_{\beta}\omega_j^\beta a_{\beta,j}^\dagger a_{\beta,j} + \frac{1}{2}\sum_{j>l=1}^{N}\sum_{\beta} t_{j,l}^\beta (a_{\beta,j}^\dagger a_{\beta,l} + \text{H.c.}), \tag{2.39}$$

with the on-site frequency and Coulomb mediated long-range hopping given by

$$\omega_j^\beta = \omega_\beta - \frac{1}{2}\sum_{p\neq j}\frac{c_\beta e^2}{m\omega_\beta |r_j^{(0)} - r_p^{(0)}|^3}, \qquad t_{j,l}^\beta = \frac{c_\beta e^2}{m\omega_\beta |r_j^{(0)} - r_l^{(0)}|^3}. \tag{2.40}$$

In the final Hamiltonian (2.39), we have neglected terms of the form $a_{\beta,j}^\dagger a_{\beta,l}^\dagger$ and $a_{\beta,j}a_{\beta,l}$. This is justified as long as $\omega_\beta \gg t_{j,l}^\beta$, since then processes that do not conserve the particle number are highly suppressed.

Hamiltonian (2.39) shows that cooled Coulomb crystals in an ion trap are described by a model of hopping phonons. As such, (2.39) can be expressed in terms

of collective modes of motion $a_{\beta,n} = \sum_{j=1}^{N} M_{j,n}^{\beta} a_{\beta,j}$,

$$H_{\text{phonon}} = \sum_{N=1}^{N} \sum_{\beta} \omega_n^{\beta} a_{\beta,n}^{\dagger} a_{\beta,n}. \tag{2.41}$$

2.3.2 Atom-light interactions

In principle, the former collective phonons are not coupled to the internal degrees of freedom of the ions. To induce their coupling we need to add laser forces, that can act differently depending on the internal state of the ion. We can always regard every ion as an effective two-level system, or a qubit, as long as (i) the frequency of the field inducing the coupling of the two internal levels is close to resonance, and (ii) the couplings to any other levels are fairly smaller than the detuning relative to off-resonant transitions [149]. The corresponding Hamiltonian for a single qubit is given as

$$H_{\text{qubit}} = \omega_{\downarrow}|\downarrow\rangle\langle\downarrow| + \omega_{\uparrow}|\uparrow\rangle\langle\uparrow| = \frac{\omega_{\downarrow} + \omega_{\uparrow}}{2}(|\downarrow\rangle\langle\downarrow| + |\uparrow\rangle\langle\uparrow|) + \frac{\omega}{2}(|\uparrow\rangle\langle\uparrow| - |\downarrow\rangle\langle\downarrow|), \tag{2.42}$$

where $\omega_{\downarrow}$ and $\omega_{\uparrow}$ are the energies of the 'ground' and 'excited' states of the qubit, and $\omega \equiv \omega_{\uparrow} - \omega_{\downarrow}$.

Any operator in the Hilbert space of a single qubit can be written in terms of the Pauli matrices associated with the spin-1/2 algebra. In particular, we have that

$$|\downarrow\rangle\langle\downarrow| + |\uparrow\rangle\langle\uparrow| \to \mathbb{I}, \quad |\uparrow\rangle\langle\uparrow| - |\downarrow\rangle\langle\downarrow| \to \sigma^z, \quad |\uparrow\rangle\langle\downarrow| \to \sigma^+, \quad |\downarrow\rangle\langle\uparrow| \to \sigma^-. \tag{2.43}$$

Thus, the qubit Hamiltonian can be reexpressed in terms of an effective spin

$$H_{\text{spin}} = \frac{\omega}{2}\sigma^z, \tag{2.44}$$

where we have neglected the contribution $\propto \mathbb{I}$.

Physically, the qubit can be encoded in a dipole-forbidden transition at optical frequencies. The typical coherence times of these systems is of 1s [142]. Other possible qubits utilize Zeeman/hyperfine levels, which may achieve coherence times in the order of minutes [150, 151].

There are two types of effective atom-light interactions that can be implemented with trapped ions: the σ^x/σ^y, and the σ^z interactions. In both cases, the coupling between the spin and phonon degrees of freedom is realized by means of optical

fields, for optical and Zeeman/hyperfine qubits. These latter can utilize microwave fields as well, but they require magnetic field gradients to create a momentum kick [152, 153].

We describe now these interactions in two particular experimental instances.

σ^x/σ^y interaction

The interaction of N ions with the electric field $\mathbf{E}(\mathbf{r},t)$ of a laser is described by [154]

$$H_{\text{int}} = -\sum_{j=1}^{N} \boldsymbol{\mu}_j \cdot \mathbf{E}(\mathbf{r}_j, t), \tag{2.45}$$

where $\boldsymbol{\mu}_j = e\mathbf{r}_j$ is the dipole operator for the transition $|\downarrow\rangle \leftrightarrow |\uparrow\rangle$. Assuming a bichromatic field, with momenta $\mathbf{k}_1, \mathbf{k}_2$ and frequencies ω_1, ω_2, the Hamiltonian describing situation (a) in Fig. 2.9 is given as [155]

$$\begin{aligned} H_{\text{int}} = &\sum_{j=1}^{N} \Omega_{1,j}(\left|\downarrow^{(j)}\right\rangle \left\langle \text{virt}^{(j)}\right| + \text{H.c.})(e^{i(\mathbf{k}_1\cdot\mathbf{r}_j - \omega_1 t)} + \text{H.c.}) \\ &+ \sum_{j=1}^{N} \Omega_{2,j}(\left|\uparrow^{(j)}\right\rangle \left\langle \text{virt}^{(j)}\right| + \text{H.c.})(e^{i(\mathbf{k}_2\cdot\mathbf{r}_j - \omega_2 t)} + \text{H.c.}). \end{aligned} \tag{2.46}$$

The Rabi frequencies $\Omega_{1,2}$ depend on the matrix element of the dipole operator

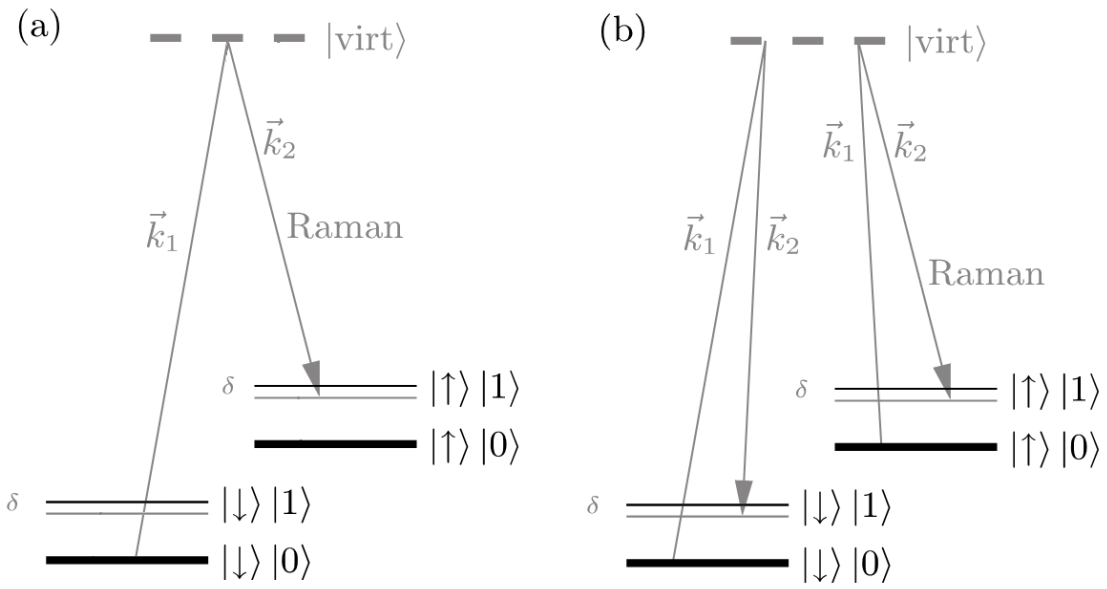

Figure 2.9: Level scheme for the implementation of the (a) σ^x/σ^y and (b) σ^z interactions (Image reproduced from ref. [28]).

upon the atomic orbitals, and the laser intensities and polarizations [156]. If the laser (detuning) frequencies $\Delta_{1,2} \equiv \omega_{\text{virt}} - \omega_{1,2} - \omega_{\downarrow,\uparrow}$ from the state $|\text{virt}\rangle$ fulfil that $\Delta_{1,2} \gg \Omega_{1,2}$, the upper state can be adiabatically eliminated [157]. Then, the interaction Hamiltonian reads [155]

$$H_{\text{int}} = \sum_{j=1}^{N} \Omega_j (\sigma_j^+ + \text{H.c.})(e^{i(\Delta\mathbf{k}\cdot\mathbf{r}_j - \omega_{\text{L}} t)} + \text{H.c.}), \tag{2.47}$$

where $\Omega_j = \Omega_{1,j}^* \Omega_{2,j}/\Delta_{\text{R}}$, $\Delta\mathbf{k} = \mathbf{k}_1 - \mathbf{k}_2$, and $\omega_{\text{L}} = \omega_1 - \omega_2$.

Now we move into an interaction picture with respect to

$$H_0 = \sum_{j=1}^{N} \sum_{\beta} \omega_n^\beta a_{\beta,n}^\dagger a_{\beta,n} + \frac{\omega}{2} \sum_{j=1}^{N} \sigma_j^z, \tag{2.48}$$

so that

$$H_{\text{int}} \to \hat{H}_{\text{int}} = \sum_{j=1}^{N} \Omega_j (\sigma_j^+ e^{i\omega t} + \text{H.c.})(e^{i(\Delta\mathbf{k}\cdot\mathbf{r}_j(t) - \omega_{\text{L}} t)} + \text{H.c.}). \tag{2.49}$$

We consider that $\omega_{\text{L}} = \omega - \delta$. Applying the Rotating Wave Approximation (RWA) leads then to

$$\hat{H}_{\text{int}} = \sum_{j=1}^{N} \Omega_j (\sigma_j^+ e^{i(\Delta\mathbf{k}\cdot\mathbf{r}_j(t) + \delta t)} + \text{H.c.}). \tag{2.50}$$

The product $\Delta\mathbf{k} \cdot \mathbf{r}_j(t)$ can be expressed as

$$\begin{aligned}(\Delta k_x, \Delta k_y, \Delta k_z) \cdot (\delta r_{x,j}(t), \delta r_{y,j}(t), r_j^{(0)} + \delta r_{z,j}(t)) \\ = \sum_{n=1}^{N} \sum_{\beta} (\eta_n^\beta M_{j,n}^\beta a_{\beta,n} e^{-i\omega_n^\beta t} + \text{H.c.}) + \Delta k_z r_j^{(0)},\end{aligned} \tag{2.51}$$

where $\eta_n^\beta = \Delta k_\beta / \sqrt{2m\omega_n^\beta}$ are known as the Lamb-Dicke parameters [149]. If the extension of every ion's wave function is much smaller than $1/k$, which is known as the Lamb-Dicke regime, then $\eta_n^\beta \ll 1$, and

$$\hat{H}_{\text{int}} = \sum_{j=1}^{N} \Omega_j \sigma_j^+ \left[1 + i \sum_{n=1}^{N} \sum_{\beta} (\eta_n^\beta M_{j,n}^\beta a_{\beta,n} e^{-i\omega_n^\beta t} + \text{H.c.})\right] e^{i\Delta k_z r_j^{(0)}} e^{i\delta t} + \text{H.c.} \tag{2.52}$$

This Hamiltonian is further simplified by making the (detuning) frequencies $\delta_n^\beta \equiv \omega_{n_0}^{\beta_0} - \omega_n^\beta - \delta$ almost resonant with a particular motional band β_0 and mode n_0. We distinguish the following three cases:

1. Carrier transition ($\delta = 0$): In this case, the Hamiltonian reduces to

$$\hat{H}_{\text{int}} = \sum_{j=1}^{N} \Omega_j \sigma_j^+ e^{i\Delta k_z r_j^{(0)}} + \text{H.c.} \tag{2.53}$$

The effective interaction acts exclusively in the internal degrees of freedom of the ions, changing the qubit state. Assuming that $\Delta k_z = 0$ and $\Omega_j = \Omega$,

$$\hat{H}_{\text{int}} = \Omega \sum_{j=1}^{N} \sigma_j^x. \tag{2.54}$$

This interaction allows to prepare the qubit in a particular state, or the simulation of a magnetic field acting on the spins [28].

2. Red sideband ($\delta = \omega_n^\beta - \omega_{n_0}^{\beta_0} + \delta_n^\beta$): If the laser frequency is red detuned with respect to the qubit frequency ω, and it is made almost resonant with a particular band β_0 and mode n_0, the only non-fast-rotating processes are those conserving the total excitation number

$$\hat{H}_{\text{int}} = \sum_{j,n=1}^{N} \Omega_j (i\eta_n^{\beta_0} e^{i\Delta k_z r_j^{(0)}} e^{i\delta_n^\beta t} M_{j,n}^{\beta_0} a_{\beta_0,n} \sigma_j^+ + \text{H.c.}). \tag{2.55}$$

Motional bands in the axial and transverse directions are well separated [28], so we can assume that the laser is resonant with the processes along β_0 alone, and drop the band index. Making $i\Omega_j\eta_n \equiv \Omega_{\text{rsb}}$ and setting $\Delta k_z = 0$, we get

$$\hat{H}_{\text{int}} = \Omega_{\text{rsb}} \sum_{j,n=1}^{N} (M_{j,n} e^{i\delta_n t} a_n \sigma_j^+ + \text{H.c.}). \tag{2.56}$$

This is the Jaynes-Cummings Hamiltonian, that arises naturally in cavity QED systems. It permits the population transfer between the qubit and the phonon degrees of freedom.

3. Blue sideband ($\delta = -\omega_n^\beta + \omega_{n_0}^{\beta_0} - \delta_n^\beta$): In this case, the frequency of the laser is tuned above ω, and the resonant processes are given by

$$\hat{H}_{\text{int}} = \sum_{j,n=1}^{N} \Omega_j (i\eta_n^{\beta_0} e^{i\Delta k_z r_j^{(0)}} e^{i\delta_n^\beta t} M_{j,n}^{\beta_0} a_{\beta_0,n}^\dagger \sigma_j^+ + \text{H.c.}), \tag{2.57}$$

which do not conserve particle number any more. Making the same assumptions that for the red sideband interaction, the Hamiltonian reduces to

$$\hat{H}_{\text{int}} = \Omega_{\text{bsb}} \sum_{j,n=1}^{N} (M_{j,n} e^{i\delta_n t} a_n^\dagger \sigma_j^+ + \text{H.c.}), \quad \Omega_{\text{bsb}} \equiv i\Omega_j\eta_n. \tag{2.58}$$

This anti-Jaynes-Cummings Hamiltonian has no counterpart in atom-photon systems, since it would violate energy conservation. Therefore, trapped-ion experiments can support richer dynamics than typical cavity QED systems.

We note that by simultaneously addressing the red and blue sidebands, we can generically implement the Hamiltonian

$$\hat{H}_{\text{int}} = g \sum_{j,n=1}^{N} \sigma_j^{x,y} (M_{j,n} e^{i\delta_n t} e^{i\Delta k_z r_j^{(0)}} a_n^\dagger + \text{H.c.}). \tag{2.59}$$

where the final, effective Rabi frequency, is customarily renamed as g. The Pauli operator in (2.59) can be chosen at will. This is done by fixing the relative phase between the 'red' and 'blue' detuned lasers [158, 159]. This interaction, known as the Rabi Hamiltonian, will be considered in the implementation of the IR model in chapter 4.

σ^z interaction

Another possibility to give rise to a spin-phonon interaction is to excite the motional modes alone (cf. (b) in Fig. 2.9). A spin-dependent force is realized by imposing different AC Stark shifts for the processes $|\downarrow\rangle \langle \text{virt}|$ and $|\uparrow\rangle \langle \text{virt}|$ [156]. The Hamiltonian describing the interaction is given by

$$\begin{aligned} H_{\text{int}} = &\sum_{s=\uparrow,\downarrow} \sum_{j=1}^{N} \Omega_{1,j}(s) (\left|s^{(j)}\right\rangle \left\langle \text{virt}^{(j)}\right| + \text{H.c.}) (e^{i(\mathbf{k}_1 \cdot \mathbf{r}_j - \omega_1 t)} + \text{H.c.}) \\ &+ \sum_{s=\uparrow,\downarrow} \sum_{j=1}^{N} \Omega_{2,j}(s) (\left|s^{(j)}\right\rangle \left\langle \text{virt}^{(j)}\right| + \text{H.c.}) (e^{i(\mathbf{k}_2 \cdot \mathbf{r}_j - \omega_2 t)} + \text{H.c.}). \end{aligned} \tag{2.60}$$

Performing the adiabatic elimination of the upper level, we get [156]

$$H_{\text{int}} = \sum_{j=1}^{N} (\Omega_j(\uparrow) \left|\uparrow^{(j)}\right\rangle \left\langle \uparrow^{(j)}\right| + \Omega_j(\downarrow) \left|\downarrow^{(j)}\right\rangle \left\langle \downarrow^{(j)}\right|) (e^{i(\Delta \mathbf{k} \cdot \mathbf{r}_j - \omega_{\text{L}} t)} + \text{H.c.}), \tag{2.61}$$

where $\Omega_j(s) = \Omega_{1,j}(s)\Omega_{2,j}(s)/\Delta_{\text{R}}$. By choosing suitable laser polarizations it is possible to make $\Omega_j(\downarrow) = -2\Omega_j(\uparrow) \equiv \Omega_j$ [160]. Physically this stems from the fact that the phase of the (sinusoidally varying at frequency ω_{L}) laser force upon states $|\uparrow\rangle$ and $|\downarrow\rangle$ is different. The corresponding Hamiltonian, in the rotating frame of the phonons, is given as

$$\hat{H}_{\text{int}} = \sum_{j=1}^{N} \Omega_j \sigma_j^z (e^{i(\Delta \mathbf{k} \cdot \mathbf{r}_j(t) - \omega_{\text{L}} t)} + \text{H.c.}), \tag{2.62}$$

where we drop the contribution $\propto \mathbb{I}$. We consider the case $\omega_{\text{L}} = \omega_n^\beta - \omega_{n_0}^{\beta_0} + \delta_n^\beta$. Following the same manipulations as for the σ^x/σ^y interaction, we arrive at the

effective Hamiltonian

$$\hat{H}_{\text{int}} = g \sum_{j,n=1}^{N} \sigma_j^z (M_{j,n} e^{i\delta_n t} e^{i\Delta k_z r_j^{(0)}} a_n^\dagger + \text{H.c.}). \tag{2.63}$$

Hamiltonian (2.63) is completely analogous to (2.59), since they just differ by a local rotation. We will use this interaction in the implementation of the cJT, IR and SSH models in chapters 3, 4 and 5.

2.3.3 Initialization and readout

The internal states of the ions can be prepared with very high efficiency by optical pumping [161]. This process utilizes spontaneous emission to make the qubit decay to the ground state. On the other hand, motional modes must be cooled down to reach the condition $\eta_n^\beta \ll 1$, known as the Lamb-Dicke regime. This is necessary to be able to resolve the sideband transitions. Doppler cooling [128, 129] along the three spatial directions leads to a thermal state with $\bar{n} \lesssim 10$. Subsequently, one can utilize cycles of red sideband transitions plus spontaneous emission to lower the phonon number up to $\bar{n} \simeq 0.05$ [149]. This procedure is known as resolved sideband cooling [162].

State-dependent fluorescence is used to read the states of the qubits. A dipole allowed transition to an excited state from $|\downarrow\rangle$ is driven in a closed cycle. At the same time, spontaneous decay into the state $|\uparrow\rangle$ is forbidden due to selection rules. Also, the laser frequency is off-resonant for the transition from this latter level. As a consequence, an ion in the state $|\downarrow\rangle$ appears 'bright' when the laser is switched on, whereas the state $|\uparrow\rangle$ appears 'dark' [163–166]. Regarding the motional states, they are mapped into the qubit state by means of the red or blue sideband transitions, and subsequently read from the fluorescence signal.

2.4 The Density Matrix Renormalization Group

One of the aspects that arouses the interest in quantum simulators is the possibility of simulating many-body models, whose complexity lies beyond the computational capabilities of classical computers [18, 61]. Remarkably, though, there are situations in which classical simulation of many-body problems is still possible. This is the

case of 1D systems, for which the Density Matrix Renormalization Group (DMRG) is able to provide the value of any observable up to the desired accuracy [32, 33]. We will use this method in chapters 3 and 4 to discuss different ground-state properties. In this chapter, we present an introduction to the DMRG, which is the most accurate numerical method for many-body problems known to date [34, 35].

Historically, the huge dimension of the Hilbert spaces associated with many-body problems remained an insurmountable obstacle for many years. Fortunately, in 1975, Kenneth Wilson realized that the Kondo Hamiltonian –which models a single magnetic impurity in a metal– could be effectively described in a state space whose dimension remains constant, regardless of the size of the system [167]. He discovered that many states in the Hilbert space offered redundant information, and could be disposed of at no expense of the accuracy of the description of the problem. Wilson devised a method, known as the numerical renormalization group (NRG), to find an effective description of the model in a reduced state space, bypassing the need for an exponentially large amount of resources.

After the success of the NRG in the Kondo problem, physicists tried to apply Wilson's ideas to other models. In the particular case of the quantum Ising chain, for instance, the NRG evolved into the block renormalization group [168, 169]. In this method, the chain is divided into two blocks of identical size. Initially comprised of only two sites, one starts adding two new sites to the blocks to grow the chain. To keep the dimension of the Hilbert space manageable, one has to discard some states at every step. Let us imagine that we want to describe the ground state. In that case, it is natural to discard all but the ground and low-lying states of the Hamiltonian in every iteration. The states kept are then used as an effective basis. By projecting the ground state and the Hamiltonian in this basis, we obtain new effective representations, which are used in the next iteration. Since the dimension of the effective basis remains constant, the size of the state and operators is kept bound in spite of having an increasingly longer chain.

The former algorithm, though, provided unexpectedly inaccurate results in some instances [32, 33]. The explanation for this bad performance had to wait until 1992, when Steven White realized that the choice of effective basis in the block renormalization group method was highly inadequate. He found out that the optimal

truncation procedure was to demand that the distance between the ground state and its representation in the effective basis was minimal. Also, he proved that this reduced basis must be given by the eigenstates of the density matrix of the ground state in one block. The method was consequently named as the Density Matrix Renormalization Group (DMRG) [32, 33].

The DMRG was a breakthrough not only because it provided an efficient method to simulate any local Hamiltonian in 1D. It also brought to light the role of entanglement in many-body problems [170, 171]. Very roughly speaking, the DMRG works because the amount of entanglement in the ground state remains bound. Otherwise, the dimension of the effective basis would have to be infinite to describe the ground state. The interplay of quantum information theory and many-body physics is a very active field of research nowadays, and has provided techniques that generalize the DMRG to more than 1D, such as PEPS [172, 173] or MERA [174, 175].

There are two versions of the algorithm, concerned with finding $|\Psi\rangle$ in the thermodynamic limit, $L \to \infty$, or for finite L. We refer to them as *infinite-system* DMRG and *finite-system* DMRG respectively. Both of them assume Open Boundary Conditions (OBC). We will deal with finite chains throughout the thesis, so we are interested in the finite-system version of the DMRG. Nevertheless, the algorithm requires us to apply sequentially the infinite-system and then the finite-system DMRG to achieve the optimal accuracy [32]. Thus we need to discuss both versions.

2.4.1 Infinite-system algorithm

In the infinite-system DMRG one builds up the chain iteratively, by inserting two sites at every step, so that $L = 2, 4, 6, \ldots$ We always think of the chain as two blocks, A and B, comprised of ℓ sites each, where ℓ is the block size at a given step of the growing process (cf. Fig. 2.10).

Block A (B) is generically associated with a D-dimensional Hilbert space spanned by the states $\left\{|a_\ell\rangle_{\mathrm{A(B)}}\right\}$. D is the constant dimension of the effective basis, and is known as *bond dimension*. The value of D, typically of $O(100)$, is chosen by the user to achieve the desired accuracy in the simulation.

The block representation of the Hamiltonian is given by the matrix elements ${}_{\mathrm{A(B)}}\langle a|H_\ell\,|a'\rangle_{\mathrm{A(B)}}$. Any local operator is analogously obtained as ${}_{\mathrm{A(B)}}\langle a|O_\ell^{(j)}\,|a'\rangle_{\mathrm{A(B)}}$.

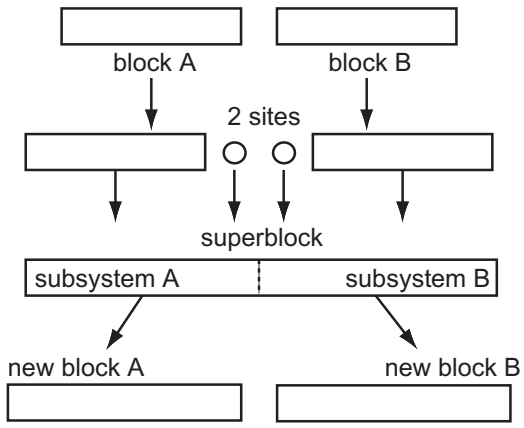

Figure 2.10: Iteration taken in the infinite-system DMRG. We integrate one new site into each block, then form the *superblock*. The algorithm provides the Hamiltonian and operators on the superblock in terms of two new blocks, comprised of a truncated state space. We note that the integration of a new site into the block happens on both sides of the chain, leading to a net system growth. (Image reproduced from ref. [35]).

On the other hand, individual sites are associated with basis states $\left\{|\sigma_\ell\rangle_{\mathrm{A(B)}}\right\}$, whose local space is of dimension d.

In every iteration, we form the representation of the Hamiltonian in the resulting structure of joining blocks A and B, and inserting two new sites between them. We refer to this arrangement as superblock, or schematically as $\mathrm{A}\bullet\bullet\mathrm{B}$. By diagonalizing the Hamiltonian of the superblock, we obtain the ground state

$$|\Psi\rangle = \sum_{a_\mathrm{A}\sigma_\mathrm{A}\sigma_\mathrm{B}a_\mathrm{B}} \Psi_{a_\mathrm{A}\sigma_\mathrm{A}\sigma_\mathrm{B}a_\mathrm{B}} |a\rangle_\mathrm{A}|\sigma\rangle_\mathrm{A}|\sigma\rangle_\mathrm{B}|a\rangle_\mathrm{B}. \tag{2.64}$$

This state is comprised of $(Dd)^2$ numbers. Nevertheless, we aim at finding a representation in terms of only D quantities. To this end, we form the representation of the state in subsystems $\mathrm{A}\bullet$ and $\bullet\mathrm{B}$, which is given as

$$|\Psi\rangle = \sum_{i_\mathrm{A}j_\mathrm{B}} \Psi_{i_\mathrm{A},j_\mathrm{B}} |i\rangle_\mathrm{A}|j\rangle_\mathrm{B}, \tag{2.65}$$

where $|i\rangle_\mathrm{A} = |a\rangle_\mathrm{A}|\sigma\rangle_\mathrm{A}$ and $|j\rangle_\mathrm{B} = |\sigma\rangle_\mathrm{B}|a\rangle_\mathrm{B}$. Now we consider the reduced density operator for $\mathrm{A}\bullet$ and $\bullet\mathrm{B}$, that is

$$\rho_{\mathrm{A}\bullet} = \mathrm{Tr}_{\bullet\mathrm{B}}\,|\Psi\rangle\langle\Psi|, \quad \rho_{\bullet\mathrm{B}} = \mathrm{Tr}_{\mathrm{A}\bullet}\,|\Psi\rangle\langle\Psi|. \tag{2.66}$$

These matrices are still of size $Dd \times Dd$. The reduced bases are constructed from the eigenvectors of these matrices corresponding to the D larger eigenvalues. As shown in [33], this choice minimizes the distance between $|\Psi\rangle$ and its truncation into the effective basis of each new block.

Let us sketch how the whole algorithm would be implemented, as originally presented in [33]:

1. At the beginning blocks A and B are comprised of just one site, so that $\ell = 1$. We add two new sites at the centre of the chain, and obtain the matrix representations of the Hamiltonian and operators for the two sites and blocks A and B.

2. The Hamiltonian on the resulting superblock A $\bullet\bullet$ B is constructed by means of Kronecker products, observing the block-site-site-block structure.

3. We diagonalize the superblock Hamiltonian to obtain the ground state

$$|\Psi\rangle = \sum_{a_{\mathrm{A}}\sigma_{\mathrm{A}}\sigma_{\mathrm{B}}a_{\mathrm{B}}} \Psi_{a_{\mathrm{A}}\sigma_{\mathrm{A}}\sigma_{\mathrm{B}}a_{\mathrm{B}}} |a\rangle_{\mathrm{A}} |\sigma\rangle_{\mathrm{A}} |\sigma\rangle_{\mathrm{B}} |a\rangle_{\mathrm{B}}. \tag{2.67}$$

   The expectation value of any operator can be measured at this point.

4. We form the reduced density matrices of subsystems A$\bullet$ and $\bullet$B, $\rho_{\mathrm{A}\bullet} = \mathrm{Tr}_{\bullet\mathrm{B}} |\Psi\rangle\langle\Psi|$ and $\rho_{\bullet\mathrm{B}} = \mathrm{Tr}_{\mathrm{A}\bullet} |\Psi\rangle\langle\Psi|$, and diagonalize these as well.

5. We keep the eigenvectors corresponding to the D largest eigenvalues of $\rho_{\mathrm{A}\bullet}$ and $\rho_{\bullet\mathrm{B}}$, and discard the rest. We form with these the state space $\left\{ |a_{\ell+1}\rangle_{\mathrm{A(B)}} \right\}$.

6. We form the matrix representation of H and any operators of interest in A$\bullet$ and $\bullet$B.

7. The former matrix representations are decimated by projecting them upon the bases $\{|a_{\ell+1}\rangle_{\mathrm{A}}\}$ and $\{|a_{\ell+1}\rangle_{\mathrm{B}}\}$.

8. The resulting matrices are stored as the block representations for block size $\ell + 1$.

9. We proceed again from step 2, up to a desired length L is reached.

We note that for a finite D, there is a certain iteration for which $D \leq N_{\text{site}}^{\ell+1}$. From then on, the effective block representations of the operators are of size D: this is the way in which the DMRG circumvents the exponential scaling-up. Block representations of all the operators must be stored for every ℓ, and expectation values can be taken whenever $|\Psi\rangle$ is obtained in every iteration.

2.4.2 Finite-system algorithm

The infinite-system DMRG can be applied until we reach a desired system size L. Finite-system DMRG consists of the same decimation procedure as the infinite-system version, but this time blocks A and B do not grow simultaneously (cf. Fig. 2.11). On the contrary, if we add one new site to, e.g., block A, we must consider

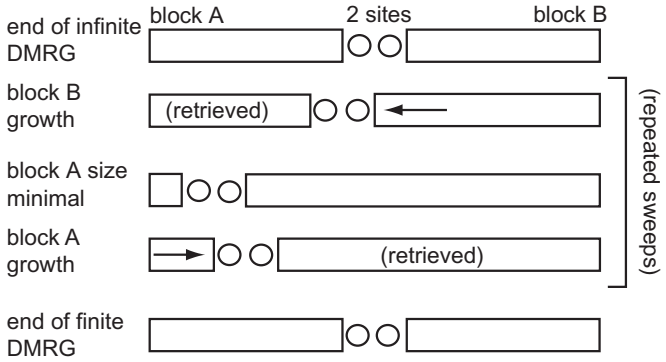

Figure 2.11: Iteration taken in the finite-system DMRG. The growth in this case happens only in one side of the chain, at the expense of the other. (Image reproduced from ref. [35]).

that block B has shrunk by one site. Thus, the block Hamiltonian and operators are updated only for block A in this case. This process continues until block B is comprised of one site only. Then, the growth direction is reversed. A whole sequence of growth and shrinkage is known as a sweep. To check if the method has converged, we can monitor the value of a particular observable, such as the energy. Since the DMRG can be regarded as the optimization of a variational ansatz [35], it approximates the exact solution 'from above', meaning that increasing the number of sweeps must necessarily lower the energy. Eventually this quantity must reach a steady value within the goal tolerance. This value can be compared with further simulations for increasing bond dimension D. Again, we expect that there is a value

of D beyond which there are no further changes in the energy, showing that the method has finally converged.

Chapter 3

Magnetic frustration and quantum annealing in the cooperative Jahn-Teller model

3.1 Introduction

In this chapter we present the quantum simulation of a system exhibiting magnetic frustration. In the context of magnetism, frustration arises if spins are coupled through competing interactions that cannot be simultaneously satisfied [176]. This leads to an extensive amount of degeneracy in the ground state.

We can illustrate the concept of frustration in a simple model comprised of three spins. We assume that their energy is given by the following Hamiltonian

$$J \sum_{j,l=1}^{N=3} \sigma_j^z \sigma_l^z, \quad J > 0. \tag{3.1}$$

The positive sign of the interaction strength favours configurations in which all the three spins are antiparallel, since these lower the overall energy. However, as illustrated in Fig. 3.1, the 'infinite range' of the interactions prevents the spins from arranging simultaneously in this way. Consequently, the system has six different ground states, with the same energy. This type of frustration, that stems from the interactions alone, is known as interaction-induced frustration. There are many occasions, however, where it has a geometrical origin, and it is referred to as geometric frustration [177]. The study of frustrated magnetism is an old discipline in

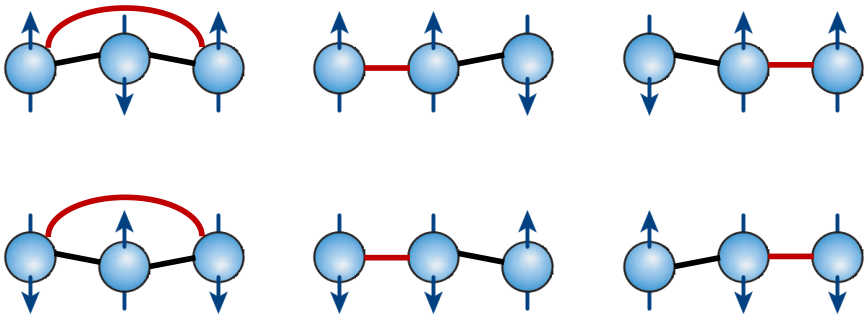

Figure 3.1: Antiferromagnetic (AF) configurations of Hamiltonian (3.1). The black (red) lines denote bonds where the antiferromagnetic interactions are (are not) satisfied.

material science. However, it keeps being a very active field of research, since there are theoretically-predicted properties that have eluded experimental confirmation so far. In particular, under certain circumstances, a frustrated system should become a quantum spin liquid [7].

In a system with frustrated interactions, an extensive amount of spins are free to fluctuate among many low-energy configurations. Consequently, there is no average spin order, and the system is a paramagnet. Usually these fluctuations are arbitrary, and have no structure, but in some occasions they are severely restricted by the form of the interactions. Although these restrictions stem from local constraints, they can give rise to long-range effects, and therefore fluctuations may be long ranged. This is the defining feature of a spin liquid, in which spins are free to fluctuate, but in a correlated manner. Although there are many solid-state systems featuring frustrated interactions, such as the spin-ice materials [178, 179], spin-liquid phases have been difficult to observe in reality. This is because interactions are not always ideal, lattice structures leading to spin liquids may be difficult to realize, and phonons, temperature, or any other sources of noise may prevent their occurrence.

Quantum simulators are ideal test-beds for the exploration of the effects associated with frustrated interactions. There have been several proposals for the realization of frustrated magnetism. One possible route is to introduce randomness

in the spin interactions, for example by coupling a set of dipoles to a linear random combination of cavity modes [180, 181]. Another possibility is to directly realize a Hamiltonian analogous to (3.1). This has been accomplished for trapped-ion chains up to N = 16 [124, 125]. In these experiments, a particular (collective) phononic mode with long-range correlations, such as the centre-of-mass (COM) mode of the longitudinal motion, is driven by a slightly off-resonant laser force. If the laser frequency is suitably detuned from the mode, phonons are not excited, but they can still mediate interactions between the spins. Because of the correlations present in the COM mode, the effective interactions are ferromagnetic, and have long range [182]. We stress that these experiments rely on the possibility of individually addressing the modes in the phononic band. Nevertheless, this becomes increasingly difficult for long chains, since the energies of neighbouring modes get closer, and they are more difficult to resolve. As a consequence, these implementations suffer the serious drawback of not being scalable to larger numbers of ions.

In this chapter we depart from these proposals and consider an alternative, scalable scheme to give rise to frustrated interactions. Furthermore, our model exhibits a far richer phenomenology than previously considered works, since it combines randomness in the effective couplings with long-range interactions. We focus on a generalized cooperative Jahn-Teller (cJT) [114, 122], or Rabi lattice model [183–185], that can be readily implemented in trapped-ions chains. The cooperative Jahn-Teller Hamiltonian is defined as [114]

$$H_{\mathrm{cJT}}^{\Delta k} = \sum_{n=1}^{N} \omega_n a_n^\dagger a_n + \frac{\Omega_x}{2} \sum_{j=1}^{N} \sigma_j^x + g \sum_{j,n=1}^{N} \sigma_j^z (a_n M_{j,n} e^{-i\Delta k r_j^{(0)}} + \mathrm{H.c.}). \tag{3.2}$$

This model describes a set of N coupled oscillators, each of which interacts with an effective spin. Alternatively, it can be understood as a collection of spins coupled to N normal bosonic modes. Δk is the projection of the effective Raman wave vector induced by the lasers on the chain axis. This model is invariant under the parity transformation $\sigma_j^z \to -\sigma_j^z, a_n \to -a_n$. The ground state consists of the vacuum of the phonons and no magnetization in z for $g \ll \omega_n, \Omega_x$, but a large enough spin-phonon coupling can induce a phase transition into a symmetry-breaking state with $\langle a_n \rangle \neq 0$ and $\langle \sigma_j^z \rangle \neq 0$.

We present now the implementation of the model with trapped ions. Then we

proceed to the discussion of the phase diagram in the absence of optical phases, that is, with $\Delta k = 0$. Once we establish the different regimes of the ground state in this case, we explain how to give rise to the frustration of the interactions by choosing a suitable $\Delta k \neq 0$. We show that some features of the spin liquid phase are observable in our implementation. Finally, we present an adiabatic protocol to prepare the frustrated phase of our model. This protocol is an instance of a generic algorithm known as quantum annealing [186–188]. We will discuss the properties of the protocol and its suitability for finding the ground state in the event of frustration. We conclude the chapter presenting realistic experimental parameters for the implementation of $H_{\mathrm{cJT}}^{\Delta k}$ in state-of-the-art trapped-ion platforms, and giving some conclusions.

3.2 Implementation with trapped ions

The cJT Hamiltonian arises naturally in a trapped-ion chain. Let us assume a set of N trapped ions along the z axis. The transverse oscillations of the ions, in the x direction, for instance, are described by the phonon Hamiltonian (cf. (2.39))

$$H_{\mathrm{phonon}} = \sum_{j=1}^{N} \omega_j^x a_{x,j}^\dagger a_{x,j} + \frac{1}{2} \sum_{j>l=1}^{N} t_{j,l}^x (a_{x,j}^\dagger a_{x,l} + \mathrm{H.c.}), \tag{3.3}$$

where ω_j^x and $t_{j,l}^x$ are given in (2.40). As we deal with oscillations in this direction alone, we drop the index x in the following discussion.

We consider homogeneous chains (ions equally spaced by a distance d_0, so that $r_j^{(0)} = d_0 j$), a situation that gives an approximate description of the centre of a linear Coulomb crystal, or describes linear arrays of ion microtraps. The phonon tunnelling is expressed in the homogeneous case like

$$t_{j,l}^x = \frac{t_{\mathrm{C}}}{|j-l|^3}, \quad t_{\mathrm{C}} = \frac{e^2}{m\omega_x d_0^3}, \tag{3.4}$$

and local trapping frequencies ω_j are constant and approximately equal to ω_x. Therefore, we can write the Hamiltonian for the phonon chain as

$$H_{\mathrm{phonon}} = \sum_{j,l=1}^{N} \left(\omega_x \delta_{j,l} + \frac{1}{2} \frac{t_{\mathrm{C}}}{|j-l|^3} \right) a_j^\dagger a_l = \sum_{n=1}^{N} \omega_n a_n^\dagger a_n, \tag{3.5}$$

where $a_n = \sum_{j=1}^{N} M_{j,n} a_j$ are the normal mode phonon operators, and $M_{j,n}$ are the eigenstates of the matrix in the former parenthesis.

The spin degrees of freedom can be simulated by encoding qubits in Zeeman or hyperfine states of the ions. The transverse field in (3.2) is implemented directly by a microwave, or via Raman transitions driving the carrier resonance. In any case, we identify the effective Rabi frequency with the magnitude of the transverse field Ω_x.

Finally, the spin-boson interaction can be created by two lasers inducing an AC Stark shift between the two spin levels. This corresponds to the σ^z interaction already discussed (cf. (2.63)),

$$H_{\text{int}}(t) = g \sum_{j,n=1}^{N} \sigma_j^z (M_{j,n} e^{i\delta_n t} e^{i\Delta k d_0 j} a_n^\dagger + \text{H.c.}). \tag{3.6}$$

The lasers push the ions in the x direction, to couple the spins with the transverse oscillations. Nevertheless, there is also some momentum Δk along the trap axis, creating the phase dependence. The (detuning) frequencies $\delta_n = \omega_n - \omega_{\text{L}}$ will be defined with respect to the lowest energy configuration of the phonon chain, corresponding to the zigzag mode $\omega_{n=N/2}$ [114]. We will work in an interaction picture in which phonons rotate with frequency ω_{L}, so $H_{\text{int}}(t) \to H_{\text{int}}(0)$ and the energy of the phonons in H_{phonon} is given by δ_n.

3.3 Phase diagram for undressed couplings

In this section we present the phase diagram of the model with no optical phases $H_{\text{cJT}}^{\Delta k=0} \to H_{\text{cJT}}$. We establish that its phase transition belongs to the same universality class as the quantum Ising chain [42].

3.3.1 The polaron transformation

Consider the canonical transformation $U = e^S$ with

$$S = \sum_{j,n=1}^{N} \frac{g}{\delta_n} \sigma_j^z \left(M_{j,n}^* a_n^\dagger - \text{H.c.} \right). \tag{3.7}$$

This is known as the polaron transformation [118]. It can be written as a displacement in phase space,

$$U = D\left(\sum_{n=1}^{N} \alpha_n \right), \text{ with } \alpha_n = \sum_{j=1}^{N} \frac{g}{\delta_n} \sigma_j^z M_{j,n}^*, \tag{3.8}$$

where $D(x)$ is the displacement operator [189]. We note that because of the σ_j^z operator, this displacement acts differently on states $|\uparrow\rangle_j$ and $|\downarrow\rangle_j$. Its action on the boson operators is given as

$$a_n^\dagger \mapsto U a_n^\dagger U^\dagger = a_n^\dagger - \sum_{j=1}^{N} \frac{g}{\delta_n} \sigma_j^z M_{j,n}. \tag{3.9}$$

If we apply U to H_{cJT}, so that $e^S H_{\mathrm{cJT}} e^{-S} \equiv \bar{H}_{\mathrm{cJT}}$, the resulting Hamiltonian is

$$\bar{H}_{\mathrm{cJT}} = \sum_{n=1}^{N} \delta_n a_n^\dagger a_n + \sum_{j,l=1}^{N} J_{j,l} \sigma_j^z \sigma_l^z + \frac{\Omega_x}{2} \sum_{j=1}^{N} \left(\sigma_j^+ e^{\sum_{n=1}^{N} \frac{2g}{\delta_n} \left(M_{j,n}^* a_n^\dagger - \mathrm{H.c.} \right)} + \mathrm{H.c.} \right). \tag{3.10}$$

This expression tells us that the Jahn-Teller model is equivalent to an Ising model with interaction strength,

$$J_{j,l} = -\sum_{n=1}^{N} M_{j,n}^* \frac{g^2}{\delta_n} M_{l,n}, \tag{3.11}$$

plus some residual spin-boson coupling. In the perturbative regime of the spin-boson coupling, $g \ll \delta_n$, one obtains the Ising limit of the Jahn-Teller Hamiltonian

$$\bar{H}_{\mathrm{cJT}} \simeq \sum_{n=1}^{N} \delta_n a_n^\dagger a_n + \sum_{j,l=1}^{N} J_{j,l} \sigma_j^z \sigma_l^z + \frac{\Omega_x}{2} \sum_{j=1}^{N} \sigma_j^x. \tag{3.12}$$

This procedure is equivalent to the adiabatic elimination of the phonons [190]. The former derivation makes possible the simulation of the quantum Ising chain with trapped ions [93, 182].

In the Ising limit of the cJT model, the ground state of the problem is completely defined by the magnetic order. We distinguish two cases:

1. The classical limit ($\Omega_x = 0$): The ground state is separable. Once we find the spin configuration that minimizes the energy for the couplings $J_{j,l}$, which we call $|\Psi_{\mathrm{spin}}\rangle$, it maps onto the ground state of the phonons upon undoing the transformation U, so that

$$|\Psi_{\mathrm{GS}}\rangle = |\alpha\rangle |\Psi_{\mathrm{spin}}\rangle, \quad |\alpha\rangle = e^{-\sum_{j,n=1}^{N} \frac{g}{\delta_n} m_z \left(M_{j,n}^* a_n^\dagger - \mathrm{H.c.} \right)} |0\rangle, \tag{3.13}$$

where $m_z = \langle \Psi_{\mathrm{spin}} | \sigma_j^z | \Psi_{\mathrm{spin}} \rangle$, and $|0\rangle$ is the vacuum of the phonons. This result expresses that the motional (structural) configuration is inextricably linked to the magnetic order (cf. Fig. 3.2). This fact has been exploited for instance for the quantum simulation of the Jahn-Teller effect with trapped ions [122].

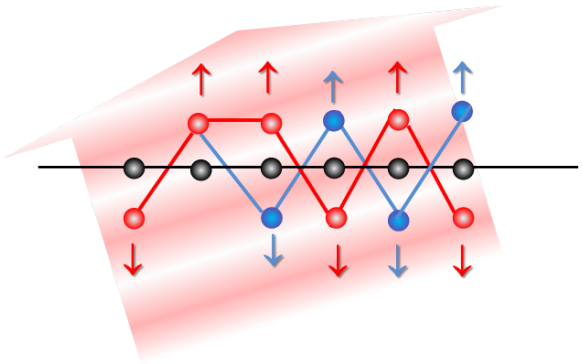

Figure 3.2: Two different examples of how the magnetic order maps into the structural configuration of the chain. This situation corresponds to the ordered phase of the ground state of H_{cJT} with $\Omega_x < \Omega_{x,\mathrm{c}}$.

2. The quantum regime ($\Omega_x \neq 0$): The ground state is still of the form (3.13), but $|\Psi_{\mathrm{spin}}\rangle$ does not need to be separable any more. The phases of the ground state correspond to those of the quantum Ising chain [42]. We expect that the two following cases are separated by a continuous phase transition at some critical $\Omega_{x,\mathrm{c}}$:

   - Ordered phase ($\Omega_x < \Omega_{x,\mathrm{c}}$): Below some critical value of the transverse field, the $\sigma_j^z\sigma_l^z$ interactions favour a state with long-range order in the z direction. This state breaks the parity symmetry of H_{cJT} –invariance under $\sigma_j^z \to -\sigma_j^z, a_j \to -a_j$– since $\langle\sigma_j^z\rangle \neq 0$. As $|\alpha\rangle \neq |0\rangle$, we have $\sum_{j=1}^N \langle a_j^\dagger a_j\rangle/N \neq 0$.
   - Paramagnetism ($\Omega_x > \Omega_{x,\mathrm{c}}$): Above the critical transverse field, the terms σ_j^x favour a state in which spins point in the x direction. This state respects the parity symmetry of H_{cJT}, and the phononic chain is in the ground state, so that $\sum_{j=1}^N \langle a_j^\dagger a_j\rangle/N = 0$.

In the non-perturbative, or strong-coupling regime $g \gtrsim \delta_n$, $|\Psi_{\mathrm{GS}}\rangle$ is of the form (3.13) only in the classical limit. For finite Ω_x, the ground state of H_{cJT} does not need to be a separable wave function of spins and bosons any more, and one has to rely on a numerical diagonalization of the Hamiltonian to establish the properties of $|\Psi_{\mathrm{GS}}\rangle$.

Our aim for the rest of the chapter is to study the phase diagram of H_{cJT} in the strong-coupling regime. We split the discussion into the classical limit and the

quantum regime. We start with the study of the classical limit, that is completely determined by the couplings $J_{j,l}$.

3.3.2 The classical limit

Whenever $\Omega_x = 0$, H_{cJT} in the polaron basis reads

$$\bar{H}_{\mathrm{cJT}} = \sum_{n=1}^{N} \delta_n a_n^\dagger a_n + \sum_{j,l=1}^{N} J_{j,l}\sigma_j^z\sigma_l^z. \tag{3.14}$$

The ground state is then given as

$$|\Psi_{\mathrm{GS}}\rangle = |\alpha\rangle|\Psi_{\mathrm{spin}}\rangle, \tag{3.15}$$

where α is written in Eq. (3.13), and $|\Psi_{\mathrm{spin}}\rangle$ is the ground state of

$$\sum_{j,l=1}^{N} J_{j,l}\sigma_j^z\sigma_l^z. \tag{3.16}$$

Since there are no transverse terms σ_j^x in H_{cJT}, the spin ground state fulfils $\langle\sigma_j^z\rangle = \pm 1$. In particular, $|\Psi_{\mathrm{spin}}\rangle$ is the configuration that minimizes the energy for the couplings

$$J_{j,l} = -\sum_{n=1}^{N} M_{j,n}^* \frac{g^2}{\delta_n} M_{l,n}. \tag{3.17}$$

We have derived an analytical expression for these terms in appendix A. Specifically, we have shown that in the thermodynamic limit $N \to \infty$,

$$J_{j,l} \simeq -(-1)^{j-l} J_{\mathrm{exp}} e^{-|j-l|/\xi} + \frac{J_{\mathrm{dip}}}{|j-l|^3}_{j\neq l}, \tag{3.18}$$

where

$$J_{\mathrm{exp}} = \frac{g^2\xi}{t_{\mathrm{C}}\ln(2)},\ J_{\mathrm{dip}} = \frac{g^2 t_{\mathrm{C}}}{2(\delta_{N/2} + 7/4\, t_{\mathrm{C}}\zeta(3))^2},\ \xi = \sqrt{\frac{t_{\mathrm{C}}\ln(2)}{2\delta_{N/2}}}. \tag{3.19}$$

In this expression, $\delta_{N/2}$ is the (detuning) frequency of the spin-phonon force with respect to the bottom of the band of transverse phonons, t_{C} is the width of their dispersion relation (cf. 3.4), and $\zeta(3) \simeq 1.20$ is the Riemman zeta function [46].

Eq. (3.18) showcases the two different regimes of the effective Ising interaction $J_{j,l}$: the exponential and the dipolar decays. By changing the detuning frequency from the zigzag mode $\delta_{N/2}$, and the width of band t_{C}, we can tune ξ as well, so that we have control over the range of the couplings. Regarding the consequences for the ground state of H_{cJT}, we distinguish two limits:

- Short-range limit ($\delta_{N/2} \gg t_{\rm C}, \xi \ll 1$).- The effective Ising interaction shows a dipolar decay, $J_{j,l} \simeq J_{\rm dip}/|j-l|^3$. Effectively, this coupling is among first neighbours. Since $J_{\rm dip} > 0$, the classical ground state is antiferromagnetic.

- Long-range limit ($\delta_{N/2} \ll t_{\rm C}$, $\xi \gg 1$).- The exponential decay is dominant, and for regions of length L, with $L \ll \xi$, it becomes independent of j, l. The classical ground state remains antiferromagnetic, because of the alternation of signs in the first term in Eq. (3.18).

We see that for any range of the couplings, the spin ground state is antiferromagnetic. This means that the structural configuration of the chain is the zigzag arrangement, that breaks the reflection symmetry $x \to -x$ (cf. blue line in Fig. 3.2).

Usually, the appearance of long-range spin interactions is associated with making the spin-dependent force nearly resonant with one particular, motional mode –such as the center-of-mass mode, $M_{j,n}, n = 0$–, which features distant spatial correlations [125]. These are imprinted in $J_{j,l}$ through the wave function $M_{j,n}$. This approach may be problematic for $N \gg 1$, since then the energies of the different modes get closer between each other and are more difficult to resolve individually. However, from Eq. (3.18), we see that in the event of many ions, the range of $J_{j,l}$ relies on the relative values of $\delta_{N/2}$ and $t_{\rm C}$, and not necessarily on some frequency matching condition between the laser force and the motional modes. Furthermore, these parameters are independently tunable. Specifically, $\delta_{N/2}$ depends on the frequency of the force, while $t_{\rm C}$ is fixed by means of the trap frequency ω_x.

3.3.3 Phase diagram in the quantum regime

The quantum ground state of

$$H_{\rm cJT} = \sum_{n=1}^{N} \delta_n a_n^\dagger a_n + \frac{\Omega_x}{2} \sum_{j=1}^{N} \sigma_j^x + g \sum_{j,n=1}^{N} \sigma_j^z \left(M_{j,n} a_n + \text{H.c.}\right) \tag{3.20}$$

outside the perturbative regime of the spin-boson coupling is no longer a separable wave function of the spins and the bosons. However, the analogy with the Ising model is still valid. We expect a critical value of $\Omega_{x,\rm c}$ separating the antiferromagnetic regime from a paramagnetic phase. This line of reasoning is based on symmetry arguments: the invariance of $H_{\rm cJT}$ under the parity transformation

$\sigma_j^z \to -\sigma_j^z, a_j \to -a_j$ is analogous to the $\mathbb{Z}_2$ symmetry of the quantum Ising chain [40]. This suggests that the physics of $H_{\rm cJT}$ is similar, including its critical behaviour.

To study the phase diagram we have carried out calculations with the DMRG [32, 35]. In our simulations, we neglect the dipolar character of the vibrational couplings and keep nearest-neighbour interactions only, $t_{j,l} = t_{\rm C}\delta_{j,l+1}$. The phase diagram of the model is presented in Fig. 3.3 for a wide range of transverse fields Ω_x and Coulomb couplings $t_{\rm C}$. Because of the parity symmetry, the z-magnetization is zero, so we have to choose a different order parameter. We define the antiferromagnetic order parameter (OAF) as

$$\text{OAF} := \sum_{j,l} (-1)^{|j-l|} \frac{\langle \sigma_j^z \sigma_l^z \rangle}{N(N-1)}. \tag{3.21}$$

This observable captures the appearance of the ordered phase for $\Omega_x < \Omega_{x,\rm c}$, whereas is zero in the paramagnetic phase. We signal the boundary between these two regimes with a white line in Fig. 3.3.

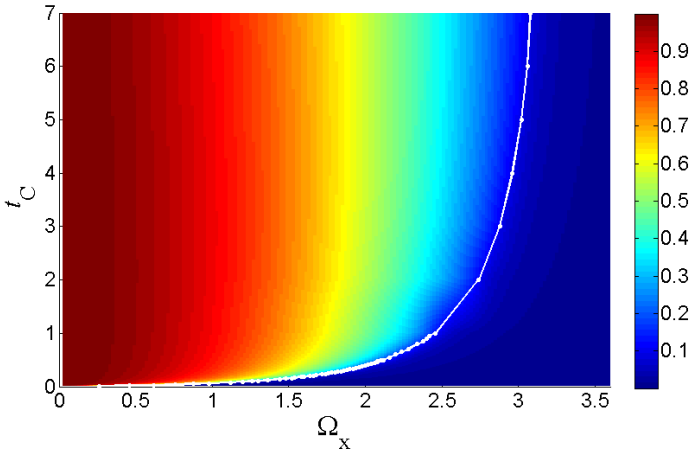

Figure 3.3: DMRG phase map, for $N = 40$ sites, in units such that $\delta_{N/2} = g = 1$. We depict the expectation value of the OAF (3.21). For the DMRG algorithm we used the parameters $D = 22$, number of states kept, and maximum number of phonons per site $n = 8$.

We note a marked contrast in the response to the transverse field depending on the value of $t_{\rm C}$. The two different regimes correspond to the limits of the Ising couplings:

- Short-range limit ($\delta_{N/2} \gg t_{\rm C}$).- In this case, the transition to the paramagnetic phase occurs for weak transverse field Ω_x. Since the detuning frequency $\delta_{N/2}$ is large, phonon excitations are largely suppressed. Thus, the problem is described by an effective Ising model on the phonon vacuum subspace

$$\langle 0|\bar{H}_{\rm cJT}|0\rangle = \sum_{j,l=1}^{N} J_{j,l}\sigma_j^z\sigma_l^z + \frac{\Omega_x}{2}\sum_{j=1}^{N}\sigma_j^x e^{-2n_j}, \tag{3.22}$$

where we have used the fact that the local phonon number fulfils that

$$n_j = \langle\alpha_j|a_j^\dagger a_j|\alpha_j\rangle = |\alpha_j|^2, \tag{3.23}$$

with $\alpha_j = \sum_{n=1}^{N} g/\delta_n M_{j,n}^*$ (cf. (3.13)). In the case of $t_{j,l} = t_{\rm C}\delta_{j,l+1}$, the dispersion relation is

$$\delta_n = \delta_{N/2} + t_{\rm C}\left(1 + \cos\left(\frac{2\pi n}{N}\right)\right), \tag{3.24}$$

and the effective Ising couplings are given as

$$J_{j,l} = -\sum_{n=1}^{N} M_{j,n}^*\frac{g^2}{\delta_n}M_{l,n} \simeq \frac{g^2 t_{\rm C}}{2\delta_{N/2}^2}(\delta_{j,l+1} + \delta_{j,l-1}). \tag{3.25}$$

Since the critical point of a quantum Ising chain with first-neighbours couplings J and transverse field Γ is located at $\Gamma = J$ [42], we conclude that

$$\Omega_{x,{\rm c}} = \frac{g^2 t_{\rm C}}{\delta_{N/2}^2}e^{2\bar{n}} \tag{3.26}$$

where we assume an homogeneous value of n_j, so that $n_j = \bar{n} = \sum_{j=1}^{N}\langle a_j^\dagger a_j\rangle/N$.

The former prediction states that –at weak phonon coupling– the critical field separating the AF and paramagnetic phases scales linearly with $t_{\rm C}$. We have shown that this is consistent with the DMRG calculations in Fig. 3.4.

- Long-range limit ($\delta_{N/2} \ll t_{\rm C}$).- For large values of the hopping amplitude, we note that the critical line becomes independent of $t_{\rm C}$. This is a consequence of the fact that the detuning frequency is such that it singles out the zigzag mode alone. Then $H_{\rm cJT}$ reduces to a set of qubits coupled to a collective bosonic mode, a situation reminiscent of the Dicke model of quantum optics [191]. It is known that in this case a separable solution such as (3.13) is a good approximation to the exact ground state at finite system size [192].

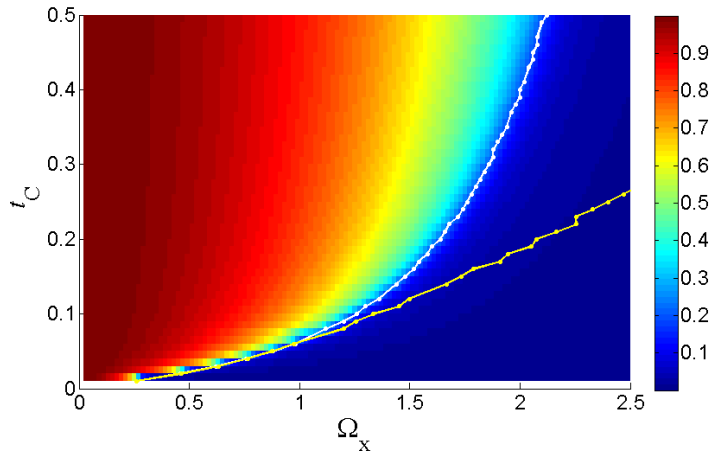

Figure 3.4: OAF values for $t_C \to 0$. We show the DMRG (upper line) vs. the short-range predictions (3.26) (bottom line). There is agreement in the short-range limit $t_C \ll \delta_{N/2} = 1$. The rest of the parameters are the same as in Fig. 3.3.

This last claim is supported by the increasing degree of correlation for larger t_C between the mean phonon number $\bar{n}$ (Fig. 3.5) and the OAF parameter (Fig. 3.3). We note that $\bar{n}$ is non-monotonic in t_C. This is a consequence of the fact that when $t_C \to 0$ we recover again the Dicke model, for which the boson number at $\Omega_x \ll g$ is different from zero. The change of $\bar{n}$ at $\Omega_x = \Omega_{x,c}$ signals the quantum magnetic/structural equivalent of the zigzag structural phase transition [193, 194].

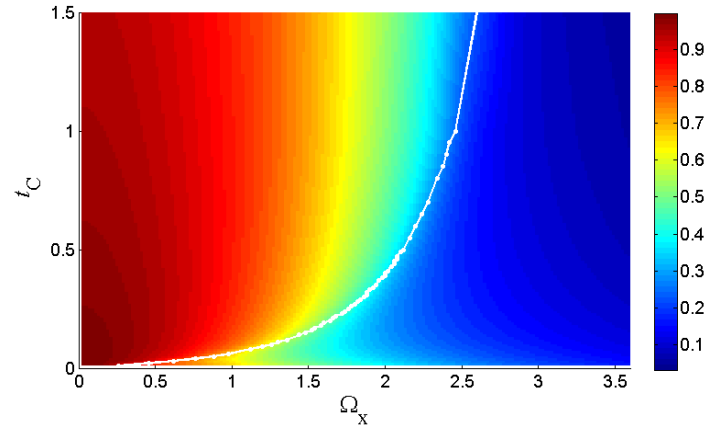

Figure 3.5: DMRG mean phonon number. Same parameters as in Fig. 3.3. The white line indicates the phase boundary according to the AF order parameter, and pinpoints the correlation with the mean phonon number for large values of t_C.

3.3.4 Universality class of the cooperative Jahn-Teller model

So far, we have established that –in the regime of strong coupling– there is a phase transition between the ordered phase ($\langle\sigma_j^z\rangle \neq 0, \langle a_j^\dagger a_j\rangle \neq 0$) and the paramagnetic phase ($\langle\sigma_j^z\rangle = 0, \langle a_j^\dagger a_j\rangle = 0$). The calculations show that this is a second-order phase transition. In particular we have studied the behaviour of the correlation functions

$$C_{j,l}^{xx} = \langle\sigma_j^x\sigma_l^x\rangle - \langle\sigma_j^x\rangle\langle\sigma_l^x\rangle. \tag{3.27}$$

We see that the $C_{j,l}^{xx}$ decay exponentially for values $\Omega_x \neq \Omega_{x,\mathrm{c}}$ and show a power-law decay, $C_{j,l}^{xx} \sim |j-l|^{-\nu}$ for $\Omega_x = \Omega_{x,\mathrm{c}}$, with $\nu \simeq 2$, consistent with a phase transition within the quantum Ising universality class [42] (cf. Fig. 3.6). By calculating the

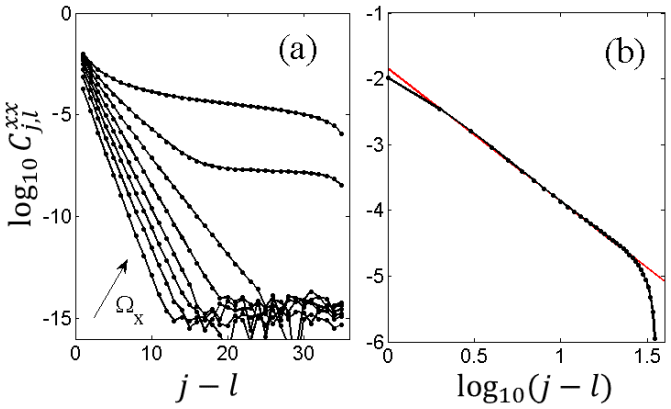

Figure 3.6: DRMG correlations $C_{j,l}^{xx}$ for $t_{\mathrm{C}} = 0.2$. Same parameters as in Fig. 3.3. (a) Values $\Omega_x = 2 \times 0.1, 0.2, 0.3, 0.4, 0.5, 0.6, 0.7, 0.82$. (b) $\log 10 - \log 10$ plot for $\Omega_x = \Omega_{x,\mathrm{c}} = 1.64$. We fit the result to a line, resulting in a slope $\nu \simeq 2.02$.

points in the phase diagram for which the correlation functions have the longest range we are able to identify the critical line shown in Fig. 3.3.

3.4 Emergence of frustration for dressed couplings

Now we discuss the effect of non-trivial optical phases into the ground state of $H_{\mathrm{cJT}}^{\Delta k}$. We will see that they lead to the frustration of the interactions. We explore the consequences of this phenomenon for the classical and quantum regimes of the Jahn-Teller model.

3.4.1 Introduction

In this section we assume non-zero optical phases Δk, and consider the dressed cJT model

$$H_{\rm cJT}^{\Delta k} = \sum_{n=1}^{N} \delta_n a_n^\dagger a_n + \frac{\Omega_x}{2} \sum_{j=1}^{N} \sigma_j^x + g \sum_{j,n=1}^{N} \sigma_j^z (a_n M_{j,n} e^{i\Delta k d_0 j} + \text{H.c.}). \tag{3.28}$$

Let us make $\Omega_x = 0$ for simplicity, and apply the polaron transformation (3.7) to the former Hamiltonian, so that

$$\bar{H}_{\rm cJT}^{\Delta k} = \sum_{n=1}^{N} \delta_n a_n^\dagger a_n + \sum_{j,l=1}^{N} J_{j,l}^{\Delta k} \sigma_j^z \sigma_l^z. \tag{3.29}$$

In this expression

$$J_{j,l}^{\Delta k} = \cos[\Delta k\, d_0 (j-l)]\, J_{j,l}, \tag{3.30}$$

that is, the optical phases dress the effective spin couplings. The dependence in the momentum may favour ground state orders beyond the AF/F magnetic phases of the Ising model. In particular, we shall see that for long-range interactions there are two different patterns that we can identify as the ground states of $H_{\rm cJT}^{\Delta k}$. This is reminiscent of the Hopfield model of associative memory [195], that we briefly review now.

3.4.2 The Hopfield model of associative memory

The Hopfield model of associative memory is a dynamical system in statistical mechanics with an energy function given by the Hamiltonian [196]

$$H_{\rm Hopfield} = -\frac{1}{2} \sum_{j,l=1}^{N} J_{j,l} \sigma_j^z \sigma_l^z, \ \langle \sigma_j^z \rangle = \pm 1, \tag{3.31}$$

where

$$J_{j,l} = \frac{1}{N} \sum_{\mu=1}^{p} \xi_j^\mu \xi_l^\mu. \tag{3.32}$$

The interactions are comprised of p patterns ξ_j^μ, or memories, with random values ± 1 at every site. The patterns are (quasi-) orthogonal, meaning that $1/N \sum_{j=1}^{N} \xi_j^\mu \xi_j^\nu = \delta_{\mu,\nu}$ when $N \to \infty$. There are two minimum energy states associated with every memory, $\langle \sigma_j^z \rangle = \pm \xi_j^\mu$. This can be seen by noticing that any spin flip from the previous configurations leads to an increase of the overall energy. We refer to the ground states as Hopfield orders, which amount to $2p$ because of the $\mathbb{Z}_2$ symmetry.

The Hopfield model acts as an associative memory because an initial random state always evolve into one of the memories at the end of the dynamics generated by H_{Hopfield}. That is to say that any input gets associated with a previously learned memory. This can only happen if the overlap between the initial state and a given pattern ξ_j^μ is above a certain threshold [197].

Now let us turn back to the dressed Ising couplings (3.30). In the long-range limit of the couplings $\delta_{N/2} \ll t_{\text{C}}$, and assuming that the interaction range $\xi \simeq N$, we can approximate

$$J_{j,l}^{\Delta k} \simeq -J_{\text{exp}} \sum_{\mu=\text{c,s}} \xi_j^\mu \xi_l^\mu, \tag{3.33}$$

with $\xi_j^{\text{c}} = (-1)^j \cos(\Delta k\, d_0 j)$, $\xi_j^{\text{s}} = (-1)^j \sin(\Delta k\, d_0 j)$. These two different configurations of the couplings can be independently satisfied, because they are (quasi-) orthogonal. The orders $\langle \sigma_j^z \rangle = \text{sign}(\xi_j^{\text{c}})$ and $\langle \sigma_j^z \rangle = \text{sign}(\xi_j^{\text{s}})$ are ground states of the problem. Thus, we conclude that the classical limit of $H_{\text{cJT}}^{\Delta k}$ is equivalent to a Hopfield model with two memories. We note that $\xi_j^\mu \neq \pm 1$, and that they are not random, since they are determined by the momentum of the lasers Δk. Nevertheless, we will refer to the previous ground states as Hopfield states.

On the other hand, in the limit of short-range interactions $\delta_{N/2} \gg t_{\text{C}}$, $J_{j,l}^{\Delta k} \simeq \cos[\Delta k\, d_0 (j-l)]\, J_{\text{dip}} \delta_{j,l+1}$. The ground state is either antiferromagnetic (AF) or ferromagnetic (F), depending on the sign of the nearest-neighbour couplings: $\langle \sigma_j^z \rangle_{\text{F}} = \langle \sigma_{j+1}^z \rangle_{\text{F}}$ if $J_{j,j+1}^{\Delta k} < 0$, and $\langle \sigma_j^z \rangle_{\text{AF}} = -\langle \sigma_{j+1}^z \rangle_{\text{AF}}$ if $J_{j,j+1}^{\Delta k} > 0$.

In the regime in which $\delta_{N/2} \simeq t_{\text{C}}$, the ground state must be an interplay of the Hopfield and AF/F orders. However, the interactions favouring both types of orders cannot be simultaneously satisfied. This leads to an extensive amount of degeneracy in the ground state, which is a defining feature of magnetic frustration [176]. We note that this regime must showcase some of the features of a phase transition, despite of the fact that is not clear whether an order parameter can be defined in this context.

3.4.3 Frustration in the classical limit of the Hamiltonian

The classical limit of $H_{\text{cJT}}^{\Delta k}$ is given in (3.29). The motional ground state consists of ions arranged in the structural configuration dictated by the magnetic state $\langle \sigma_j^z \rangle$.

On the other hand, the ground state of the spins is determined by the dressed interactions $J_{j,l}^{\Delta k}$.

To locate the region in which the frustration occurs, we have depicted the weights of the exponential and dipolar components of $J_{j,l}$, that is, $J_{\rm exp}e^{-1/\xi}$ and $J_{\rm dip}$ (cf. Fig. 3.7). We see that around the value $t_{\rm C} = \bar{t}_{\rm C} \simeq 0.5$, the dipolar contribution is overtaken by the exponential decay. Therefore, we expect that the interactions leading to the AF/F and Hopfield orders are competing in this region.

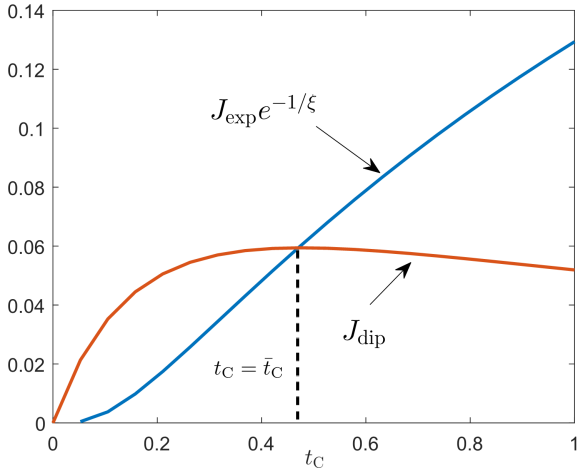

Figure 3.7: Dependence on $t_{\rm C}$ of the different contributions to the effective couplings $J_{j,l}$. Units such that $\delta_{N/2} = g = 1$.

Let us consider the ground state for $\Delta k = 5\pi/3d_0$. In this case, the short-range limit leads to an antiferromagnetic state, whereas the long-range limit is given by $\langle\sigma_j^z\rangle = \text{sign}[(-1)^j \cos(5\pi/3j)]$ or $\langle\sigma_j^z\rangle = \text{sign}[(-1)^j \sin(5\pi/3j)]$. When $t_{\rm C} = \bar{t}_{\rm C}$, there is an extensive number of spins for which pointing either upwards or downwards gives the same contribution to the energy (cf. Fig. 3.8). As a consequence, many different states have energies that are very close to the global energy minimum.

Having understood the classical limit of $H_{\rm cJT}^{\Delta k}$, we proceed now to study the regime with $\Omega_x > 0$. We focus exclusively on the magnetic ground state in the following.

3.4.4 Spin-liquid features in the quantum regime

The interplay of the transverse field and the magnetic frustration gives rise to the most interesting phenomena. Because of the extensive amount of degeneracy when

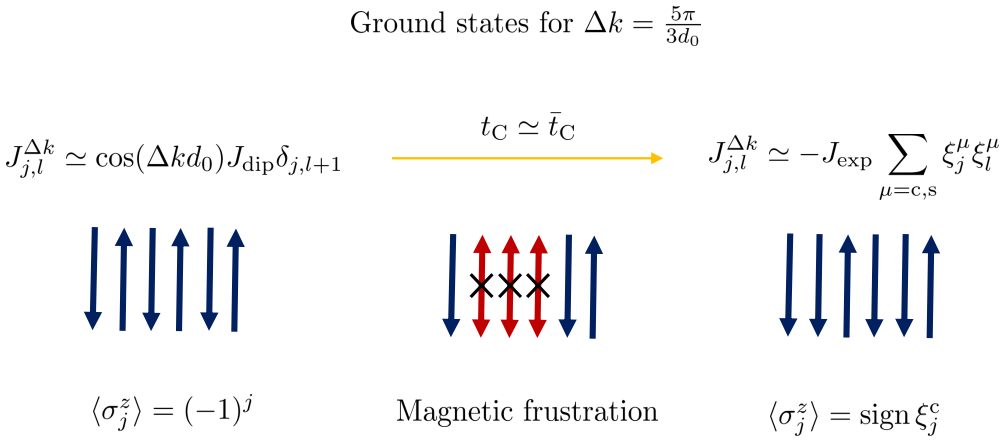

Figure 3.8: Magnetic ground states for $\Delta k = 5\pi/3d_0$. The frustrated spins contribute equally to the ground state energy regardless of the direction they point at.

$t_{\rm C} \simeq \bar{t}_{\rm C}$, a small value of the field can trigger an observable magnetization in the transverse direction. At the same time, spins are free to fluctuate, but they can only explore the low-lying energy states, that are an interplay of the Hopfield and AF/F orders. As a consequence, the fluctuations may feature emergent long-range correlations. This regime with enhanced correlations should survive up to infinitesimal values of Ω_x, and is reminiscent of a spin-liquid phase [7].

We depict the mean transverse magnetization, $m_x = (1/N)\sum_j \langle \sigma_j^x \rangle$ in Fig. 3.9. For $t_{\rm C} \gtrsim 0.5$ many spins are subjected to frustrated interactions, and they must align appreciably with σ^x for infinitesimal values of Ω_x. Outside the frustrated regime, we recover either the AF/F or the Hopfield orders, which are more resilient against perturbations. Therefore, we see a sudden change in m_x depending on whether the system is in the frustrated region or not. We have calculated some spin orders for different values of $t_{\rm C}$, that illustrate the transition between the ordered and the frustrated phases (Fig. 3.10).

For the calculations of the spatial quantum correlations

$$C_{j,l}^{xx} = \langle \sigma_j^x \sigma_l^x \rangle - \langle \sigma_j^x \rangle \langle \sigma_l^x \rangle, \tag{3.34}$$

we have performed a simulation for a slightly longer chain. This is depicted in Fig. 3.11. We see that $C_{j,l}^{xx}$ exhibits the typical exponential decay of gapped phases,

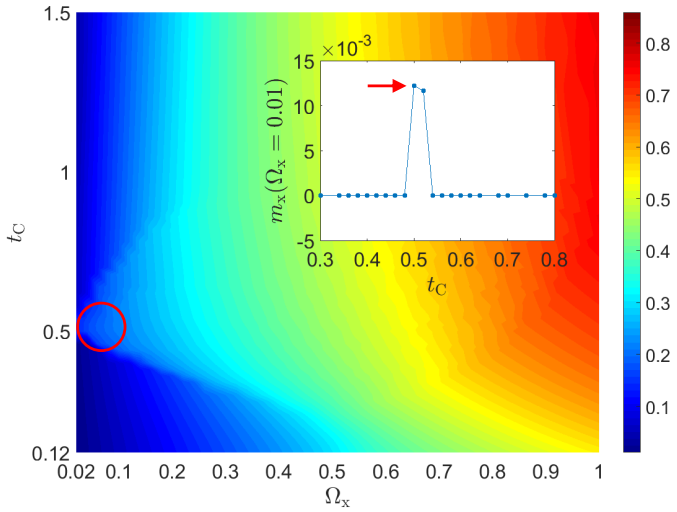

Figure 3.9: Magnetization m_x in the dressed cJT model, for $N = 40$ ions. Energy units $\delta_{N/2} = g = 1$. We show the DMRG calculations for $\Delta k = 5\pi/(3d_0)$. Rest of parameters as in Fig. 3.3. The red circle pinpoints the highly frustrated regime. The inset shows the sudden appearance of magnetization at $t_C \simeq \bar{t}_C$ for small Ω_x.

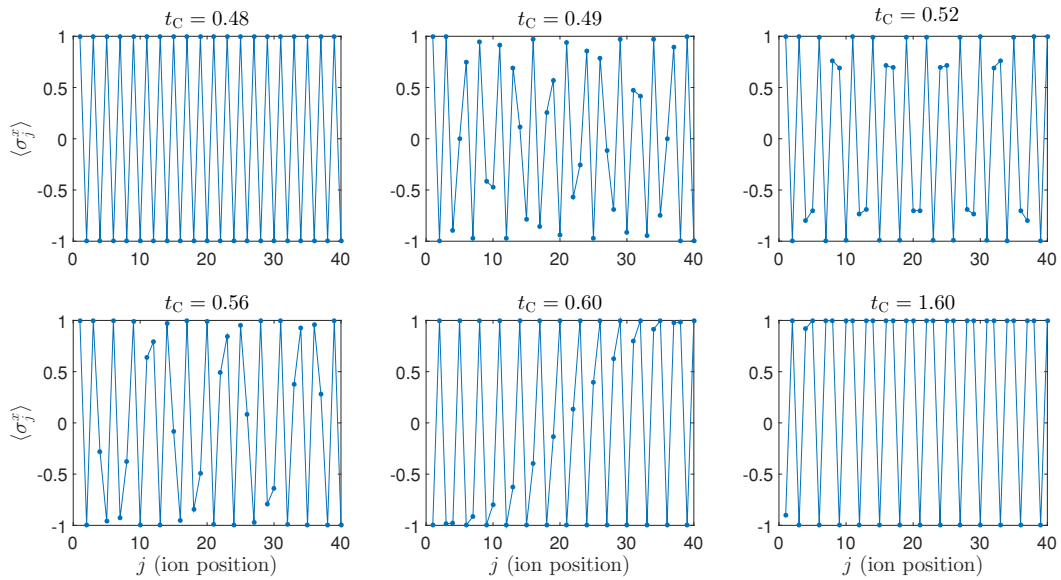

Figure 3.10: Different ground states for $\Delta k = 5\pi/(3d_0), \Omega_x = 0.01$. The rest of the parameters are the same as in Fig. 3.3. For $t_C = 0.48$ the system is in the AF phase. It suddenly jumps into the frustrated regime for $t_C = 0.49$, and features different exotic configurations in the highly frustrated regime, around the value $\bar{t}_C \simeq 0.5$. Finally, for $t_C = 1.6$ the system is well inside the non-frustrated Hopfield phase.

for the short- and long-range coupling regimes [40]. The correlations in the AF/F

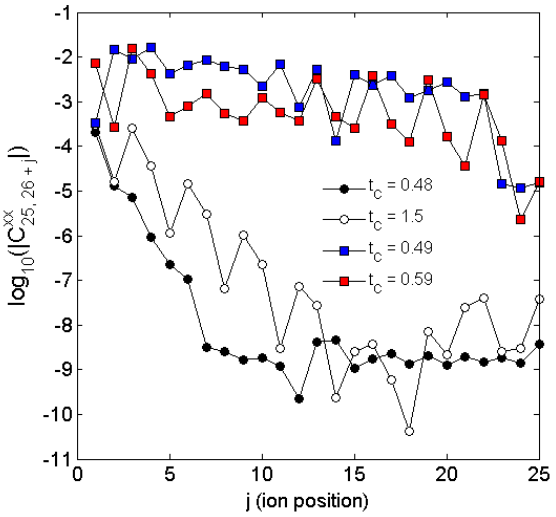

Figure 3.11: Correlation functions $C^{xx}_{j,l}$ for values of $t_{\rm C}$ in the AF/F, Hopfield and frustrated phases. Results for the ground state of a chain with $N = 50$ ions calculated with a DMRG algorithm (number of states kept $D = 18$, maximum number of phonons $n = 9$), in units of $g = 1$, $\delta_{N/2} = 1$, with $\Omega_x = 0.01$, and $\Delta k = 5\pi/(3d_0)$.

phase ($t_{\rm C} = 0.48$), exhibit no structure apart from the exponential decay. On the contrary, in the Hopfield phase ($t_{\rm C} = 1.5$), the periodicity imprinted by the laser force, $\Delta k = 5\pi/(3d_0)$, shows up clearly on the spatial correlations. However, the most interesting effect is the enhancement of correlations in the highly frustrated regime. The abrupt change in correlation range between $t_{\rm C} = 0.48$ (no frustration) and the value $t_{\rm C} = 0.49$ (frustrated region) shows that the variation on the physical properties of the ground state between these two regimes happens very sharply. This provides us with another accurate resource to pinpoint the frustrated regime, along with the sudden appearance of transverse magnetization.

3.5 Quantum annealing in the cooperative Jahn-Teller model

Finding the ground state of $H^{\Delta k}_{\rm cJT}$ in the frustrated region is a difficult problem, since the degeneracy in the low-lying sector of the Hamiltonian is enormous. Fortunately, there are algorithms that may be able to ease this task. In this section we discuss one of the most popular, known as quantum annealing [186–188]. This al-

gorithm involves performing a unitary dynamics on the ground state, and therefore its classical simulation is in general a complex problem [18, 61]. Therefore, we have assessed the success of the algorithm within a mean-field approximation. We show that trapped-ion quantum simulators are perfect test-beds for quantum annealing.

3.5.1 Introduction

Quantum annealing is an algorithm to find the ground state of a quantum model [186–188]. The algorithm relies on the adiabatic approximation to the quantum dynamics. Let us assume that we are given a time-dependent Hamiltonian, with typical energies E_n, and an associated time scale $\tau_{\rm ev}$. The adiabatic approximation establishes that every eigenstate $|E_n(0)\rangle$ evolves into $|E_n(t)\rangle$ at a later time t as long as $E_n \gg \hbar/\tau_{\rm ev}$ [51]. In quantum annealing one simulates the evolution of the ground state under a time-dependent Hamiltonian with two limits: at time $t_0 = 0$, it describes a 'trivial' model whose ground state can be exactly computed; for $t_f \gg \tau_{\rm ev}$, one arrives at the 'target' Hamiltonian, whose ground state may be a complicated many-body state. Assuming that the adiabatic approximation holds, the initial ground state must have evolved into the ground state of the target Hamiltonian.

Quantum annealing can be advantageous in finding the ground state of a quantum Ising chain with frustrated interactions [198, 199]. The energy landscape of a system with frustration is a rough surface, with many local minima separated by steep 'hills'. Intuitively, tunnelling through narrow barriers during quantum annealing decreases the probability of getting stuck in a 'false' minimum, and increases the chance of hitting the actual ground state. Nevertheless, quantum annealing suffers from the same difficulty as any other classical algorithm dealing with quantum systems: if the problem is comprised of many degrees of freedom, the exponential increase of the dimension of the Hilbert space prevents its efficient simulation with a computer. This has triggered the creation of quantum annealing devices, which are machines that simulate the Hamiltonian for the annealing protocol [200–202]. These devices are based on superconducting circuits, because of the large number of qubits available in these systems, but there is no restriction in which physical platform can simulate quantum annealing.

Trapped-ion systems exhibiting frustration in its ground state would also be

perfect test-beds for implementing quantum annealing. Therefore, we are going to study this algorithm for the case of the cJT model. To gain some insight into the outcome of the protocol in a real experiment, we are going to solve the dynamics in a mean-field approximation. This approach may describe the quantum evolution correctly, as it has been shown that its predictions match the results of an actual quantum annealing device [203]. As the mean-field wave function is separable, one can argue that the build-up of quantum correlations along the evolution is not critical for the performance of quantum annealers. However, this may not be true in general. Only an eventual deviation of the mean-field prediction from the experimental result can settle if there is an emergence of correlations in quantum annealing. Here we limit ourselves to assess the performance of the protocol within mean-field, as presented in the next section.

3.5.2 Mean-field theory

We present a study of quantum annealing for the ground state of $H_{\rm cJT}^{\Delta k}$ in the different regimes of the couplings. The simulation of the algorithm in trapped-ion chains is straightforward, and proceeds by switching the different terms in the Hamiltonian following a suitable schedule. In particular, we consider

$$H_{\rm ad}(t) = \sum_{n=1}^{N} \delta_n a_n^\dagger a_n + \frac{\Omega_x(t)}{2} \sum_{j=1}^{N} \sigma_j^x + g(t) \sum_{j,n=1}^{N} \sigma_j^z (a_n M_{j,n} e^{i\Delta k d_0 j} + \text{H.c.}), \tag{3.35}$$

where the parameters follow the annealing schedules

$$\begin{aligned} \Omega_x(t) &= \Omega_x e^{-\frac{t}{\tau_{\rm ev}}}, \\ g(t)^2 &= g^2(1 - e^{-\frac{t}{\tau_{\rm ev}}}). \end{aligned} \tag{3.36}$$

According to (3.36), at $t_0 = 0$ there is no spin-phonon coupling. We initialize the dynamics in the ground state

$$|\Psi_{\rm GS}(t=0)\rangle = |0\rangle \bigotimes_{j=1}^{N} |{\leftarrow}\rangle_j \,. \tag{3.37}$$

The vector $|{\leftarrow}\rangle_j$ is an eigenstate of the σ_j^x operator, with $\langle \sigma_j^x \rangle = -1$. $|\Psi_{\rm GS}(t=0)\rangle$ corresponds to the paramagnetic phase. The system evolves towards the ordered phase in the strongly coupled spin-phonon regime $\Omega_x \to 0, g \neq 0$, and at some

time $t_f \gg \tau_{\rm ev}$, it reaches a final state, that under ideal adiabatic evolution would correspond to

$$|\Psi_{\rm GS}(t=t_f)\rangle = |0\rangle\,|\Psi_{\rm spin}\rangle\,, \tag{3.38}$$

where $|\Psi_{\rm spin}\rangle$ is the ground state of $\sum_{j,l=1}^{N} J_{j,l}^{\Delta k}\sigma_j^z\sigma_l^z$.

The evolution of any observable $\hat{O}$ under (3.35) follows the Heisenberg equations of motion

$$\frac{d\hat{O}(t)}{dt} = i[H_{\rm ad}(t), \hat{O}(t)]. \tag{3.39}$$

In the mean-field approximation, we assume for all times that the wave function does not contain any spin-boson or spin-spin correlations, so the former equations applied to the expectation values are given as

$$\begin{cases} \dfrac{d}{dt}\langle a_n(t)\rangle = -i\delta_n\langle a_n(t)\rangle - ig(t)\displaystyle\sum_{j=1}^{N}\langle\sigma_j^z(t)\rangle M_{j,n}^* e^{i\Delta k d_0 j}, \\ \dfrac{d}{dt}\langle a_n^\dagger(t)\rangle = i\delta_n\langle a_n^\dagger(t)\rangle + ig(t)\displaystyle\sum_{j=1}^{N}\langle\sigma_j^z(t)\rangle M_{j,n} e^{-i\Delta k d_0 j}, \\ \dfrac{d}{dt}\langle\sigma_j^x(t)\rangle = -2g(t)\displaystyle\sum_{n=1}^{N}\langle\sigma_j^y(t)\rangle(M_{j,n}\langle a_n(t)\rangle e^{-i\Delta k d_0 j} + \text{c.c.}), \\ \dfrac{d}{dt}\langle\sigma_j^y(t)\rangle = -\Omega_x(t)\langle\sigma_j^z\rangle + 2g(t)\displaystyle\sum_{n=1}^{N}\langle\sigma_j^x(t)\rangle(M_{j,n}\langle a_n(t)\rangle e^{-i\Delta k d_0 j} + \text{c.c.}), \\ \dfrac{d}{dt}\langle\sigma_j^z(t)\rangle = \Omega_x(t)\langle\sigma_j^y(t)\rangle. \end{cases} \tag{3.40}$$

To solve these equations, we write them in the interaction picture with respect to $\sum_{n=1}^{N}\delta_n a_n^\dagger a_n$. We focus on the first of these equations, that in the interaction picture reads

$$\frac{d}{dt}\langle\tilde{a}_n(t)\rangle = -ig(t)\sum_{j=1}^{N}\langle\sigma_j^z(t)\rangle e^{i\Delta k d_0 j} M_{j,n}^* e^{i\delta_n t}, \quad \tilde{a}_n = a_n e^{i\delta_n t}. \tag{3.41}$$

Since the protocol starts in the paramagnetic phase, where $\langle\tilde{a}_n(0)\rangle = 0$, we get after an integration by parts,

$$\begin{aligned}\langle\tilde{a}_n(t)\rangle = &-\frac{g(t)}{\delta_n}\sum_{j=1}^{N}\langle\sigma_j^z(t)\rangle e^{i\Delta k d_0 j} M_{j,n}^* e^{i\delta_n t} \\ &+ \frac{1}{\delta_n}\int_0^t dt' e^{i\delta_n t'}\frac{d}{dt'}\left[g(t')\sum_{j=1}^{N}\langle\sigma_j^z(t')\rangle e^{i\Delta k d_0 j} M_{j,n}\right].\end{aligned} \tag{3.42}$$

We can drop the second term in the right hand side of Eq. (3.42) as long as we assume that

$$\frac{d}{dt}\langle\sigma_j^x(t)\rangle \ll \delta_n, \tag{3.43}$$

and $\tau_{\rm ev}^{-1} \ll \delta_n$. The latter requirement is fulfilled for large enough $\tau_{\rm ev}$, but the first condition must be validated a posteriori from the self-consistency of the results. We will return to this point at the end of the discussion. With this approximation, the relation (3.42) renders a closed set of equations for the spin observables

$$\begin{cases} \dfrac{d}{dt}\langle\sigma_j^x(t)\rangle = 2\displaystyle\sum_{l=1}^{N}(1-e^{-\frac{t}{\tau_{\rm ev}}})J_{j,l}^{\Delta k}\langle\sigma_j^y(t)\rangle\langle\sigma_l^z(t)\rangle, \\ \dfrac{d}{dt}\langle\sigma_j^y(t)\rangle = -\Omega_x(t)\langle\sigma_j^z(t)\rangle - 2\displaystyle\sum_{l=1}^{N}(1-e^{-\frac{t}{\tau_{\rm ev}}})J_{j,l}^{\Delta k}\langle\sigma_j^x(t)\rangle\langle\sigma_l^z(t)\rangle, \\ \dfrac{d}{dt}\langle\sigma_j^z(t)\rangle = \Omega_x(t)\langle\sigma_j^y(t)\rangle. \end{cases} \tag{3.44}$$

We recall that the expectation values are taken with respect to the initial state (3.37), $|\Psi_{\rm GS}(t=0)\rangle = |0\rangle\bigotimes_{j=1}^{N}|{\leftarrow}\rangle_j$. By plugging this initial condition in the former equations we see that this state is actually a stationary solution. Nevertheless, this result cannot be physical, as the spin-phonon coupling does not commute with σ_j^x, and must favour the orientation of the spins in the z direction. The explanation to this contradiction is that the stationary solution is a spurious artefact of the mean-field approximation. We can cure this by adding an extra driving field into the adiabatic protocol

$$H_{\rm ad}(t) \to H_{\rm ad}(t) + \frac{\Omega_z(t)}{2}\sum_{j=1}^{N}\sigma_j^z, \quad \Omega_z(t) = \Omega_z e^{-\frac{t}{\tau'_{\rm ev}}}. \tag{3.45}$$

The typical time of $\Omega_z(t)$ is such that $\tau'_{\rm ev} \ll \tau_{\rm ev}$. The reason for this convention is that the extra field plays a role at the beginning of the protocol exclusively. This term must be zero when the evolution gets close to the classical limit, so it does not spoil the form of the target Hamiltonian. The initial state must be modified accordingly,

$$|\Psi_{\rm GS}(t=0)\rangle = |0\rangle\bigotimes_{j=1}^{N}|\theta_j\rangle\,, \tag{3.46}$$

where $\bigotimes_{j=1}^{N}|\theta_j\rangle$ corresponds to the spin ground state, which depends on the relative value of Ω_x and Ω_z. The evolution equations change as well, and we get

$$\frac{d}{dt}\langle\sigma_j^x(t)\rangle = -\Omega_z(t)\langle\sigma_j^y(t)\rangle + 2\sum_{l=1}^{N}(1-e^{-\frac{t}{\tau_{\rm ev}}})J_{j,l}^{\Delta k}\langle\sigma_j^y(t)\rangle\langle\sigma_l^z(t)\rangle, \tag{3.47}$$

and

$$\frac{d}{dt}\langle\sigma_j^y(t)\rangle = \Omega_z(t)\langle\sigma_j^x(t)\rangle - \Omega_x(t)\langle\sigma_j^z(t)\rangle - 2\sum_{l=1}^{N}(1-e^{-\frac{t}{\tau_{\rm ev}}})J_{j,l}^{\Delta k}\langle\sigma_j^x(t)\rangle\langle\sigma_l^z(t)\rangle. \tag{3.48}$$

The equation for $\langle\sigma^z(t)\rangle$ remains the same.

3.5.3 Discussion of the algorithm

We have integrated these equations for different values of the hopping amplitudes $t_{\rm C}$ (cf. Fig. 3.12). We calculate $\langle\sigma_j^z(t)\rangle$, and at a time $t = t_f \gg \tau_{\rm ev}, \tau'_{\rm ev}$, we quantify

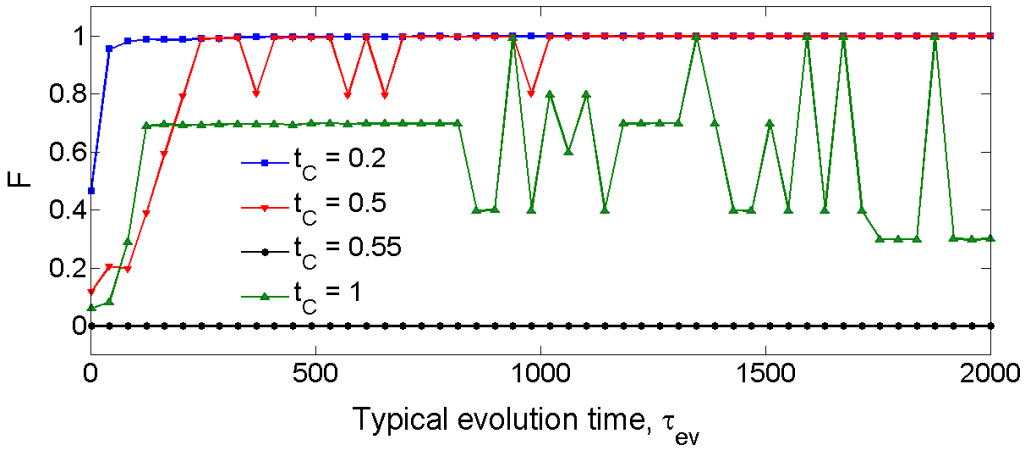

Figure 3.12: Outcome of the quantum annealing protocol. $N = 20$, in energy units such that $\delta_{N/2} = g = 1$, and values of $t_{\rm C}$ as indicated in the figure. $\Delta k = 2\pi/(3d_0)$, and $\Omega_x = 5$, $\Omega_z = 10^{-1}\ \Omega_x$, and $\tau_{\rm ev} = 10\ \tau'_{\rm ev}$.

the resemblance between the exact ground state in the classical limit, $\langle\sigma_j^z\rangle_{\rm ex}$, and the result of quantum annealing , $\langle\sigma_j^z\rangle_{\rm QA}$, by the overlap,

$$F = \frac{1}{N}\left|\sum_j \langle\sigma_j^z\rangle_{\rm ex}\langle\sigma_j^z\rangle_{\rm QA}\right|. \tag{3.49}$$

This calculation is performed for increasing typical evolution times $\tau_{\rm ev}$. The exact ground state $\langle\sigma_j^z\rangle_{\rm ex}$ is the configuration that minimizes the energy of the Hamiltonian $\sum_{j,l=1}^{N} J_{j,l}^{\Delta k}\sigma_j^z\sigma_l^z$, and it can be computed by means of a minimization routine. However, because of the large amount of degeneracy in the event of frustration, the most reliable way to proceed is to consider all the possible configurations of the spins, and single out the one with the minimum energy. Because of the exponential enlargement of the configuration space, this approach becomes rapidly infeasible with an increasing number of spins. Thus, we had to restrict our simulations to $N = 20$ ions.

We depart from the previously considered value of Δk, and focus on the case $\Delta k = 2\pi/3d_0$. The regimes of the ground state at $\Omega_x = 0$ are analogous to those of $\Delta k = 5\pi/3d_0$ (cf. sect. 3.4.3), except for the short-range interactions limit,

in which the ferromagnetic order minimizes the energy. The mean-field adiabatic evolution of the spin-phonon system is predicted to reach the global ground state far from the highly frustrated regime. Accordingly, for values of the coupling $t_C \ll \bar{t}_C$, the evolution hits the F phase (upper line in Fig. 3.12). Quite remarkably, when $t_C = \bar{t}_C \simeq 0.5$ (second line from the top), the mean-field dynamics is still able to reproduce the exact solution.

The fact that it takes a longer time to converge signals the appearance of a more convoluted energy landscape. We note as well that before reaching the value $F = 1$ steadily, the protocol explores other orders, pinpointing the existence of quasi-degenerate solutions. On the contrary, deeper in the highly frustrated regime $t_C = 0.55$ (bottom line), the mean-field approximation performs very poorly, and it does not abandon the initial condition for any of the time scales considered. For $t_C = 1$ (third line from the top), the simulation is also unable to converge in the time scales considered. These two latter results may imply that in this regime there are features that cannot be captured by the mean-field approximation.

The mean-field approximation is only justified in the regimes where correlations do not play a major role. We know that the ground state is well described by a mean-field ansatz in the limit of $\Omega_x \to \infty$, and in the event of long-range interactions $t_C \gg \delta_{N/2}$ [192]. Outside these regions, only an exact simulation of the full quantum dynamics would assess the validity of quantum annealing. In the light of the previous results, we cannot claim that the mean-field approach correctly predicts the exact annealing dynamics, nor that it does not. Therefore, this system is an ideal scenario for experiments to test whether a quantum correlated annealer would yield results which cannot be described by the mean-field (separable) wave function.

Regarding the condition (3.43), we present in Fig. 3.13 the evolution of the spin mean values during the annealing process. The inset shows the spin precession as a result of the asymmetry in the typical times of evolution between the field Ω_x and the symmetry breaking term Ω_z. We estimate the time derivative of $\langle \sigma_j^z(t) \rangle$ as the product of the amplitude of the oscillation divided by its period, so that

$$\frac{d}{dt}\langle \sigma_j^z(t) \rangle \sim 10^{-3} \ll \min_n \delta_n = \delta_{N/2} = 1. \tag{3.50}$$

Therefore, we see that dropping the integral term in Eq. (3.42) is justified in this case.

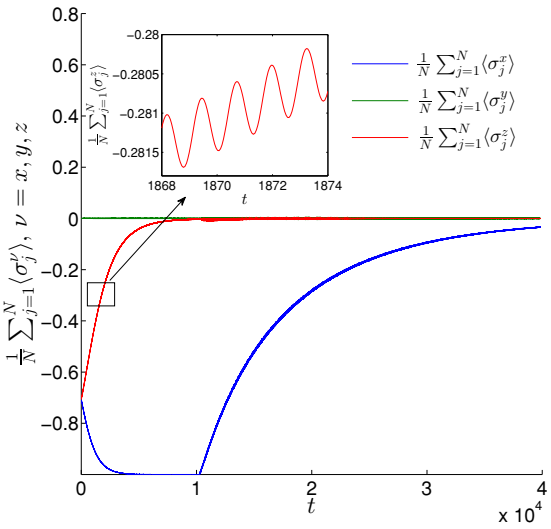

Figure 3.13: Evolution of the spin expectation values. We set $t_{\rm C}=2$, for units such that $g=\delta_{N/2}=1$, with $\Delta k=0, \Omega_x=\Omega_z=5, \tau_{\rm ev}=8\tau'_{\rm ev}=10^{-4}$.

3.6 Trapped-ion experimental parameters

The cooperative Jahn-Teller Hamiltonian can be naturally implemented in state-of-the-art trapped-ion experiments. In order to explore its phase diagram, the system is initialized by cooling the chain close to the vibrational ground state. Then, by tuning the different parameters, it is possible to realize the symmetry-breaking phase transition into the frustrated region, as well as the adiabatic protocol for quantum annealing.

Let us consider the parameters for the phonon Hamiltonian (3.5). A typical average distance between ions is $d_0=10\ \mu$m [28]. Considering $^9{\rm Be}^+$ ions ($m=1.49650\cdot10^{-23}$ g) and a radial trapping frequency $\omega_x=5\ (2\pi)$ MHz, we get a Coulomb coupling ($e=3.33564\cdot10^{-10}\,{\rm cm}^{3/2}{\rm g}^{1/2}{\rm s}^{-1}$)

$$t_{\rm C}=\frac{e^2}{m\omega_x d_0^3}\simeq 38\,(2\pi)\,{\rm kHz}. \tag{3.51}$$

The latter is the most important experimental energy scale, limiting the overall speed of an experiment. For the effective Rabi frequency Ω_x we assume an optical driving of the carrier resonance. Typical values for these processes are around 100 kHz [149], and therefore on the same order of $t_{\rm C}$. Regarding the spin-phonon coupling with the transverse modes, the interaction Hamiltonian is given as

$$\hat{H}_{\rm int}=\sum_{j=1}^{N}\Omega_j\sigma_j^z(e^{i(\Delta\mathbf{k}\cdot\mathbf{r}_j(t)-\omega_{\rm L}t)}+{\rm H.c.}). \tag{3.52}$$

Let us assume an optical force with $|\Delta\mathbf{k}| \approx 2\pi/320$ nm^{-1}. We focus on the value of laser momentum considered for quantum annealing, $\Delta k = 2\pi/(3d_0)$. This can be achieved by using an angle $\theta \approx 0.6$ degrees between the incident optical force and the perpendicular to the ion chain, such that $\Delta k_x = \cos(\theta)|\Delta\mathbf{k}|$, and $\Delta k_z = \sin(\theta)|\Delta\mathbf{k}|$. The laser phase is then given as

$$\begin{aligned}&(\Delta k_x, 0, \Delta k_z)\cdot(\delta r_{x,j}(t), \delta r_{y,j}(t), r_j^{(0)} + \delta r_{z,j}(t))\\ &= \sum_{n=1}^{N}(\eta_n^x M_{j,n}^x a_{x,n} e^{-i\omega_n^x t} + \text{H.c.}) + \sum_{n=1}^{N}(\eta_n^z M_{j,n}^z a_{z,n} e^{-i\omega_n^z t} + \text{H.c.}) + \Delta k_z r_j^{(0)}, \quad (3.53)\end{aligned}$$

where $\eta_n^\beta = \Delta k_\beta/\sqrt{2m\omega_n^\beta}$. For the values considered above, the Lamb-Dicke parameter of the transverse motion is $\max_n \eta_n^x \approx 0.21$. This ensures that the sidebands can be addressed. Assuming that the processes on the axial direction are fast-rotating, we have that

$$\hat{H}_{\text{int}} \to g\sum_{j,n=1}^{N}\sigma_j^z(M_{j,n}e^{i\delta_n t}e^{i\Delta k d_0 j}a_n^\dagger + \text{H.c.}). \quad (3.54)$$

As in the case of the transverse field, the typical magnitude of the Rabi frequency g is around 100 kHz [149]. The (detuning) frequency δ_n is referred to the zigzag mode of transverse motion.

We have still to justify that the momentum $\Delta\mathbf{k}$ in the trap direction does not excite the axial modes. The corresponding axial trapping frequencies for $d_0 = 10$ μm and $^9Be^+$ ions, in the event of $N = 20$ and 50, are $\omega_z = 192$ and 94 (2π) kHz, as can be read from a calculation of the ions' equilibrium positions. The maximum axial normal mode energies can be computed from a numerical diagonalization of the elasticity matrix of the chain [118], and they are $\max_n \omega_n^z = 2.29$ $(2\pi$ MHz) and $\max_n \omega_n^z = 2.5$ (2π) MHz, respectively. Therefore, the normal axial modes are not resonant with the transverse, centred around $\omega_x = 5$ (2π) MHz. Furthermore, the spin-dependent force can be slightly off-resonant with respect to the transverse modes, while far detuned from the axial modes. Also, with the former values, we get Lamb-Dicke parameters $\max_n \eta_n^z = 0.011$ (for $N = 20$, $\omega_z = 192$ (2π) kHz) and $\max_n \eta_n^z = 0.016$ (for $N = 50$, $\omega_z = 94$ (2π) kHz). The condition $\max_n \eta_n^z \ll \max_n \eta_n^x$ ensures that the coupling to the axial modes is negligible.

With the values considered above, the evolution time for quantum annealing in Fig. 3.12 would be of the order of milliseconds. This time scale is within the

experimental coherence times of these experiments, since typical simulation times for adiabatic preparation of frustrated ground states are of 0.3 ms [124].

3.7 Conclusions

The aim of this chapter was to realize frustrated interactions with trapped-ion quantum matter. Associated with the frustrated region in the phase diagram, we expected to unveil some features of a quantum spin-liquid (QSL) phase. Also, we wanted to assess the performance of quantum annealing in finding the ground state in the presence of frustration.

In order to give rise to the frustrated interactions, we studied the effect of an inhomogeneous addressing of the ions. This led to a competition between the dressing by optical phases and the effective spin couplings mediated by the phonon collective excitations. Since the resulting interactions could not be simultaneously satisfied, we were able to realize the desired frustrated interactions. The simulation of frustrated systems with trapped ions has been reported in [124, 125], but these experiments relied on the weak-coupling regime and on the individual addressing of motional modes. Our proposal opens up a scalable method to induce frustrated interactions while allowing for fast simulation times. Furthermore, the dressing by optical phases gives rise to far richer physics. Δk provides us with a parameter to tune the frustration, while the range of the interactions can be independently adjusted. The interplay of these two elements originates a plethora of strongly-correlated states, whose physics is still largely unexplored. Also, dressing by optical phases could be carried over to other experimental platforms where long-range interactions are available as well, such as ions in 2D Penning traps.

Regarding the features of the quantum spin-liquid phase, we performed DMRG simulations focusing on the properties of the frustrated region. We established the emergence of enhanced quantum fluctuations and correlations, which are typical of QSL phases. In general, we have indications of the QSL behaviour, but a deeper qualitative analysis is missing. The proper characterization of the quantum fluctuations must be performed for increasing system size, as well as the enhancement of quantum correlations. This would allow us to eliminate finite size effects, and to

properly establish a possibly diverging susceptibility to external perturbations in the frustrated phase. Also, an extensive simulation could shine light on the functional form of the correlations in the frustrated region, which could be power-law because of the underlying order in the fluctuations of the frustrated phase. A possible extension of this work could consider the generalization to 2D experiments with trapped-ions. This is specially appealing since one of the most popular quantum spin-liquid states, the resonating-valence-bond, was originally proposed for a 2D lattice [204].

We recall that our DMRG approximated the dipolar coupling of the phonons by a first-neighbours interaction. In general, DMRG is difficult to implement with long-range interactions. This is because in the construction of the block Hamiltonian, one must redefine the matrix representations of every operator within the block at every step. This translates into a significant increase of computational time. In any case, we must stress that neglecting the dipolar decay has not prevented us from simulating spin interactions effectively long-ranged. Therefore, one can avoid the implementation of DMRG with long-range couplings for the spins at the expense of introducing the phononic degrees of freedom. The addition of the phonons means also an overhead for the method, since the effective on-site dimension is no longer that of the spin alone. Thus, it is interesting to assess if there is a trade-off in including the phonons in these simulations. From the calculations presented in this chapter, we cannot claim that there is an advantage or not, because we have not compared the efficiency of our method with the DMRG in the event of long-range interactions. Therefore, this issue could be settled by performing this latter calculation.

Finally, trapped-ion quantum simulators are perfect test-beds to assess the potential of quantum annealing. State-of-the-art trapped-ion experiments perform adiabatic preparation of states routinely, and it is possible to ensure the quantum coherence during the evolution [124]. This would allow us to settle the role played by correlations in quantum annealing, since our mean-field calculation neglected this feature. Thus, our calculations were not conclusive about the success of quantum annealing. This could be supplemented with the use of Quantum Monte Carlo simulations, that are able to tackle the exact unitary dynamics [202].

Chapter 4

Gauge symmetry and first-order phase transition in the Ising-Rabi lattice model

4.1 Introduction

Our aim in this chapter is the realization of a minimal model with a local (gauge) symmetry. Given a model defined on a lattice, a gauge symmetry is an invariance of the Hamiltonian that holds independently at every site [205]. In contrast, we have been discussing so far global symmetries, which act simultaneously on every site of the lattice.

Models endowed with a gauge symmetry are very important in physics, in particular in the realm of high energies. For instance, the theory of the strong interactions, QCD, enjoys a SU(3) gauge symmetry [13, 14]. This theory is well understood in the weak-coupling limit, but a thorough study of its non-perturbative regime is still lacking. Since the coupling strengths in quantum simulators can be tuned at will, an eventual realization of QCD with synthetic quantum matter could gain access to its whole phase diagram. Nevertheless, this goal is still beyond current experimental capabilities. For this reason, several works have suggested the implementation of simpler 'toy models' first, such as compact QED [206], or a lattice Schwinger model [207]. Actually, the digital quantum simulation of the latter in a few-qubit quantum computer has been recently reported [81].

Following these advances, we present in this chapter the implementation of a minimal system exhibiting a gauge symmetry. Actually, this can be accomplished by a simple generalization of the Rabi lattice model [185]. Consider an Ising model such as

$$H_{\mathrm{I}} = \sum_j h_j \sigma_j^x - J \sum_j \sigma_j^z \sigma_{j+1}^z. \tag{4.1}$$

We provide this Hamiltonian with a local discrete invariance by promoting the classical field h_j to a quantum variable, for instance the position operator of a local bosonic field

$$h_j \to g(a_j + a_j^\dagger).$$

After this substitution, we get an Ising spin model where the transverse field is a variable with quantum dynamics of its own. This Hamiltonian possesses a discrete local symmetry, since it is invariant under a set of local transformations defined at each site j, $\sigma_j^x \to -\sigma_j^x$, $a_j \to -a_j$. If we include a finite energy for the bosonic modes, we arrive at

$$H_{\mathrm{IR}} = \delta \sum_{j=1}^{N} a_j^\dagger a_j + g \sum_{j=1}^{N} \sigma_j^x (a_j^\dagger + a_j) - J \sum_{j=1}^{N-1} \sigma_j^z \sigma_{j+1}^z. \tag{4.2}$$

This model turns out to be a Rabi lattice, where different sites are coupled by an Ising interaction between spins. Thus, we refer to H_{IR} as the Ising-Rabi lattice (IR) model. We expect that, analogously to the cooperative Jahn-Teller model, the Ising-Rabi lattice undergoes a phase transition between phases of different symmetry.

We proceed now to a systematic study of the invariances of H_{IR}. Then we explain the implementation of the model with trapped-ion microtraps. We discuss the phase diagram of the model by means of perturbation theory and two variational wave functions. Finally, we present the results of an exact diagonalization of the Ising-Rabi Hamiltonian with DMRG, and conclude the chapter giving the experimental parameters for an eventual implementation, and some conclusions.

4.2 Symmetry properties of the model

As stated above, Hamiltonian (4.2) is invariant under a *gauge* (local) $\mathbb{Z}_2$ transformation, generated by

$$\mathcal{P}_{\mathrm{gauge}}^{(j)} = e^{i\pi\left(a_j^\dagger a_j + \frac{\sigma_j^z}{2}\right)}. \tag{4.3}$$

Physically, this transformation corresponds to the situation depicted in Fig. 4.1. As

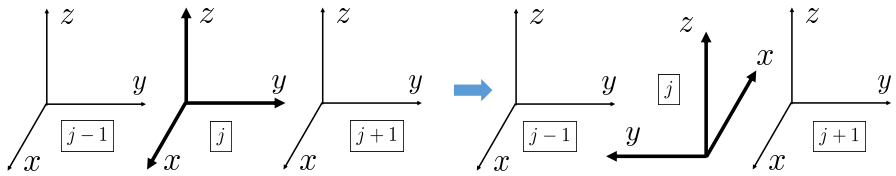

Figure 4.1: Discrete gauge transformation in the IR model.

shown, $\mathcal{P}^{(j)}_{\text{gauge}}$ is a rotation of the frame at site j, changing x by $-x$. As a consequence $\sigma^x_j \to -\sigma^x_j$ and $a_j \to -a_j$. In the event of spontaneous symmetry breaking of this invariance, we would get a phase with $\langle a_j \rangle_{\text{GS}} \neq 0$ and $\langle \sigma^x_j \rangle_{\text{GS}} \neq 0$, analogous to the antiferromagnetic phase of the cooperative Jahn-Teller model. However, this possibility is precluded by a general result known as Elitzur's theorem [205, 208]. According to the theorem, there cannot be spontaneous symmetry breaking of a gauge invariance in a lattice gauge theory.

The Hamiltonian (4.2) has also another symmetry, this time a global invariance under the change $z \to -z$, that carries $\sigma^z_j \to -\sigma^z_j$ (cf. Fig. 4.2). This symmetry is

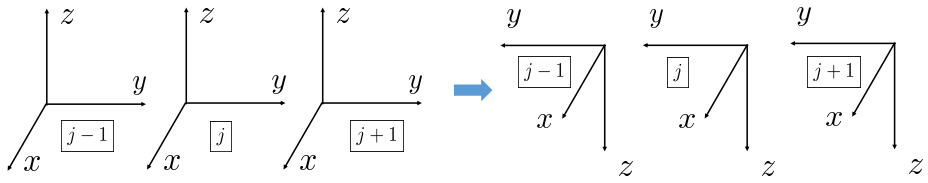

Figure 4.2: Global transformation (4.4).

global, and it is generated by the unitary operator

$$\mathcal{P} = e^{i\pi\mathcal{N}}, \text{with } \mathcal{N} = \sum_{j=1}^{N} \frac{\sigma^x_j}{2}. \tag{4.4}$$

Analogously to the Ising model, the IR model can undergo the spontaneous symmetry breaking of this invariance, so that the ground state features a magnetization $\langle \sigma^z_j \rangle \neq 0$. However, in contrast to the Ising model, the ground state of H_{IR} breaks the global symmetry all over the phase diagram *for finite system size* N. This means that an eventual phase transition in the IR model must occur between phases with the same symmetries.

4.3 Implementation with ion microtraps

Before starting with the discussion of the phase diagram of the model, we describe the realization of the IR Hamiltonian with trapped-ion chains in arrays of microtraps [134–139]. The choice of these systems instead of the usual collective ion traps stems from the necessity of different trapping frequencies at every site of the chain, to give rise to the bosonic part of $H_{\rm IR}$.

There are other experimental situations where $H_{\rm IR}$ could be implemented. For instance, superconducting qubits are a platform where Rabi lattice models are easily realized [112]. As with trapped-ion quantum simulators, the effective Ising interaction could be induced through the coupling to collective bosonic modes. Also, an eventual realization with Rydberg ions [209] could benefit from the fact that the spin couplings are directly implemented by the dipole-dipole interactions between ions.

The Ising-Rabi lattice Hamiltonian

$$H_{\rm IR} = \delta \sum_{j=1}^{N} a_j^\dagger a_j + g \sum_{j=1}^{N} \sigma_j^x (a_j^\dagger + a_j) - J \sum_{j=1}^{N-1} \sigma_j^z \sigma_{j+1}^z \tag{4.5}$$

consists of three parts. We begin by describing how to give rise to the bosonic part of $H_{\rm IR}$. We recall that the quantized oscillations of the ions around their equilibrium positions are given by a phonon Hamiltonian such as (2.39),

$$H_{\rm phonon} = \sum_{j=1}^{N} \sum_{\beta} \omega_j^\beta a_{\beta,j}^\dagger a_{\beta,j} + \frac{1}{2} \sum_{j>l=1}^{N} \sum_{\beta} t_{j,l}^\beta (a_{\beta,j}^\dagger a_{\beta,l} + \text{H.c.}). \tag{4.6}$$

The gauge symmetry of the IR model is based on the fact that we can make the transformation $a_j \to -a_j$ for a particular j, and this leaves the Hamiltonian unchanged. The terms $t_{j,l}^\beta$ in (4.6) necessarily break this invariance. Thus, we would like to get rid of $t_{j,l}^\beta$ for at least one direction. At the same time, the phonon coupling between modes in another direction needs to mediate the effective spin coupling $J_{j,l}\sigma_j^z\sigma_l^z$. A possible way of meeting these requirements is using different local frequencies for the phonons in a particular direction (cf. Fig. 4.3). We assume a set of different trap frequencies along the transversal direction, ω_j^x. Then, the hopping events in (4.6) associated with the motion in the x direction are fast rotating. Specifically, if ions j and l are subjected to frequencies ω_j^x and ω_l^x, the terms $a_{x,j}^\dagger a_{x,l}$ would rotate

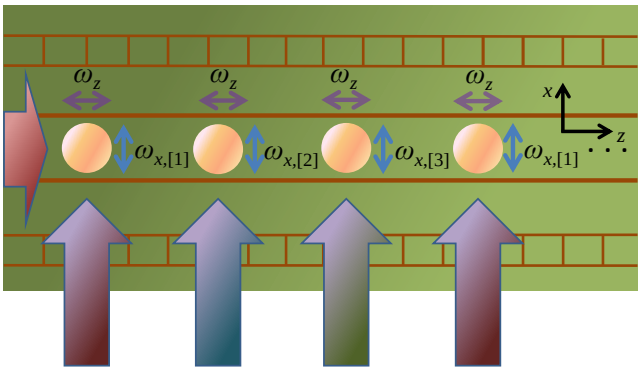

Figure 4.3: Scheme representing trapped ions in a linear array of microtraps with the electrodes printed on the surface. Solid arrows represent the laser fields acting on the ion chain. We indicate the trap frequencies at every site.

with $\exp[-it(\omega_j^x - \omega_l^x)]$ in the interaction picture for the motion. We can perform the Rotating Wave Approximation (RWA) as long as $t_{j,l}^x \ll |\omega_j^x - \omega_l^x|$. Assuming that this is the case, hopping terms in H_{phonon} can be safely ignored, and we are led to the Hamiltonian for the transverse modes

$$H_x = \sum_{j=1}^{N} \omega_j^x a_{x,j}^\dagger a_{x,j}. \tag{4.7}$$

The common frequency $\omega_j^x \to \delta$ can be achieved by means of local laser detunings, discussed later on. We recall that the motional coupling between different traps decays fast as a function of the inter-ion distance, $t_{j,l}^\beta \sim 1/|r_j^{(0)} - r_l^{(0)}|^3$. Thus, it is only necessary to eliminate the coupling between nearest or next-to-nearest neighbour ions, since longer-range terms will give negligible contributions.

Regarding the motion in the z direction, we set $\omega_j^z \to \omega_z$. The Hamiltonian for the longitudinal motion is

$$H_z = \sum_{n=1}^{N} \omega_n^z a_{z,n}^\dagger a_{z,n} \tag{4.8}$$

in the basis of collective modes of motion, $a_{z,n} = \sum_{j=1}^{N} M_{j,n}^z a_{z,j}$, with normal frequencies ω_n^z. These normal modes will mediate the effective spin-spin interaction. To this end, we add a pair of laser fields along the trap axis z, that induce a σ^z

interaction (cf. (2.63))

$$H_{z-\text{force}}(t) = g_z \sum_{j,n=1}^{N} \sigma_j^z \left(M_{j,n}^z a_{z,n} e^{it\delta_0^z} e^{i\Delta k_z r_j^{(0)}} + \text{H.c.} \right), \tag{4.9}$$

of strength g_z. The laser (detuning) frequency is defined with respect to the lowest energy mode of the longitudinal motion, which is the centre-of-mass (COM) mode $n = 0$ [118]. We assume that $r_j^{(0)} = d_0 j$, with d_0 the separation of the traps, and Δk_z is chosen as to give the same phase on every ion. We work in a rotating frame such that $H_{z-\text{force}}(t) \to H_{z-\text{force}}(0) \implies e^{\pm it\delta_0^z} \to 1$. If δ_0^z is fairly off-resonant with the bottom of the band, and $g_z \ll \delta_0^z$, a polaron transformation as in the cJT model allows us to express (4.9) as

$$H_{\text{spin}-\text{spin}} = \sum_{j,l=1}^{N} J_{j,l} \sigma_j^z \sigma_l^z. \tag{4.10}$$

We will assume the short-range limit $t_{j,j+1}^z \ll \delta_0^z$ of the effective couplings (cf. (3.18)),

$$J_{j,l} \simeq -\frac{J_{\text{dip}}}{|j-l|^3}, \quad J_{\text{dip}} \simeq \frac{g_z^2 t_{j,j+1}^z}{2(\delta_0^z)^2}, \; t_{j,j+1}^z = \frac{2e^2}{m\omega_z d_0^3}, \tag{4.11}$$

which can be assimilated by a first-neighbours interaction.

Finally, local spin-phonon couplings in H_{IR} require driving simultaneously red and blue sideband transitions for the transverse oscillations (cf. (2.59)). However, as we have already discussed, ω_j^x are different among close traps. This means that matching the resonance conditions for the spin-dependent forces requires as many laser wavelengths as different trapping frequencies. Let us consider the array of traps as consisting of N/n, $n \in \mathbb{N}$ sequential sets of traps. Within these, neighbouring traps frequencies are different. We set a constant difference between one trap and the next, $\omega_j^x - \omega_{j+1}^x \equiv \Delta\omega_x$. All the sets have the same arrangement of n frequencies, and they appear one after the other along the chain. Let us call these frequencies $\omega_1^x, \ldots, \omega_n^x$. Any frequency can be written as $\omega_{[j]}^x$, where $[j] = (j-1) \bmod n + 1$. Now, we apply n laser fields transversally to the chain, with mutual detunings $\Delta\omega_x, \ldots, (n-1)\Delta\omega_x$. Because of this frequency difference, they can address the whole chain at the same time. In this way, the matching condition only happens between a given laser with, let us say $\omega_{\text{L}} = \omega + \omega_{[j]}^x - \delta_{[j]}^x$, and the ions that are trapped at frequencies $\omega_{[j]}^x$ (ω is the spin transition frequency). This gives rise to

the σ^x-force (cf. (2.59))

$$H_{x-\text{force}}(t) = g_x \sum_{j=1}^{N} \sigma_j^x (a_{x,j}^\dagger e^{i\delta_{[j]}^x t} + a_{x,j} e^{-i\delta_{[j]}^x t}), \tag{4.12}$$

where $g_x = i\Omega_{x,[j]}\eta_{[j]}^x$, the laser Rabi frequency and Lamb-Dicke parameters of the coupling, respectively. We rely on the local dependence of $\Omega_{x,[j]}$ to achieve a homogeneous g along the chain, as $\eta_{[j]}^x$ depend on the on-site trap frequencies. Moving into a rotating frame with frequencies $\omega_{x,[j]}^{\text{L}}$, we get $\omega_{[j]}^x \to \delta_{[j]}^x$ in (4.7), and $H_{x-\text{force}}(t) \to H_{x-\text{force}}(0)$, so that

$$H_{x-\text{force}} = g_x \sum_{j=1}^{N} \sigma_j^x (a_{x,j}^\dagger + a_{x,j}). \tag{4.13}$$

Since laser detunings are site-dependent, they can be shifted to give common on-site phonon energies δ, $\forall j$, which leads to

$$H_x = \sum_{j=1}^{N} \delta a_{x,j}^\dagger a_{x,j} \tag{4.14}$$

as the effective phonon energy contribution.

The IR Hamiltonian is eventually implemented as the sum of H_x, $H_{\text{spin}-\text{spin}}$ and $H_{x-\text{force}}$, with $g_x \to g$ and $J_{\text{dip}} \to J$.

4.4 Qualitative discussion of the phase diagram

In this section we discuss, qualitatively, the phase diagram of the Ising-Rabi lattice model. We begin by presenting a perturbative study of the Hamiltonian, and a conjectural phase diagram. Then, we support these claims by studying two different variational wave functions for the ground state.

4.4.1 Perturbative study of the phase diagram

We are going to consider two different regimes of

$$H_{\text{IR}} = \delta \sum_{j=1}^{N} a_j^\dagger a_j + g \sum_{j=1}^{N} \sigma_j^x (a_j^\dagger + a_j) - J \sum_{j=1}^{N-1} \sigma_j^z \sigma_{j+1}^z, \tag{4.15}$$

e.g.: (a) the case with $\delta, J \gg g$, which we refer to as the *ferromagnetic* (F) phase of the model, and (b) the case with $g, \delta \gg J$, that we call the *dressed-ferromagnetic* (DF) phase. The nomenclature will become clear after the following discussion.

Ferromagnetic phase ($\delta, J \gg g$)

We begin by considering the limit $g \to 0$ of H_{IR}

$$H_{\mathrm{F}}^{0} = \delta \sum_{j=1}^{N} a_j^{\dagger} a_j - J \sum_{j=1}^{N-1} \sigma_j^z \sigma_{j+1}^z. \tag{4.16}$$

The two possible ground states of this Hamiltonian, for $J > 0$, are

$$|\phi_{\mathrm{F},\uparrow}\rangle = |0\rangle_{\mathrm{b}} \bigotimes_{j=1}^{N} |\uparrow_z\rangle_j, \quad |\phi_{\mathrm{F},\downarrow}\rangle = |0\rangle_{\mathrm{b}} \bigotimes_{j=1}^{N} |\downarrow_z\rangle_j. \tag{4.17}$$

They are completely analogous to the ordered states of the Ising model, so we refer to them as the ferromagnetic states. These states break the global parity symmetry $z \to -z$.

If the IR Hamiltonian were analogous to the quantum Ising chain, the addition of the spin-phonon coupling

$$H_{\mathrm{F}}' = g \sum_{j=1}^{N} \sigma_j^x (a_j^{\dagger} + a_j) \tag{4.18}$$

would lift the degeneracy of the ferromagnetic states at finite N, and restore the global parity symmetry (cf. section 2.1.3). By applying degenerate perturbation theory up to an arbitrary order, we find that, actually, H_{F}' does not lift the degeneracy. Therefore, the phases of the ground state of the Ising-Rabi lattice are in clear contrast with the quantum Ising model, where the degeneracy is lifted at finite size N in the ferromagnetic phase by an energy gap scaling like $\propto h^N$ [210], with h the value of transverse field in Eq. (4.1).

We establish the absence of parity restoration by means of the *Brillouin-Wigner* perturbation theory [50]. We study if the addition of H_{F}' as a perturbation to H_{F}^0 mixes the states $|\phi_{\mathrm{F},\uparrow}\rangle$ and $|\phi_{\mathrm{F},\downarrow}\rangle$. If this were the case, the new ground state at $g \to 0$ would be a particular superposition $|\phi_{\mathrm{F}}'\rangle = c_\uparrow |\phi_{\mathrm{F},\uparrow}\rangle + c_\downarrow |\phi_{\mathrm{F},\downarrow}\rangle$ with lower energy. At order n of perturbation theory, the weights $c_\uparrow$ and $c_\downarrow$ are the solutions to the secular equations [49]

$$\begin{cases} E_{\mathrm{GS}}^{(n)} c_\uparrow = E_\uparrow c_\uparrow + \langle \phi_{\mathrm{F},\uparrow}| \dfrac{H_{\mathrm{F}}'}{1 - R_{\mathrm{GS}} H_{\mathrm{F}}'} |\phi_{\mathrm{F},\uparrow}\rangle c_\uparrow + \langle \phi_{\mathrm{F},\uparrow}| \dfrac{H_{\mathrm{F}}'}{1 - R_{\mathrm{GS}} H_{\mathrm{F}}'} |\phi_{\mathrm{F},\downarrow}\rangle c_\downarrow, \\ E_{\mathrm{GS}}^{(n)} c_\downarrow = E_\downarrow c_\downarrow + \langle \phi_{\mathrm{F},\downarrow}| \dfrac{H_{\mathrm{F}}'}{1 - R_{\mathrm{GS}} H_{\mathrm{F}}'} |\phi_{\mathrm{F},\downarrow}\rangle c_\downarrow + \langle \phi_{\mathrm{F},\downarrow}| \dfrac{H_{\mathrm{F}}'}{1 - R_{\mathrm{GS}} H_{\mathrm{F}}'} |\phi_{\mathrm{F},\uparrow}\rangle c_\uparrow. \end{cases} \tag{4.19}$$

In the former expressions the right-hand side is expanded up to n-th order, $E_\uparrow = E_\downarrow$ are the ground state energies for $g = 0$, and

$$R_{\rm GS} = \frac{1}{E_{\rm GS}^{(n)} - H_{\rm F}^0} \left(1 - |\phi_{\rm F}\rangle\langle\phi_{\rm F}|\right), |\phi_{\rm F}\rangle \in \text{l. c.} \left\{ |0\rangle_{\rm b} \bigotimes_{j=1}^{N} |\uparrow_z\rangle \, , |0\rangle_{\rm b} \bigotimes_{j=1}^{N} |\downarrow_z\rangle \right\}, \quad (4.20)$$

is known as the *resolvent*. $E_{\rm GS}^{(n)}$ are the eigenvalues of the secular problem. We aim at showing that there is no degeneracy lifting, and thus $E_{\rm GS}^{(n)} = E_\uparrow = E_\downarrow$ for every n. Two necessary and sufficient conditions are that

$$\begin{cases} \langle\phi_{\rm F,\uparrow}| \dfrac{H'_{\rm F}}{1 - R_{\rm GS} H'_{\rm F}} |\phi_{\rm F,\uparrow}\rangle = \langle\phi_{\rm F,\downarrow}| \dfrac{H'_{\rm F}}{1 - R_{\rm GS} H'_{\rm F}} |\phi_{\rm F,\downarrow}\rangle, \\ \langle\phi_{\rm F,\downarrow}| \dfrac{H'_{\rm F}}{1 - R_{\rm GS} H'_{\rm F}} |\phi_{\rm F,\uparrow}\rangle = 0. \end{cases} \quad (4.21)$$

The first of these equations is trivially fulfilled because of the invariance of $H'_{\rm F}/(1 - R_{\rm GS} H'_{\rm F})$ under the global $\mathbb{Z}_2$ transformation $\sigma_j^z \to -\sigma_j^z$, and the action of this symmetry upon the states, such that $|\phi_{\rm F,\uparrow}\rangle \leftrightarrow |\phi_{\rm F,\downarrow}\rangle$. The second condition holds as well, but this time we must rely on the local symmetry $a_j \to -a_j$, $\sigma_j^x \to -\sigma_j^x$, that acting inside the expectation value leads to

$$\begin{aligned} \langle\phi_{\rm F,\downarrow}| \quad & (\mathcal{P}_{\rm gauge}^{(j)})^\dagger \mathcal{P}_{\rm gauge}^{(j)} \frac{H'_{\rm F}}{1 - R_{\rm GS} H'_{\rm F}} (\mathcal{P}_{\rm gauge}^{(j)})^\dagger \mathcal{P}_{\rm gauge}^{(j)} |\phi_{\rm F,\uparrow}\rangle \\ & = -\langle\phi_{\rm F,\downarrow}| \frac{H'_{\rm F}}{1 - R_{\rm GS} H'_{\rm F}} |\phi_{\rm F,\uparrow}\rangle = 0, \; \forall j, \end{aligned} \quad (4.22)$$

where the effect of the parity upon the states is straightforwardly computed as $\mathcal{P}_{\rm gauge}^{(j)} |\phi_{\rm F,\uparrow\downarrow}\rangle = e^{s_j i \frac{\pi}{2}} |\phi_{\rm F,\uparrow\downarrow}\rangle$, where $s_j = +1\,(-1)$ for $|\phi_{\rm F,\uparrow}\rangle\,(|\phi_{\rm F,\downarrow}\rangle)$.

To sum up, we have established that the spin-boson coupling $H'_{\rm F}$ does not restore the global parity symmetry. Thus, we can choose any of the ferromagnetic states to study the effect of $H'_{\rm F}$ by means of conventional perturbation theory. Assuming that the ground state is $|\phi_{\rm F,\uparrow}\rangle$, the leading-order corrections to the ground state energy when $\delta, J \gg g$ are

$$E_{\rm F} \simeq -J(N-1) - g^2 \left[\frac{N-2}{\delta + 4J} + \frac{2}{\delta + 2J} \right]. \quad (4.23)$$

Perturbation theory also gives the leading-order corrections to any of the states

(4.17), for example

$$|\mathrm{GS}^{(\mathrm{F})}\rangle \simeq |\phi_{\mathrm{F},\uparrow}\rangle - \frac{g}{\delta+4J}\sum_{j=2}^{N-1}|1\rangle_{\mathrm{b},j}|\downarrow_z\rangle_j \bigotimes_{k=1}^{N}{}' |\uparrow_z\rangle_k - \frac{g}{\delta+2J}\sum_{\{j=1,2\}}|1\rangle_{\mathrm{b},j}|\downarrow_z\rangle_j \bigotimes_{k=1}^{N}{}' |\uparrow_z\rangle_k, \tag{4.24}$$

where the prime denotes that terms such that $k = j$ do not occur in the tensor product. From this expression it is clear that corrections to the F ground states scale as $g/(\delta + 4J)$. Thus, the F phase is stable for any relative value of δ and J, provided that any of them are much larger than g.

Dressed-ferromagnetic phase ($g, \delta \gg J$)

In the $J = 0$ limit of H_{IR},

$$H^0_{\mathrm{DF}} = \delta\sum_{j=1}^{N} a_j^\dagger a_j + g\sum_{j=1}^{N}\sigma_j^x(a_j^\dagger + a_j), \tag{4.25}$$

the ground states are obtained by making a polaron transformation as in the cJT model. For further convenience, we work in a rotated basis where $x \leftrightarrow z$, so that $H_{\mathrm{IR}} \to \bar{H}_{\mathrm{IR}}$,

$$\bar{H}_{\mathrm{IR}} = \mathcal{R}_{xz} H_{\mathrm{IR}} \mathcal{R}_{xz}^\dagger, \text{ with } \mathcal{R}_{xz} = \frac{1}{2^{N/2}}\bigotimes_{j=1}^{N}(\sigma_j^x + \sigma_j^z). \tag{4.26}$$

Then, the transformation

$$U = \bigotimes_{j=1}^{N} e^{S_j}, \quad S_j = \frac{g}{\delta}\sigma_j^z(a_j^\dagger - a_j), \tag{4.27}$$

renders

$$U\bar{H}^0_{\mathrm{DF}}U^\dagger = \delta\sum_{j=1}^{N} a_j^\dagger a_j - N\frac{g^2}{\delta}. \tag{4.28}$$

In this basis, the ground state of $\bar{H}^0_{\mathrm{DF}}$ is the vacuum of the phonons, for any spin configuration. This means that there are as many as 2^N degenerate ground states, as a consequence of the lack of inter-site couplings in H^0_{DF}. This degeneracy is removed by the Ising interaction, that acting within the ground state manifold leads to

$$\langle 0|\bar{H}'_{\mathrm{DF}}|0\rangle = -Je^{-4\alpha^2}\sum_{j=1}^{N-1}\sigma_j^x\sigma_{j+1}^x, \quad \alpha = \frac{g}{\delta}. \tag{4.29}$$

The states that minimize the energy of this Hamiltonian are the ferromagnetic configurations. Thus, undoing the rotation and the polaron transformation, the ground states of H_{IR} in this regime are given as

$$|\phi_{\mathrm{DF},\pm}\rangle = \frac{1}{2^{N/2}} \bigotimes_{j=1}^{N} (|-\alpha, \uparrow_x\rangle_j \pm |\alpha, \downarrow_x\rangle_j). \tag{4.30}$$

We refer to these states as dressed-ferromagnetic (DF). The surviving two-fold degeneracy is consistent with that of the F phase.

Analogously to the ferromagnetic phase, we can compute perturbative corrections upon any of the DF states. The leading-order correction to the energy is given as

$$E_{\mathrm{DF}} \simeq -\frac{Ng^2}{\delta} - J(N-1)e^{-4\alpha^2} - (N-1)\frac{J^2}{\delta}P(\alpha), \tag{4.31}$$

where we have defined

$$P(\alpha) = \sum_{p=1}^{\infty} \frac{1}{p} \frac{e^{-8\alpha^2}(8\alpha^2)^p}{p!}. \tag{4.32}$$

The leading-order correction to the state is given by $(J/\delta)P(g/\delta)$. This correction is negligible if $\delta \gg J$ in the limit $g \ll \delta$, and if $g^2 \gg J\delta$ in the limit $g \gg \delta$. This is because $P(\alpha) \sim 8\alpha^2$ if $\alpha \to 0$, and $P(\alpha) \sim (8\alpha^2)^{-1}$ if $\alpha \to \infty$. In addition, $P(\alpha)$ is upper bounded for any ratio g/δ, as $\max_\alpha P(\alpha) \simeq 0.52$. Therefore, the DF phase occurs as long as $\delta \gg J$, for any value of g.

Perturbative insights into the quantum phase diagram

The previous considerations allow us to make a conjecture about the phase diagram. We distinguish two cases:

(i) Slow-boson regime, $\delta \ll J$. In this case, the condition $g \ll J$ ensures that the F states (4.17) are possible ground states of H_{IR}. On the other hand, the DF states are possible ground states if $g \gg \sqrt{J\delta}$. Thus, in the interval $\sqrt{J\delta} < g < J$, the domain of the F and DF solutions overlap, and we expect a crossover between these energy levels (cf. Fig. 4.4). Indeed, comparing the energies of the F and DF states, we find that there must be a level crossing at $g := g_{\mathrm{c}} = \sqrt{J\delta}$, where we expect the appearance of a F-DF phase transition. We hypothesise that this transition is first-order, since the first derivative of the energy must be discontinuous at the level crossing.

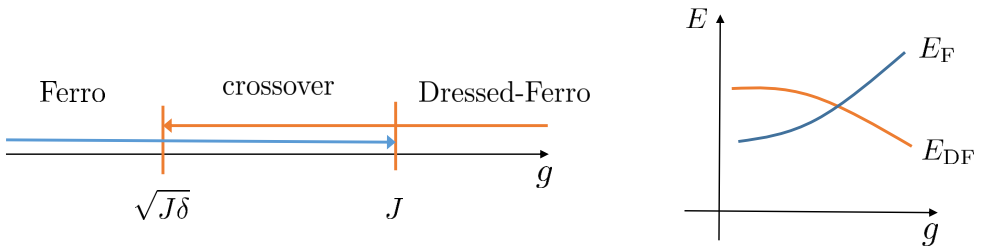

Figure 4.4: Crossover of the F and DF phases in the slow-boson regime.

(ii) Fast-boson regime, $\delta \gg J$. Here, the F states are valid ground states if $g \ll \delta$ because their corrections scale as $g/(\delta + 4J)$. Also, the DF states are valid ground states for any value of g. In the interval $g \ll \delta$, F and DF solutions overlap, however, here the DF state continuously converges to the F state. Thus we expect a continuous transition from the DF to the F solution.

Putting together all the previous arguments, we expect that H_{IR} presents a first-order quantum phase transition along the critical line $g_{\mathrm{c}}(\delta, J)$, featuring a jump from the F to the DF ground states in the regime of low-boson energies $\delta \to 0$. This is in clear contrast with the quantum Ising chain in a transverse field, where there is no coexistence of the ferro- and paramagnetic phases at neither side of the (second-order) phase transition. In the H_{IR}, however, there is a coexistence of the phases already addressed if $\sqrt{\delta J} \ll g \ll J$. This last set of inequalities cannot be longer fulfilled if $\delta \gg J$, and therefore the discontinuous behaviour is bound to disappear for a given $\delta \sim J$. At this point, we could have either a second-order phase transition or a critical end-point, but we are not going to address this question within the present study. We have summarized these considerations in Fig. 4.5, where we choose as order parameter the average boson number

$$n = \frac{1}{N} \sum_{j=1}^{N} \langle a_j^\dagger a_j \rangle \tag{4.33}$$

to capture the sudden change from the boson vacuum state (F phase) to a displaced state (DF phase).

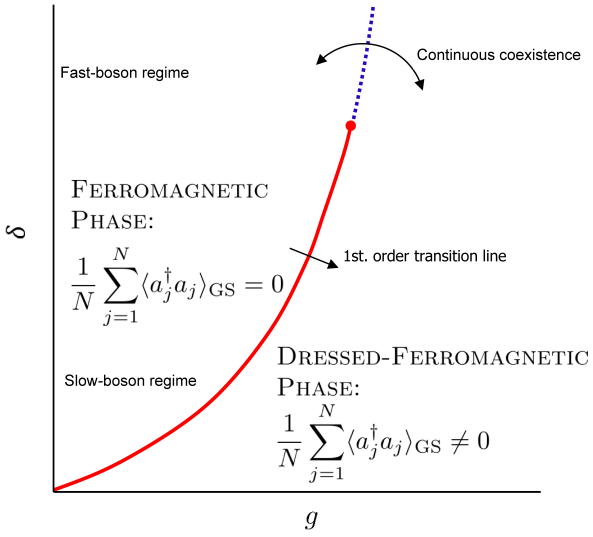

Figure 4.5: Scheme of the phase map depicting the disappearance (at the dot) of the discontinuous jump in the number of bosons along the critical line (solid) for a given value of δ, g, J. The dashed line represents no boundary but a continuous transition from the ferromagnetic to the dressed-ferromagnetic phase.

Leaving aside perturbative arguments, one can rely on clever guesses about the form of the ground state wave function, to gain some insight into the phase diagram of the model. The energy associated with these guesses, or wave functions, can be variationally minimized with respect to the parameters occurring in the wave function. We are going to pursue this strategy to validate the previous picture about the phases and the transition in the $H_{\rm IR}$. In particular, we are going to consider two different variational wave functions, that are separately suited for the regimes of $\delta \ll J$ and $\delta \gg J$.

4.4.2 Born-Oppenheimer variational ansatz ($\delta \ll J$)

In the regime of slow-boson dynamics, $\delta \to 0$, the bosonic degrees of freedom are effectively classical. This is a consequence of the correspondence principle [49]: the low-energy associated with bosonic excitations gives rise to large quantum numbers, such as the boson occupation. Thus, ladder operators can be treated as numbers,

$a_j \to \alpha_j \in \mathbb{C}$, and $H_{\rm IR}$ is reduced to a spin Hamiltonian,

$$H_{\rm BO} = \delta \sum_{j=1}^{N} |\alpha_j|^2 + g \sum_{j=1}^{N} \sigma_j^x (\alpha_j^* + \alpha_j) - J \sum_{j=1}^{N-1} \sigma_j^z \sigma_{j+1}^z. \tag{4.34}$$

This Hamiltonian describes a quantum Ising chain in a transverse field, for which an exact ground state, $|\Psi_{\rm I}(\alpha_j)\rangle$ can be exactly found [42]. The energy of $H_{\rm BO}$ is then given as

$$E_{\rm BO}(\{\alpha_j\}) = \delta \sum_{j=1}^{N} |\alpha_j|^2 + E_{\rm I,0}(\{\alpha_j\}), \tag{4.35}$$

where $E_{\rm I,0}(\{\alpha_j\})$ is the ground state energy of the quantum Ising chain with transverse fields[1] $2g\alpha_j$ and interaction strength J. Assuming that $E_{\rm I,0}(\{\alpha_j\})$ is a known function, we can minimize (4.35) with respect to the (classical) amplitudes of the bosonic fields. This gives rise to the final variational ansatz

$$|\Psi_{\rm BO}\rangle = |\Psi_{\rm I}(-\alpha_j)\rangle \bigotimes_{j=1}^{N} |\alpha_j\rangle, \tag{4.36}$$

from which we can compute any observable. We notice that, due to the underlying gauge symmetry in the $H_{\rm IR}$ Hamiltonian, (4.36) can be transformed into a solution with the same energy if we change locally the sign of the displacement α_j, and simultaneously transform $\sigma_j^x \to -\sigma_j^x$. There are thus 2^N degenerate solutions of the form $|\Psi_{\rm BO}\rangle$, given by the values $\alpha_j = s_j|\alpha_j|$, with $s_j = \pm 1$.

The self-consistent approach we have just described, where one solves the Hamiltonian for the 'fast' degrees of freedom first, and then plugs the solution into the equations for the 'slow' modes, is analogous to the Born-Oppenheimer approximation of molecular physics [211], from which we draw the name for the ansatz. In that context, the degrees of freedom of the positions of the nuclei enter the electronic Hamiltonian as parameters in the same way the boson amplitudes appear in the spin Hamiltonian (4.34).

Let us consider the solution of $H_{\rm BO}$ for $N \to \infty$. We are going to assume that the α_j take homogeneous values such that $\alpha_j \to \alpha$. The energy of the Hamiltonian is then given as

$$\frac{E_{\rm BO}}{N} = \delta\alpha^2 - 2\alpha g \frac{2}{\pi}(1+\lambda)\mathcal{E}\left[\frac{4\lambda}{(1+\lambda)^2}\right], \lambda = \frac{J}{2\alpha g}, \tag{4.37}$$

[1] We assume that $\alpha_j \in \mathbb{R}$ without loss of generality.

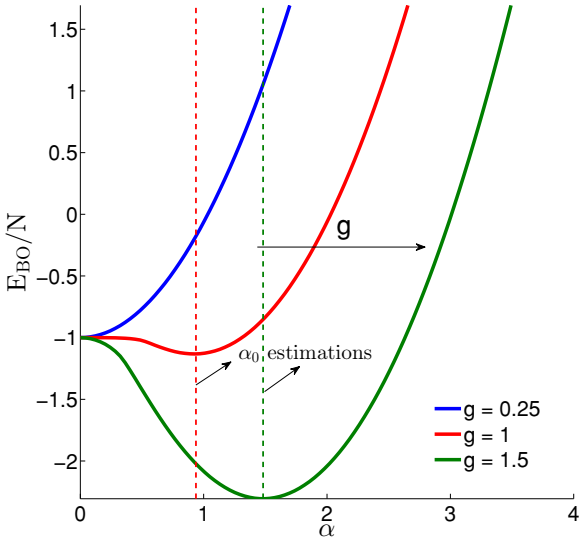

Figure 4.6: Variational energy (4.37) for $\delta = J$, with energy units such that $J = 1$, as a function of the parameter α and different values of the spin-phonon coupling g. Note that close to the origin there is a curvature change for a given $g \geq g_c$. This point marks the criticality condition.

where $\mathcal{E}$ is the complete elliptic integral of the second kind [42]. By inspecting this formula, one can realize that the energy attains a minimum for $\alpha = 0$ as long as $g \to 0$, whereas the minimum gets shifted to a finite bosonic displacement for $g > J$ (cf. Fig. 4.6). We can estimate when this change occurs by performing a Taylor expansion of E_{BO} around $\alpha = 0$, which renders

$$\frac{E_{\mathrm{BO}}}{N} = -J + (\delta - \frac{g^2}{J})\alpha^2 + O(\alpha^4). \tag{4.38}$$

By looking at the values for which the curvature changes its sign, we find that the minimum shifts from the origin whenever

$$g \geq \sqrt{\delta J} \equiv g_c. \tag{4.39}$$

Thus, (4.38) predicts a transition from a phase in which bosonic displacements are inhibited ($\alpha = 0$), and the spins point in the $\pm z$ directions, to a phase with $\alpha = \alpha_0 \neq 0$, and the spin state is the lowest energy state of a quantum Ising chain in a transverse field of magnitude $2\alpha_0 g$. This F-DF phase transition is consistent with the level crossing picture that we gained from the perturbative study.

The Born-Oppenheimer wave function offers an estimate for the boson displace-

ment in the DF phase. Assuming $g \gg J$, we can approximate

$$\frac{E_{\mathrm{BO}}}{N} \sim \delta\alpha^2 - 2\alpha g - \frac{J^2}{2\alpha g}. \tag{4.40}$$

This energy is minimum as a function of α whenever

$$\alpha^3 - \frac{g}{\delta}\alpha^2 + \frac{J^2}{4\delta g} = 0. \tag{4.41}$$

Assuming a root of the form $\alpha_0 = \alpha_1 + \alpha_2\epsilon$, with $\epsilon = J^2/16\delta g$, and keeping up to first order in ϵ, we obtain

$$\alpha_0 = \frac{g}{\delta}\left(1 - \frac{J^2\delta^2}{16g^4}\right), \tag{4.42}$$

from which we can extract the prediction for the order parameter

$$n = \alpha_0^2 \simeq \left(\frac{g}{\delta}\right)^2. \tag{4.43}$$

According to (4.42), in the regime $g \gg \delta$ we have that $\alpha_0 = g/\delta$, and we must recover the DF ground states from the Born-Oppenheimer wave function. In this case $|\Psi_{\mathrm{BO}}\rangle$ converges to $\bigotimes_{j=1}^{N} |-\alpha_0, \uparrow_x\rangle_j$ and $\bigotimes_{j=1}^{N} |\alpha_0, \downarrow_x\rangle_j$. Since these kets are degenerate, we can restore the $\mathbb{Z}_2$ gauge symmetry by considering a symmetric superposition,

$$|\Psi_{\mathrm{BO}}^{\mathrm{sym}}\rangle = \frac{1}{2^{N/2}} \sum_{\substack{s_1,\ldots,s_N \\ s_j=\pm 1}} \left|\Psi_{\mathrm{I}}\left(-s_j\frac{g}{\delta}\right)\right\rangle \bigotimes_{j=1}^{N} \left|s_j\frac{g}{\delta}\right\rangle, \tag{4.44}$$

such that we recover the solution $|\phi_{\mathrm{DF},+}\rangle$. The solution $|\phi_{\mathrm{DF},-}\rangle$ would correspond to the antisymmetric linear combination of the former states.

4.4.3 Silbey-Harris variational ansatz ($\delta \gg J$)

Now we investigate the regime of fast-boson dynamics, for which there is no longer a first-order phase transition (cf. Fig. 4.5). To this end, we consider a displaced trial wave function whose distance away from the origin in phase space is no longer fixed, rather the variational parameter [212]. This approach has been shown to yield an accurate description of the quantum phase diagram in Rabi lattice models [184, 213].

We start by considering H_{IR} after a rotation $x \leftrightarrow z$,

$$\bar{H}_{\mathrm{IR}} = \delta \sum_{j=1}^{N} a_j^\dagger a_j + g \sum_{j=1}^{N} \sigma_j^z (a_j^\dagger + a_j) - J \sum_{j=1}^{N-1} \sigma_j^x \sigma_{j+1}^x. \tag{4.45}$$

Then, we define the Silbey-Harris wave function as the one-parameter variational ansatz

$$|\Psi_{\rm SH}\rangle = e^{-S(\eta)}|0\rangle_{\rm b}\bigotimes_{j=1}^{N}|\uparrow_x\rangle_j\,, S(\eta) = \eta\frac{g}{\delta}\sum_{j=1}^{N}\sigma_j^z(a^\dagger - a), \tag{4.46}$$

where the parameter η continuously interpolates the bosonic displacement between 0 and g/δ for fixed values of these. The energy upon this state is given as

$$E_{\rm SH}(\eta) = N\frac{g^2}{\delta}(\eta^2 - 2\eta) - J(N-1)e^{-4\eta^2\left(\frac{g}{\delta}\right)^2}. \tag{4.47}$$

In contrast to $E_{\rm BO}$, the variational energy in this case does not admit a simple estimate for the emergence of the phase transition. Nevertheless, we can compute the number of phonons upon the Silbey-Harris solution, that is given as

$$n = \left(\frac{\eta_0 g}{\delta}\right)^2, \tag{4.48}$$

by minimizing $E_{\rm SH}(\eta)$ for given values of J, δ and g. We present the results of the Silbey-Harris phase diagram in Fig. 4.7. As shown, the Silbey-Harris ansatz predicts

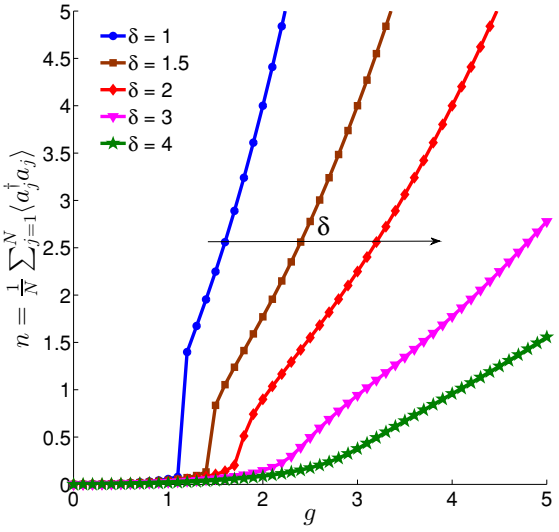

Figure 4.7: Silbey-Harris mean boson number n as a function of g, for different values of δ, and energy units such that $J = 1$, and $N = 50$ sites.

two very different behaviours in the regimes of slow- and fast-boson dynamics. When $\delta \ll J$, the number of phonons features a discontinuous jump at some critical $g = g_{\rm c}$. This jump happens between a phase with $n = 0$ and another with $n > 0$, which is consistent with the perturbative prediction of a phase transition. However, the

most important result of the Silbey-Harris ansatz is that it correctly predicts the dissapearance of the transition when $\delta \gg J$. Thus, the SB solution validates the qualitative phase diagram of Fig. 4.5.

We conclude this part by studying the convergence of $|\Psi_{\rm SH}\rangle$ to the F and DF ground states in their correspondent phases. When $\eta \to 0$, the ansatz is just

$$|\Psi_{\rm SH}\rangle = |0\rangle_{\rm b} \bigotimes_{j=1}^{N} |\uparrow_x\rangle_j \,, \tag{4.49}$$

that once we rotate into the original frame $x \leftrightarrow z$ gives one of the F states. On the other hand, when $\eta > 0$, the wave function (4.46) can be written as

$$|\Psi_{\rm SH}\rangle = \bigotimes_{j=1}^{N} \frac{1}{\sqrt{2}} \left(e^{-S(\eta)} |0\rangle_{\rm b} \, |\uparrow_z\rangle_j + e^{-S(-\eta)} |0\rangle_{\rm b} \, |\downarrow_z\rangle_j \right). \tag{4.50}$$

Undoing the rotation $x \leftrightarrow z$, this state converges to the symmetric DF state in the event of $\eta \to 1$.

4.5 DMRG phase diagram

In this section we present the quasi-exact numerical calculations of the ground state properties of the IR Hamiltonian for a chain of $N = 50$ spins, obtained by means of the DMRG algorithm [33]. We compare these results with the predictions of the Born-Oppenheimer and Silbey-Harris variational wave functions. Finally, we discuss the results relative to the critical line and correlations at the phase transition.

4.5.1 Comparison with the variational wave functions

To establish the different phases of the IR model, we rely on the mean boson number

$$n = \frac{1}{N} \sum_{j=1}^{N} \langle a_j^\dagger a_j \rangle \tag{4.51}$$

as the order parameter. We have plotted the results as a function of g for various values of δ in Fig. 4.8, along with the predictions of the variational wave functions. The solid lines represent the DMRG results. We note that there is a sudden jump in n, between a phase with $n \simeq 0$ and another with $n > 0$. The jump smears out for increasing δ. This is consistent with the perturbative and variational studies, that

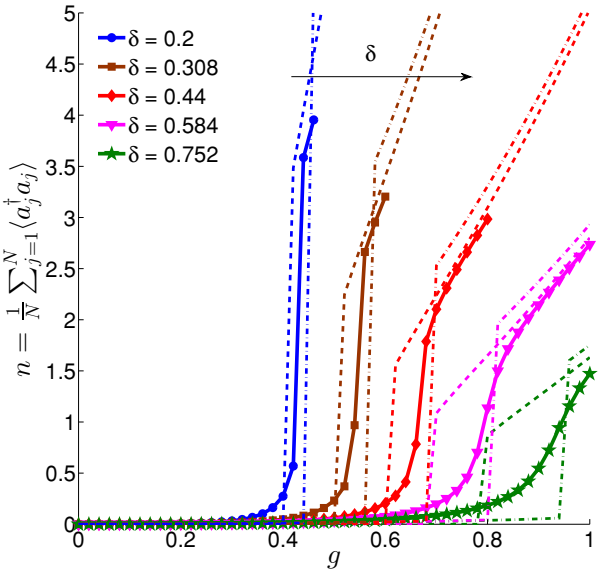

Figure 4.8: Mean boson number prediction for Born-Oppenheimer (dashed lines), Silbey-Harris-type ansatz (dashed-dotted lines) and DMRG (solid lines) of a $N = 50$ sites chain, and energy units such that $J = 1$. For the DMRG method we set a bond dimension $D = 10$, on-site boson cut-off $N_c = 10$ and local dimension $d = 2 \cdot N_c$.

predict a jump in the number of phonons in the slow-boson regime $\delta \ll J$. However, this jump should be a proper discontinuity stemming from a level crossing. Thus, we expect a divergence in the derivative of the phonon number at the critical line $g_C(\delta, J)$.

We show the derivative of the mean phonon number in Fig. 4.9. From this calculation, we infer that the jumps diverge in the limit of $\delta \to 0$, what is consistent with the infinite number of phonons predicted by the BO and SB solutions (cf. (4.43) and (4.48)). Nevertheless, the jumps are not infinite at finite δ. This is a consequence of performing the calculation for a finite system. The phase transition only occurs, strictly speaking, in the thermodynamic limit $N \to \infty$. The most rigorous way of establishing the transition is by computing the derivative for increasing N, and inferring that it is actually infinite in the thermodynamic limit. This method, known as finite-size scaling, is nevertheless very computationally intensive, and we have not carried it out. The numerical results, however, are consistent with the fact that there is a transition at some critical g, as predicted by our qualitative arguments.

We note that the solid lines in Figs. 4.8 and 4.9 are cut at some value of g. This

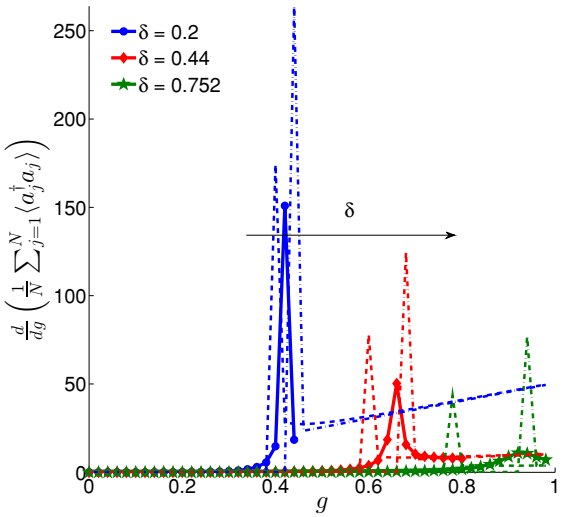

Figure 4.9: Derivatives of the average boson number for different values of δ ($N = 50$, energy units such that $J = 1$). Note that the DMRG diagonalization (solid lines) gets closer to the Born-Oppenheimer prediction (dashed lines) for decreasing δ, whereas the Silbey-Harris ansatz (dashed-dotted lines) improves for bigger values of the boson energy. The step for the derivatives in all cases is the same and stems from the precision used in the DMRG diagonalization: $\Delta g = 0.02 \cdot J$.

is a consequence of a technical detail of the DMRG algorithm. When simulating bosonic degrees of freedom, one is forced to introduce a cut-off of the number of phonons. In our calculations, we have considered that this cut-off is $N_c = 10$. This imposes some limitations in the description of the DF phase in the event of $\delta \ll g$. Because of the low energetic cost of bosonic excitations, the ground state wave function projects upon many different occupation number states. Thus, an accurate description may require higher values of N_c. Consequently, we present exclusively DMRG results fulfilling $2n \leq N_c$.

We expect a good agreement between the exact calculations and the BO ansatz in the regime of slow-boson dynamics $\delta \ll J$. In particular, we look for a closer resemblance between the BO solution and the exact diagonalization for decreasing values of δ (cf. Fig. 4.8). We see that the smaller the δ, the nearer the BO prediction for the number of bosons lies to the DMRG observable. This is also true in the case of the derivative of the number of bosons where, in contrast to the Silbey-Harris ansatz, the BO approximation quantitatively predicts the height of the derivative

when $\delta \to 0$ (Fig. 4.9).

Regarding the predictions of the Silbey-Harris wave function, Fig. 4.8 shows that it correctly describes the existence of the discontinuity. However, this solution must also give a suitable description of the phase with $\delta \gg J$, as we know that the dressed-ferromagnetic phase consists of a displaced state. We have therefore run simulations for bigger values of δ and g (cf. Fig. 4.10) and compared them with the SH ansatz, that effectively coincides with the exact solution when $\delta, g \gg J$.

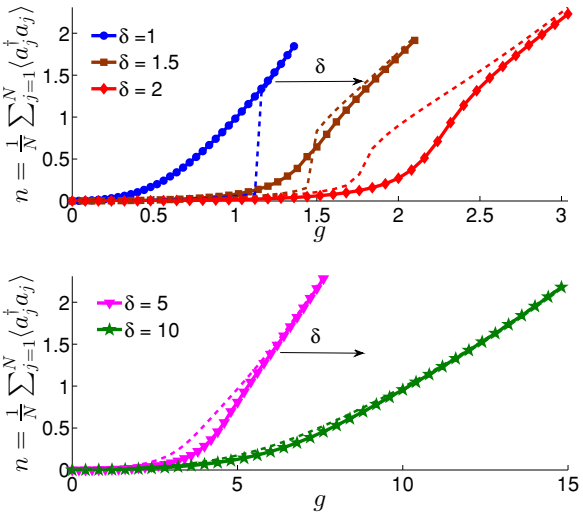

Figure 4.10: DMRG average boson number (solid lines with symbols) vs. Silbey-Harris ansatz (dashed line) for $\delta \geq J$ ($N = 50$, energy units such that $J = 1$).

4.5.2 Criticality in the Ising-Rabi lattice model

The DMRG results allow us to extract the position of the critical line $g_c(\delta, J)$. To this end, we have localized the maximum values of the derivatives of n (cf. Fig. 4.9) for different values of g and δ. The perturbative study predicted a power-law dependence for the transition line (cf. (4.39)), so we have extracted the exponent from the fit to a line in a log-log plot (cf. Fig. 4.11). The result is consistent with a power-law decay

$$g_c \sim \delta^\alpha, \text{ with } \alpha \simeq 0.66. \tag{4.52}$$

This value of the exponent departs from the one extracted from the Born-Oppenheimer ansatz, which predicts $g_c = \sqrt{\delta J}$, that is, $\alpha = 1/2$.

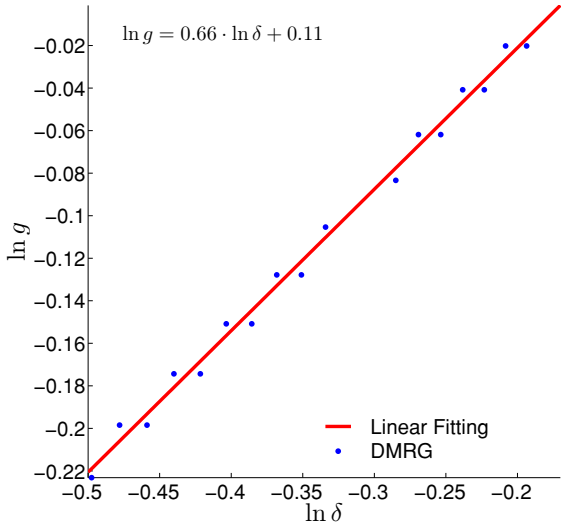

Figure 4.11: Linear fit of the critical line $g_c(\delta)$ from the DMRG results ($N = 50$, energy units such that $J = 1$). We depict the natural logarithm of δ, g.

Our numerical results should also show features of the first-order nature of the transition. To this end, we have computed the spin correlation function

$$C^{zz}_{j,l} = \langle \sigma^z_j \sigma^z_l \rangle - \langle \sigma^z_j \rangle \langle \sigma^z_l \rangle. \tag{4.53}$$

The DMRG shows that $C^{zz}_{j,l} \propto e^{-|j-l|/\chi}$ along the whole phase diagram, where χ is the correlation length. The exponential decay is observed even close to the first-order phase transition in the regime $\delta < J$ (cf. Fig. 4.12). This is consistent with our picture of the transition as a level crossing: F and DF states are both close to eigenstates of H_{IR} at the critical point, and both of them show exponentially decaying correlations.

We note that this situation is in clear contrast with what one would expect in a second-order phase transition [40]. For first-order phase transitions, the gap does not close at criticality, and there is no divergence of the correlation length. Therefore, we cannot rely on the framework of universality classes for the classification of the critical behaviour. However, the appearance of a quantum critical endpoint is shared in common with other models featuring first-order phase transitions, as the liquid-gas transition of magnetic monopoles in spin ice [30], or the sudden magnetization jump in metamagnetic samples [31].

At the critical line in our model, δ can be identified as the energy gap separating the ground state sector from the lowest energy excitations. We thus expect that

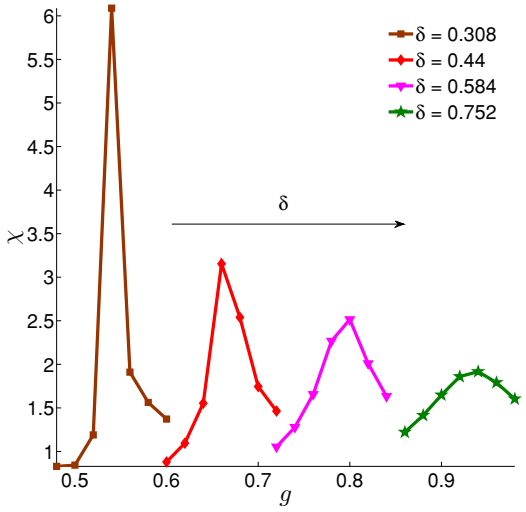

Figure 4.12: Correlation lengths χ obtained as the inverse of the slope of $-\log(C^{zz}_{25,25+l}/N)$, across the critical line as a function of g, for different values of δ ($N = 50$, energy units such that $J = 1$).

the correlation length on the critical line, χ_c, must be a decreasing function of δ. Our DMRG calculations confirm this picture (cf. Fig. 4.12), and yield the scaling $\chi_c \propto 1/\delta$ (cf. Fig. 4.13).

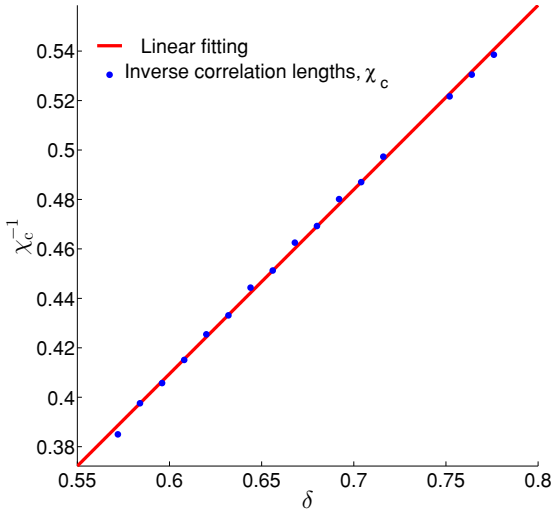

Figure 4.13: Fitting of χ_c^{-1} to a line, from the DMRG with $N = 50$, and energy units such that $J = 1$. The results are consistent with the fact that the gap scales linearly with the energy of the bosons along the critical line.

4.6 Trapped-ion experimental parameters

For the implementation of

$$H_{\rm IR} = \delta \sum_{j=1}^{N} a_j^\dagger a_j + g \sum_{j=1}^{N} \sigma_j^x (a_j^\dagger + a_j) - J \sum_{j=1}^{N-1} \sigma_j^z \sigma_{j+1}^z, \tag{4.54}$$

we consider a linear array of microtraps [134–139] along the z direction (cf. Fig. 4.3). We assume that the traps are separated by a distance $d_0 = 30\,\mu$m, each of them containing one $^9Be^+$ ion. We have that $|r_j^{(0)} - r_l^{(0)}| = d_0$. The spin-spin interaction stems from the spin-phonon coupling (4.9), which is justified only in the Lamb-Dicke regime

$$\max_n \eta_n^z = \frac{\Delta k_z}{\sqrt{2m\omega_0^z}} \ll 1. \tag{4.55}$$

We propose a common $\omega_z = 500\,(2\pi)$ kHz for all traps, which leads to

$$t_{j,j+1}^z = \frac{2e^2}{m\omega_z d_0^3} \simeq 29\,(2\pi)\,\text{kHz}, \tag{4.56}$$

and to $\omega_0^z \simeq 431\,(2\pi)$ kHz for the ground state centre-of-mass (COM) frequency of the axial modes band. Therefore, a laser wavelength $\lambda_{\rm L}^z \simeq 870$ nm would give $\max_n \eta_n^z \simeq 0.26$ for beams on axis with the trap. The magnitude of the spin-spin coupling is given as $J = g_z^2 t_{j,j+1}^z/(2(\delta_0^z)^2)$. Typical values of g_z are $100(2\pi)$ kHz [149], whereas we impose $\delta_0^z \simeq 2g_z$ to neglect residual spin-phonon couplings [118]. This renders the value $J \simeq 7(2\pi)$ kHz, which is the lowest energy scale involved in the simulation.

Regarding the residual dipolar coupling between the transverse modes, we are going to consider it as an error bound, so that every effective parameter in $H_{\rm IR}$ must be above this threshold. We quantify this error bound $\text{Err}(n)$ depending on the number n of different frequencies $\omega_{x,j}$ present in the experiment. For the sake of concreteness, let us assume $n = 3$. Assuming $\omega_{[1]}^x = 10\,(2\pi)$ MHz, $\omega_{[2]}^x = 9\,(2\pi)$ MHz, and $\omega_{[3]}^x = 8\,(2\pi)$ MHz, we have $\max_j(t_{j,j+1}^x) \simeq 0.9\,(2\pi)$ KHz. This amount scales with the distance, so $\text{Err}(n=3) = \max_j(t_{j,j+1}^x/n^3) \simeq 33\,(2\pi)$ Hz. Accordingly, we prescribe $\delta, g, J \gg \text{Err}(n=3)$ as the condition to be fulfilled to safely neglect residual couplings. Furthermore, with the former choice of parameters, the RWA condition is also fulfilled, as $\max_{j,l}(t_{j,l}^x/|\omega_j^x - \omega_l^x|) \simeq 10^{-3}, l = j+1, \cdots, n$.

For the spin-boson interaction in $H_{\rm IR}$, we consider laser beams with effective wavelength $\lambda_{\rm L}^x \simeq 320$ nm acting transversely to the axis of the trap. With the former

values for the transverse frequencies, the Lamb-Dicke parameters are $\max \eta_n^x \simeq 0.16$, so the blue and red sidebands can be resolved. Typical values for g are again of the order of $100\,(2\pi)$ KHz. The energy of the transverse phonons is set by locally detuning from ω_j^x to the common value δ for every site, and it can chosen such that $\delta \sim g$, as we have theoretically studied.

In order to probe the phase transition we propose preparing the ferromagnetic phase by cooling to the ground state of the phonons, while optical pumping to the $\bigotimes_j |{\downarrow_z}\rangle_j$ spin state, where $|{\downarrow_z}\rangle_j$ is one of the qubit states. An adiabatic protocol crossing the critical line would require evolution times of the order of the inverse of the smallest of the parameters (J), which lies around $t^{-1} \sim 23\,\mu$s.

4.7 Conclusions

The aim of this chapter was to realize a gauge theory with trapped-ion quantum matter, and to understand its phase diagram. We considered a minimal extension of the spin-boson models typically arising in quantum simulators. By promoting the transverse field of the quantum Ising model to a dynamical variable, we were able to realize the desired gauge theory: the Ising-Rabi lattice. This result is important within the quantum simulation community, since there are many different experimental platforms where the IR model could be naturally implemented. This stems from the fact that spin and boson degrees of freedom are available in cavity QED, superconducting qubits in resonators, or Rydberg atoms.

Our model served as a perfect test-bed for the variational wave functions considered. Although any mean-field theory is expected to give only a qualitative insight into the phase diagram, both Born-Oppenheimer and Silbey-Harris wave functions matched the numerical results in their respective regimes of applicability. This supports their suitability in the description of spin-boson chains, as exemplified in other works, such as [184, 213, 214].

We have got perturbative and numerical evidences of the fact that the IR lattice model undergoes a first-order transition. Also, we have shown that the there is a point that separates the first-order phase transition from a continuous crossover region. The perturbative arguments allowed us to estimate that this point happens

around $\delta \sim J$. However, this result was based on a first-order expansion. Higher-order terms in perturbation theory may feature significant deviations. Thus, it would be interesting to analyse higher orders, to check the consistency with the current results and the DMRG predictions. Regarding the numerical calculation, establishing the discontinuity at the transition would require a finite-size scaling of the derivative of the phonon number, that is divergent at the critical line. Only by extrapolating to the thermodynamic limit we can claim that there is indeed a first-order phase transition. Also, we have not discussed the location of the critical end-point from the DMRG. A possible way to accurately characterize its position, and its associated phenomenology, that may be related with a second-order phase transition, is to perform DMRG calculations focused in that particular regime. The emergence of a second-order phase transition is supported by the fact that $\delta \sim J$ at the critical point, and this competition between spin and phonon degrees of freedom may cause the closing of the gap.

We have not explored other aspects associated with first-order phase transitions, such as metastability or hysteresis [215]. If we drive the system through the discontinuous transition, for example from the F to the DF phase, it is natural to expect that we remain on the F state, because of the level crossing. The F state is then a metastable state in the DF phase. If we provide a relaxation mechanism, such as a coupling to a reservoir, this state should decay into the DF state. This decay time is an internal time scale, that can compete with an external time scale stemming from a time-modulated driving, leading to the phenomenon of hysteresis. Because of the possibility of driving the phonons, that act as an external field for the spins in the IR model, the former considerations can be naturally explored in an eventual implementation of this system. Furthermore, metastable states could be considered for quantum metrological purposes, since they can decay into the actual ground state for very small perturbations. This has been actually explored for second-order phase transitions in spin-boson systems [210].

In conclusion, the IR lattice is an example of the potential of spin-boson models arising in quantum simulators to give rise to complex and rich physics. So far, these models have been used mainly for the simulation of quantum magnetism, and experiments have disregarded the phonons. Proposals such as the IR lattice can

motivate further efforts for the realization of more ambitious implementations.

Chapter 5

Emergence of topological edge states in the Su-Schrieffer-Heeger model

5.1 Introduction

This chapter is devoted to a new kind of phases of quantum matter, known as topological insulators [21–23]. Topological insulators are gapped phases of non-interacting fermions. They are insulating in the bulk, but feature conducting zero-energy modes at the edges whenever the system is spatially cut into two. It is this dependence on the boundary conditions that makes topological insulators 'topological'. The different phases of a topological insulator cannot be described by a local order parameter [216], and only a special quantity –called bulk or topological invariant– is able to distinguish between them.

Topological phase transitions are associated with highly non-local order parameters. Although some of them have been measured [217], it is unclear how to define a Landau-like theory for these transitions [23]. On the other hand, edge states can be observed, but only a particular value of the bulk invariant, along with the symmetries of the Hamiltonian, can prove their topological origin [218]. Since computing the bulk invariant for real materials is generally difficult, topological phase transitions are not easy to establish. Nevertheless, it has been proved that topological order should arise in some systems, like graphene [219] or quantum wells [220], and

actual topological insulators have been experimentally confirmed [221].

The difficulty of realizing and probing topological order has spurred the interest on simulating topological insulators with synthetic degrees of freedom. For instance, there have been proposals for the preparation and characterization of topological states of matter with ultracold atomic gases in optical lattices [106, 222–226], or trapped ions [227–229]. These latter systems are specially suited for the study of the interplay between interactions and topological order, since the range of the interactions can be precisely tuned [114]. This is of great practical interest, as real systems are usually strongly interacting. A proof-of-principle experiment to realize a proposal to implement the S=1 Haldane chain [227] has been successfully realized with 3 atomic ions [228], and subsequent works have explored the consequences of long-range interactions in this system [229]. Nevertheless, it is not necessary to rely on simulating higher-dimensional spins to give rise to topological order. The Su-Schrieffer-Heeger (SSH) model [230–232]

$$H_{\mathrm{SSH}} = J\sum_{j=1}^{N-1}(1+\delta(-1)^j)(\sigma_j^+\sigma_{j+1}^- + \mathrm{H.c.}), \tag{5.1}$$

is a well-known example of a topological insulator comprised of S=1/2 spin degrees of freedom. One goal of this chapter is to show that this Hamiltonian can be implemented with trapped-ion quantum simulators, in the regime of adiabatic elimination of the phonons [119, 190].

It may seem puzzling that a spin model such as (5.1) is deemed a topological insulator, since these systems are comprised of fermions and not spins. This differentiation is actually irrelevant. Both degrees of freedom can be unequivocally identified by means of the Jordan-Wigner transformation [43],

$$\begin{aligned}
\sigma_1^- &= c_1, \quad \sigma_i^- = \prod_{j=1}^{i-1}(1-2c_j^\dagger c_j)c_i, \quad (i=2,\ldots,N),\\
\sigma_1^+ &= c_1^\dagger, \quad \sigma_i^+ = c_i^\dagger\prod_{j=1}^{i-1}(1-2c_j^\dagger c_j), \quad (i=2,\ldots,N),
\end{aligned} \tag{5.2}$$

and (5.1) can be equally represented as

$$H_{\mathrm{SSH}} = J\sum_{j=1}^{N-1}(1+\delta(-1)^j)(c_j^\dagger c_{j+1} - c_j c_{j+1}^\dagger). \tag{5.3}$$

The properties of the SSH model are easier to introduce in terms of fermions, so we will stick to this representation in the beginning.

We start now by illustrating the phases of the SSH model, its edge states and symmetries, and its associated bulk invariant. Then, we show how to implement the model with trapped ions. We consider a periodic driving, which dresses the effective spin-spin interactions to give rise to the two-fold periodicity of the couplings associated with the SSH model. The next-to-nearest neighbour terms induce interactions upon the original H_{SSH}, that we discuss in detail. We deal as well with the non-interacting limit of the generalized SSH model, and perform a continuum description to predict the localization length of the edge states. We discuss the parameter values needed to ensure the existence of edge states, and suggest an experimental protocol to probe them. Finally, we study the effect of the interactions upon the many-body ground state within the Hartree-Fock approximation, and conclude presenting the experimental parameters for an eventual implementation and some conclusions.

5.2 The Su-Schrieffer-Heeger model

In this section we are going to illustrate the concepts of edge states and bulk invariant in the particular example of the SSH model. This will pave the way for the study of the implementation with trapped ions.

5.2.1 Edge states

The SSH model

$$H_{\mathrm{SSH}} = J\sum_{j=1}^{N-1}(1+\delta(-1)^j)(c_j^\dagger c_{j+1} - c_j c_{j+1}^\dagger), \tag{5.4}$$

describes electrons hopping along a chain comprised of two different species, A and B, which comprise a unit called dimer (cf. Fig. 5.1). The hopping strengths $A-B$ and $B-A$ are different, and their ratio is measured by the *dimerization* δ.

This model hosts a topological phase, since its spectrum depends on the boundary conditions [233]. Under PBC, the spectrum is gapped for any value of $\delta \neq 0$ (cf. Fig. 5.2). On the other hand, when the chain is open, and the dimerization is positive, there are two modes in the mid-gap (cf. Fig. 5.3), but they disappear when

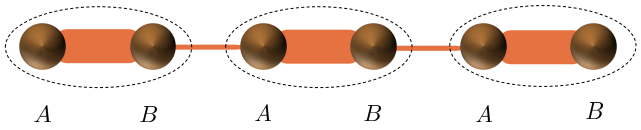

Figure 5.1: Example of a dimerized chain. The units $A - B$ are known as dimers. The thickness of the bonds represents the different strengths of the hoppings in the SSH Hamiltonian between $A - B$ and $B - A$, for $\delta < 0$.

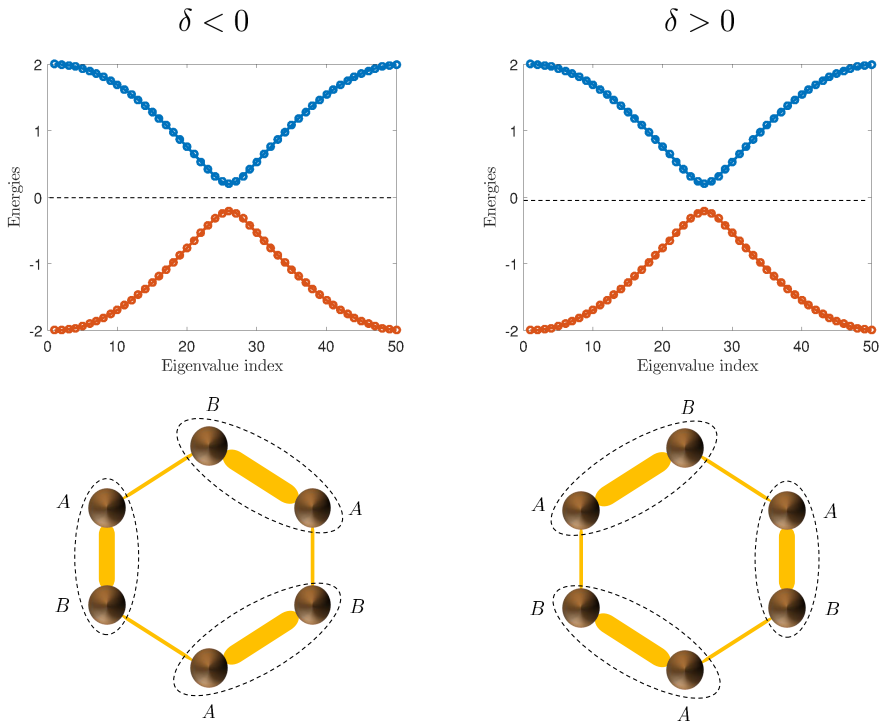

Figure 5.2: Phases of the SSH model under PBC. $N = 100$, $J = 1, \delta = \pm 0.1$. The lower schemes show the corresponding arrangement of bonds for δ negative or positive respectively, and $N = 6$.

$\delta < 0$. Thus, changing the sign of the dimerization gives rise to two different phases, with and without mid-gap states. The phase with zero-energy modes is considered topologically non-trivial, because only in this situation the associated topological invariant will take a value different from zero.

If we depict the wave function of any of the states lying in the mid-gap, we find that they are exponentially localized at the edges (cf. Fig. 5.4). We can approximately write the wave function of any of these *edge states* near the left end of the chain as $M_{j,n} \sim e^{(N-j+1)/\xi_{\text{loc}}}$. The typical length associated with the

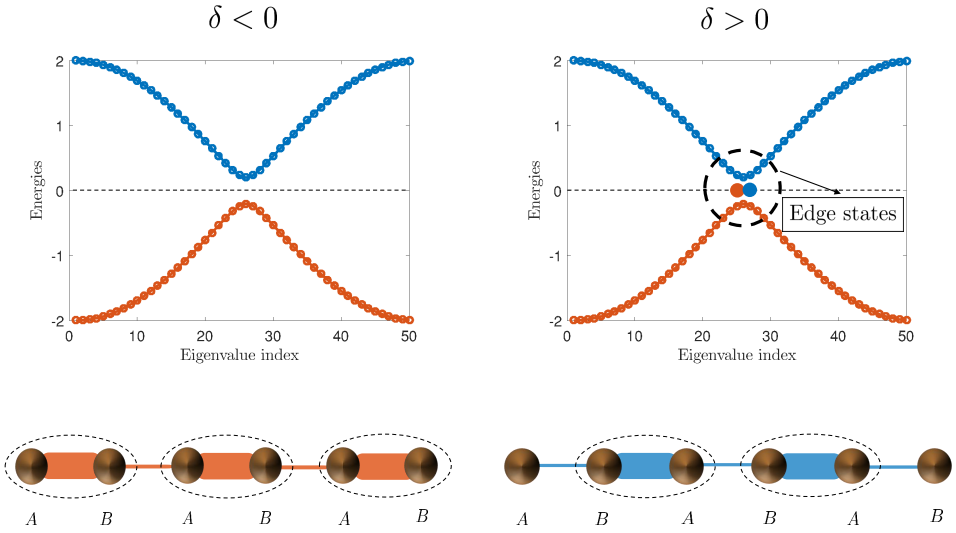

Figure 5.3: Phases of the SSH model under OBC. The two modes in the mid-gap correspond to the edge states. $N = 100$, $J = 1, \delta = \pm 0.1$.

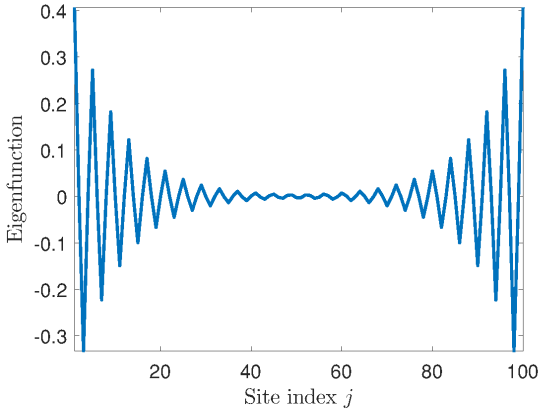

Figure 5.4: One of the zero-energy eigenstates of the Hamiltonian (5.5). The wave function (blue line) is localized at the edges, and it features an exponential decay into the bulk. $N = 100$, $J = 1, \delta = 0.1$.

exponential decay is known as the localization length of the edge states.

We can estimate the localization length as a function of the dimerization with a simple procedure [233]. We start by writing (5.3) as

$$H_{\text{SSH}} = \sum_{j,l=1}^{N} h_{j,l} \hat{c}_j^\dagger \hat{c}_l, \text{ where } h_{j,l} = J(1 + \delta(-1)^j)\delta_{j+1,l}. \tag{5.5}$$

Then, we look for particular eigenfunctions M_{j,n_0} such that they have zero energy,

e.g., $\sum_{l=1}^{N} h_{j,l} M_{l,n_0} = 0, \forall j$. This leads to the set of equations

$$\begin{cases} (1-\delta)M_{2m-1,n_0} + (1+\delta)M_{2m+1,n_0} = 0, \\ (1+\delta)M_{2m,n_0} + (1-\delta)M_{2m+2,n_0} = 0, \end{cases} \tag{5.6}$$

for $m = 1, \ldots, N/2-1$, with boundary conditions $M_{2,n_0} = 0$ and $M_{N-1,n_0} = 0$. These equations can be solved iteratively, so that

$$\begin{cases} M_{2m+1,n_0} = (-1)^m e^{-2m/\xi_{\mathrm{loc}}} M_{1,n_0}, \\ M_{N-2m,n_0} = (-1)^m e^{-2m/\xi_{\mathrm{loc}}} M_{N,n_0}, \end{cases} \tag{5.7}$$

where we have introduced the localization length ξ_{loc}, that is consistently defined as

$$\xi_{\mathrm{loc}} = -2/\ln\frac{1-\delta}{1+\delta}, \quad 0 < \delta < 1. \tag{5.8}$$

Since M_{1,n_0} and M_{N,n_0} are two independent initial conditions, we have two possible solutions with zero energy, that are exponentially localized at the ends of the chain.

The existence of a topological insulator is not necessarily connected with the emergence of edge states. A non-trivial topological phase is only defined through a non-zero value of the bulk invariant. Nevertheless, if this argument is supplemented with a particular symmetry of the Hamiltonian, then there is a direct correspondence between the occurrence of edge states and the topological phase [218]. In the case of the SSH model, this symmetry is the chiral symmetry, that we introduce now. It will prove central in locating the boundary modes in more complex situations.

5.2.2 Chiral symmetry

Chiral symmetry is associated with an operator Γ, whose action upon the Hamiltonian is to change the sign of the fermionic operators defined on sites A (it can be defined for sites B as well). It is straightforward to check that

$$\Gamma H_{\mathrm{SSH}} \Gamma = -H_{\mathrm{SSH}}. \tag{5.9}$$

This symmetry has a very important consequence for *any* Hamiltonian that admits a *pseudo-spin representation*. Let us illustrate this concept for the SSH model. To write H_{SSH} in its pseudo-spin representation, we introduce operators a_n and b_n associated with sites A and B, respectively, so that

$$H_{\mathrm{SSH}} = J(1-\delta)\sum_{n=1}^{M}(a_n^\dagger b_n + \mathrm{H.c.}) + J(1+\delta)\sum_{n=1}^{M-1}(b_n^\dagger a_{n+1} + \mathrm{H.c.}), \quad M = \frac{N}{2}. \tag{5.10}$$

In the plane wave basis $a_n = \frac{1}{\sqrt{M}} \sum_{\mu=-M/2}^{M/2} e^{i\frac{2\pi n}{M}\mu} a_\mu$, and recasting the former operators into a spinor, the pseudo-spin representation of the SSH model is given as

$$H_{\text{SSH}} = J(1-\delta) \sum_{\mu=-M/2}^{M/2} \left(a_\mu^\dagger, b_\mu^\dagger\right) h_\mu \begin{pmatrix} a_\mu \\ b_\mu \end{pmatrix}, \tag{5.11}$$

with

$$h_\mu = \begin{pmatrix} 0 & 1 + \dfrac{1+\delta}{1-\delta} e^{i\frac{2\pi\mu}{M}} \\ 1 + \dfrac{1+\delta}{1-\delta} e^{-i\frac{2\pi\mu}{M}} & 0 \end{pmatrix}. \tag{5.12}$$

One can always parametrize h_μ with a vector $\mathbf{d}(\mu)$, through the identification,

$$h_\mu = d_0(\mu)\mathbb{I} + \mathbf{d}(\mu) \cdot \boldsymbol{\sigma}, \tag{5.13}$$

where $\boldsymbol{\sigma} = (\sigma^x, \sigma^y, \sigma^z)$, and $\mathbb{I}$ is the 2×2 identity matrix. The vector describes a loop around $d_0(\mu)$, and as long as $\mathbf{d}(\mu) \neq 0$, h_μ represents a gapped Hamiltonian.

Let us denote by γ the pseudo-spin representation of the chiral symmetry operator Γ. It must fulfil that $\gamma \mathbf{d}(\mu) \cdot \boldsymbol{\sigma} \gamma = -\mathbf{d}(\mu) \cdot \boldsymbol{\sigma}$. Some trial and error shows that actually $\gamma = \sigma^z$. Since this must hold for any chiral-symmetric pseudo-spin Hamiltonian

$$h_\mu \propto \begin{pmatrix} d_z(\mu) & d_x(\mu) - i d_y(\mu) \\ d_x(\mu) + i d_y(\mu) & -d_z(\mu) \end{pmatrix}, \tag{5.14}$$

we have that

$$\gamma h_\mu \gamma = -h_\mu \implies d_z(\mu) \equiv 0. \tag{5.15}$$

Thus, we conclude that chiral symmetry implies that the loop parametrizing the Hamiltonian lies in the XY-plane.

We finish now the introduction to the SSH model by finally presenting its bulk invariant.

5.2.3 Topological invariant: the Zak phase

The topological invariant associated with the SSH is the Zak phase [234]. It is defined as the Berry phase [235] acquired by the wave function of the ground state in an excursion along the first Brillouin zone [236],

$$\nu = i \oint \langle \text{G.S.}(k) | \partial_k | \text{G.S.}(k) \rangle dk. \tag{5.16}$$

Assuming that the Hamiltonian admits a pseudo-spin representation, the ket $|\text{G.S.}(k)\rangle$ is the eigenvector of $h_\mu \overset{N\to\infty}{\to} h(k)$ corresponding to the lowest energy state. Although this quantity can be exactly computed for the SSH model [233], usually is not easy to obtain analytically. Therefore, we are going to describe how to compute it numerically using the SSH model as illustration, and show that it indeed takes different values depending on the sign of the dimerization.

We note that (5.16) assumes continuous values of k, but any numerical integration must proceed by discretizing the domain. Following reference [237], we introduce the discrete version[1] of the Zak phase,

$$\nu \simeq -\operatorname{Im}\ln\prod_{s=0}^{M-1}\langle\text{G.S.}(k_{s+1})|\text{G.S.}(k_s)\rangle. \tag{5.18}$$

In this expression, we have partitioned the momentum k into $N+1$ different values, so that

$$k_s = -\frac{M}{2} + \left(\frac{s}{M}\right)\cdot M, \quad s = 0,\ldots,M. \tag{5.19}$$

The kets $|\text{G.S.}(k_s)\rangle$ stem from a numerical diagonalization of h_μ for every k_s. Since they are comprised of complex values, there is an overall phase freedom in their definition. The particular form of ν that we just introduced is defined in a way that removes these arbitrary phase factors [237]. Now we are in position to see if ν actually is able to distinguish the two phases of the SSH model. We have depicted its value in Fig. 5.5. We see that as long as $\delta < 0$, the Zak phase is zero, whereas for positive dimerization its value can be $\pm\pi$. Actually, 0 and $\pm\pi$ are the only possible values of the Zak phase for inversion symmetric systems [234]. We will refer to the non-zero value of ν as the non-trivial Zak phase, which is associated with the non-trivial topological insulator featuring edge states. This procedure can be applied to any Hamiltonian, and we will use it for the generalized SSH model arising with trapped-ion quantum matter.

Now that we have introduced the main concepts of the edge states and the bulk invariant in the context of the SSH model, we are ready to study their realization

[1] To convince oneself that (5.18) is actually equal to (5.16), we note that one can write $\langle\text{G.S.}(k+\Delta k)|\text{G.S.}(k)\rangle$ as

$$1 - \langle\text{G.S.}(k+\Delta k)|\left(|\text{G.S.}(k+\Delta k)\rangle - |\text{G.S.}(k)\rangle\right) \simeq e^{-\langle\text{G.S.}(k)|\partial_k|\text{G.S.}(k)\rangle\Delta k}. \tag{5.17}$$

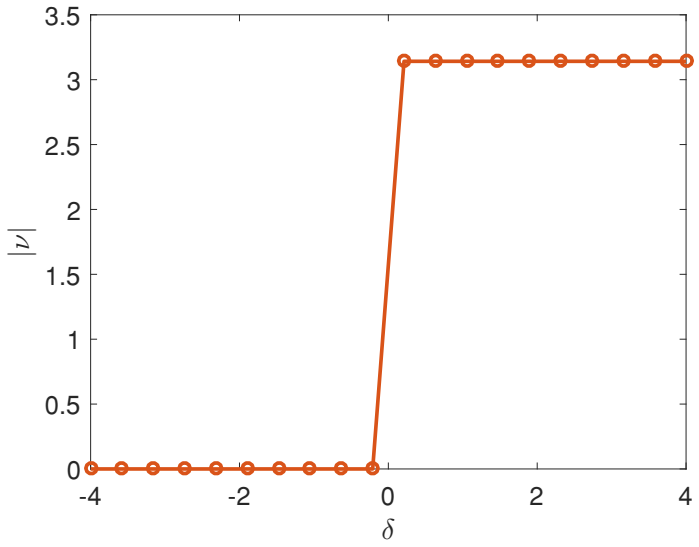

Figure 5.5: Zak phase of the ground state of the SSH model. The dimerization δ tunes the topological phase transition between the topologically trivial regime ($\delta < 0$), and the topological regime ($\delta > 0$), associated with a non-zero value of the Zak phase.

in a trapped-ion experiment. This will be the aim of the following section.

5.3 Implementation with trapped ions

In this section we show how to implement the SSH model

$$H_{\text{SSH}} = J \sum_{j=1}^{N-1} (1 + \delta(-1)^j)(\sigma_j^+ \sigma_{j+1}^- + \text{H.c.}) \tag{5.20}$$

in a quantum simulator with trapped ions. To begin with, we need to realize the terms $\sigma_j^+ \sigma_{j+1}^-$ and $\sigma_j^- \sigma_{j+1}^+$, whereas terms such as $\sigma_j^+ \sigma_{j+1}^+$ and $\sigma_j^- \sigma_{j+1}^-$ should not occur. This can be accomplished via a periodic driving of the Ising chain [238], to make the latter terms fast-rotating. On the other hand, the alternating tunnellings of the SSH model are not straightforward to realize, specially if we are restricted to global operations on the ions. We suggest the dressing by optical phases analogous to that of the generalized cJT model in chapter 3, which provides the desired site-dependent couplings.

We know already that in the regime of adiabatic elimination of phonons, trapped-ion quantum matter is described by an effective Ising Hamiltonian as the one derived

in chapter 3. Likewise, we assume that the spin-spin interactions are mediated by the transverse modes. We take the Ising limit of the cJT Hamiltonian (cf. (3.12)) as our starting point, but we rotate the reference frame so that $\sigma_j^x \to \sigma_j^z$ and $\sigma_j^z \to \sigma_j^x$, and therefore

$$H_{\text{Ising}} = \sum_{j,l=1}^{N} J_{j,l}^{(\text{ions})} \sigma_j^x \sigma_l^x + \frac{\Omega}{2} \sum_{j=1}^{N} \sigma_j^z. \tag{5.21}$$

We recall that the effective spin-spin interaction is given by

$$J_{j,l}^{(\text{ions})} = -(-1)^{j-l} J_{\text{exp}} e^{-|j-l|/\xi_{\text{int}}} + \frac{J_{\text{dip}}}{|j-l|^3}, N \gg 1. \tag{5.22}$$

These *ion couplings* –we will use this nomenclature in this part of the thesis, to distinguish them from the Bessel couplings that we discuss below– have two different regimes depending on the detuning: for $\delta_{N/2} \ll t_{\text{C}}$ they decay exponentially, and their typical length can be made large, whereas for large $\delta_{N/2}$ they decay like $1/|j-l|^3$.

The first difference between H_{Ising} and the SSH model (5.1) is that the first is not invariant under arbitrary rotations around the z-axis. Also, $J_{j,l}^{(\text{ions})}$ do not have a spatially repeating structure. To remedy these limitations, we introduce the periodic laser driving

$$H_{\text{driving}} = \frac{\eta \omega_{\text{d}}}{2} \cos(\omega_{\text{d}} t) \sum_{j=1}^{N} \cos(\phi_j) \sigma_j^z, \tag{5.23}$$

with frequency ω_{d}, (dimensionless) coupling strength η, and a site dependent phase ϕ_j (see Fig. 5.6). To analyse the effect of the driving, let us move into a frame

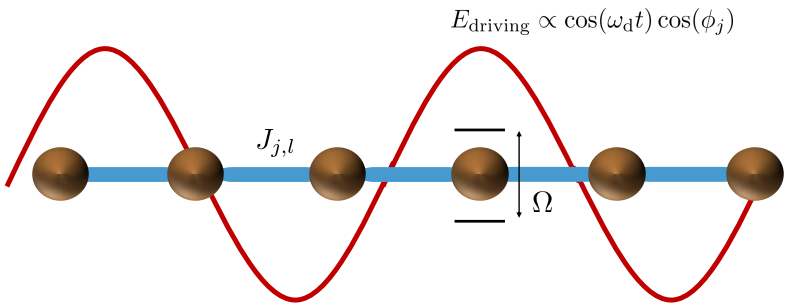

Figure 5.6: Two-level systems, separated by an energy Ω, and coupled through a $\sigma_j^x \sigma_l^x$ interaction of magnitude $J_{j,l}^{(\text{ions})}$. The interaction is induced by a standing wave E_{driving}, periodically modulated at frequency ω_{d}.

rotating with both H_{driving} and the spin frequency Ω. Then, $H_{\text{Ising}} + H_{\text{driving}} \equiv$

$H_{\text{total}} \to \bar{H}_{\text{total}}$, with

$$\bar{H}_{\text{total}} = U(t)H_{\text{total}}U^{\dagger}(t) - iU(t)\frac{d}{dt}U^{\dagger}(t), \tag{5.24}$$

where $U(t) = \exp\left[i\sum_{j=1}^{N}\Delta_j(t)\sigma_j^z\right]$, and

$$\Delta_j(t) = \frac{\Omega}{2}t + \frac{\eta\omega_{\text{d}}}{2}\cos(\phi_j)\int_0^t \cos(\omega_{\text{d}}t')dt'. \tag{5.25}$$

This transformation leads to

$$\begin{aligned}\bar{H}_{\text{total}} = \sum_{j,l=1}^{N} & J_{j,l}^{(\text{ions})}\left(e^{2i(\Delta_j(t)+\Delta_l(t))}\sigma_j^+\sigma_l^+ + e^{-2i(\Delta_j(t)+\Delta_l(t))}\sigma_j^-\sigma_l^-\right) \\ & + J_{j,l}^{(\text{ions})}\left(e^{2i(\Delta_j(t)-\Delta_l(t))}\sigma_j^+\sigma_l^- + e^{-2i(\Delta_j(t)-\Delta_l(t))}\sigma_j^-\sigma_l^+\right).\end{aligned} \tag{5.26}$$

The terms of the form $\sigma_j^+\sigma_l^+$ ($\sigma_j^-\sigma_l^-$) rotate with a constant offset Ω ($-\Omega$), which is cancelled in the prefactors of $\sigma_j^+\sigma_l^-$ and $\sigma_j^-\sigma_l^+$. Now, let us assume that $\max_{j,l}|J_{j,l}^{(\text{ions})}| \ll \omega_{\text{d}} \ll \Omega$. Applying the rotating wave approximation, only the processes in the second line of (5.26) are non-negligible, and they rotate with the phase

$$e^{\pm i\eta(\cos\phi_j - \cos\phi_l)\sin\omega_{\text{d}}t} = e^{\mp 2i\eta\sin(\frac{\phi_j+\phi_l}{2})\sin(\frac{\phi_j-\phi_l}{2})\sin\omega_{\text{d}}t}. \tag{5.27}$$

We rely on the Jacobi-Anger expansion to express this phase as a Fourier series in terms of the Bessel functions $\mathcal{J}_n$ (see, e.g., [47]), i.e.,

$$e^{iz\sin\theta} = \sum_{n=-\infty}^{\infty}\mathcal{J}_n(z)e^{in\theta}. \tag{5.28}$$

This allows us to write the prefactors of the surviving terms in (5.26) as

$$J_{j,l}^{(\text{ions})}\sum_{n=-\infty}^{\infty}\mathcal{J}_n\left(\mp 2\eta\sin(\frac{\Delta k}{2}(r_j^{(0)}+r_l^{(0)})+\phi)\sin\frac{\Delta k}{2}(r_j^{(0)}-r_l^{(0)})\right)e^{itn\omega_{\text{d}}}, \tag{5.29}$$

where we set $\phi_j = \Delta k\cdot r_j^{(0)} + \phi$, with Δk the total momentum of the driving, $r_j^{(0)}$ the equilibrium position of the ions, and ϕ a homogeneous phase. We suppose that the $r_j^{(0)}$ are equally spaced by a distance d_0, and we use units such that $d_0 = 1$, so $r_j^{(0)} = j$. Since $\omega_{\text{d}} \gg \max_{j,l}|J_{j,l}^{(\text{ions})}|$, any term with $n \neq 0$ gives a negligible contribution to the dynamics, compared with the constant component stemming from $n = 0$. Consequently, we ignore all the time-dependent terms, and we arrive at the effective description of the dynamics dictated by

$$H_{\text{eff}}^{\Delta k}(\eta,\phi) = \sum_{j,l=1}^{N}J_{j,l}^{(\text{ions})}\mathcal{J}_{j,l}^{\Delta k}(\eta,\phi)\left(\sigma_j^+\sigma_l^- + \sigma_j^-\sigma_l^+\right), \tag{5.30}$$

with

$$\mathcal{J}_{j,l}^{\Delta k}(\eta,\phi) \equiv \mathcal{J}_0(2\eta \sin(\frac{\Delta k}{2}(j+l)+\phi)\sin\frac{\Delta k}{2}(j-l)). \tag{5.31}$$

The signs of the argument of the Bessel functions in (5.29) have disappeared in this last expression, because the zeroth order Bessel function is even under parity.

To understand the structure encoded in $\mathcal{J}_{j,l}^{\Delta k}(\eta,\phi)$, we consider, only for illustration purposes, the idealized limit of first-neighbours couplings $J_{j,l}^{(\text{ions})} \to J\delta_{j+1,l}$, so that

$$H_{\text{eff}}^{\Delta k}(\eta,\phi) \to \sum_{j=1}^{N-1} J\mathcal{J}_{j,j+1}^{\Delta k}(\eta,\phi)\left(\sigma_j^+\sigma_{j+1}^- + \sigma_j^-\sigma_{j+1}^+\right). \tag{5.32}$$

The terms $\mathcal{J}_{j,j+1}^{\Delta k}(\eta,\phi)$ are periodic in the site index j, with period $T=\pi/\Delta k$. The parameters η,ϕ set their magnitude, as illustrated for some generic values in Fig. 5.7(a). The periodicity gives rise to repeating units, or clusters, of strongly coupled spins, which in turn interact weakly with those of neighbouring groups. The size of these clusters is given by T. This is depicted in Fig. 5.7(b), where the chain is comprised of clusters of strongly coupled spins $AB, ABC, \cdots$, and the thickness of the bonds represents the coupling strengths. Setting $\Delta k=\pi/2$, the Bessel couplings are able to reproduce the alternating behaviour of the tunnellings in the SSH model. Thus, we finally obtain Hamiltonian (5.1), e.g.,

$$H_{\text{SSH}} = J\sum_{j=1}^{N}\mathcal{J}_{j,j+1}^{\pi/2}(\sigma_j^+\sigma_{j+1}^- + \text{H.c.}), \tag{5.33}$$

where $\mathcal{J}_{j,j+1}^{\pi/2}$ can take one of the possible values

$$\begin{cases} \mathcal{J}^{\text{odd}} \equiv \mathcal{J}_{j,j+1}^{\pi/2}\Big|_{j\ \text{odd}} = \mathcal{J}_0\left[2\eta\sin\left(\frac{\pi}{4}\right)\cos\left(\frac{\pi}{4}+\phi\right)\right], \\ \mathcal{J}^{\text{even}} \equiv \mathcal{J}_{j,j+1}^{\pi/2}\Big|_{j\ \text{even}} = \mathcal{J}_0\left[2\eta\sin\left(\frac{\pi}{4}\right)\sin\left(\frac{\pi}{4}+\phi\right)\right]. \end{cases} \tag{5.34}$$

By analogy with (5.1), we see that

$$\frac{1-\delta}{1+\delta} = \frac{\mathcal{J}^{\text{odd}}}{\mathcal{J}^{\text{even}}}, \tag{5.35}$$

so that the dimerization is given by the ratio

$$\delta = \frac{\mathcal{J}^{\text{even}} - \mathcal{J}^{\text{odd}}}{\mathcal{J}^{\text{even}} + \mathcal{J}^{\text{odd}}}. \tag{5.36}$$

The former first-neighbours limit is an approximation to the realistic ion couplings $J_{j,l}^{(\text{ions})}$. Only in that case the spin and fermion representations of H_{SSH} are

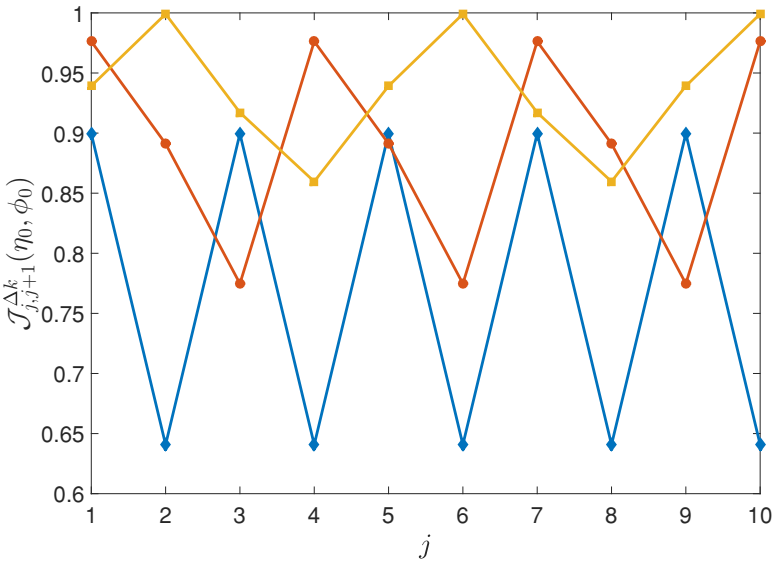

(a)

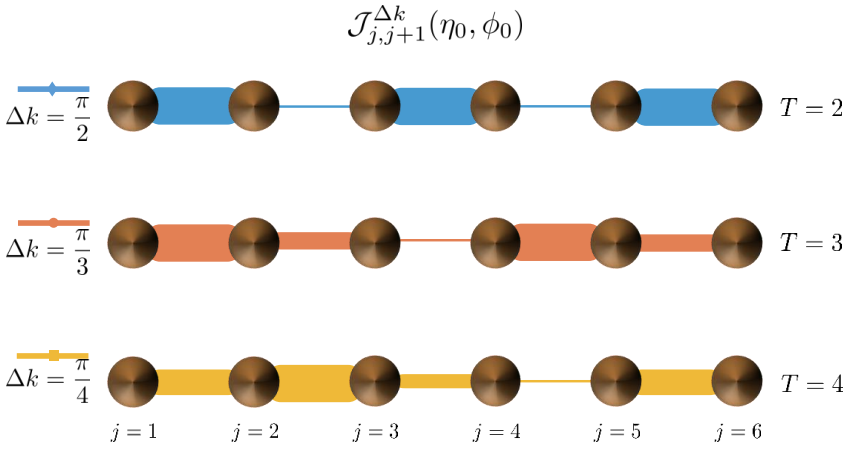

(b)

Figure 5.7: (a) Magnitude of $\mathcal{J}^{\Delta k}_{j,j+1}(\eta_0,\phi_0)$, in units of J, for $\eta_0 = 1, \phi_0 = 2\pi/5$, and $\Delta k = \pi/2, \pi/3$ and $\pi/4$. (b) Corresponding bond strengths for different periods.

alike, and consist of simple spin-spin or fermion-fermion couplings

$$H_{\text{SSH}} = J\sum_{j=1}^{N} \mathcal{J}^{\pi/2}_{j,j+1}(\sigma^+_j\sigma^-_{j+1} + \text{H.c.}) = J\sum_{j=1}^{N} \mathcal{J}^{\pi/2}_{j,j+1}(c^\dagger_j c^-_{j+1} + \text{H.c.}). \tag{5.37}$$

However, the former resemblance is an artefact of this limit. If we take into account the arbitrary range of the ion couplings, the fermion representation of the spin

Hamiltonian becomes a complex interacting problem. This is a consequence of the string operator associated with the Jordan-Wigner transformation. Although the resulting fermion problem is no longer the SSH model, changing the range of the couplings allows us to switch on the interactions, and assess their effect on the topological properties of $H_{\rm SSH}$.

Let us consider the SSH model with the ion couplings

$$H_{\rm SSH}^{\rm (ions)} = \sum_{j,l=1}^{N} J_{j,l}^{\rm (ions)} \mathcal{J}_{j,l}^{\pi/2}(\eta,\phi)\left(\sigma_j^+\sigma_l^- + \sigma_j^-\sigma_l^+\right), \tag{5.38}$$

where

$$\mathcal{J}_{j,l}^{\pi/2}(\eta,\phi) = \mathcal{J}_0(2\eta\sin(\frac{\pi}{4}(j+l)+\phi)\sin\frac{\pi}{4}(j-l)). \tag{5.39}$$

Now, we perform the Jordan-Wigner transformation (5.2) upon $H_{\rm SSH}^{\rm (ions)}$, that leads to

$$H_{\rm SSH}^{\rm (ions)} = \sum_{l>j}^{N} 2J_{j,l}^{\rm (ions)} \mathcal{J}_{j,l}^{\pi/2}\left(c_j^\dagger K_{j,l} c_l + c_j K_{j,l} c_l^\dagger\right), \tag{5.40}$$

where we have introduced the notation

$$K_{j,l} \equiv \prod_{m=j}^{l-1}(1-2c_m^\dagger c_m). \tag{5.41}$$

We note from (5.40) that the longer the range of the interactions, the more terms of the string operator $K_{j,l}$ appear in the Hamiltonian. These terms involve four, six, etc. fermionic operators. They play the role of interactions among the one-body eigenstates associated with the *non-interacting Hamiltonian*

$$\bar{H}_{\rm SSH}^{\rm (ions)} = \sum_{l>j}^{N} 2J_{j,l}^{\rm (ions)} \mathcal{J}_{j,l}^{\pi/2}\left(c_j^\dagger c_l - c_j c_l^\dagger\right) = \sum_{j\neq l}^{N} J_{j,l}^{\rm (ions)} \mathcal{J}_{j,l}^{\pi/2}\left(c_j^\dagger c_l - c_j c_l^\dagger\right), \tag{5.42}$$

which consists of terms involving only two fermionic operators. The minus sign comes from the contribution of the string operator.

Our strategy to study $H_{\rm SSH}^{\rm (ions)}$ is going to be the following: we think of this problem as primarily associated with $\bar{H}_{\rm SSH}^{\rm (ions)}$, whereas interactions among fermions stemming from the Jordan-Wigner transformation introduce deviations from the non-interacting limit. We ignore a priori if this approach is correct, since the magnitudes of the interactions can be as large as those appearing in $\bar{H}_{\rm SSH}^{\rm (ions)}$, so we will have to justify it a posteriori. Accordingly, we first need to characterize the topological features of the non-interacting limit, and then assess the role of the remaining

terms in $H_{\mathrm{SSH}}^{(\mathrm{ions})}$ upon these physics. This is going to be the aim of the following sections.

5.4 Localization length of the edge states in the non-interacting limit

In this section we are going to establish the properties of the edge states of $\bar{H}_{\mathrm{SSH}}^{(\mathrm{ions})}$. To this end, we perform a continuum description of its low-energy sector. This framework allows us to extract the localization length of the edge states in the event of long-range interactions. Finally, we discuss how to encode this information in the survival probability of an excitation at the end of the chain.

5.4.1 Effective theory in the continuum limit

It is usual in condensed-matter physics to derive a continuum description of the low-energy sector of a given problem, since the effective theory is often simpler to solve than the underlying lattice model. We are going to illustrate how this is done for the SSH model, following [239], and how it transfers into the more complex situation of $\bar{H}_{\mathrm{SSH}}^{(\mathrm{ions})}$. To begin with, we note that

$$H_{\mathrm{SSH}} = J\sum_{j=1}^{N} \mathcal{J}_{j,j+1}^{\pi/2}(\sigma_j^+\sigma_{j+1}^- + \mathrm{H.c.}), \tag{5.43}$$

can be written as

$$H_{\mathrm{SSH}} = \sum_{j=1}^{N} J\mathcal{J}^{(+)}(c_j^\dagger c_{j+1} + \mathrm{H.c.}) + \sum_{j=1}^{N} J\mathcal{J}^{(-)}(-1)^j(c_j^\dagger c_{j+1} + \mathrm{H.c.}), \tag{5.44}$$

where $\mathcal{J}^{(\pm)} = (\mathcal{J}^{\mathrm{even}} \pm \mathcal{J}^{\mathrm{odd}})/2$ (cf. (5.34)). In the plane wave basis under PBC, we get

$$H_{\mathrm{SSH}} = \sum_{\mu=-N/2}^{N/2-1} \epsilon_\mu c_\mu^\dagger c_\mu + \sum_{\mu=-N/2}^{N/2-1} \Delta_\mu c_{\mu+N/2}^\dagger c_\mu + \mathrm{H.c.}, \tag{5.45}$$

with

$$\epsilon_\mu = 2J\cos\left(\frac{2\pi\mu}{N}\right) \text{ and } \Delta_\mu = iJ\delta\sin\left(\frac{2\pi\mu}{N}\right). \tag{5.46}$$

Now we take the continuum limit, $N \to \infty$, which entails substituting $2\pi\mu/N$ by $k \in [-\pi, \pi]$ in the expressions involving sums over μ. The dispersion relation of the

low-energy processes associated with ϵ_μ, which are located around the Fermi energy (cf. Fig. 5.8), can be approximated by

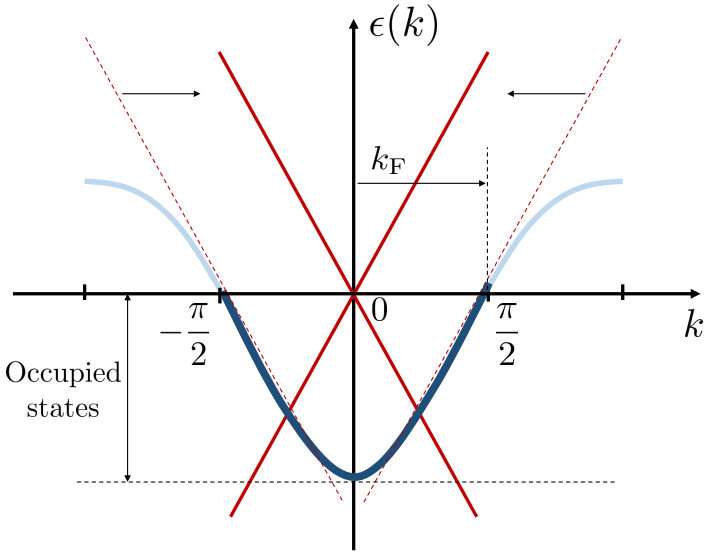

Figure 5.8: Band diagram of $H_{\rm SSH}$ for $\Delta_\mu = 0$ (sinusoid). The (many-body) ground state is comprised by all the eigenstates of $H_{\rm SSH}$ with $\epsilon(k) < 0$ (dark blue). The energy bands of the continuum theory (red lines) are linear in k, and their slope is set by the derivative of $\epsilon(k)$ at the Fermi points $k_{\rm F} = \pm\pi/2$. The low-energy physics occurs just above $\epsilon(k) = 0$.

$$\epsilon(k \pm k_{\rm F}) = 2J\cos(k \pm k_{\rm F}) = \pm 2J\sin(k) \simeq \pm 2Jk \equiv \pm v_{\rm F} k. \tag{5.47}$$

On the other hand, according to (5.45), the role of Δ_μ is to mix fermions with a given momentum with those that differ by $\mu = \pm N/2$ ($k = \pm\pi/2$). If we assume that $\delta \ll 1$, the leading processes induced by Δ_μ are those lifting the degeneracy, which incidentally occurs at the Fermi momenta $k_{\rm F} = \pm\pi/2$.

By making the final substitution

$$\frac{1}{N}\sum_{\mu=-N/2}^{N/2-1} \to \frac{1}{2\pi}\int_{-\pi}^{\pi} dk, \tag{5.48}$$

into (5.45), and keeping only the previously described processes, we arrive at the effective theory for the low-energy sector of the SSH model,

$$\frac{N}{2\pi}\int_{-\pi}^{\pi} dk\, \bar{\psi}^\dagger(k)\left(v_{\rm F} k\sigma^z + \Delta_0\sigma^y\right)\bar{\psi}(k), \quad \bar{\psi}(k)^\dagger = \left(c_{\rm R}^\dagger(k), c_{\rm L}^\dagger(k)\right), \tag{5.49}$$

where we have defined

$$v_{\mathrm{F}} = 2J, \Delta_0 \equiv \Delta(\pm\pi/2) = 2J\delta. \tag{5.50}$$

The two in the last definition stems from the fact that the processes mixing the left- and right-moving fermion bands occur twice in the Hamiltonian. The operators $c^\dagger_{\mathrm{R}}(k)$ and $c^\dagger_{\mathrm{L}}(k)$ create right- and left-moving fermions respectively, with dispersion relation $\pm v_{\mathrm{F}} k$ (cf. Fig. (5.8)).

The effective theory (5.49) captures the low-energy physics of the SSH model and, when solved, it presents a 'continuum version' of the edge states of the lattice model [233, 239]. The localization length of these states must depend on the only parameters available, v_{F} and Δ_0, which fulfil

$$\frac{v_{\mathrm{F}}}{\Delta_0} = \frac{1}{\delta}. \tag{5.51}$$

Recalling that (cf. (5.8))

$$\xi_{\mathrm{loc}} = -2/\ln\frac{1-\delta}{1+\delta}, \tag{5.52}$$

we can write

$$\xi_{\mathrm{loc}} = -2/\ln\frac{1-\Delta_0/v_{\mathrm{F}}}{1+\Delta_0/v_{\mathrm{F}}} \simeq \frac{v_{\mathrm{F}}}{\Delta_0}. \tag{5.53}$$

This result tells us something important. The continuum theory that we have just derived is not exclusive to the SSH model. We are going to see that the low-energy sector of $\bar{H}^{(\mathrm{ions})}_{\mathrm{SSH}}$ can be effectively described by (5.49) as well, although the actual values of v_{F} and Δ_0 depend on the parameters of the original lattice problem. The fact that these two models share the same low-energy limit allows us to establish an equivalence between them. In particular, we have that the localization length as given by (5.53) applies to $\bar{H}^{(\mathrm{ions})}_{\mathrm{SSH}}$, with properly renormalized values of v_{F} and Δ_0.

To derive the corresponding values of v_{F} and Δ_0 for $\bar{H}^{(\mathrm{ions})}_{\mathrm{SSH}}$, let us write

$$\bar{H}^{(\mathrm{ions})}_{\mathrm{SSH}} = \sum_{j=1}^{N}{\sum_{d=1-j}^{N-j}}' J_d^{(\mathrm{ions})}\mathcal{J}_d^{(+)}(c_j^\dagger c_{j+d}+\mathrm{H.c.})+\sum_{j=1}^{N}{\sum_{d=1-j}^{N-j}}' J_d^{(\mathrm{ions})}\mathcal{J}_d^{(-)}(-1)^j(c_j^\dagger c_{j+d}+\mathrm{H.c.}), \tag{5.54}$$

where $\mathcal{J}_d^{(\pm)} = (\mathcal{J}_d^{\mathrm{even}} \pm \mathcal{J}_d^{\mathrm{odd}})/2$, and

$$\begin{cases} \mathcal{J}_d^{\mathrm{odd}} \equiv \mathcal{J}^{\pi/2}_{j,j+d}\Big|_{j\ \mathrm{odd}} = \mathcal{J}_0\left[2\eta\sin\left(\frac{\pi}{4}d\right)\cos\left(\frac{\pi}{4}d+\phi\right)\right], \text{and} \\ \mathcal{J}_d^{\mathrm{even}} \equiv \mathcal{J}^{\pi/2}_{j,j+d}\Big|_{j\ \mathrm{even}} = \mathcal{J}_0\left[2\eta\sin\left(\frac{\pi}{4}d\right)\sin\left(\frac{\pi}{4}d+\phi\right)\right]. \end{cases} \tag{5.55}$$

The prime in the sum indicates that we exclude the term with $d = 0$. In the plane wave basis, and assuming PBC, we get

$$\bar{H}_{\mathrm{SSH}}^{(\mathrm{ions})} = \sum_{\mu=-N/2}^{N/2-1} \epsilon_\mu c_\mu^\dagger c_\mu + \sum_{\mu=-N/2}^{N/2-1} \Delta_\mu c_{\mu+N/2}^\dagger c_\mu + \mathrm{H.c.}, \tag{5.56}$$

where we have defined

$$\epsilon_\mu = 4 \sum_{d=1}^{\frac{N}{2}-1} J_d^{(\mathrm{ions})} \mathcal{J}_d^{(+)} \cos\left(\frac{2\pi\mu}{N} d\right), \tag{5.57}$$

and

$$\Delta_\mu = 2i \sum_{d=1}^{\frac{N}{2}-1}{}' J_d^{(\mathrm{ions})} \mathcal{J}_d^{(-)} \sin\left(\frac{2\pi\mu}{N} d\right) + 2 \sum_{d=2}^{\frac{N}{2}-2}{}' J_d^{(\mathrm{ions})} \mathcal{J}_d^{(-)} \cos\left(\frac{2\pi\mu}{N} d\right) + J_{\frac{N}{2}}^{(\mathrm{ions})} \mathcal{J}_{\frac{N}{2}}^{(-)} (-1)^\mu. \tag{5.58}$$

The primes in the first and second sum in Δ_μ mean that the index d runs only over odd and even values respectively. To obtain v_{F} from ϵ_μ we must compute its derivative around $\mu = \pm N/2$, whereas Δ_0 is given as $\Delta_{\mu=\pm N/2}$. We have computed these quantities numerically for large N, and this has given us a prediction for ξ_{loc} according to (5.53). We shall see that this prediction is actually quite accurate, and that it leads to non-trivial consequences in the long-range limit of $J_{j,l}^{(\mathrm{ions})}$.

5.4.2 Discussion of the edge states

The localization length of the edge states of $\bar{H}_{\mathrm{SSH}}^{(\mathrm{ions})}$ depends on the parameters of the Hamiltonian, which determine the values of $J_{j,l}^{(\mathrm{ions})}$ and $\mathcal{J}_{j,l}^{\pi/2}$. They have two kind of effects: (i) the modification of the range of $J_{j,l}^{(\mathrm{ions})}$, which depends on the detuning from the bottom of the band of motional modes, $\delta_{N/2}$, and (ii) controlling the Bessel couplings through the values of η and ϕ. Altogether, $\delta_{N/2}, \eta$ and ϕ define the parameter space of the problem. Naturally, we need to locate the edge states in parameter space, before being able to check our prediction for the localization length. We recall that the Bessel couplings fixed the dimerization pattern along the chain, so they must play a major role in the presence or absence of edge states. Thus, we study the emergence of edge states in $\bar{H}_{\mathrm{SSH}}^{(\mathrm{ions})}$ in terms of η and ϕ, and consider $\delta_{N/2}$ only as a tuning parameter.

We already know from the discussion of the original SSH model that there is an argument to prove the existence of edge states [218], based on (i) the chiral symmetry

of the model, and (ii) the non-trivial value of the Zak phase. That reasoning should carry over to $\bar{H}^{(\text{ions})}_{\text{SSH}}$, so let us seek under which conditions it fulfils the two previous requirements.

In the event of the Hamiltonian being chiral-symmetric, its pseudo-spin representation had no component $d_z(\mu)$ (cf. (5.15)). If we define the two species of operators a_μ, b_μ as we did for the SSH model (cf. 5.10), the corresponding matrix h_μ for $\bar{H}^{(\text{ions})}_{\text{SSH}}$ reads

$$h_\mu = \begin{pmatrix} \sum_{d=0}^{N-1} J_d^{(A)} \mathcal{J}_d^{(A)} e^{i\frac{2\pi\mu}{N}d} & \sum_{d=0}^{N-1} J_d^{(C)} \mathcal{J}_d^{(C)} e^{i\frac{2\pi\mu}{N}d} \\ \sum_{d=0}^{N-1} J_d^{(C)} \mathcal{J}_d^{(C)} e^{-i\frac{2\pi\mu}{N}d} & \sum_{d=0}^{N-1} J_d^{(B)} \mathcal{J}_d^{(B)} e^{i\frac{2\pi\mu}{N}d} \end{pmatrix}, \tag{5.59}$$

where $d \equiv n - m$ is the distance between dimers n and m, and we have defined

$$J^{(A)}_{n,m} = J^{(B)}_{n,m} = J^{(\text{ions})}_{2n-1,2m-1} = J^{(\text{ions})}_{2n,2m}, \quad J^{(C)}_{n,m} = J^{(\text{ions})}_{2n-1,2m}, \tag{5.60}$$

and

$$\begin{cases} \mathcal{J}^{(A)}_{n,m} = \mathcal{J}^{\pi/2}_{2n-1,2m-1} = \mathcal{J}_0\left[2\eta \sin\tfrac{\pi}{2}d \cos\left(\tfrac{\pi}{2}d + \phi\right)\right], \\ \mathcal{J}^{(B)}_{n,m} = \mathcal{J}^{\pi/2}_{2n,2m} = \mathcal{J}_0\left[2\eta \sin\tfrac{\pi}{2}d \sin\left(\tfrac{\pi}{2}d + \phi\right)\right], \\ \mathcal{J}^{(C)}_{n,m} = \mathcal{J}^{\pi/2}_{2n-1,2m} = \mathcal{J}_0\left[2\eta \sin(\tfrac{\pi}{2}d - \tfrac{\pi}{4}) \sin\left(\tfrac{\pi}{2}d - \tfrac{\pi}{4} + \phi\right)\right]. \end{cases} \tag{5.61}$$

To make $d_z(\mu) \equiv 0$ in (5.59) we need that $\mathcal{J}_d^{(A)} = \mathcal{J}_d^{(B)}$. This is indeed possible for two different values of ϕ, that have to fulfil

$$\sin\left(\frac{\pi}{2} + \phi\right) = \pm\cos\left(\frac{\pi}{2} + \phi\right), \phi \in [0, \pi], \tag{5.62}$$

which renders $\phi = \pi/4, 3\pi/4$. We conclude that these two values of ϕ are the chiral-symmetric points of the non-interacting limit in parameter space.

On the other hand, it turns out that η plays a minor role for the occurrence of the edge states. However, it allows us to fix the actual value of the dimerization. We recall that, in terms of the Bessel couplings, this quantity is given by (5.36)

$$\delta = \frac{\mathcal{J}_d^{\text{even}} - \mathcal{J}_d^{\text{odd}}}{\mathcal{J}_d^{\text{even}} + \mathcal{J}_d^{\text{odd}}}, \; d = 1. \tag{5.63}$$

We have depicted δ as a function of η in Fig. 5.9. We see that for any η, the dimerization is positive for $\phi = 3\pi/4$, whereas $\delta < 0$ in the case of $\phi = \pi/4$. By analogy with the SSH model, we expect that the topologically non-trivial phase

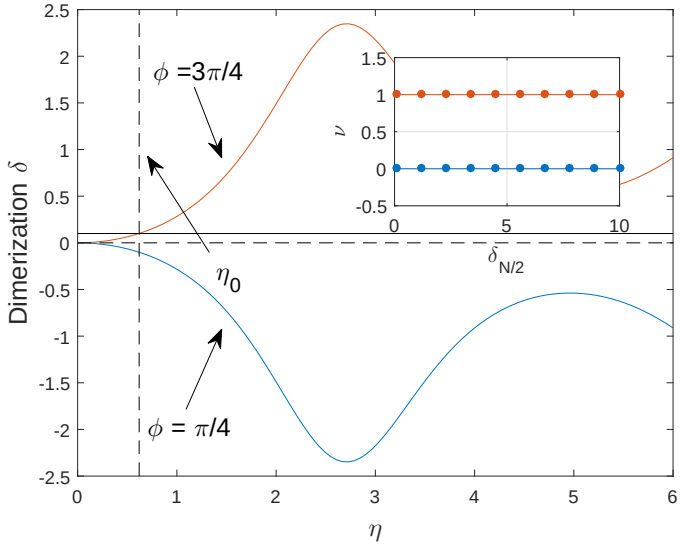

Figure 5.9: Plot of (5.63) as a function of η for the two values of ϕ leading to chiral symmetry. We take $\eta_0 \simeq 0.62$, which renders $\delta = 0.1$. The inset corresponds to the Zak phase for $\phi = \pi/4$ and $\phi = 3\pi/4$, in units of π, signalling the topologically trivial and non-trivial phases, respectively.

arises when $\delta > 0$, that is $\phi = \pi/4$. This is confirmed by the fact that the Zak phase is π in this latter case, as shown in the inset of the figure. Furthermore, we verify that this value is robust against the continuous variation of the range of the couplings, by changing the detuning $\delta_{N/2}$.

We conclude this section by finally presenting the localization length of the edge states for different ranges of $J_{j,l}^{(\text{ions})}$. We recall that the edge states are eigenfunctions of the form $M_{j,\pm n} \sim e^{(N-j+1)/\xi_{\text{loc}}}$, for instance near the left end, and that their energy lies in the mid-gap. Therefore, we can identify these states in the numerical diagonalization of the non-interacting limit,

$$\bar{H}_{\text{SSH}}^{(\text{ions})} = \sum_{j\neq l}^{N} J_{j,l}^{(\text{ions})} \mathcal{J}_{j,l}^{\pi/2} \left(c_j^\dagger c_l - c_j c_l^\dagger \right), \tag{5.64}$$

and extract their exact localization length from a fitting to an exponential decay. We have computed ξ_{loc} in this fashion for different values of $\delta_{N/2}$, to check the prediction of the effective description in terms of v_{F} and Δ_0. These are calculated from the expressions for ϵ_μ and Δ_μ in the previous section. Fig. 5.10 shows that, for any range of the ion couplings, the localization length of the edge states of $\bar{H}_{\text{SSH}}^{(\text{ions})}$ is smaller than the one for the original SSH model. This means that the long-range

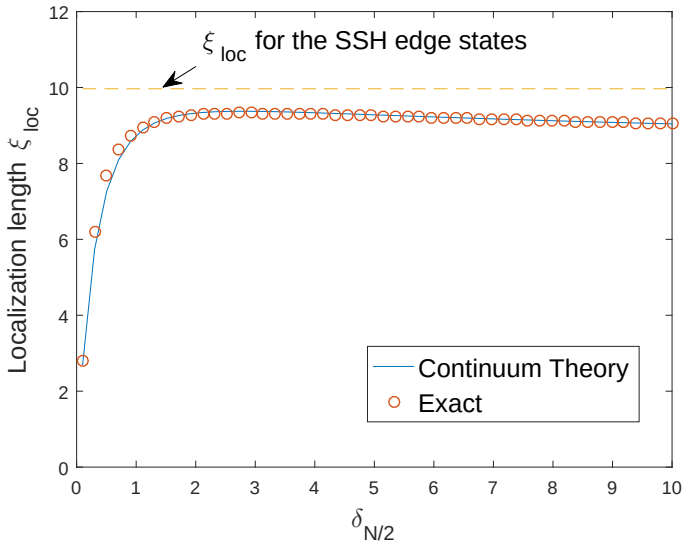

Figure 5.10: Localization length of the edge states of $\bar{H}^{(\mathrm{ions})}_{\mathrm{SSH}}$, from the exact diagonalization of the one-body Hamiltonian, for $N = 100$ sites, and from expression (5.53). The dimerization is $\delta = 0.1$, that is, $\phi = 3\pi/4$, $\eta = \eta_0 \simeq 0.62$. In units of t_{C}, the width of the band of transverse motional modes, the long-range limit of the ion couplings is attained for $\delta_{N/2} < 1$, whereas the dipolar decay occurs for large detunings. We depict the results for $\delta_{N/2}$ from 0.1 to 10.

components of $J^{(\mathrm{ions})}_{j,l}$ yield an *increase in the localization of the wave functions* $M_{j,\pm n}$ *at the ends of the chain*. Physically, the effect of $J^{(\mathrm{ions})}_{j,l}$ on the edge states is better understood within the continuum theory. The prediction for the localization length establishes that this quantity is just the interplay of v_{F} and Δ_0. The Fermi velocity sets the typical energy of the fluctuations upon the ground state, whereas Δ_0 is just the effective dimerization. Our results show that these quantities get renormalized by the ion couplings, so that v_{F} decreases and Δ_0 increases. This means that the long-range interactions lower the typical energy of the excitations over the ground state, and that the periodic nature of the couplings between distant sites reinforces the dimerized structure of the problem.

The former result is highly non-trivial, and it would be interesting to realize in an experiment. However, as we have discussed before, the eigenstates of $\bar{H}^{(\mathrm{ions})}_{\mathrm{SSH}}$ get mixed because of the interactions in

$$H^{(\mathrm{ions})}_{\mathrm{SSH}} = \sum_{j,l=1}^{N} J^{(\mathrm{ions})}_{j,l} \mathcal{J}^{\pi/2}_{j,l}(\eta,\phi) \left(\sigma^{+}_{j}\sigma^{-}_{l} + \sigma^{-}_{j}\sigma^{+}_{l}\right), \tag{5.65}$$

stemming from the Jordan-Wigner transformation. This seems to prevent us from accessing the modes of the non-interacting limit, unless we could effectively eliminate the fermion-fermion interactions. Fortunately, it turns out that removing the interactions is physically very simple: if we can prepare the system in a subspace with only one fermion or, equivalently, one spin, then the interactions will play no role. We have exploited this idea for an eventual protocol to prepare and measure the localized solutions.

5.4.3 Protocol for the detection of the edge states

We have established that under certain conditions, the Hamiltonian $\bar{H}^{(\text{ions})}_{\text{SSH}}$ supports solutions localized at the edges of the chain. Nevertheless, the detection of these edge states is not straightforward. The naive approach of preparing the many-body ground state and looking for some magnetization at the edges is useless: the parity and rotational symmetries of $H^{(\text{ions})}_{\text{SSH}}$ imply that all local spin observables are zero. Furthermore, the edge states may mix with the bulk eigenfunctions because of the interactions, and this would spoil their properties. Ideally then, we would like to isolate the edge states from the rest of the spectrum. We note that the wave function of an edge state located near the left end of the chain reads

$$|\text{E.S.}\rangle \sim \sum_{j=1}^{N} e^{(N-j+1)/\xi_{\text{loc}}} c_j^\dagger |0\rangle. \tag{5.66}$$

Since, in terms of spins,

$$c_j^\dagger |0\rangle = \sigma_j^+ \prod_{m=1}^{j-1} (-\sigma_m^z) \, |\downarrow\downarrow\downarrow \ldots\rangle = \sigma_j^+ \, |\downarrow\downarrow\downarrow \ldots\rangle \,, \tag{5.67}$$

we can write

$$|\text{E.S.}\rangle \sim \sum_{j=1}^{N} e^{(N-j+1)/\xi_{\text{loc}}} \sigma_j^+ \, |\downarrow\downarrow\downarrow \ldots\rangle \,. \tag{5.68}$$

This state has a very important feature: it is a superposition of single excitations upon $|\downarrow\downarrow\downarrow \ldots\rangle$. These excitations span the *single-excitation* subspace, whose dynamics under the whole Hamiltonian $H^{(\text{ions})}_{\text{SSH}}$ is dictated by

$$h_{j,l} \equiv \langle j | H^{(\text{ions})}_{\text{SSH}} | l \rangle = 2 J^{(\text{ions})}_{j,l} \mathcal{J}^{\pi/2}_{j,l}, \tag{5.69}$$

where $|j\rangle = \sigma_j^+ |\downarrow\downarrow\cdots\rangle$. The former claim stems from solving the Schrödinger equation ($\hbar = 1$),

$$i|\dot{\psi}(t)\rangle = H_{\rm SSH}^{\rm (ions)}|\psi(t)\rangle, \text{ where } |\psi(t)\rangle = \sum_{j=1}^{N} c_j(t)\,|j\rangle\,, \text{ with } \sum_{j=1}^{N}|c_j(t)|^2 = 1. \quad (5.70)$$

The coefficients $c_j(t)$ are just c-numbers, not to be confused with fermion operators. Multiplying by $\langle j|$, we see that

$$i\dot{c}_j(t) = \sum_{l=1}^{N} h_{j,l}c_l(t). \quad (5.71)$$

We note that the former derivation is based upon the property that $H_{\rm SSH}^{\rm (ions)}$ decomposes into subspaces of constant value of $S_z = \sum_{j=1}^{N}\sigma_j^z/2$, because of its invariance under rotations around the z axis. Consequently, states with different number of excitations are not mixed in the evolution. Equation (5.71) is straightforwardly solved by diagonalizing the matrix $h_{j,l}$, so that $h_{j,l} = \sum_{n=1}^{N}\epsilon_n M_{j,n}M_{l,n}$, and therefore

$$c_j(t) = \sum_{n,j'=1}^{N} e^{-i\epsilon_n t}M_{j,n}M_{j',n}c_{j'}(0). \quad (5.72)$$

Finally, we point out that the matrix $h_{j,l}$ coincides with the one-body Hamiltonian of the non-interacting limit. Thus, $M_{j,n}$ is comprised of the eigenstates of $\bar{H}_{\rm SSH}^{\rm (ions)}$, and in particular must feature the state $|\text{E.S.}\rangle$.

We cannot physically prepare $|\text{E.S.}\rangle$ in a simple manner. However, $|\uparrow\downarrow\downarrow\ldots\rangle$ is trivial to initialize. Now we note that $|\text{E.S.}\rangle$ has a large overlap with $|\uparrow\downarrow\downarrow\ldots\rangle$. Since the edge state is an eigenstate of $h_{j,l}$, the spin at the left end should take a long time to evolve under $H_{\rm SSH}^{\rm (ions)}$. We define the survival probability of this state as

$$P \equiv |\langle\psi(t)|\sigma_1^+\sigma_1^-|\psi(t)\rangle|^2, t\to\infty, \quad (5.73)$$

for $|\psi(t)\rangle = \sum_{j=1}^{N} c_j(t)|j\rangle$, with $c_j(0) = \delta_{1,j}$. This initial condition corresponds to the spin excitation at the left of the chain. P is computed straightforwardly from the application of (5.72), so that $\langle\psi(t)|\sigma_1^+\sigma_1^-|\psi(t)\rangle$ is given by

$$\sum_{j,k,n,m=1}^{N}\langle\downarrow\downarrow\downarrow\ldots|\,\sigma_j^-\sigma_1^+\sigma_1^-\sigma_k^+\,|\downarrow\downarrow\downarrow\ldots\rangle\, M_{j,n}M_{1,n}M_{k,m}M_{1,m}e^{i(\epsilon_n-\epsilon_m)t}, \quad (5.74)$$

and for long times,

$$\langle\psi(t)|\sigma_1^+\sigma_1^-|\psi(t)\rangle \simeq \sum_{n=1}^{N}|M_{1,n}|^4 \implies P \simeq \left(\sum_{n=1}^{N}|M_{1,n}|^4\right)^2. \quad (5.75)$$

We expect that the only contribution in this sum that depends on the localization length is the one associated with the edge state. This dependence can be estimated in the following fashion. We recall that the eigenfunction corresponding to the edge state was given as

$$M_{j,n_0} \simeq e^{(N-j+1)/\xi_{\rm loc}}, \text{ and therefore, } M_{1,n_0} = \frac{1}{Z} e^{N/\xi_{\rm loc}}, \tag{5.76}$$

where Z is the normalization factor of the edge state. Z can be computed from the fact that

$$\frac{1}{Z^2}\sum_{j=1}^{N} e^{2(N-j+1)/\xi_{\rm loc}} = 1 \implies Z = \sqrt{\frac{e^{2N/\xi_{\rm loc}}-1}{1-e^{-2/\xi_{\rm loc}}}} \simeq \sqrt{\frac{\xi_{\rm loc}}{2}}\sqrt{e^{2N/\xi_{\rm loc}}-1}, \tag{5.77}$$

where we have used the formula for the sum of a geometric series [47]

$$\sum_{k=a}^{b} r^k = \frac{r^a - r^{b+1}}{1-r}. \tag{5.78}$$

Therefore, we conclude that

$$|M_{1,n_0}|^4 \propto \xi_{\rm loc}^{-2}. \tag{5.79}$$

On the other hand, we expect that the rest of the states in the sum comprising P contribute each with $1/\sqrt{N}$, so that

$$P(1/\xi_{\rm loc}) \simeq \left(\frac{c_1}{\xi_{\rm loc}^2} + \frac{c_2}{N}\right)^2. \tag{5.80}$$

We have numerically confirmed the dependence of P on $\xi_{\rm loc}$ in Fig. 5.11. We note that the survival probability attains a constant value whenever $1/\xi_{\rm loc} \to 0$. On the other hand, for $1/\xi_{\rm loc} \to 1$, the survival probability scales as the edge state support at the end of the chain, with exponent 4. Furthermore, we have checked that this result holds for any regime of the range of the ion couplings, e.g., different $\delta_{N/2}$.

The former result states that the probability of measuring a spin excitation at the end of the chain, evolving under $H_{\rm SSH}^{\rm (ions)}$, is proportional to the localization length of the state: the more localized it is, the greater the chance of finding it at long times. The typical time to obtain P is given by $\max_{n,m} 1/|\epsilon_n - \epsilon_m|$, which can be estimated as the inverse of the effective gap Δ_0, as long as $|\mathcal{J}_d^{(-)}| \ll |\mathcal{J}_d^{(+)}|$. Following the discussion on this section, we now suggest a possible experimental procedure to study the prediction for $\xi_{\rm loc}$ of the edge states:

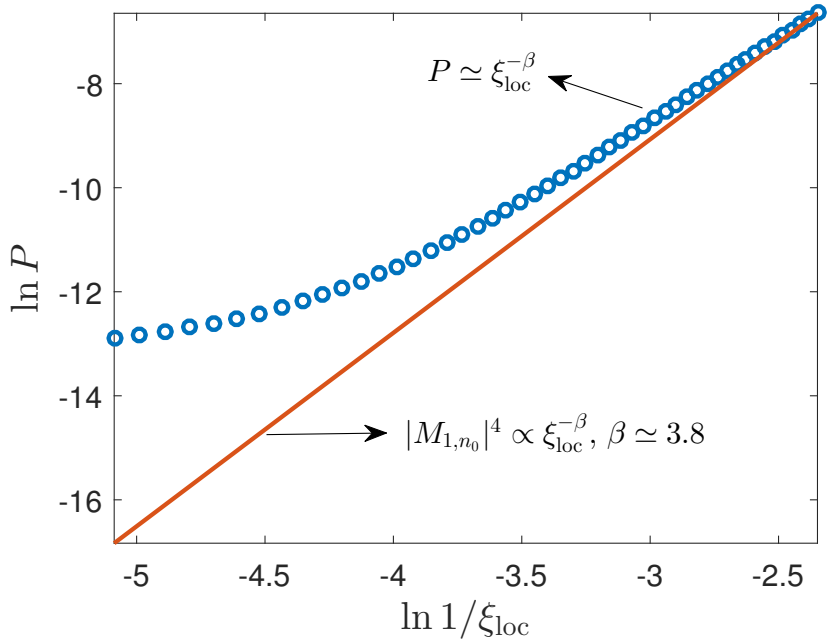

Figure 5.11: Log-log plot of the survival probability P as a function of the inverse of the localization length $\xi_{\rm loc}$. P follows a power-law dependence for $\xi_{\rm loc} \to 1$, with exponent $\beta \simeq 3.8$, consistent with the prediction $\beta = 4$. We have taken $\delta_{N/2} = 1/3$, $N = 1000$, and values of η in the interval $0.13 - 0.5$, for $\phi = 3\pi/4$.

1. Prepare the chain in the vacuum state $|\downarrow\downarrow\downarrow \ldots\rangle$.

2. Apply a π-pulse to the ion in site 1, so that $|\downarrow\downarrow\downarrow \ldots\rangle \to |\uparrow\downarrow\downarrow \ldots\rangle$.

3. Switch on $H_{\rm SSH}^{\rm (ions)}$ with $\phi = 3\pi/4$ and $\eta = \eta_0$, and wait until $t > \Delta_0^{-1}$.

4. Measure the population on site 1.

5. Repeat for different values of the detuning from the band of transverse modes $\delta_{N/2}$, to check for the dependence on the range of the interactions.

Finally, we would like to recall that the edge states are one-body eigenstates. These states should occur on the many-body ground state of $H_{\rm SSH}^{\rm (ions)}$, which is comprised of all the modes up to $k = k_{\rm F}$ (cf. Fig. 5.8). However, there is a mixing of all these states stemming from the interactions. The immediate question is if the interactions spoil this picture for the ground state, and if the edge states survive outside the non-interacting limit. To settle this, we are going to focus on the ground state of the problem in the following section.

5.5 Ground state of the interacting problem

In the previous section we have been dealing with the single-excitation subspace. Nevertheless, the true many-body ground state of $H_{\mathrm{SSH}}^{(\mathrm{ions})}$ has not been yet addressed. In this section, we compute the ground-state correlations between the ends of the chain, which must be non-zero only if there is some localization present at the edges. We see that the correlations degrade in the event of long-range interactions. We reproduce this phenomenon in an effective model that shows that it stems from the hybridization between the localized solutions and the bulk modes.

5.5.1 End-to-end correlations in the ground state

We seek to unveil any trace of localization at the edges in the ground state of the Hamiltonian

$$H_{\mathrm{SSH}}^{(\mathrm{ions})} = \sum_{j,l=1}^{N} J_{j,l}^{(\mathrm{ions})} \mathcal{J}_{j,l}^{\pi/2}(\eta,\phi)\left(\sigma_j^+\sigma_l^- + \sigma_j^-\sigma_l^+\right). \tag{5.81}$$

To begin with, we have to find an observable suited for this purpose. The symmetries of the model rule out any on-site magnetization, since there is no preferred spin direction in the xy-plane or along the z-axis. Therefore, we must rely on the correlations between different spins in the chain.

Since the edge states are the only eigenfunctions of $H_{\mathrm{SSH}}^{(\mathrm{ions})}$ that localize at the ends of the chain, they must play the main role in giving rise to the end-to-end correlations. In a finite chain, states localized at each end hybridize to give rise to solutions that have support at the left and right boundaries. We expect that the correlations between the ends are zero if there is no localization at the edges, whereas they must have a non-zero value otherwise. This result has been established for the SSH model [240], and it has been shown that the correlations stem from the entanglement between the ends of the chain. We illustrate this fact in Fig. 5.12, where we have computed $\langle\sigma_1^z\sigma_L^z\rangle$ as a function of the dimerization for both H_{SSH} and $H_{\mathrm{SSH}}^{(\mathrm{ions})}$. The correlations in the ground state of the SSH model are non-zero for $\delta > 0$ as expected. This holds qualitatively true for $H_{\mathrm{SSH}}^{(\mathrm{ions})}$ as well. Therefore, this result reassures us that the edge states of the non-interacting limit are not destroyed by the fermion-fermion interactions within (5.81). Indeed, in the regime of large detuning, or short range, the correlations are larger than those of the SSH model, for any value

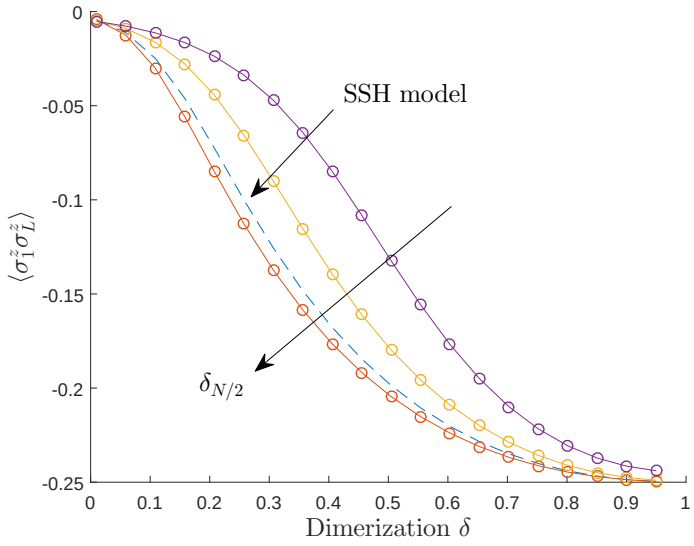

Figure 5.12: Correlations $\langle\sigma_1^z\sigma_L^z\rangle$ for $N = 16$, $\phi = 3\pi/4$ and using η to tune the dimerization. The arrow shows the direction of decreasing range of the interactions, or increasing detuning from the bottom of the motional band. We have plotted curves for $\delta_{N/2} = 0.5, 1$ and 10.

of dimerization. This is consistent with the enhanced localization of the one-body edge state predicted in the previous section (cf. Fig. 5.10).

Nevertheless, we observe a degradation of the end-to-end correlations in the long-range regime of $J_{j,l}^{(\text{ions})}$. The explanation for this is that the interactions are inducing the mixing of the edge states with the bulk modes, so that the localized components in the many-body ground state no longer follow a pure exponential decay. This renders an effective decrease of the localization at the edges. To illustrate this point, we are going to consider an effective model that captures the former effect.

5.5.2 Effective interacting Hamiltonian

Hamiltonian (5.81) does not admit an exact diagonalization in general. This is because it is describing a highly-interacting model. Applying the Jordan-Wigner transformation to the Hamiltonian,

$$H_{\text{SSH}}^{(\text{ions})} = \sum_{l>j}^{N} 2J_{j,l}^{(\text{ions})}\mathcal{J}_{j,l}^{\pi/2}\left(c_j^\dagger K_{j,l}c_l + c_j K_{j,l}c_l^\dagger\right), K_{j,l} \equiv \prod_{m=j}^{l-1}(1-2c_m^\dagger c_m), \qquad (5.82)$$

shows that as long as there are long-range interactions, $H_{\mathrm{SSH}}^{(\mathrm{ions})}$ is comprised by interaction terms between an arbitrary large number of fermions. On the other hand, the problem is straightforwardly diagonalizable for short-range interactions, since then

$$H_{\mathrm{SSH}}^{(\mathrm{ions})} = \sum_{j}^{N} 2J_{j,j+1}^{(\mathrm{ions})} \mathcal{J}_{j,j+1}^{\pi/2} \left(c_j^\dagger c_{j+1} - c_j c_{j+1}^\dagger \right), \tag{5.83}$$

is quadratic in the fermionic operators.

As we want to address the long-range limit of the ion couplings, we need to rely on some approximation. Let us assume that we truncate the fermionic interactions after the next-to-nearest-neighbours term. Then, (5.82) reduces to a Hamiltonian with two-body interactions,

$$H_{\mathrm{eff}} = \sum_{j=1}^{N} J_j^{(1)} (c_j^\dagger c_{j+1} + \mathrm{H.c.}) + \sum_{j=1}^{N} J_j^{(2)} (c_j^\dagger (1 - 2c_{j+1}^\dagger c_{j+1}) c_{j+2} + \mathrm{H.c.}). \tag{5.84}$$

Equivalently, we can write $H_{\mathrm{eff}} = H_0 + H_{\mathrm{int}}$, where

$$H_0 = \sum_{j=1}^{N} (J_j^{(1)} c_j^\dagger c_{j+1} + J_j^{(2)} c_j^\dagger c_{j+2} + \mathrm{H.c.}), \tag{5.85}$$

and

$$H_{\mathrm{int}} = -2 \sum_{j=1}^{N} J_j^{(2)} (c_j^\dagger c_{j+1}^\dagger c_{j+1} c_{j+2} + \mathrm{H.c.}). \tag{5.86}$$

We assume that we can diagonalize H_0, that is, we can write

$$H_0 = \sum_{\mu=1}^{N} \epsilon_\mu c_\mu^\dagger c_\mu, \text{ with } c_j = \sum_{\mu=1}^{N} M_{j,\mu} c_\mu, \; M_{j,\mu} \in \mathbb{R}. \tag{5.87}$$

In terms of the new operators c_μ, the interaction term reads

$$H_{\mathrm{int}} = -2 \sum_{\mu_1,\mu_2,\mu_3,\mu_4=1}^{N} U_{\mu_1,\mu_2,\mu_3,\mu_4} c_{\mu_1}^\dagger c_{\mu_2}^\dagger c_{\mu_3} c_{\mu_4}, \tag{5.88}$$

where

$$U_{\mu_1,\mu_2,\mu_3,\mu_4} \equiv \sum_{j=1}^{N} J_j^{(2)} (M_{j,\mu_1} M_{j+1,\mu_2} M_{j+1,\mu_3} M_{j+2,\mu_4} + M_{j+2,\mu_1} M_{j+1,\mu_2} M_{j+1,\mu_3} M_{j,\mu_4}). \tag{5.89}$$

So far, we have not made any approximation. However, the interaction term is difficult to deal with in general, so we rely on the following procedure, which we refer to as the Hartree-Fock approximation: we form all the possible pairings of two

operators $c^\dagger_\mu c_{\mu'}$ in $H_{\rm int}$, and evaluate them upon the ground state of H_0. The other two remaining operators are left unevaluated, and everything is placed in normal order. There are four different pairings possible, e.g.,

$$\overbrace{c^\dagger_{\mu_1} c^\dagger_{\mu_2} c_{\mu_3} c_{\mu_4}}, \quad \overbrace{c^\dagger_{\mu_1} c^\dagger_{\mu_2} c_{\mu_3} c_{\mu_4}}, \quad c^\dagger_{\mu_1} \overbrace{c^\dagger_{\mu_2} c_{\mu_3}} c_{\mu_4} \quad \text{and} \quad c^\dagger_{\mu_1} \overbrace{c^\dagger_{\mu_2} c_{\mu_3} c_{\mu_4}}.$$

Since $\langle c^\dagger_\mu c_{\mu'} \rangle = \delta_{\mu,\mu'}$ for $\mu \ni \epsilon_\mu < 0$, we can compute straightforwardly the sums in $H_{\rm int}$, in terms of which we define the Hartree-Fock Hamiltonian

$$H_{\rm HF} = \sum_{\mu=1}^{N} \epsilon_\mu c^\dagger_\mu c_\mu - 2 \sum_{\mu,\mu'=1}^{N} V_{\mu,\mu'} c^\dagger_\mu c_{\mu'}, \tag{5.90}$$

where

$$V_{\mu,\mu'} = \sum_{q \ni \epsilon_q < 0}^{N} \left(-U_{q,\mu,q,\mu'} + U_{q,\mu,\mu',q} + U_{\mu,q,q,\mu'} - U_{\mu,q,\mu',q} \right). \tag{5.91}$$

We transform $H_{\rm HF}$ back to the 'real space' operators c_j, and compute the ground state to check for the correlations. These are shown in Fig. 5.13. We find a good

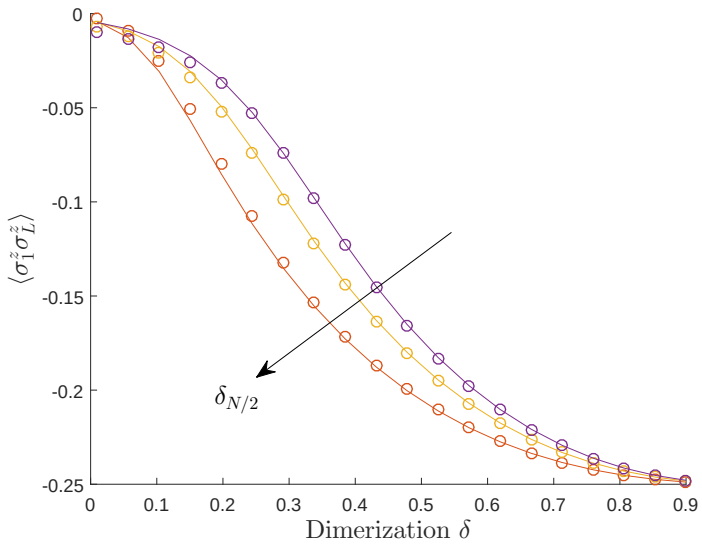

Figure 5.13: Correlations $\langle \sigma^z_1 \sigma^z_L \rangle$ predicted by the HF approximation (circles) vs. the exact diagonalization of $H_{\rm eff}$ (lines). Values of $\delta_{N/2} = 0.5, 1, 10$. $N = 16$, $\phi = 3\pi/4$ and η sweeps the values of the dimerization shown in the figure.

agreement between $H_{\rm eff}$ and $H_{\rm HF}$. We must stress, however, that this effective model fails to match the original correlations shown in Fig. 5.12. In any case, $H_{\rm eff}$ captures the fact that the interactions induce the degradation of the correlations. Nevertheless, in contrast to $H^{\rm (ions)}_{\rm SSH}$, the current model allows us to understand the

physical origin of these effects in terms of the one-body eigenstates, as we are going to discuss.

5.5.3 Mixing between the edge and bulk states

The diminished end-to-end correlations in the ground state in the event of long-range interactions stem from the hybridization of the edge states with the bulk modes. This claim is based on the role of the potential $V_{\mu,\mu'}$ in the Hartree-Fock approximation. In particular, $V_{\mathrm{E.S.},\mu'}$ gives the amplitude for the mixing of any of the edge states with the other modes of the spectrum. Performing perturbation theory up to first order in $V_{\mu,\mu'}$, we see that the edge state changes into

$$|\mathrm{E.S.}\rangle = |\mathrm{E.S.}^{(0)}\rangle - \sum_{\mu\neq \mathrm{E.S.}}^{N} |\mu^{(0)}\rangle \frac{2V_{E.S.,\mu}}{\epsilon_{E.S.}-\epsilon_{\mu}}. \tag{5.92}$$

We note that this particular form of the perturbative expansion fulfils the condition $\langle \mathrm{E.S.}^{(0)}|\mathrm{E.S.}\rangle = 1$ [51]. The normalized version of (5.92), that we call $|\mathrm{E.S.}^{(\mathrm{N})}\rangle$, differs from $|\mathrm{E.S.}\rangle$ by an overall factor. Let us assume that $|\mathrm{E.S.}^{(\mathrm{N})}\rangle = Z^{1/2}|\mathrm{E.S.}\rangle$. Then, we have that

$$\langle \mathrm{E.S.}^{(0)}|\mathrm{E.S.}^{(\mathrm{N})}\rangle = Z^{1/2}, \tag{5.93}$$

i.e., Z represents the probability for the perturbed ket $|\mathrm{E.S.}^{(\mathrm{N})}\rangle$ to be in any of the original edge states. Since $\langle \mathrm{E.S.}^{(\mathrm{N})}|\mathrm{E.S.}^{(\mathrm{N})}\rangle = Z\langle \mathrm{E.S.}|\mathrm{E.S.}\rangle = 1$, we have that, to first order in the potential,

$$Z^{-1} = \langle \mathrm{E.S.}|\mathrm{E.S.}\rangle = 1 + \sum_{\mu\neq \mathrm{E.S.}}^{N} \frac{4|V_{E.S.,\mu}|^2}{(\epsilon_{E.S.}-\epsilon_{\mu})^2}, \tag{5.94}$$

so that

$$Z \simeq 1 - \sum_{\mu\neq \mathrm{E.S.}}^{N} \frac{4|V_{E.S.,\mu}|^2}{(\epsilon_{E.S.}-\epsilon_{\mu})^2}. \tag{5.95}$$

The second term in Z represents the probability for finding the perturbed ket in any of the bulk states. This bulk-edge mixing is behind of the detriment of the correlations between the edges.

We conclude this section by studying the behaviour of Z with the range of the interactions (cf. Fig. 5.14). As expected, the mixing between the edge states and the bulk modes is larger the longer the range of the ion couplings ($\delta_{N/2}$). Physically, we

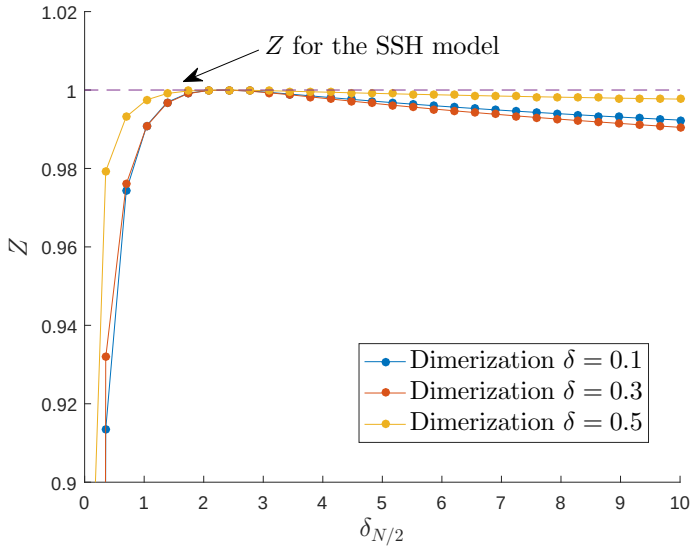

Figure 5.14: Value of the parameter Z as a function of the detuning $\delta_{N/2}$. $N = 16, \phi = 3\pi/4$ and the values of the dimerization shown in the figure.

interpret that, because of the interactions, the localized components in the many-body ground state do not longer behave as exponentially decaying functions into the bulk, although they are still responsible for the amount of localization observed. This degradation of the one-body edge state induced by the interactions constitutes an example of the physics beyond the usual framework of non-interacting topological insulators.

5.6 Trapped-ion experimental parameters

The Hamiltonian for the simulation of the SSH is the sum of two terms,

$$H_{\text{Ising}} + H_{\text{driving}} = \sum_{j,l=1}^{N} J_{j,l}^{(\text{ions})} \sigma_j^z \sigma_l^z + \frac{\Omega}{2} \sum_{j=1}^{N} \sigma_j^x + \frac{\eta\omega_{\text{d}}}{2} \cos(\omega_{\text{d}} t) \sum_{j=1}^{N} \cos(\phi_j) \sigma_j^x. \quad (5.96)$$

The Ising part originates from the adiabatic elimination of the phonons in the typical cJT model (cf. chapter 3)

$$H_{\text{cJT}} = \sum_{n=1}^{N} \delta_n a_n^\dagger a_n + \frac{\Omega}{2} \sum_{j=1}^{N} \sigma_j^z + g \sum_{j,n=1}^{N} \sigma_j^x (a_n M_{j,n} + \text{H.c.}), \quad (5.97)$$

We consider a couple of lasers inducing a spin-dependent force upon the transverse modes. Analogously to the implementation of the cJT model, let us assume a (homogeneous) crystal of $^9\text{Be}^+$ ions along a Paul trap, separated by distances $d_0 =$

$10\,\mu$m. The transversal trapping frequency is $\omega_x = 5(2\pi)$ MHz, so that the width of the radial modes is $t_{\rm C} \simeq 38\,(2\pi)$ kHz. In the short-range limit of the effective couplings, we have that

$$J_{j,l}^{(\rm ions)} \simeq \frac{J}{|j-l|^3}, \text{ with } J \simeq \frac{g^2 t_{\rm C}}{2(\delta_{N/2})^2}, \tag{5.98}$$

where $\delta_{N/2}$ is the detuning from the bottom of the radial modes dispersion relation. We assume that $\delta_{N/2} \simeq 2g$, so that we estimate $J \simeq 30$ kHz as the lowest time scale in the simulation. $\delta_{N/2}$ can be changed further to match the values considered in the theory, that are given in units of $t_{\rm C}$. One could explore as well if there is a trade-off for faster simulation times stemming from fixing $\delta_{N/2}$ and tuning $t_{\rm C}$ instead. The magnetic field σ_j^z in $H_{\rm cJT}$ can be implemented via a microwave or Raman transition. Typical magnitudes of the effective Rabi frequency Ω are 100 kHz [149].

Regarding the periodic driving, the standing wave can be implemented with two couterpropagating running waves, or with the aid of a cavity. In turn, the effective coupling stems from two-photon stimulated Raman transitions, and the resulting interaction Hamiltonian is [241]

$$H_{\rm int} = \sum_{j=1}^{N} \Omega' \sigma_j^x \cos(\Delta\mathbf{k}\cdot\mathbf{r}_j)\cos(\omega_{\rm L} t), \tag{5.99}$$

where $\omega_{\rm L}$ is the frequency of the wave created by the lasers, and Δk is the wave vector projected on the chain axis. We choose the laser intensities to match the condition $\Omega' = \eta\omega_{\rm d}/2$. Moving into the interaction picture, and making the rotating-wave approximation, we get

$$\hat{H}_{\rm int} \simeq \sum_{j=1}^{N} \Omega'(\sigma_j^+ e^{i\omega_d t} + \text{H.c.})\cos(\Delta\mathbf{k}\cdot\mathbf{r}_j(t)), \tag{5.100}$$

where we have chosen $\omega_{\rm L} = \omega_{\rm d} - \omega$, with ω being the frequency of the hyperfine/Zeeman qubit. The argument of the cosine can be expanded as

$$\begin{aligned}\Delta\mathbf{k}\cdot\mathbf{r}_j(t) &= (\Delta k_x, 0, \Delta k_z)\cdot(\delta r_{x,j}(t), \delta r_{y,j}(t), r_j^{(0)} + \delta r_{z,j}(t)) \\ &= \sum_{n=1}^{N}(\eta_n^x M_{j,n}^x a_{x,n} e^{-i\omega_n^x t} + \text{H.c.}) + \sum_{n=1}^{N}(\eta_n^z M_{j,n}^z a_{z,n} e^{-i\omega_n^z t} + \text{H.c.}) + \Delta k_z r_j^{(0)} + \phi.\end{aligned} \tag{5.101}$$

To give rise to $\Delta k_z = \sin(\theta)|\Delta\mathbf{k}| = \pi/(2d_0)$, and assuming $\lambda = 320$ nm and $d_0 = 10\,\mu$m, the laser must be almost perpendicular to the chain, with a small tilting of

$\theta \simeq 0.46$ degrees. We consider trapping frequencies $\omega_x = 5\,(2\pi)$ MHz, and $\omega_z = 192\,(2\pi)$ kHz for $N = 20$ ions. With these values we get the Lamb-Dicke parameters $\max_n \eta_n^x \simeq 0.21$ and $\max_n \eta_n^z \simeq 0.009$. The former values justify the Taylor expansion of the cosine. We choose a value of $\omega_{\rm d} \simeq 50$ kHz, so that $|\omega_{\rm d} - \omega_n^{x,z}| \gg \omega_{\rm d}$. Then, the force is not resonant with any motional sideband, and therefore

$$\hat{H}_{\rm int} \simeq \sum_{j=1}^{N} \Omega'(\sigma_j^+ e^{i\omega_d t} + \text{H.c.}) \cos(\Delta k_z r_j^{(0)} + \phi). \tag{5.102}$$

We note that $(\sigma_j^+ e^{i\omega_d t} + \text{H.c.}) \propto \sigma_j^x \cos(\omega_d t) + \sigma_j^y \sin(\omega_{\rm d} t)$. We aim at implementing a term proportional to σ_j^x alone, so we would need to add an extra standing wave with a (detuning) frequency $-\omega_{\rm d}$ to eliminate σ_j^y. Another possibility is to utilize the frequency modulation of the laser [242], to create two sidebands with frequencies $\pm\omega_{\rm d}$ around ω. This has the additional benefit of allowing us to drive the carrier transition as well. In any case, we obtain

$$\hat{H}_{\rm int} \to H_{\rm driving} = \frac{\eta\omega_{\rm d}}{2} \cos(\omega_{\rm d} t) \sum_{j=1}^{N} \cos(\Delta k_z d_0 j + \phi)\sigma_j^x. \tag{5.103}$$

The assumption for eliminating the anomalous terms $\sigma_j^+\sigma_l^+$ and $\sigma_j^-\sigma_l^-$ in the derivation of $H_{\rm SSH}$ was that

$$\max_{j,l} |J_{j,l}^{(\rm ions)}| \ll \omega_{\rm d} \ll \Omega. \tag{5.104}$$

Since $\omega_{\rm d} \simeq 50$ kHz, the previous condition is well satisfied. Finally, we recall that the typical time associated with the detection of the edge state is Δ_0^{-1}. Since $\Delta_0 \simeq 2J\delta$, for $\delta = 0.1$ ($\eta \simeq 0.62, \phi = \pi/4$), we have that $\Delta_0^{-1} \simeq 0.17$ ms. This is consistent with experimental times for the preparation and detection of many-body spin states in trapped-ion quantum simulators [124].

5.7 Conclusions

The aim of this chapter was to prove if it was possible to realize the SSH model with trapped-ions. Since the effective interactions between spins in these systems have long range, we wanted to establish their effect on the localization of the edge states, and on the many-body ground state.

We considered a periodic driving to dress the effective couplings of the spins in the ion trap. We obtained an XY model with periodically modulated couplings, and for period two we recovered the SSH model. The ion couplings introduced some interactions in the fermionic representation of the Hamiltonian. Similar techniques to those we used have been proposed for the quantum simulation of topological insulators with trapped ions. In particular, we can mention the photon-assisted tunnelling [243], which consists in periodically driving the bosonic degrees of freedom, instead of the spins. In the end, this gives rise to similar dressed, effective spin-ion couplings. Periodic drivings have been used as well to probe localization effects [238]. Also, it is well-established that the spatial modulation of the couplings can give rise to a kaleidoscope of topological phases with fermions [244]. The case of long-range interactions has also been addressed in [245]. It is known that the addition of a transverse field to $H_{\mathrm{SSH}}^{(\mathrm{ions})}$ gives rise to magnetization plateaus [246], associated with non-trivial topological phases. Direct realization of this physics would be straightforward with our scheme.

We relied on a continuum theory of the low-lying sector of the spectrum to obtain a prediction for ξ_{loc} of the edge states. This effective description proceeded along the same lines of the original continuum limit for the SSH model, known as Takayama-Lin-Liu-Maki theory [239]. In this work the authors take into account the phononic degrees of freedom giving rise to the dimerization. However, one can dispose of this technicality, as we did, or rely on other arguments to justify the existence of localized solutions in the continuum limit, as the envelope-function approximation [233]. We concluded that the long-range couplings induce an extra localization of the edge states. In order to realize the boundary modes experimentally, we discussed the parameter regime where they appear, and a protocol to prepare them. Similar ideas have been put forward in the field of cold-atoms in optical lattices [247]. However, our method addresses the one-body edge states, in contrast to other proposals, where they deal with the many-body ground state. This is an advantage of the implementation with trapped ions, where we count with individual addressing. Furthermore, our setup offers the possibility to probe the prediction for the localization length of the non-interacting limit, and the range of the interactions can be tuned at will. The extra localization of the edge states raises the question

of whether other topological models may present this same phenomenology when subjected to long-range couplings, and therefore opens up a prospect for further investigations. Also, the method to experimentally access the non-interacting limit, bypassing the interactions, may apply to other problems as well. This is relevant to systems where interactions cannot be rigorously neglected in any regime.

Finally, we computed the end-to-end correlations from an exact diagonalization of the Hamiltonian. The reason behind this is that as long as there is any localization at the ends of the chain, this amount will be different from zero. Taking into account that the only one-body eigenstates with appreciable support at the edges are the boundary modes, there is a direct correspondence between $\langle \sigma_1^z \sigma_L^z \rangle$ and the presence of edge states within the many-body ground state. The calculation showed that the edge states of the non-interacting limit were present as well in the interacting problem. Nevertheless, for long-range ion couplings, the decrease in the correlation between the ends indicated that the edge states were gradually disappearing. We concluded that the origin of this phenomenon was the mixing between these modes and the bulk states. This effect reminds of the depletion of the boundary mode in the superlattice Bose-Hubbard model [247]. In this work, the authors claim that this feature stems from the lack of chiral symmetry of the interacting problem, and put forward a generalized bulk-boundary correspondence.

The existence of edge states in the presence of interactions is a very important result. An immediate extension of this work would consist in the computation of a topological invariant of the many-body ground state, such as the Zak phase, as presented in [247], for instance. The behaviour of this quantity could shed light on the non-trivial nature of the ground state as a function of the interactions. Also, it would be interesting to check the behaviour of the correlations between the edges and the bulk for long chains. This could be provided by a DMRG diagonalization of the problem, but it would require the implementation of long-range interactions, and a subsequent computational overhead.

Chapter 6

Conclusions and Outlook

Our objective in this thesis was to exploit, from a theoretical perspective, the current capabilities of trapped-ion quantum simulators for the implementation of models hosting strongly-correlated phases. We have shown that spin-liquid phenomenology, gauge theories and topological insulators can be realized and characterized in state-of-the-art trapped-ion systems. To finalize, let us summarize the main conclusions drawn from the former chapters, and suggest questions that merit of further investigation.

A first conclusion is that spin liquids may arise in trapped-ion quantum matter, although further investigation is needed. The frustrated region presents enhanced fluctuations and correlations, but we do not know if they survive the thermodynamic limit. This question could be answered with more extensive DMRG calculations, and we expect that the susceptibility to a quantum field in the frustrated region diverges in the thermodynamic limit. Also, spin liquids present a temperature region $T_{\text{freezing}} < T < T_{\text{c}}$ in which they are free to fluctuate in a correlated manner, but do not present magnetic order. It would be interesting to establish if there is an analogous transition field between the paramagnet and the liquid phase. To this end, we would need to find suitable order parameters to establish clearly the phase boundaries between AF/frustrated/Hopfield regimes, and the paramagnetic phase.

From our results we can also draw that there is an emergence of long-range correlations in the cJT model, but the physical origin for this is not clear. The correlations must arise from the constraints upon the fluctuations dictated by the frustrated interactions. A possible method to gain insight into these constraints

could be to study excited states, and establish some common features.

We have seen that the correlations in the Hopfield regime feature some interesting structures as well. The spatially modulated periodic couplings can give rise to a more regular instance of frustration. These kind of couplings have been studied in connection with systems featuring modulated structures, whose physics is captured by the ANNNI model [42]. Since the frustration in the Hopfield regime is better understood, we could look for the onset of a spin liquid in a more controlled environment.

Regarding quantum annealing, we have concluded that, within mean-field theory, it does not perform well in the cJT model. This may indicate that quantum correlations are important for the success of the algorithm, or that the frustration in the cJT is a 'hard' problem for the algorithm. We must note that quantum annealing is a topic that has attracted a lot of attention since it was claimed that certain commercial devices were performing the algorithm for hundreds of qubits [202]. These devices are based on superconducting qubits, since they are easy to scale up. Although the presence of quantum coherence on these machines is out of doubt [248], the status of the algorithm as a way to outperform classical simulations remains contested. In particular, it is not clear if quantum annealing would be able to tackle computationally hard problems such as finding the ground state of a spin glass, since it can require an exponentially large running time [203, 249]. In our particular case, it would be interesting to assess the complexity in finding the ground state of the cJT model, and compare it with the hardness of the problems encoded in superconducting quantum annealers. This study could highlight that trapped-ion simulators showcase harder problems than those that can be encoded in commercial quantum annealers.

We have concluded that the IR lattice undergoes a first-order phase transition. We have backed up this claim by our perturbative, variational and numerical studies. Nevertheless, we have already insisted on the necessity of performing a finite-size scaling study of the divergences in the problem to put on sounder footing the emergence of the transition. This should be amenable for our DMRG routines as long as the phonon number is low. Further simulations would be useful to accurately locate the critical endpoint, and to characterize it. We do not know if there is

actual criticality associated with this point, and it would be interesting to check if at this point, for which $\delta \sim J$, there is a vanishing of the energy of the fluctuations. The phenomenon of hysteresis in spin systems [215] could be studied in the IR lattice as well. In particular, the periodic driving of the phonons would allow the study of metastability around the transition. Finally, the IR lattice is a perfect test-bed for the accuracy of other spin-boson variational wave functions, such as the multipolaron ansatz [250], which has been introduced in the study of dissipative systems.

The classification of topological orders in topological insulators is well-established [21], but less is known when interactions are added into these systems [251]. We have proven that the interacting SSH model features topological edge states, although a proper characterization in terms of the localization length of the many-body ground state is missing. This would require the simulation of longer chains. We could try to perform a DMRG simulation of this problem, but the long-range interactions introduce an overhead of the method. On the other hand, the versatility of the periodic drivings would allow us to implement other interesting models, such as the Kitaev wire [252]. Another possible direction is the study of 2D systems, where dressed interactions can be explored for simulation of more general models of topological order, such Kitaev's honeycomb model [45].

The systems that we have studied do not necessarily exceed the computational capability of a classical computer, owing to their 1D nature. This has not prevented us from studying phases that are scientifically very appealing, since they cannot be easily realized in nature. The implementation of our proposals may serve as proof-of-principle experiments that could be later scaled up. For example, the IR lattice, if implemented, would be the first analogical simulation of a lattice gauge theory. The extension of our work to further dimensions is an exciting research direction, since the generalization of our phases to 2D would give rise to richer spin-liquid and topological orders.

On the other hand, we must stress that quantum simulation with trapped ions, although usually restricted to 1D, where we can perform DMRG, is getting very close to the major goal of outperforming classical computers. This is the case of trapped-ion experiments where normal modes, along with the spins, play a role

in the dynamics. In these cases, the complexity of the spin-phonon Hamiltonian increases exponentially with the number of modes. This places a restriction for the system sizes that can be simulated with DMRG. Current works are exploiting this route to study fundamental questions in quantum statistical mechanics, such as the emergence of thermalization in the dynamics of a single qubit coupled to an engineered bosonic bath [117].

This thesis has showcased the exciting possibilities for simulating phases of matter featuring strong correlations with trapped ions. Although current experiments are limited to $N \lesssim 20$ ions [125], this does not prevent the implementation of physics that, because of the subtle conditions required for its onset, can only occur in these systems, owing to the exquisite control over all the degrees of freedom available. The prospects for quantum simulation are exciting, since simulations are already giving answers about the behaviour of exotic phases of matter, and are closer than ever to outperform classical computers. This would mean a new scientific revolution, not only because of finally succeeding in dominating the elusive nature of quantum mechanics, but because this power may have technological applications that we are not able to devise yet.

Bibliography

[1]A. Auerbach, *Interacting electrons and quantum magnetism* (Springer, 1988) (cit. on p. 1).

[2]F. Alet, A. M. Walczak and M. P. Fisher, "Exotic quantum phases and phase transitions in correlated matter", Physica A **369**, 122 –142 (2006) (cit. on p. 1).

[3]M. Potthoff, A. Avella and F. Mancini, *Strongly correlated systems: theoretical methods* (Springer Berlin Heidelberg, 2012) (cit. on p. 1).

[4]X.-G. Wen, "Quantum orders and symmetric spin liquids", Phys. Rev. B **65**, 165113 (2002) (cit. on p. 1).

[5]P. A. Lee, "An end to the drought of quantum spin liquids", Science **321**, 1306–1307 (2008) (cit. on p. 1).

[6]A. P. Ramirez, "Quantum spin liquids: a flood or a trickle?", Nature Phys. **4**, 442–443 (2008) (cit. on p. 1).

[7]L. Balents, "Spin liquids in frustrated magnets", Nature (London) **464**, 199–208 (2010) (cit. on pp. 1, 44, 59).

[8]X.-G. Wen, *Quantum field theory of many-body systems* (OUP Oxford, 2010) (cit. on p. 1).

[9]S.-H. Lee, C. Broholm, W. Ratcliff, G. Gasparovic, Q. Huang, T. H. Kim and S.-W. Cheong, "Emergent excitations in a geometrically frustrated magnet", Nature (London) **418**, 856–858 (2002) (cit. on p. 2).

[10]T. Senthil and M. P. A. Fisher, "Fractionalization in the cuprates: detecting the topological order", Phys. Rev. Lett. **86**, 292–295 (2001) (cit. on p. 2).

[11]A. Kitaev, "Fault-tolerant quantum computation by anyons", Ann. Phys. (N. Y.) **303**, 2 –30 (2003) (cit. on p. 2).

[12]C. Nayak, S. H. Simon, A. Stern, M. Freedman and S. Das Sarma, "Non-abelian anyons and topological quantum computation", Rev. Mod. Phys. **80**, 1083–1159 (2008) (cit. on p. 2).

[13]F. Halzen and A. D. Martin, *Quarks and leptons: an introductory course in modern particle physics* (New York: Wiley, 1984) (cit. on pp. 2, 72).

[14]P. Langacker, *The standard model and beyond (series in high energy physics, cosmology and gravitation)* (London: Taylor & Francis, 2011) (cit. on pp. 2, 72).

[15]L. McLerran, "The physics of the quark-gluon plasma", Rev. Mod. Phys. **58**, 1021–1064 (1986) (cit. on p. 2).

[16]J. B. Kogut and M. A. Stephanov, *The phases of quantum chromodynamics: from confinement to extreme environments* (Cambridge University Press, Cambridge, Dec. 2003) (cit. on p. 2).

[17]K. Fukushima and T. Hatsuda, "The phase diagram of dense QCD", Rep. Prog. Phys. **74**, 014001 (2011) (cit. on p. 2).

[18]R. P. Feynman, "Simulating physics with computers", Int. J. Theor. Phys. **21**, 467–488 (1982) (cit. on pp. 2, 19–21, 36, 62).

[19]V. M. Kendon, K. Nemoto and W. J. Munro, "Quantum analogue computing", Phil. Trans. R. Soc. London, Ser. A **368**, 3609–3620 (2010) (cit. on p. 2).

[20]T. H. Johnson, S. R. Clark and D. Jaksch, "What is a quantum simulator?", EPJ Quantum Technol. **1**, 10 (2014) (cit. on p. 2).

[21]S. Ryu, A. P. Schnyder, A. Furusaki and A. W. W. Ludwig, "Topological insulators and superconductors: tenfold way and dimensional hierarchy", New J. Phys. **12**, 065010 (2010) (cit. on pp. 2, 99, 136).

[22]X.-L. Qi and S.-C. Zhang, "Topological insulators and superconductors", Rev. Mod. Phys. **83**, 1057–1110 (2011) (cit. on pp. 2, 99).

[23]B. A. Bernevig, *Topological insulators and topological superconductors* (Princeton University Press, 2013) (cit. on pp. 2, 99).

[24]T. Schaetz, D. Leibfried, J. Chiaverini, M. Barrett, J. Britton, B. DeMarco, W. Itano, J. Jost, C. Langer and D. Wineland, "Towards a scalable quantum computer/simulator based on trapped ions", Appl. Phys. B **79**, 979–986 (2004) (cit. on p. 2).

[25]T. Schaetz, A. Friedenauer, H. Schmitz, L. Petersen and S. Kahra, "Towards (scalable) quantum simulations in ion traps", J. Mod. Opt. **54**, 2317–2325 (2007) (cit. on p. 2).

[26]B. P. Lanyon, C. Hempel, D. Nigg, M. Müller, R. Gerritsma, F. Zähringer, P. Schindler, J. T. Barreiro, M. Rambach, G. Kirchmair, M. Hennrich, P. Zoller, R. Blatt and C. F. Roos, "Universal digital quantum simulation with trapped ions", Science **334**, 57–61 (2011) (cit. on p. 2).

[27]R. Blatt and C. F. Roos, "Quantum simulations with trapped ions", Nature Phys. **8**, 277–284 (2012) (cit. on p. 2).

[28]C. Schneider, D. Porras and T. Schaetz, "Experimental quantum simulations of many-body physics with trapped ions", Rep. Prog. Phys. **75**, 024401 (2012) (cit. on pp. 2, 27, 29, 32, 34, 68).

[29]L. Lamata, A. Mezzacapo, J. Casanova and E. Solano, "Efficient quantum simulation of fermionic and bosonic models in trapped ions", EPJ Quantum Technol. **1**, 9 (2014) (cit. on p. 2).

[30]C. Castelnovo, R. Moessner and S. L. Sondhi, "Magnetic monopoles in spin ice", Nature (London) **451**, 42–45 (2008) (cit. on pp. 5, 93).

[31]S. A. Grigera, R. S. Perry, A. J. Schofield, M. Chiao, S. R. Julian, G. G. Lonzarich, S. I. Ikeda, Y. Maeno, A. J. Millis and A. P. Mackenzie, "Magnetic field-tuned quantum criticality in the metallic ruthenate $Sr_3Ru_2O_7$", Science **294**, 329–332 (2001) (cit. on pp. 5, 93).

[32]S. R. White, "Density matrix formulation for quantum renormalization groups", Phys. Rev. Lett. **69**, 2863–2866 (1992) (cit. on pp. 7, 37, 38, 52).

[33]S. R. White, "Density-matrix algorithms for quantum renormalization groups", Phys. Rev. B **48**, 10345–10356 (1993) (cit. on pp. 7, 37, 38, 40, 89).

[34]U. Schollwöck, "The density-matrix renormalization group", Rev. Mod. Phys. **77**, 259–315 (2005) (cit. on pp. 7, 37).

[35]U. Schollwöck, "The density-matrix renormalization group in the age of matrix product states", Ann. Phys. (N.Y.) **326**, 96–192 (2011) (cit. on pp. 7, 37, 39, 41, 52).

[36]S. Sachdev, "Quantum criticality: competing ground states in low dimensions", Science **288**, 475–480 (2000) (cit. on p. 8).

[37]M. Vojta, "Quantum phase transitions", Rep. Prog. Phys. **66**, 2069 (2003) (cit. on p. 8).

[38]S. Sachdev, "Quantum magnetism and criticality", Nature Phys. **4**, 173–185 (2008) (cit. on p. 8).

[39]L. D. Carr, *Understanding quantum phase transitions* (CRC Press, Taylor & Francis Group, 2011) (cit. on p. 8).

[40]S. Sachdev, *Quantum phase transitions* (Cambridge University Press, 2011) (cit. on pp. 8, 12, 13, 15–17, 52, 60, 93).

[41]J. J. Binney, N. Dowrick, A. J. Fisher and M. E. J. Newman, *The theory of critical phenomena: an introduction to the renormalization group* (Clarendon Press Oxford, 1992) (cit. on p. 8).

[42]S. Suzuki, J. Inoue and B. K. Chakrabarti, *Quantum Ising phases and transitions in transverse Ising models* (Springer, 2013) (cit. on pp. 9, 11–13, 18, 47, 49, 53, 55, 85, 86, 135).

[43]E. Lieb, T. Schultz and D. Mattis, "Two soluble models of an antiferromagnetic chain", Ann. Phys. (N.Y.) **16**, 407 –466 (1961) (cit. on pp. 10, 11, 100).

[44]P. Ray and B. Chakrabarti, "Exact ground-state excitations of the XY model in a transverse field in one dimension", Phys. Lett. A **98**, 431 –432 (1983) (cit. on p. 10).

[45]A. Kitaev, "Anyons in an exactly solved model and beyond", Ann. Phys. (N. Y.) **321**, January Special Issue, 2 –111 (2006) (cit. on pp. 10, 25, 136).

[46]M. Abramowitz and I. A. Stegun, *Handbook of mathematical functions: with formulas, graphs, and mathematical tables*, Vol. 55 (Courier Corporation, 1964) (cit. on pp. 13, 50, 164).

[47]H. J. Weber and G. B. Arfken, *Esential mathematical methods for physicists* (Elsevier Academic Press, 2004) (cit. on pp. 13, 109, 122, 164).

[48]G. C. Wick, "The evaluation of the collision matrix", Phys. Rev. **80**, 268–272 (1950) (cit. on p. 13).

[49]L. I. Schiff, *Quantum mechanics* (McGraw-Hill, 1968) (cit. on pp. 15, 17, 18, 79, 84).

[50]L. E. Ballentine, *Quantum mechanics: a modern development* (World Scientific, Singapore, 1998) (cit. on pp. 15, 17, 18, 79).

[51]J. J. Sakurai and J. J. Napolitano, *Modern quantum mechanics* (Pearson, 2010) (cit. on pp. 15, 17, 18, 62, 128).

[52]V. L. Ginzburg, "Some remarks on phase transitions of the 2nd kind and the microscopic theory of ferroelectric materials", Sov. Phys. Solid State **2**, 1824–1834 (1961) (cit. on p. 15).

[53]J. Als-Nielsen and R. J. Birgeneau, "Mean field theory, the ginzburg criterion, and marginal dimensionality of phase transitions", Am. J. Phys. **45**, 554–560 (1977) (cit. on p. 15).

[54]L. D. Landau, "On the theory of phase transitions", JETP Lett. **7** (1937) (cit. on pp. 16, 17).

[55]L. D. Landau and V. L. Ginzburg, "On the theory of superconductivity", Zh. Eksp. Teor. Fiz. **20**, 1064 (1950) (cit. on pp. 16, 17).

[56]M. E. Fisher, "The renormalization group in the theory of critical behavior", Rev. Mod. Phys. **46**, 597–616 (1974) (cit. on pp. 17, 19).

[57]P. de Gennes, "Collective motions of hydrogen bonds", Solid State Commun. **1**, 132 –137 (1963) (cit. on p. 19).

[58]R. Coldea, D. A. Tennant, E. M. Wheeler, E. Wawrzynska, D. Prabhakaran, M. Telling, K. Habicht, P. Smeibidl and K. Kiefer, "Quantum criticality in an ising chain: experimental evidence for emergent e8 symmetry", Science **327**, 177–180 (2010) (cit. on p. 19).

[59]N. Metropolis, A. W. Rosenbluth, M. N. Rosenbluth, A. H. Teller and E. Teller, "Equation of state calculations by fast computing machines", J. Chem. Phys. **21**, 1087–1092 (1953) (cit. on p. 19).

[60]M. Troyer and U.-J. Wiese, "Computational complexity and fundamental limitations to fermionic Quantum Monte Carlo simulations", Phys. Rev. Lett. **94**, 170201 (2005) (cit. on p. 19).

[61]S. Lloyd, "Universal quantum simulators", Science **273**, 1073–1078 (1996) (cit. on pp. 20–22, 36, 62).

[62]I. Buluta and F. Nori, "Quantum simulators", Science **326**, 108–111 (2009) (cit. on pp. 20, 24).

[63]J. I. Cirac and P. Zoller, "Goals and opportunities in quantum simulation", Nature Phys. **8**, 264–266 (2012) (cit. on pp. 20, 22).

[64]I. M. Georgescu, S. Ashhab and F. Nori, "Quantum simulation", Rev. Mod. Phys. **86**, 153–185 (2014) (cit. on pp. 20, 23, 24, 26).

[65]R. Babbush, P. J. Love and A. Aspuru-Guzik, "Adiabatic quantum simulation of quantum chemistry", Sci. Rep. **4**, 6603– (2014) (cit. on p. 20).

[66]P. J. J. O'Malley, R. Babbush, I. D. Kivlichan, J. Romero, J. R. McClean, R. Barends, J. Kelly, P. Roushan, A. Tranter, N. Ding, B. Campbell, Y. Chen, Z. Chen, B. Chiaro, A. Dunsworth, A. G. Fowler, E. Jeffrey, E. Lucero, A. Megrant, J. Y. Mutus, M. Neeley, C. Neill, C. Quintana, D. Sank, A. Vainsencher, J. Wenner, T. C. White, P. V. Coveney, P. J. Love, H. Neven, A. Aspuru-Guzik and J. M. Martinis, "Scalable quantum simulation of molecular energies", Phys. Rev. X **6**, 031007 (2016) (cit. on p. 20).

[67]J. Eisert, M. Friesdorf and C. Gogolin, "Quantum many-body systems out of equilibrium", Nature Phys. **11**, 124–130 (2015) (cit. on p. 20).

[68]D. P. DiVincenzo, "Quantum computation", Science **270**, 255–261 (1995) (cit. on p. 21).

[69]M. A. Nielsen and I. L. Chuang, *Quantum computation and quantum information* (Cambridge University Press, Cambridge, England, 2000) (cit. on p. 22).

[70]G. Ortiz, J. E. Gubernatis, E. Knill and R. Laflamme, "Quantum algorithms for fermionic simulations", Phys. Rev. A **64**, 022319 (2001) (cit. on p. 22).

[71]R. Somma, G. Ortiz, J. E. Gubernatis, E. Knill and R. Laflamme, "Simulating physical phenomena by quantum networks", Phys. Rev. A **65**, 042323 (2002) (cit. on p. 22).

[72]S. Wiesner, "Simulations of many-body quantum systems by a quantum computer", arXiv:quant-ph/9603028 (1996) (cit. on p. 22).

[73]D. S. Abrams and S. Lloyd, "Simulation of many-body Fermi systems on a universal quantum computer", Phys. Rev. Lett. **79**, 2586–2589 (1997) (cit. on p. 22).

[74]D. A. Lidar and O. Biham, "Simulating Ising spin glasses on a quantum computer", Phys. Rev. E **56**, 3661–3681 (1997) (cit. on p. 22).

[75]C. Zalka, "Efficient simulation of quantum systems by quantum computers", Fortschr. Phys. **46**, 877–879 (1998) (cit. on p. 22).

[76]C. Zalka, "Simulating quantum systems on a quantum computer", Proc. R. Soc. London, Ser. A **454**, 313–322 (1998) (cit. on p. 22).

[77]B. M. Terhal and D. P. DiVincenzo, "Problem of equilibration and the computation of correlation functions on a quantum computer", Phys. Rev. A **61**, 022301 (2000) (cit. on p. 22).

[78]A. Marzuoli and M. Rasetti, "Spin network quantum simulator", Phys. Lett. A **306**, 79 –87 (2002) (cit. on p. 22).

[79]F. Verstraete, J. I. Cirac and J. I. Latorre, "Quantum circuits for strongly correlated quantum systems", Phys. Rev. A **79**, 032316 (2009) (cit. on p. 22).

[80]S. Raeisi, N. Wiebe and B. C. Sanders, "Quantum-circuit design for efficient simulations of many-body quantum dynamics", New J. Phys. **14**, 103017 (2012) (cit. on p. 22).

[81]E. A. Martínez, C. A. Muschik, P. Schindler, D. Nigg, A. Erhard, M. Heyl, P. Hauke, M. Dalmonte, T. Monz, P. Zoller and R. Blatt, "Real-time dynamics of lattice gauge theories with a few-qubit quantum computer", Nature (London) **534**, 516–519 (2016) (cit. on pp. 23, 27, 72).

[82]R. Barends, A. Shabani, L. Lamata, J. Kelly, A. Mezzacapo, U. L. Heras, R. Babbush, A. G. Fowler, B. Campbell, Y. Chen, Z. Chen, B. Chiaro, A. Dunsworth, E. Jeffrey, E. Lucero, A. Megrant, J. Y. Mutus, M. Neeley, C. Neill, P. J. J. OMalley, C. Quintana, P. Roushan, D. Sank, A. Vainsencher, J. Wenner, T. C. White, E. Solano, H. Neven and J. M. Martinis, "Digitized adiabatic quantum computing with a superconducting circuit", Nature (London) **534**, 222–226 (2016) (cit. on p. 23).

[83]H. Wei and X. Xue, "Quantum isomorphic simulation", arXiv:quant-ph/9702050 (1997) (cit. on p. 23).

[84]E. Manousakis, "A quantum-dot array as model for copper-oxide superconductors: a dedicated quantum simulator for the many-fermion problem", J. Low Temp. Phys. **126**, 1501–1513 (2002) (cit. on p. 23).

[85]U. R. Fischer and R. Schützhold, "Quantum simulation of cosmic inflation in two-component Bose-Einstein condensates", Phys. Rev. A **70**, 063615 (2004) (cit. on p. 23).

[86]A. Y. Smirnov, S. Savel'ev, L. G. Mourokh and F. Nori, "Modelling chemical reactions using semiconductor quantum dots", Eur. J. Phys. **80**, 67008 (2007) (cit. on p. 23).

[87]A. M. Zagoskin, S. Savel'ev and F. Nori, "Modeling an adiabatic quantum computer via an exact map to a gas of particles", Phys. Rev. Lett. **98**, 120503 (2007) (cit. on p. 23).

[88]D. Jaksch, C. Bruder, J. I. Cirac, C. W. Gardiner and P. Zoller, "Cold bosonic atoms in optical lattices", Phys. Rev. Lett. **81**, 3108–3111 (1998) (cit. on p. 23).

[89]L. Lamata, J. León, T. Schaetz and E Solano, "Dirac equation and quantum relativistic effects in a single trapped ion", Phys. Rev. Lett. **98**, 253005 (2007) (cit. on p. 23).

[90]R. Gerritsma, G. Kirchmair, F. Zähringer, E Solano, R Blatt and C. F. Roos, "Quantum simulation of the Dirac equation", Nature (London) **463**, 68–71 (2010) (cit. on p. 23).

[91]R. Gerritsma, B. P. Lanyon, G. Kirchmair, F. Zähringer, C. Hempel, J. Casanova, J. J. García-Ripoll, E. Solano, R. Blatt and C. F. Roos, "Quantum simulation of the Klein paradox with trapped ions", Phys. Rev. Lett. **106**, 060503 (2011) (cit. on p. 23).

[92]P. Hauke, F. M. Cucchietti, L. Tagliacozzo, I. Deutsch and M. Lewenstein, "Can one trust quantum simulators?", Rep. Prog. Phys. **75**, 082401 (2012) (cit. on p. 23).

[93]A. Friedenauer, H. Schmitz, J. T. Glueckert, D. Porras and T. Schaetz, "Simulating a quantum magnet with trapped ions", Nature Phys. **4**, 757–761 (2008) (cit. on pp. 24, 28, 48).

[94]F Schmidt-Kaler, S Gulde, M Riebe, T Deuschle, A Kreuter, G Lancaster, C Becher, J Eschner, H Häffner and R Blatt, "The coherence of qubits based on single ca^+ ions", J. Phys. B **36**, 623 (2003) (cit. on p. 24).

[95]D. Jaksch and P. Zoller, "The cold atoms Hubbard toolbox", Ann. Phys. (Leipzig) **315**, 52 (2005) (cit. on p. 24).

[96]M. Lewenstein, A. Sanpera, V. Ahufinger, B. Damski, A. Sen(De) and U. Sen, "Ultracold atomic gases in optical lattices: mimicking condensed matter physics and beyond", Adv. Phys. **56**, 243–379 (2007) (cit. on pp. 24, 25).

[97]I. Bloch, J. Dalibard and W. Zwerger, "Many-body physics with ultracold gases", Rev. Mod. Phys. **80**, 885–964 (2008) (cit. on p. 24).

[98]J. Dalibard, F. Gerbier and P. Öhberg, "Colloquium: artificial gauge potentials for neutral atoms", Rev. Mod. Phys. **83**, 1523–1543 (2011) (cit. on pp. 24, 25).

[99]I. Bloch, J. Dalibard and S. Nascimbene, "Quantum simulations with ultracold quantum gases", Nature Phys. **8**, 267–276 (2012) (cit. on p. 24).

[100]J. You and F. Nori, "Superconducting circuits and quantum information", Phys. Today **58**, 42–47 (2005) (cit. on pp. 24, 26).

[101] J. Clarke and F. K. Wilhelm, "Superconducting quantum bits", Nature (London) **453**, 1031–1042 (2008) (cit. on pp. 24, 26).

[102] R. J. Schoelkopf and S. M. Girvin, "Wiring up quantum systems", Nature (London) **451**, 664–669 (2008) (cit. on pp. 24, 26).

[103] J. Q. You and F. Nori, "Atomic physics and quantum optics using superconducting circuits", Nature (London) **474**, 589–597 (2011) (cit. on pp. 24, 26).

[104] M. Greiner, O. Mandel, T. Esslinger, T. W. Hansch and I. Bloch, "Quantum phase transition from a superfluid to a Mott insulator in a gas of ultracold atoms", Nature (London) **415**, 39–44 (2002) (cit. on p. 25).

[105] G.-B. Jo, J. Guzman, C. K. Thomas, P. Hosur, A. Vishwanath and D. M. Stamper-Kurn, "Ultracold atoms in a tunable optical kagome lattice", Phys. Rev. Lett. **108**, 045305 (2012) (cit. on p. 25).

[106] P. Hauke, O. Tieleman, A. Celi, C. Ölschläger, J. Simonet, J. Struck, M. Weinberg, P. Windpassinger, K. Sengstock, M. Lewenstein and A. Eckardt, "Non-abelian gauge fields and topological insulators in shaken optical lattices", Phys. Rev. Lett. **109**, 145301 (2012) (cit. on pp. 25, 100).

[107] C. Weitenberg, M. Endres, J. F. Sherson, M. Cheneau, P. Schausz, T. Fukuhara, I. Bloch and S. Kuhr, "Single-spin addressing in an atomic Mott insulator", Nature (London) **471**, 319–324 (2011) (cit. on p. 25).

[108] A. Micheli, G. K. Brennen and P. Zoller, "A toolbox for lattice-spin models with polar molecules", Nature Phys. **2**, 341–347 (2006) (cit. on p. 25).

[109] H. Weimer, M. Müller, I. Lesanovsky, P. Zoller and H. P. Büchler, "A Rydberg quantum simulator", Nature Phys. **6**, 382–388 (2010) (cit. on p. 25).

[110] A. W. Glaetzle, M. Dalmonte, R. Nath, C. Gross, I. Bloch and P. Zoller, "Designing frustrated quantum magnets with laser-dressed Rydberg atoms", Phys. Rev. Lett. **114**, 173002 (2015) (cit. on p. 25).

[111] D. I. Tsomokos, S. Ashhab and F. Nori, "Using superconducting qubit circuits to engineer exotic lattice systems", Phys. Rev. A **82**, 052311 (2010) (cit. on p. 27).

[112] A. A. Houck, H. E. Türeci and J. Koch, "On-chip quantum simulation with superconducting circuits", Nature Phys. **8**, 292–299 (2012) (cit. on pp. 27, 75).

[113]S. Schmidt and J. Koch, "Circuit QED lattices: towards quantum simulation with superconducting circuits", Ann. Phys. (Leipzig) **525**, 395–412 (2013) (cit. on p. 27).

[114]P. Nevado and D. Porras, "Hidden frustrated interactions and quantum annealing in trapped-ion spin-phonon chains", Phys. Rev. A **93**, 013625 (2016) (cit. on pp. 27, 45, 47, 100).

[115]P. Jurcevic, B. P. Lanyon, P. Hauke, C. Hempel, P. Zoller, R. Blatt and C. F. Roos, "Quasiparticle engineering and entanglement propagation in a quantum many-body system", Nature (London) **511**, 202–205 (2014) (cit. on p. 27).

[116]P. Richerme, Z.-X. Gong, A. Lee, C. Senko, J. Smith, M. Foss-Feig, S. Michalakis, A. V. Gorshkov and C. Monroe, "Non-local propagation of correlations in quantum systems with long-range interactions", Nature (London) **511**, 198–201 (2014) (cit. on p. 27).

[117]G. Clos, D. Porras, U. Warring and T. Schaetz, "Time-resolved observation of thermalization in an isolated quantum system", Phys. Rev. Lett. **117**, 170401 (2016) (cit. on pp. 27, 137).

[118]D Porras and J. I. Cirac, "Effective quantum spin systems with trapped ions", Phys. Rev. Lett. **92**, 1–4 (2004) (cit. on pp. 28, 30, 47, 69, 77, 95, 162).

[119]D. Porras and J. I. Cirac, "Bose-Einstein condensation and strong-correlation behavior of phonons in ion traps", Phys. Rev. Lett. **93**, 263602 (2004) (cit. on pp. 28, 100).

[120]D. Porras, F. Marquardt, J. Von Delft and J. I. Cirac, "Mesoscopic spin-boson models of trapped ions", Phys. Rev. A **78**, 10101 (2008) (cit. on p. 28).

[121]X. L. Deng, D. Porras and J. I. Cirac, "Quantum phases of interacting phonons in ion traps", Phys. Rev. A **77**, 33403 (2008) (cit. on p. 28).

[122]D. Porras, P. A. Ivanov and F. Schmidt-Kaler, "Quantum simulation of the cooperative Jahn-Teller transition in 1D ion crystals", Phys. Rev. Lett. **108**, 235701 (2012) (cit. on pp. 28, 45, 48).

[123]R. Islam, E. Edwards, K. Kim, S. Korenblit, C. Noh, H. Carmichael, G.-D. Lin, L.-M. Duan, C.-C. Joseph Wang, J. Freericks and C. Monroe, "Onset of a quantum phase transition with a trapped ion quantum simulator", Nat. Commun. **2**, 377–(2011) (cit. on p. 28).

[124]K. Kim, M.-S. Chang, S. Korenblit, R. Islam, E. E. Edwards, J. K. Freericks, G.-D. Lin, L.-M. Duan and C. Monroe, "Quantum simulation of frustrated Ising spins with trapped ions", Nature (London) **465**, 590–593 (2010) (cit. on pp. 28, 45, 70, 71, 131).

[125]R. Islam, C. Senko, W. C. Campbell, S. Korenblit, J. Smith, A. Lee, E. E. Edwards, C.-C. J. Wang, J. K. Freericks and C. Monroe, "Emergence and frustration of magnetism with variable-range interactions in a quantum simulator", Science **340**, 583–587 (2013) (cit. on pp. 28, 45, 51, 70, 137).

[126]I. Waki, S. Kassner, G. Birkl and H. Walther, "Observation of ordered structures of laser-cooled ions in a quadrupole storage ring", Phys. Rev. Lett. **68**, 2007–2010 (1992) (cit. on p. 28).

[127]G. Birkl, S. Kassner and H. Walther, "Multiple-shell structures of laser-cooled $^{24}Mg^{+}$ ions in a quadrupole storage ring", Nature (London) **357**, 310–313 (1992) (cit. on p. 28).

[128]T. W. Hänsch and A. L. Schawlow, "Cooling of gases by radiation pressure", Opt. Commun. **13**, 68–69 (1975) (cit. on pp. 28, 36).

[129]D. J. Wineland, R. E. Drullinger and F. L. Walls, "Radiation-pressure cooling of bound resonant absorbers", Phys. Rev. Lett. **40**, 1639–1642 (1978) (cit. on pp. 28, 36).

[130]W. Paul, "Electromagnetic traps for charged and neutral particles", Rev. Mod. Phys. **62**, 531–540 (1990) (cit. on p. 29).

[131]J. Chiaverini, R. B. Blakestad, J. Britton, J. D. Jost, C. Langer, D. Leibfried, R. Ozeri and D. J. Wineland, "Surface-electrode architecture for ion-trap quantum information processing", Quantum Info. Comput. **5**, 419–439 (2005) (cit. on p. 29).

[132]S. Seidelin, J. Chiaverini, R. Reichle, J. J. Bollinger, D. Leibfried, J. Britton, J. H. Wesenberg, R. B. Blakestad, R. J. Epstein, D. B. Hume, W. M. Itano, J. D. Jost, C. Langer, R. Ozeri, N. Shiga and D. J. Wineland, "Microfabricated surface-electrode ion trap for scalable quantum information processing", Phys. Rev. Lett. **96**, 253003 (2006) (cit. on p. 29).

[133]J. P. Home, D. Hanneke, J. D. Jost, J. M. Amini, D. Leibfried and D. J. Wineland, "Complete methods set for scalable ion trap quantum information processing", Science **325**, 1227–1230 (2009) (cit. on p. 29).

[134]R. Schmied, J. H. Wesenberg and D. Leibfried, "Optimal surface-electrode trap lattices for quantum simulation with trapped ions", Phys. Rev. Lett. **102**, 233002 (2009) (cit. on pp. 29, 75, 95).

[135]M. Kumph, M. Brownnutt and R. Blatt, "Two-dimensional arrays of radio-frequency ion traps with addressable interactions", New J. Phys. **13**, 073043 (2011) (cit. on pp. 29, 75, 95).

[136]R. Sterling, H Rattanasonti, S Weidt, K Lake, P Srinivasan, S. Webster, M Kraft and W. Hensinger, "Fabrication and operation of a two-dimensional ion-trap lattice on a high-voltage microchip", Nat. Commun. **5**, 3637– (2014) (cit. on pp. 29, 75, 95).

[137]A. C. Wilson, Y. Colombe, K. R. Brown, E. Knill, D. Leibfried and D. J. Wineland, "Tunable spin-spin interactions and entanglement of ions in separate potential wells", Nature (London) **512**, 57–60 (2014) (cit. on pp. 29, 75, 95).

[138]M Kumph, P Holz, K Langer, M Meraner, M Niedermayr, M Brownnutt and R Blatt, "Operation of a planar-electrode ion-trap array with adjustable RF electrodes", New J. Phys. **18**, 023047 (2016) (cit. on pp. 29, 75, 95).

[139]M. Mielenz, H. Kalis, M. Wittemer, F. Hakelberg, U. Warring, R. Schmied, M. Blain, P. Maunz, D. L. Moehring, D. Leibfried and T. Schaetz, "Arrays of individually controlled ions suitable for two-dimensional quantum simulations", Nat. Commun. **7**, 11839 (2016) (cit. on pp. 29, 75, 95).

[140]H. Dehmelt, "Experiments with an isolated subatomic particle at rest", Rev. Mod. Phys. **62**, 525–530 (1990) (cit. on p. 29).

[141]W. D. Phillips, "Nobel lecture: laser cooling and trapping of neutral atoms", Rev. Mod. Phys. **70**, 721–741 (1998) (cit. on p. 29).

[142]C. Schneider, M. Enderlein, T. Huber and T. Schaetz, "Optical trapping of an ion", Nat. Photon. **4**, 772–775 (2010) (cit. on pp. 29, 31).

[143]C. Cormick, T. Schaetz and G. Morigi, "Trapping ions with lasers", New J. Phys. **13**, 043019 (2011) (cit. on p. 29).

[144]J. N. Tan, J. J. Bollinger, B. Jelenkovic and D. J. Wineland, "Long-range order in laser-cooled, atomic-ion Wigner crystals observed by Bragg scattering", Phys. Rev. Lett. **75**, 4198–4201 (1995) (cit. on p. 29).

[145]W. M. Itano, J. J. Bollinger, J. N. Tan, B. Jelenković, X.-P. Huang and D. J. Wineland, "Bragg diffraction from crystallized ion plasmas", Science **279**, 686–689 (1998) (cit. on p. 29).

[146]T. B. Mitchell, J. J. Bollinger, D. H. E. Dubin, X.-P. Huang, W. M. Itano and R. H. Baughman, "Direct observations of structural phase transitions in planar crystallized ion plasmas", Science **282**, 1290–1293 (1998) (cit. on p. 29).

[147]D. Porras and J. I. Cirac, "Quantum manipulation of trapped ions in two dimensional Coulomb crystals", Phys. Rev. Lett. **96**, 250501 (2006) (cit. on p. 29).

[148]J. W. Britton, B. C. Sawyer, A. C. Keith, C.-C. J. Wang, J. K. Freericks, H. Uys, M. J. Biercuk and J. J. Bollinger, "Engineered two-dimensional Ising interactions in a trapped-ion quantum simulator with hundreds of spins", Nature (London) **484**, 489–492 (2012) (cit. on p. 29).

[149]D. Leibfried, R. Blatt, C. Monroe and D. Wineland, "Quantum dynamics of single trapped ions", Rev. Mod. Phys. **75**, 281–324 (2003) (cit. on pp. 29, 31, 33, 36, 68, 69, 95, 130).

[150]J. J. Bollinger, D. J. Heizen, W. M. Itano, S. L. Gilbert and D. J. Wineland, "A 303-MHz frequency standard based on trapped Be^+ ions", IEEE Trans. Instrum. Meas. **40**, 126–128 (1991) (cit. on p. 31).

[151]P. T. H. Fisk, M. J. Sellars, M. A. Lawn, C. Coles, A. G. Mann and D. G. Blair, "Very high Q microwave spectroscopy on trapped $^{171}Yb^{+}$ ions: application as a frequency standard", IEEE Trans. Instrum. Meas. **44**, 113–116 (1995) (cit. on p. 31).

[152]F. Mintert and C. Wunderlich, "Ion-trap quantum logic using microwave radiation", Phys. Rev. Lett. **87**, 257904 (2001) (cit. on p. 32).

[153]M Johanning, N. Braun, V. Timoney, W. Elman, W. Neuhauser and C. Wunderlich, "Individual addressing of trapped ions and coupling of motional and spin states using RF radiation", Phys. Rev. Lett. **102**, 073004 (2009) (cit. on p. 32).

[154]C. Cohen-Tannoudji, J. Dupont-Roc and G. Grynberg, *Photons & atoms* (Wiley, New York, 1989) (cit. on p. 32).

[155]D. Wineland, C. Monroe, W. Itano, D. Leibfried, B. King and D. Meekhof, "Experimental issues in coherent quantum-state manipulation of trapped atomic ions", J. Res. Natl. Inst. Stand. Technol. **103**, 259–328 (1998) (cit. on pp. 32, 33).

[156]D. J. Wineland, M. Barrett, J. Britton, J. Chiaverini, B. DeMarco, W. M. Itano, B. Jelenković, C. Langer, D. Leibfried, V. Meyer, T. Rosenband and T. Schaetz, "Quantum information processing with trapped ions", Phil. Trans. R. Soc. London, Ser. A **361**, 1349–1361 (2003) (cit. on pp. 33, 35).

[157]E. Brion, L. H. Pedersen and K. Mølmer, "Adiabatic elimination in a lambda system", J. Phys. A **40**, 1033 (2007) (cit. on p. 33).

[158]P. J. Lee, K. Brickman, L. Deslauriers, P. C. Haljan, L.-M. Duan and C. Monroe, "Phase control of trapped ion quantum gates", J. Opt. B **371**, 21 (2005) (cit. on p. 35).

[159]C. F. Roos, "Ion trap quantum gates with amplitude-modulated laser beams", New J. Phys. **10**, 13002 (2008) (cit. on p. 35).

[160]D Leibfried, B DeMarco, V Meyer, D Lucas, M Barrett, J Britton, W. M. Itano, B Jelenković, C Langer, T Rosenband and D. J. Wineland, "Experimental demonstration of a robust, high-fidelity geometric two ion-qubit phase gate", Nature (London) **422**, 412–5 (2003) (cit. on p. 35).

[161]W. Happer, "Optical pumping", Rev. Mod. Phys. **44**, 169–249 (1972) (cit. on p. 36).

[162]D. J. Wineland and W. M. Itano, "Laser cooling of atoms", Phys. Rev. A **21**, 1521 (1979) (cit. on p. 36).

[163]D. J. Wineland, J. C. Bergquist, W. M. Itano and R. E. Drullinger, "Double-resonance and optical-pumping experiments on electromagnetically confined, laser-cooled ions", Opt. Lett. **5**, 245 (1980) (cit. on p. 36).

[164]W. Nagourney, J. Sandberg and H. Dehmelt, "Shelved optical electron amplifier: observation of quantum jumps", Phys. Rev. Lett. **56**, 2797–2799 (1986) (cit. on p. 36).

[165]T. Sauter, W. Neuhauser, R. Blatt and P. Toschek, "Observation of quantum jumps", Phys. Rev. Lett. **57**, 1696–1698 (1986) (cit. on p. 36).

[166]J. C. Bergquist, R. G. Hulet, W. M. Itano and D. J. Wineland, "Observation of quantum jumps in a single atom", Phys. Rev. Lett. **57**, 1699 (1986) (cit. on p. 36).

[167]K. G. Wilson, "The renormalization group: critical phenomena and the Kondo problem", Rev. Mod. Phys. **47**, 773–840 (1975) (cit. on p. 37).

[168]S. D. Drell, M. Weinstein and S. Yankielowicz, "Quantum field theories on a lattice: variational methods for arbitrary coupling strengths and the Ising model in a transverse magnetic field", Phys. Rev. D **16**, 1769–1781 (1977) (cit. on p. 37).

[169]R. Jullien, P. Pfeuty, J. N. Fields and S. Doniach, "Zero-temperature renormalization method for quantum systems. I. Ising model in a transverse field in one dimension", Phys. Rev. B **18**, 3568–3578 (1978) (cit. on p. 37).

[170]G. Vidal, J. I. Latorre, E. Rico and A. Kitaev, "Entanglement in quantum critical phenomena", Phys. Rev. Lett. **90**, 227902 (2003) (cit. on p. 38).

[171]J. I. Latorre, E. Rico and G. Vidal, "Ground state entanglement in quantum spin chains", Quant. Inf. Comput. **4**, 48–92 (2004) (cit. on p. 38).

[172]F. Verstraete and J. I. Cirac, "Renormalization algorithms for quantum-many body systems in two and higher dimensions", arXiv:cond-mat/0407066 (2004) (cit. on p. 38).

[173]F. Verstraete, M. Wolf, D. Pérez-García and J. I. Cirac, "Projected entangled states: properties and applications", Int. J. Mod. Phys. B **20**, 5142–5153 (2006) (cit. on p. 38).

[174]G. Vidal, "Entanglement renormalization", Phys. Rev. Lett. **99**, 220405 (2007) (cit. on p. 38).

[175]G. Vidal, "Class of quantum many-body states that can be efficiently simulated", Phys. Rev. Lett. **101**, 110501 (2008) (cit. on p. 38).

[176]C. Lacroix, P. Mendels and F. Mila, *Introduction to frustrated magnetism: materials, experiments, theory*, Vol. 164 (Springer Science & Business Media, 2011) (cit. on pp. 43, 57).

[177]G. H. Wannier, "Antiferromagnetism. The triangular Ising net", Phys. Rev. **79**, 357–364 (1950) (cit. on p. 43).

[178]S. T. Bramwell and M. J. P. Gingras, "Spin ice state in frustrated magnetic pyrochlore materials", Science **294**, 1495–1501 (2001) (cit. on p. 44).

[179]M. J. P. Gingras, "Spin ice", arXiv:0903.2772 (2009) (cit. on p. 44).

[180]P. Strack and S. Sachdev, "Dicke quantum spin glass of atoms and photons", Phys. Rev. Lett. **107**, 277202 (2011) (cit. on p. 45).

[181]S. Gopalakrishnan, B. L. Lev and P. M. Goldbart, "Frustration and glassiness in spin models with cavity-mediated interactions", Phys. Rev. Lett. **107**, 277201 (2011) (cit. on p. 45).

[182]K. Kim, S. Korenblit, R. Islam, E. E. Edwards, M.-S. Chang, C. Noh, H. Carmichael, G.-D. Lin, L.-M. Duan, C. C. Joseph-Wang, J. K. Freericks and C. Monroe, "Quantum simulation of the transverse Ising model with trapped ions", New J. Phys. **13**, 105003 (2011) (cit. on pp. 45, 48).

[183]G. Zhu, S. Schmidt and J. Koch, "Dispersive regime of the Jaynes-Cummings and Rabi lattice", New J. Phys. **15**, 115002 (2013) (cit. on p. 45).

[184]A. Kurcz, A. Bermudez and J. J. García-Ripoll, "Hybrid quantum magnetism in circuit QED: from spin-photon waves to many-body spectroscopy", Phys. Rev. Lett. **112**, 180405 (2014) (cit. on pp. 45, 87, 96).

[185]P. Nevado and D. Porras, "Rabi lattice models with discrete gauge symmetry: Phase diagram and implementation in trapped-ion quantum simulators", Phys. Rev. A **92**, 013624 (2015) (cit. on pp. 45, 73).

[186]E. Farhi, J. Goldstone, S. Gutmann and M. Sipser, "Quantum computation by adiabatic evolution", arXiv:quant-ph/0001106 (2000) (cit. on pp. 46, 61, 62).

[187]G. E. Santoro and E. Tosatti, "Optimization using quantum mechanics: quantum annealing through adiabatic evolution", J. Phys. A **39**, R393 (2006) (cit. on pp. 46, 61, 62).

[188]A. Das and B. K. Chakrabarti, "*Colloquium* : quantum annealing and analog quantum computation", Rev. Mod. Phys. **80**, 1061–1081 (2008) (cit. on pp. 46, 61, 62).

[189]L. Mandel and E. Wolf, *Optical coherence and quantum optics* (Cambridge University Press, 1995) (cit. on p. 48).

[190]X. L. Deng, D. Porras and J. I. Cirac, "Effective spin quantum phases in systems of trapped ions", Phys. Rev. A **72**, 63407 (2005) (cit. on pp. 48, 100).

[191]K. Hepp and E. H. Lieb, "On the superradiant phase transition for molecules in a quantized radiation field: the Dicke maser model", Ann. Phys. (N.Y.) **76**, 360–404 (1973) (cit. on p. 53).

[192]P. Nevado and D. Porras, "Mesoscopic mean-field theory for spin-boson chains in quantum optical systems", Eur. Phys. J. Spec. Top. **217**, 29–41 (2013) (cit. on pp. 53, 67).

[193]S. Fishman, G. de Chiara, T. Calarco and G. Morigi, "Structural phase transitions in low-dimensional ion crystals", Phys. Rev. B **77**, 064111, 064111 (2008) (cit. on p. 54).

[194]P. Silvi, T. Calarco, G. Morigi and S. Montangero, "*Ab initio* characterization of the quantum linear-zigzag transition using density matrix renormalization group calculations", Phys. Rev. B **89**, 094103 (2014) (cit. on p. 54).

[195]J. J. Hopfield, "Neural networks and physical systems with emergent collective computational abilities", Proc. Natl. Acad. Sci. USA **79**, 2554–2558 (1982) (cit. on p. 56).

[196]D. J. Amit, H. Gutfreund and H. Sompolinsky, "Spin-glass models of neural networks", Phys. Rev. A **32**, 1007–1018 (1985) (cit. on p. 56).

[197]E. Gardner, B. Derrida and P. Mottishaw, "Zero temperature parallel dynamics for infinite range spin glasses and neural networks", J. Phys. (Paris) **48**, 741–755 (1987) (cit. on p. 57).

[198]T. Kadowaki and H. Nishimori, "Quantum annealing in the transverse Ising model", Phys. Rev. E **58**, 5355–5363 (1998) (cit. on p. 62).

[199]Y. Seki and H. Nishimori, "Quantum annealing with antiferromagnetic transverse interactions for the Hopfield model", J. Phys. A **48**, 335301, G5301 (2015) (cit. on p. 62).

[200]M. W. Johnson, M. H. S. Amin, S. Gildert, T. Lanting, F. Hamze, N. Dickson, R. Harris, A. J. Berkley, J. Johansson, P. Bunyk, E. M. Chapple, C. Enderud, J. P. Hilton, K. Karimi, E. Ladizinsky, N. Ladizinsky, T. Oh, I. Perminov, C. Rich, M. C. Thom, E. Tolkacheva, C. J. S. Truncik, S. Uchaikin, J. Wang, B. Wilson and G. Rose, "Quantum annealing with manufactured spins", Nature (London) **473**, 194–198 (2011) (cit. on p. 62).

[201]S. Boixo, T. Albash, F. M. Spedalieri, N. Chancellor and D. A. Lidar, "Experimental signature of programmable quantum annealing", Nat. Commun. **4**, 2067 (2013) (cit. on p. 62).

[202]S. Boixo, T. F. Rønnow, S. V. Isakov, Z. Wang, D. Wecker, D. A. Lidar, J. M. Martinis and M. Troyer, "Evidence for quantum annealing with more than one hundred qubits", Nature Phys. **10**, 218–224 (2014) (cit. on pp. 62, 71, 135).

[203]S. W. Shin, G. Smith, J. A. Smolin and U. Vazirani, "How "quantum" is the D-Wave machine?", arXiv:1401.7087 (2014) (cit. on pp. 63, 135).

[204]P. W. Anderson, "The resonating valence bond state in La_2CuO_4 and superconductivity", Science **235**, 1196–1198 (1987) (cit. on p. 71).

[205]J. B. Kogut, "An introduction to lattice gauge theory and spin systems", Rev. Mod. Phys. **51**, 659–713 (1979) (cit. on pp. 72, 74).

[206]E. Zohar, J. I. Cirac and B. Reznik, "Simulating compact quantum electrodynamics with ultracold atoms: probing confinement and nonperturbative effects", Phys. Rev. Lett. **109**, 125302 (2012) (cit. on p. 72).

[207]P. Hauke, D. Marcos, M. Dalmonte and P. Zoller, "Quantum simulation of a lattice Schwinger model in a chain of trapped ions", Phys. Rev. X **3**, 041018 (2013) (cit. on p. 72).

[208]S. Elitzur, "Impossibility of spontaneously breaking local symmetries", Phys. Rev. D **12**, 3978–3982 (1975) (cit. on p. 74).

[209]M. Müller, L. Liang, I. Lesanovsky and P. Zoller, "Trapped Rydberg ions: from spin chains to fast quantum gates", New J. Phys. **10**, 093009 (2008) (cit. on p. 75).

[210]P. A. Ivanov and D. Porras, "Adiabatic quantum metrology with strongly correlated quantum optical systems", Phys. Rev. A **88**, 023803 (2013) (cit. on pp. 79, 97).

[211]G. Baym, *Lectures on quantum mechanics* (Benjamin, 1969) (cit. on p. 85).

[212]R. Silbey and R. A. Harris, "Variational calculation of the dynamics of a two level system interacting with a bath", J. Chem. Phys. **80**, 2615–2617 (1984) (cit. on p. 87).

[213]A. Kurcz, J. Garcia-Ripoll and A. Bermudez, "The interspersed spin boson lattice model", Eur. J. Phys. ST **224**, 483–496– (2015) (cit. on pp. 87, 96).

[214]G. Díaz-Camacho, A. Bermudez and J. J. García-Ripoll, "Dynamical polaron *Ansatz* : a theoretical tool for the ultrastrong-coupling regime of circuit QED", Phys. Rev. A **93**, 043843 (2016) (cit. on p. 96).

[215]V. Banerjee, S. Dattagupta and P. Sen, "Hysteresis in a quantum spin model", Phys. Rev. E **52**, 1436–1446 (1995) (cit. on pp. 97, 136).

[216]Z. Nussinov and G. Ortiz, "Sufficient symmetry conditions for topological quantum order", Proc. Natl. Acad. Sci. USA **106**, 16944–16949 (2009) (cit. on p. 99).

[217]M. Endres, M. Cheneau, T. Fukuhara, C. Weitenberg, P. Schauß, C. Gross, L. Mazza, M. C. Bañuls, L. Pollet, I. Bloch and S. Kuhr, "Observation of correlated particle-hole pairs and string order in low-dimensional Mott insulators", Science **334**, 200–203 (2011) (cit. on p. 99).

[218]S. Ryu and Y. Hatsugai, "Topological origin of zero-energy edge states in particle-hole symmetric systems", Phys. Rev. Lett. **89**, 077002 (2002) (cit. on pp. 99, 104, 116).

[219]C. L. Kane and E. J. Mele, "Quantum spin Hall effect in graphene", Phys. Rev. Lett. **95**, 226801 (2005) (cit. on p. 99).

[220]B. A. Bernevig, T. L. Hughes and S.-C. Zhang, "Quantum spin Hall effect and topological phase transition in HgTe quantum wells", Science **314**, 1757–1761 (2006) (cit. on p. 99).

[221]Y. L. Chen, J. G. Analytis, J.-H. Chu, Z. K. Liu, S.-K. Mo, X. L. Qi, H. J. Zhang, D. H. Lu, X. Dai, Z. Fang, S. C. Zhang, I. R. Fisher, Z. Hussain and Z.-X. Shen, "Experimental realization of a three-dimensional topological insulator, Bi_2Te_3", Science **325**, 178–181 (2009) (cit. on p. 100).

[222]S.-L. Zhu, L.-B. Shao, Z. D. Wang and L.-M. Duan, "Probing non-abelian statistics of Majorana fermions in ultracold atomic superfluid", Phys. Rev. Lett. **106**, 100404 (2011) (cit. on p. 100).

[223]N. Y. Yao, C. R. Laumann, A. V. Gorshkov, S. D. Bennett, E. Demler, P. Zoller and M. D. Lukin, "Topological flat bands from dipolar spin systems", Phys. Rev. Lett. **109**, 266804 (2012) (cit. on p. 100).

[224]N. Y. Yao, A. V. Gorshkov, C. R. Laumann, A. M. Läuchli, J. Ye and M. D. Lukin, "Realizing fractional Chern insulators in dipolar spin systems", Phys. Rev. Lett. **110**, 185302 (2013) (cit. on p. 100).

[225]S.-T. Wang, D.-L. Deng and L.-M. Duan, "Probe of three-dimensional chiral topological insulators in an optical lattice", Phys. Rev. Lett. **113**, 033002 (2014) (cit. on p. 100).

[226]M. Mancini, G. Pagano, G. Cappellini, L. Livi, M. Rider, J. Catani, C. Sias, P. Zoller, M. Inguscio, M. Dalmonte and L. Fallani, "Observation of chiral edge states with neutral fermions in synthetic Hall ribbons", Science **349**, 1510–1513 (2015) (cit. on p. 100).

[227]I. Cohen and A. Retzker, "Proposal for verification of the Haldane phase using trapped ions", Phys. Rev. Lett. **112**, 040503 (2014) (cit. on p. 100).

[228]C. Senko, P. Richerme, J. Smith, A. Lee, I. Cohen, A. Retzker and C. Monroe, "Realization of a quantum integer-spin chain with controllable interactions", Phys. Rev. X **5**, 021026 (2015) (cit. on p. 100).

[229]Z.-X. Gong, M. F. Maghrebi, A. Hu, M. L. Wall, M. Foss-Feig and A. V. Gorshkov, "Topological phases with long-range interactions", Phys. Rev. B **93**, 041102 (2016) (cit. on p. 100).

[230]W. P. Su, J. R. Schrieffer and A. J. Heeger, "Solitons in polyacetylene", Phys. Rev. Lett. **42**, 1698–1701 (1979) (cit. on p. 100).

[231]W. P. Su, J. R. Schrieffer and A. J. Heeger, "Soliton excitations in polyacetylene", Phys. Rev. B **22**, 2099–2111 (1980) (cit. on p. 100).

[232]A. J. Heeger, S. Kivelson, J. R. Schrieffer and W. P. Su, "Solitons in conducting polymers", Rev. Mod. Phys. **60**, 781–850 (1988) (cit. on p. 100).

[233]J. Asbóth, L. Oroszlány and A. Pályi, *A short course on topological insulators: band structure and edge states in one and two dimensions* (Springer International Publishing, 2016) (cit. on pp. 101, 103, 106, 115, 132).

[234]J. Zak, "Berry's phase for energy bands in solids", Phys. Rev. Lett. **62**, 2747–2750 (1989) (cit. on pp. 105, 106).

[235]M. V. Berry, "Quantal phase factors accompanying adiabatic changes", Proc. R. Soc. London, Ser. A **392**, 45–57 (1984) (cit. on p. 105).

[236]N. Ashcroft and N. Mermin, *Solid state physics* (Saunders College, Philadelphia, 1976) (cit. on p. 105).

[237]R. Resta, "Macroscopic polarization in crystalline dielectrics: the geometric phase approach", Rev. Mod. Phys. **66**, 899–915 (1994) (cit. on p. 106).

[238]J Almeida, P. C. de Groot, S. F. Huelga, A. M. Liguori and M. B. Plenio, "Probing quantum coherence in qubit arrays", J. Phys. B: At., Mol. Opt. Phys. **46**, 104002 (2013) (cit. on pp. 107, 132).

[239]H. Takayama, Y. R. Lin-Liu and K. Maki, "Continuum model for solitons in polyacetylene", Phys. Rev. B **21**, 2388–2393 (1980) (cit. on pp. 113, 115, 132).

[240]L. Campos Venuti, S. M. Giampaolo, F. Illuminati and P. Zanardi, "Long-distance entanglement and quantum teleportation in XX spin chains", Phys. Rev. A **76**, 052328 (2007) (cit. on p. 124).

[241]J. I. Cirac, R. Blatt, P. Zoller and W. D. Phillips, "Laser cooling of trapped ions in a standing wave", Phys. Rev. A **46**, 2668–2681 (1992) (cit. on p. 130).

[242]A. E. Siegman, *Lasers* (University Science Books, 1990) (cit. on p. 131).

[243]A. Bermudez, T. Schaetz and D. Porras, "Photon-assisted-tunneling toolbox for quantum simulations in ion traps", New J. Phys. **14**, 053049 (2012) (cit. on p. 132).

[244]H. Guo and S. Chen, "Kaleidoscope of symmetry-protected topological phases in one-dimensional periodically modulated lattices", Phys. Rev. B **91**, 041402 (2015) (cit. on p. 132).

[245]L. Li, Z. Xu and S. Chen, "Topological phases of generalized Su-Schrieffer-Heeger models", Phys. Rev. B **89**, 085111 (2014) (cit. on p. 132).

[246]H. Hu, C. Cheng, Z. Xu, H.-G. Luo and S. Chen, "Topological nature of magnetization plateaus in periodically modulated quantum spin chains", Phys. Rev. B **90**, 035150 (2014) (cit. on p. 132).

[247]F. Grusdt, M. Höning and M. Fleischhauer, "Topological edge states in the one-dimensional superlattice Bose-Hubbard model", Phys. Rev. Lett. **110**, 260405 (2013) (cit. on pp. 132, 133).

[248]T. Lanting, A. J. Przybysz, A. Y. Smirnov, F. M. Spedalieri, M. H. Amin, A. J. Berkley, R. Harris, F. Altomare, S. Boixo, P. Bunyk, N. Dickson, C. Enderud, J. P. Hilton, E. Hoskinson, M. W. Johnson, E. Ladizinsky, N. Ladizinsky, R. Neufeld, T. Oh, I. Perminov, C. Rich, M. C. Thom, E. Tolkacheva, S. Uchaikin, A. B. Wilson and G. Rose, "Entanglement in a quantum annealing processor", Phys. Rev. X **4**, 021041 (2014) (cit. on p. 135).

[249]V. Martin-Mayor and I. Hen, "Unraveling quantum annealers using classical hardness", Sci. Rep. **5**, 15324– (2015) (cit. on p. 135).

[250]S. Bera, A. Nazir, A. W. Chin, H. U. Baranger and S. Florens, "Generalized multipolaron expansion for the spin-boson model: environmental entanglement and the biased two-state system", Phys. Rev. B **90**, 075110 (2014) (cit. on p. 136).

[251]Z.-C. Gu and X.-G. Wen, "Tensor-entanglement-filtering renormalization approach and symmetry-protected topological order", Phys. Rev. B **80**, 155131 (2009) (cit. on p. 136).

[252]A. Kitaev, "Unpaired Majorana fermions in quantum wires", Phys. Usp. **44**, 131 (2001) (cit. on p. 136).

[253]A. Zee, *Quantum field theory in a nutshell* (Princeton University Press, 2010) (cit. on p. 162).

[254]H. Yukawa, "On the interaction of elementary particles. I", Proceedings of the Physico-Mathematical Society of Japan **17**, 48–57 (1935) (cit. on p. 162).

[255]L. Lewin, *Polylogarithms and associated functions* (Elsevier Science Ltd, 1981) (cit. on pp. 164, 166).

Appendix A

Analytical expression of the effective Ising couplings

In the regime of weak spin-phonon coupling, and as long as the frequency of the laser force is not resonant with any motional mode, the phonons can be adiabatically eliminated in the description of trapped-ion quantum matter [118]. The dynamics of the system is given in terms of interacting spins alone, and the effective spin interactions are mediated by virtual phonons. Since the phonons are extended objects, the interactions can be long ranged.

Situations in which virtual boson exchange leads to long-range interactions are familiar in physics. One can generically show that there is an attractive interaction between particles which couple to a massive scalar field [253]. In nuclear systems, for instance, neutrons and protons couple to the pion field, and the result of the exchange of this object is a potential energy between them. The corresponding potential is named after Hideki Yukawa, the Japanese physicist who introduced it in 1935 [254], and is given as

$$V_{\text{Yukawa}} = -g\frac{e^{-r/\xi}}{r}, \quad \xi^{-1} = k\,m. \tag{A.1}$$

In this expression, g gives the magnitude of the interaction (with units of energy and distance), and r is the separation between the particles. The range of the interaction is inversely proportional to the mass m of the scalar field (pion), and k is just a constant with units of distance and inverse of mass. Conceptually, the Yukawa potential is important since it makes a connection between the typical energy scale

of the mediating field (the mass of the pion) and the range of the interaction. In particular, we see that when $m \to 0$, the interaction is not bounded by any typical length, and is long ranged. We can carry this intuition over to the case of phonon-mediated spin interactions. In the event of many ions, the energies of phonon modes along a particular direction form a band, whose typical energy scale t_{C} is a function of the Coulomb repulsion and the trapping potential. This quantity, on the other hand, gives the hopping parameter in the phonon chain. It can be equivalently regarded as inversely proportional to the mass in the kinetic energy operator. Therefore, there is a length scale associated with the effective interactions, which is inversely proportional to the mass of the phonon, and therefore proportional to t_{C}. In the event of $t_{\mathrm{C}} \to \infty$, the typical length diverges, and the interactions are long ranged.

To derive a closed expression for the effective ion couplings $J_{j,l}$ of chapter 3, we need to assume that the (detuning) frequency of the laser lies outside the band of transverse normal modes, since otherwise we would create phonon excitations. Furthermore, we are going to assume that the force is detuned from the minimum of the band, and therefore we can approximate well the dispersion relation by a harmonic potential. We work with Periodic Boundary Conditions (PBC) without loss of generality. The dispersion relation of the collective modes of the phonon Hamiltonian (3.5) can be written as

$$H_{\text{phonon}} = \sum_{j,l=1}^{N} \left(\omega_x \delta_{j,l} + \frac{1}{2} t_{\mathrm{C}} F_{j,l} \right) a_j^\dagger a_l = \sum_{j,l=1}^{N} A_{j,l} a_j^\dagger a_l, \tag{A.2}$$

where

$$F_{j,l} = \begin{cases} 0 & \text{if } j = l, \\ \dfrac{1}{|j-l|^3} & \text{if } 0 < |j-l| \leq \dfrac{N}{2}, \\ \dfrac{1}{N - |(j-l)|^3} & \text{if } \dfrac{N}{2} < |j-l| \leq N. \end{cases} \tag{A.3}$$

The matrix $A_{j,l}$ is diagonal in terms of plane waves $M_{j,n} = e^{i\frac{2\pi n}{N} j}, n = 0, \ldots, N-1$. The dispersion relation of the radial modes is given as

$$\omega_n = \sum_{m=0}^{N-1} \sum_{j,l=1}^{N} A_{j,l} M_{j,n} M_{l,m}^* = \omega_x + \frac{t_{\mathrm{C}}}{2} \left(F_{N/2}(-1)^n + \sum_{q=0}^{N/2-1} 2\cos(\frac{2\pi q n}{N}) F_q \right). \tag{A.4}$$

The minimum of ω_n is attained for $n = N/2$, that corresponds to the zigzag configuration shown in Fig. 3.2 (blue line). The energy of this mode can be estimated

as $\omega_{N/2} \simeq \omega_x + 3/4 t_{\mathrm{C}} \zeta(3)$ in the limit $N \to \infty$, where $\zeta(x)$ is the Riemann zeta function [46]. We depict ω_n in Fig. A.1. The dispersion relation gets shifted in the

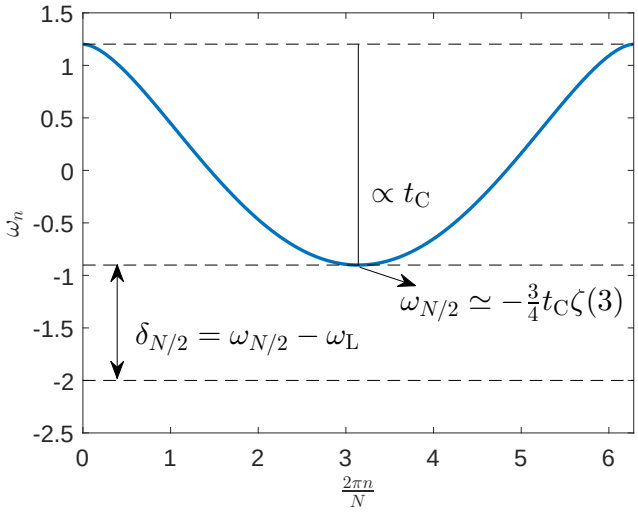

Figure A.1: Dispersion relation of the transverse modes in a trapped-ion chain. We assume $N \to \infty$, $t_{\mathrm{C}} = 1$. We shift the zero of energies so that $\omega_x = 0$. We note that the minimum energy is attained at $\omega_{N/2}$. The width of the band is proportional to t_{C}.

rotating frame of H_{cJT}, so that $\omega_x \to \delta_x = \omega_x - \omega_{\mathrm{L}}$. The continuum limit of the couplings can be written then as

$$J_{j,l} = -\sum_{n=0}^{N-1} \frac{g^2}{\delta_n} \frac{1}{N} e^{i\frac{2\pi n}{N}(j-l)} \overset{N\to\infty}{\sim} -\frac{1}{2\pi} \int_0^{2\pi} \frac{g^2 e^{ix|j-l|}}{\delta(x)} dx, \tag{A.5}$$

where $\delta(x) = \delta_x + t_{\mathrm{C}} \sum_{k=1}^{\infty} \cos(kx)/k^3$. We estimate this integral by means of the residue theorem (cf., e.g., [47]), which allows us to write

$$-\frac{1}{2\pi} \int_0^{2\pi} \frac{g^2 e^{ix|j-l|}}{\delta_x + t_{\mathrm{C}} \sum_{k=1}^{\infty} \frac{\cos(kx)}{k^3}} dx = \operatorname*{Res}_{z=z_+} \left(\frac{g^2 e^{iz|j-l|}}{i\delta(z)} \right) + \frac{1}{2\pi} \int_\gamma \frac{g^2 e^{iz|j-l|}}{\delta(z)} dz. \tag{A.6}$$

In this expression, we have introduced the analytical continuation of $\delta(x)$, that is given by

$$\delta(z) = \delta_x + \frac{t_{\mathrm{C}}}{2} (\mathrm{Li}_3(e^{-iz}) + \mathrm{Li}_3(e^{iz})),\ z = x + iy, \tag{A.7}$$

where $\mathrm{Li}_3(z) = \sum_{k=1}^{\infty} z^k/k^3, |z| \leq 1$ is the polylogarithm function [255]. The integration contour is shown in Fig. A.2(a) along with z_+, which is a simple pole of the integrand. The poles of $1/\delta(z)$ are located in the line $z = \pi$. We depict the one in

the upper complex plane in Fig. A.2(b). Their position can be estimated assuming that they lie very close to the real axis, so that

$$\delta(\pi + iy_\pm) \simeq \delta_x + t_C \sum_{k=1}^{\infty} \frac{(-1)^k}{k^3}(1 - \frac{k^2 y_\pm^2}{2}) = \delta_x - \frac{3}{4}\zeta(3)t_C - y_\pm^2 \ln(2)\frac{t_C}{2}. \quad \text{(A.8)}$$

We solve $\delta(\pi + iy_\pm) \simeq 0$, and since we are only interested in the residue of $\delta(z)$ at the pole, we further assume that $\delta(z) \simeq (z - z_+)(z - z_-)$. Then,

$$2\pi i \,\mathrm{Res}(\frac{-g^2 e^{iz|j-l|}}{2\pi\delta(z)}, z_+) \simeq -(-1)^{|j-l|}\frac{g^2\xi}{t_C \ln(2)} e^{-\frac{|j-l|}{\xi}}, \quad \text{(A.9)}$$

where

$$\xi = \sqrt{\frac{\delta_x - 3/4\zeta(3)t_C}{t_C \ln(2)/2}}. \quad \text{(A.10)}$$

We note that ξ is only well-defined as long as $\delta_x > 3/4 t_C \zeta(3)$. Any detuning frequency below that threshold is resonant with the band of normal modes, and the former argument breaks down. Indeed, the exponential decay (A.9) is the continuous version of the laser being close to resonance with the modes at the base of the dispersion relation, whose effective spread upon the chain is ξ. To estimate the

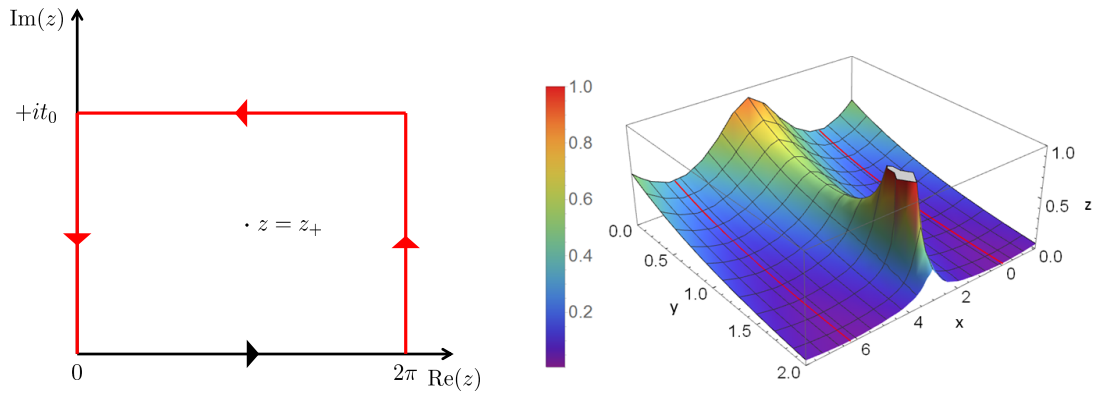

(a) (b)

Figure A.2: (a) Integration contour for the evaluation of (A.6). The curve γ corresponds to the red segments. (b) Plot of $|e^{iz}/\delta(z)|$, with $z = x + iy, \delta_x = 2 + 3/4\zeta(3), t_C = 1$.

integral along γ, we start by neglecting the contribution from the upper segment in Fig. A.2(a). This is justified since the exponential in the numerator cancels

anything far away from the real axis. Regarding the vertical segments, we can make

$$\frac{1}{2\pi}\int_\gamma \frac{g^2 e^{iz|j-l|}}{\delta(z)}dz \simeq \frac{g^2}{2\pi}\left(\int_{t_0}^{0}\frac{e^{-t|j-l|}}{\delta(it)}idt + \int_0^{t_0}\frac{e^{-t|j-l|}}{\delta(2\pi+it)}idt\right) = \frac{g^2}{2\pi}\int_0^{t_0} dt\, ie^{-t|j-l|}\left(\frac{1}{\delta(2\pi+it)}-\frac{1}{\delta(it)}\right) = \frac{g^2}{2\pi}\int_0^{t_0} dt\, ie^{-t|j-l|}(-2i)\,\mathrm{Im}\left(\frac{1}{\delta(it)}\right) \simeq \frac{g^2 t_\mathrm{C}}{4(\delta_x + t_\mathrm{C}\zeta(3))^2}\int_0^\infty t^2 e^{-t|j-l|}dt. \tag{A.11}$$

In this derivation, we have relied on the fact that $\delta(it)$ and $\delta(2\pi+it)$ belong to different branches of the polylogarithm, for which the imaginary part changes its sign [255]. Also, we approximate $1/\delta(it)$ by its series expansion, to second order, for $t \to 0^+$, since these are the only values not exponentially eliminated by $e^{-t|j-l|}$. We have assumed as well that no further error is included if we make $t_0 \to \infty$. Performing the previous integral, we arrive at

$$\frac{1}{2\pi}\int_\gamma \frac{g^2 e^{iz|j-l|}}{\delta(z)}dz \simeq \frac{g^2 t_\mathrm{C}}{2(\delta_x + t_\mathrm{C}\zeta(3))^2}\frac{1}{|j-l|^3},\ |j-l| \gg 1. \tag{A.12}$$

Finally, defining $\delta_{N/2} \equiv \delta_x - 3/4\zeta(3)t_\mathrm{C}$, which corresponds to the detuning with respect to the bottom of the band of normal modes, we can write the couplings as

$$J_{j,l} \simeq -(-1)^{j-l}J_\mathrm{exp}e^{-|j-l|/\xi} + \frac{J_\mathrm{dip}}{|j-l|^3}_{j\neq l}, \tag{A.13}$$

where

$$J_\mathrm{exp} = \frac{g^2\xi}{t_\mathrm{C}\ln(2)},\ J_\mathrm{dip} = \frac{g^2 t_\mathrm{C}}{2(\delta_{N/2}+7/4\,t_\mathrm{C}\zeta(3))^2},\ \xi = \sqrt{\frac{t_\mathrm{C}\ln(2)}{2\delta_{N/2}}}. \tag{A.14}$$

This expression gives very accurate results even for moderate N when compared to the exact result, as can be seen from Fig. A.3.

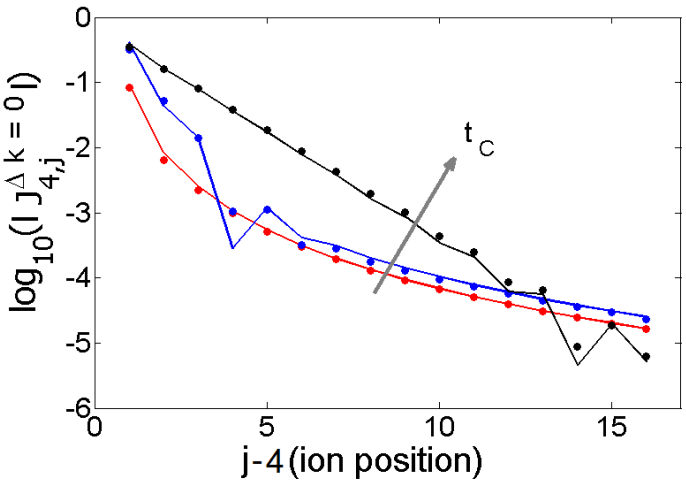

Figure A.3: Effective spin coupling as a function of ion-ion separation in a $N = 20$ ion chain, between ion $j = 4$ and the rest of the chain. Energy units such that $\delta_{N/2} = g = 1$, $t_{\rm C} = 0.1, 1, 5$. Circles: exact calculation. Continuous line: estimate from Eq. (A.13).